EFFECTS of RADIATION and LIGHT IONS BEHAVIOR in CERAMICS FOR FUSION BREEDER BLANKET

AUTHOR:

ELISABETTA CARELLA

DIRECTED BY

MARIA GONZÁLEZ

M. TERESA HERNÁNDEZ

A DISSERTATION FOR THE DEGREE OF DOCTOR OF PHILOSOPHY (MATERIALS PHYSICS)

MADRID, 2014

FACULTAD DE CIENCIAS, DEPARTAMENTO DE FÍSICA DE MATERIALES
GRUPO MIRE (MATERIALS OF INTEREST IN RENEWABLE ENERGY)
UNIVERSIDAD AUTÓNOMA DE MADRID

LABORATORIO NACIONAL DE FUSIÓN
CENTRO DE INVESTIGACIÓN MEDIOAMBIENTALES, ENERGÉTICAS Y TECNOLÓGICAS

EFFECT OF RADIATION AND LIGHT IONS BEHAVIOR IN CERAMICS FOR FUSION BREEDER BLANKET

(EFECTOS DE LA RADIACIÓN Y COMPORTAMIENTO DE LOS IONES LIGEROS EN CERÁMICAS PARA LA ENVOLTURA REGENERADORA DE FUSIÓN)

AUTORA: ELISABETTA CARELLA, LICENCIADA EN CIENCIAS FÍSICAS

DIRECTORAS DE TESIS: MARÍA GONZÁLEZ, DOCTORA EN CIENCIAS QUÍMICAS
M.TERESA HERNÁNDEZ, DOCTORA EN CIENCIAS QUÍMICAS

TUTOR: JOSÉ FRANCISCO FERNÁNDEZ, DOCTOR EN CIENCIAS FÍSICAS

2014

Según la forma de andar de cada cual, se puede ver si ha encontrado su camino.
El hombre que se acerca a su objetivo ya no camina, baila.

Friedrich Nietzsche, Así habló Zaratustra

The good life is one inspired by love and guided by knowledge.

Bertrand Russell, Why I am not a Christian

Science alone of all the subjects contains within itself the lesson of the danger of belief in the infallibility of the greatest teachers in the preceding generation ... Learn from science that you must doubt the experts. As a matter of fact, I can also define science another way:
Science is the belief in the ignorance of experts.

Richard Feynman, The Pleasure of Finding Things Out : The Best Short Works of Richard Feynman

A Giusi, Lella y Nino
con toda mi gratitud y amor por ser tan increíble familia

INDEX

FIGURE INDEX

Figure Index

Figure Index

Figure Index

TABLE INDEX

Table Index

LIST OF ABBREVIATIONS

ATR	**ATTENUATED TOTAL REFLECTION**
BB	**BREEDER BLANKET**
BCA	**BINARY COLLISION APPROXIMATION**
BU	**BREEDER UNIT**
CPS	**COOLANT PURIFICATION SYSTEM**
DCLL	**DUAL COOLANT LITHIUM LEAD BLANKET**
DEMO	**DEMONSTRATION (FUSION POWER PLANT)**
DFT	**DENSITY FUNCTIONAL THEORY**
DPA	**DISPLACEMENT PER ATOM**
DTA	**DIFFERENTIAL THERMAL ANALYSIS**
EIS	**ELECTRICAL IMPEDANCE SPECTROSCOPY**
ESR	**ELECTRON SPIN RESONANCE**
EUROFER	**EUROPEAN FERRITIC MATERIALS**
EXOTIC	**EXTRACTION OF TRITIUM IN CERAMICS**
FIB	**FOCUSED ION BEAM**
HCLL	**HELIUM-COOLED LITHIUM-LEAD**
HCPB	**HELIUM-COOLED PEBBLE-BED**
HELICA	**HELIUM-LITHIUM-CASSETTE**
HFR	**HIGH FLUX REACTOR**
HT	**HYDRIDE TRITIUM**

List of Abbreviations

IBA	**ION BEAM ANALYSIS**
ICP	**INDUCTIVELY COUPLED PLASMA**
IFMIF	**INTERNATIONAL FUSION MATERIALS IRRADIATION FACILITY**
IR	**INFRARED SPECTROSCOPY**
ITER	**INTERNATIONAL THERMONUCLEAR EXPERIMENTAL REACTOR**
Li_2SiO_2	**LITHIUM METASILICATE**
Li_4SiO_4	**LITHIUM ORTHOSILICATE**
Li_6SiO_5	**LITHIUM ESASILICATE**
Li_8SiO_6	**LITHIUM OXOSILICATE**
Li_2TiO_3	**LITHIUM METATITANATE**
MHD	**MAGNETO HYDRO DYNAMICS**
NIF	**NATIONAL IGNITION FACILITY**
NRA	**NUCLEAR REACTION ANALYSIS**
NRT	**NORGETT, ROBINSON, TORRENS**
PAS	**POSITRON ANNIHILATION SPECTROSCOPY**
PBA	**PEBBLE BED ASSEMBLY**
PKA	**PRIMARY KNOCK-ON ATOMS**
PSL	**PHOTO-LUMINESCENCE**
RAFM	**REDUCED ACTIVATION FERRITIC MARTENSITIC**
RE	**REFLUX IN ETHANOL METHOD**
RIC	**RADIATION INDUCED CONDUCTIVITY**
RIED	**RADIATION INDUCED ELECTRICAL DEGRADATION**
RV	**ROTARY EVAPORATOR METHOD**
SD	**SPRAY DRYING METHOD**

List of Abbreviations

SEM	**SCANNING ELECTRON MICROSCOPY**
SIMS	**SECONDARY ION MASS SPECTROMETRY**
SS	**SOLID STATE METHOD**
TBM	**TEST BLANKET MODULES**
TBR	**TRITIUM BREEDING RATIO**
TEM	**TRANSMISSION ELECTRON MICROSCOPY**
TES	**TRITIUM EXTRACTION SYSTEM**
TG	**THERMO-GRAVIMETRY**
TL	**THERMO LUMINESCENCE**
XRD	**X-RAY DIFFRACTION**
WCLL	**WATER COOLED LITHIUM LEAD BLANKET**
WCPB	**WATER COOLED PEBBLE BED**

INTRODUCCIÓN

1. Objetivo

Una de las áreas más importantes a comprender y desarrollar dentro del marco de la Fusión es la envoltura regeneradora (*breeder blanket*) responsable de la producción y extracción del tritio, componente fundamental del combustible para la fusión. Dada su función múltiple como generador de tritio y envoltura protectora de los imanes, este componente tiene que trabajar bajo condiciones severas de irradiación y temperatura, blindar las bobinas electromagnéticas que controlan el plasma y conservar sus características físico-químicas para seguir produciendo tritio de forma eficiente a lo largo de un tiempo. Se han desarrollado numerosos modelos, muy diferentes entre ellos, que serán testados en ITER, el primer reactor experimental de Fusión termonuclear. Entre ellos, el más antiguo y más estudiado es el modelo sólido compuesto por cerámicas de litio generadoras de tritio y berilio como multiplicador de neutrones. Este modelo a su vez puede contar con diferentes tipos de refrigeración: vía agua (WCPB) o vía helio (HCPB). El modelo desarrollado por Europa es el HCPB, aunque los resultados encontrados en esta tesis se pueden trasladar al otro, desarrollado principalmente por Japón.

La cantidad de tritio existente en un reactor en un momento dado se conoce con el término *inventario de tritio*. Debido al riesgo radiológico asociado a la liberación de tritio, resulta obvio que el inventario de tritio en un reactor debe ser mínimo, por lo tanto se debe controlar la cantidad y la velocidad de transporte (difusión). Tanto la difusión como la solubilidad son dos fenómenos fuertemente dependientes de la temperatura y de los daños de irradiación.

La idea principal del presente trabajo es estudiar el comportamiento de diferentes cerámicas de litio en distintas condiciones para entender el efecto de la radiación e intentar extrapolar una medida indirecta acerca del comportamiento del tritio.

En primer lugar, se ha intentado suplir a la falta de información sobre el comportamiento de estos materiales bajo irradiación gamma mediante simulación experimental. Si se considera la función de blindaje de los imanes, es muy

importante que su capacidad como aislante no varíe y, por lo tanto, sus propiedades eléctricas. Por otro lado es conocida la contribución iónica a la conductividad eléctrica en los óxidos de litio. A partir de estas dos consideraciones, se proponen las medidas de impedancia en el volumen de materiales previamente irradiados con radiación gamma a diferentes dosis. De esta manera se ha estudiado no solo el carácter aislante de los materiales al variar del daño de la red cristalina, sino el efecto del movimiento de los iones de litio en la estructura. Mediante el estudio de su movilidad, se propone un estudio indirecto del tritio.

Otro de los temas abordados ha sido el estudio del comportamiento de iones ligeros, deuterio y helio-3, en diferentes cerámicas de litio. Dada la dificultad en el manejo del tritio, isotopo radiactivo del hidrógeno, se propone el estudio del comportamiento del deuterio y del helio-3 por ser los isótopos más "cercanos" al tritio. Se trata de extrapolar la información obtenida a partir de sus dinámicas de difusión bajo diferentes condiciones experimentales teniendo en cuenta además, que uno de los iones estudiados, el helio-3, es también el producto de decaimiento del T y su comportamiento puede resultar de especial interés en el tratamiento de las cerámicas gastadas.

Los estudios principales se acompañan de medidas secundarias, llevadas a cabo solo en algunos de los materiales utilizados a lo largo de la tesis, con la idea de justificar y validar las hipótesis formuladas.

Cabe destacar que el estudio de estos materiales resulta especialmente complicado por tratarse de materiales policristalinos, polifásicos y con cantidades variables de fase amorfa. Estos hechos hacen difícil la explicación de los fenómenos observados.

Se ha intendado proporcionar al lector las herramientas necesarias para la comprensión de los resultados, a sabiendas de que la discusión presentada está abierta a un mejor desarrollo bajo más horas de discusión y, sobre todo, comparación de diferentes enfoques.

2. Estructura del trabajo

El trabajo se ha dividido en dos partes: una primera de revisión teórica en la que se explican las bases del estudio llevado a cabo para que el lector se sitúe y entienda mejor los resultados experimentales que se recogen en la segunda parte.

Por lo tanto en el Capítulo 1 se introduce la fusión cual una de las más importantes fuentes energéticas del futuro, acercándose de forma específica al componente del reactor del que se ocupa este estudio: la envoltura generadora de tritio (o breeder blanket). Se describen los modelos desarrollados a nivel internacional, enfocando la descripción en el modelo europeo objeto de esta tesis: la envoltura generadora sólida, basada en cerámicas de litio para la producción de tritio y helio para el enfriamiento del módulo.

En el Capítulo 2 se profundiza el concepto de envoltura regeneradora sólida de cerámicas de litio y se describen sus características principales. A raíz de las principales funciones que tiene que cumplir, se describen las propiedades relativas a su estructura cristalina. Se proporcionan los detalles de las redes cristalinas de los materiales utilizados, lo que será de gran utilidad para el entendimiento de algunos de los experimentos propuestos.

En el Capítulo 3 se presenta un resumen teórico de los parámetros principales relacionados al tritio y el combustible del reactor de fusión. Se intenta explicar, a partir de una revisión bibliográfica, los pasos fundamentales que este gas tiene que seguir desde su producción hasta su extracción. Finalmente se explica al lector la información que se pretende obtener de las medidas propuestas.

En el Capítulo 4 se encuentra una breve presentación de los efectos de la radiación en las cerámicas de litio utilizadas como envoltura regeneradora, además de una revisión sobre las principales fuentes de radiación para la producción de defectos utilizadas a lo largo de esta tesis. En este apartado se presentan los principales experimentos sobre los efectos de la radiación con el fin de definir los defectos encontrados en este trabajo.

A partir del Capítulo 5 comienza la parte experimental. En este capítulo se presenta no solo la descripción de las principales técnicas experimentales utilizadas para la caracterización sino el trabajo llevado a cabo en la búsqueda del mejor método de fabricación para conseguir esferas cerámicas con un alto contenido de litio.

El Capítulo 6 se basa en el estudio a través de la técnica de espectroscopia de impedancia del comportamiento eléctrico como medida indirecta, de las modificaciones causadas en la conductividad eléctrica por la radiación gamma en las

redes cristalinas, bien en diferentes estructuras cerámicas bien al variar el contenido en litio. La propuesta que se hace es que la diferente proporción de litio sea comparable a su quemado (*burn-up*) a lo largo del funcionamiento del reactor. Los resultados encontrados proporcionan por lo tanto, una idea de la estabilidad de estos materiales en el tiempo, dato fundamental considerado el papel de la envoltura protectora. A la vez se proponen unas medida de PAS para distinguir la diferente configuración de los defectos en los distintos materiales antes y después de la irradiación con rayos gamma. También se discutirá el papel de la temperatura en la regeneración de defectos a través de estas medidas.

En el Capítulo 7 se presenta un detallado trabajo experimental sobre el comportamiento de dos iones ligeros en las cerámicas de litio: el deuterio y el helio-3. El estudio se basa en la medida del perfil en profundidad a través de las técnicas de haces de iones más precisas y no destructiva para la detección de iones ligeros: el análisis por reacción nuclear. Dicho estudio se ha llevado a cabo en diferentes instalaciones europeas. Se trata de observar el efecto de diferentes microestructuras en la difusión del ion al variar de la temperatura. A continuación se propone un estudio más específico en una sola matriz variando las condiciones de los tratamientos térmicos (tiempo y temperatura), para finalmente observar el efecto de radiaciones ionizantes y del daño estructural en la difusión y salida del ion. Este trabajo se completa con unas medidas de fotoluminiscencia, microscopia de trasmisión y espectroscopía Raman para destacar el efecto de la radiación en la superficie y en la zona de implantación, siendo este un dato muy relevante en la dinámica de salida de los iones

Finalmente se presentarán las conclusiones con los resultados más importantes discutidos en la parte experimental.

La bibliografía así como la lista de contribuciones científicas (publicaciones y congresos) generadas a lo largo de este trabajo, se encuentran al final del documento.

PART I: THEORY

CHAPTER 1

THERMONUCLEAR FUSION ENERGY

In this chapter a brief description of Fusion reactor and of the international projects for its achievement is presented. Starting from a generic description, a focus on all the materials and subsequently on the ones used in this thesis is developed. Finally a description of the breeder blanket module object of this study is provided.

1. Motivation for FUSION research

Future economic growth will have important implications for the energy demand. By 2050, the expected raise in global population from six billion to nine billion and better living standards, could lead to a two to three fold increase in energy consumption (Figure 1.1). No single technology will fulfil this demand. Each has strengths and weaknesses, and a mix of power sources will be needed to meet the challenges of energy security, sustainable development and environmental protection. Future energy supply options may comprise fossil fuels, nuclear fission, fusion, renewable, energy storage and improved energy efficiency [1].

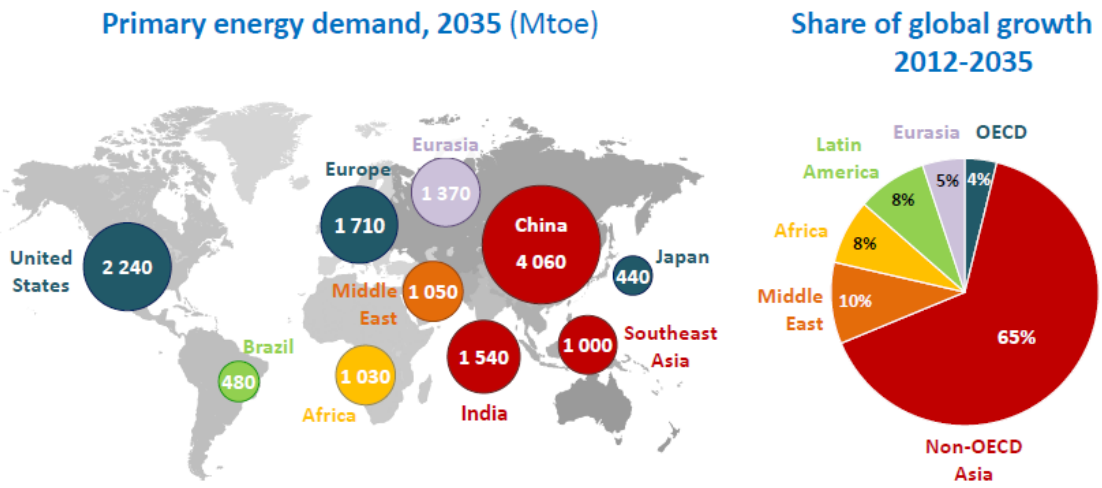

Figure 1.1: World energy consumption with estimated extrapolation. In the inset an estimation of world population growth on which energy growth is based on (Courtesy: IEA [2]).

Fusion power is a potential major source of base-load electricity with attractive features:

- **no greenhouse gas emissions** (the only by-products of fusion reactions are small amounts of helium, which is an inert gas that will not add to atmospheric pollution)**,**
- **abundant and world-wide distributed sources of fuels** (Deuterium can be extracted from water and tritium is produced from lithium, which is found in the earth's crust),
- **no long-lived radioactive waste** (only plant components become radioactive and these will be safe to recycle or dispose of conventionally within 100 years),

- **inherent safety features** (The small amounts of fuel used in fusion devices means that a large-scale nuclear accident is not possible).

In a fusion reaction, the amount of energy released is about four million times as high as the amount of energy released in an ordinary chemical reaction, like the burning of coal. That enormous difference means that a fusion power plant only needs a very small quantity of fuel. To power a fusion power plant of 1 GW for one year with 30% conversion efficiency from thermal to electrical energy, 250 kg of fusion fuel are needed. A coal-fired power plant of the same size needs 2.7 million tons of coal every year. The lithium from one laptop battery, combined with the deuterium in 100 litres of water, can cover the electricity use of an average European citizen for 30 years.

Worldwide identified reserves of lithium in 2011 were estimated by the US Geological Survey as 13 million tonnes, deposits of lithium are found in the Andes mountain chain and Chile is the leading lithium producer, followed by Argentina however, half the world's known reserves are located in Bolivia's Uyuni Desert with 5.4 million tonnes of lithium [3].The last important source is the lithium extraction from ocean sea [4], which give to the fusion energy the politically relevant aspect of presenting a uniformly distributed fuel source in the worldwide.

It is estimated that a first-generation, 'near-term' model would generate electricity for 0.09 €/kWh (the cost is dominated by construction costs, which are checked by comparison with cost estimates for ITER components that have been validated by industry) with a reduction for the first-generation of the most advanced model to 0.05 €/kWh. These costs are based on existing technologies and could be reduced significantly by new developments [5].

The production of fusion reactions can be accomplished, but nowadays such experiments always require the input of far more energy than the released by the fusion reactions. The challenge is not to produce fusion reaction, but to turn fusion into an energy source that generates more energy than it consumes. The big question is*: how long will it take to develop and test the materials and technology needed to make robust, reliable and economical fusion power stations?* [6]. It represents one of the world's most ambitious research endeavors whose results could change the world's energy landscape opening the way to a safe, peaceful, affordable, inexhaustible and CO_2 - free source energy.

1.1. Safety and environmental impact

One of the fusion power plants milestone will be its inherently safety in the sense that any perturbations of the conditions needed to sustain the reaction process lead to immediate shut-down of the fusion reaction. Fusion power plants have limited stocks of energy capable of causing accidents. Although the plasma in a fusion power plant will have a volume of 1000 m^3 or more, the total amount of fusion fuel in the vessel is very small: only few grams. If the fuel supply is closed, the reaction stops without problems within seconds.

Fusion is not a chain reaction and can therefore not run out of hand: in the normal situation, any deviation from the optimum plasma configuration leads to a decrease in temperature or density and thus to a decrease of energy production.

The intermediate fuel, tritium, is a radioactive substance with a small lifetime (about 12.3 years), and fusion power plants are constructed in such a way that a safe handling of the tritium is ensured, which is subject to appropriate laws and regulations. Techniques and expertise to handle tritium safely already exist. As tritium is produced inside the plant in a closed circuit, the total amount of tritium present can be kept as low as possible (a few kg), and outside the plant no transport of tritium is needed, except when a new fusion power plant is constructed [7]. Moreover the stable isotope ^{3}He produced when tritium decays has many uses and is very expensive. Thus a Fusion economy would provide a substantial new resource of ^{3}He, used in medical medicine for the lung and for slow-neutron detectors.

Although the products of the fusion process (helium and neutrons) are not radioactive, the structural materials of the vessel are activated by the neutrons. If proper materials are used, the half-life of most radioisotopes contained in such waste can be limited to about 10 years, meaning that after a period of e.g. 100 years the radioactivity drops to a 10.000th of its initial value, and that most materials can be largely recycled. The design of new, so called *low-activation* materials is an important and active part of the international fusion research. The three areas strongly influenced by neutron activation of materials in a fusion reactor are: (1) long-term management of activated reactor materials after removal from the reactor; (2) hands-on or "contact" reactor maintenance; and (3) reactor safety. The impact of induced radioactivity can be reduced by using materials which either have lower levels of induced activity or have very short decay half-lives (like austenitic stainless or ferritic steels, ceramics such as SiC through restrictions on alloying elements and impurities) [8].

1.2. Fusion as an energy source Fuels

The formulation of a theory in fusion energy involved several important steps regarding the history of the science. The realization that the energy radiated by the Sun and stars is due to nuclear fusion goes from Einstein's theory on energy conservation to Aston's precision measurement of atomic masses, from quantum mechanics to Mendeleev's periodic table, from Chadwick's discover of neutron to Eddington's deductions on the fusion of Hydrogen atoms [9].

Fusion is the process that heats the Sun and all the stars by the collision of atomic nuclei and the release of energy. To obtain it two hydrogen isotopes have to be brought very close together to distances comparable to their size, gaining the electrostatic repulsion, to form a heavier atom of helium. The probability that a fusion reaction will take place is given in the form of a cross section. The cross sections for the three most probable fusion reactions are shown in Figure 1.2. As evident the deuterium-tritium reaction presents a higher probability to lower energy than D-D and D-^{3}He reactions.

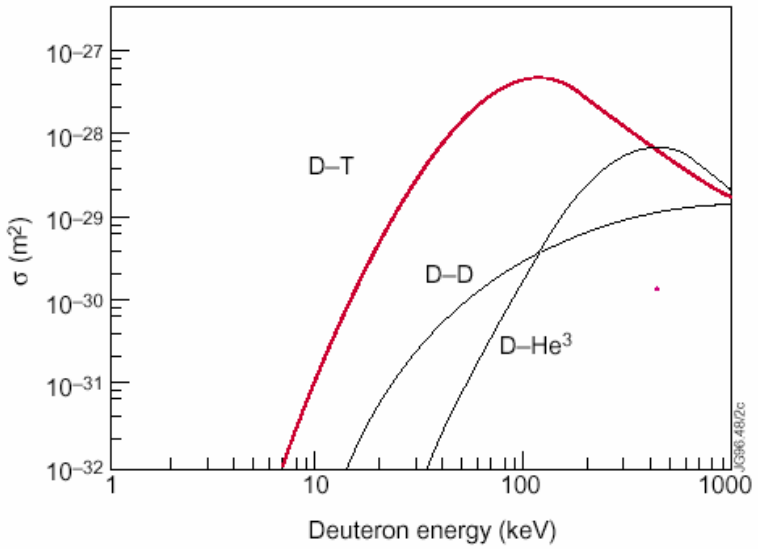

Figure 1.2: The data for three reactions are shown: deuterium plus deuterium, deuterium plus tritium, and deuterium plus helium-3. At lower energies the probability for the D-T reaction is much higher than for the other two reactions.

The only way to achieve it is heating the fuel containing these gases to about $17*10^7$ °C. At these temperatures the fuel becomes a plasma extremely thin and fragile being a million times less dense than air.

One of the fundamental questions is to determine the conditions required for a net energy output from fusion. In the 1955 John Lawson, a physicist at the UK Atomic Energy Establishment at Harwell, calculated the requirements for create more energy than is put in, and came up with a dependence on three quantities: temperature (T), density (n) and confinement time (τ). The maximum fusion power is achieved fusing deuterium and tritium to produce helium and high-speed neutrons, following the reaction:

$$D + T \longrightarrow (^4He + 3.5\ MeV) + (n + 14.1\ MeV) \qquad (1.1).$$

The 17.6 MeV energy released by the fusion reaction is shared between the alpha particle, with 20% of the total energy, and the neutron, with 80%. The neutron has no electric charge and its energy will be converted into heat and then into electricity. The alpha particle has a positive charge and is trapped by the magnetic field, thus its energy can be used to heat the plasma. Initially an external source of energy is needed to raise the plasma temperature, but when the fusion reaction rate increases and the alpha particles provide more and more of the required heating power, the alpha heating is sufficient by itself and the fusion reaction becomes self-sustaining. This point is called **ignition**.

The conditions for D-T magnetic-confinement fusion to reach ignition and run continuously are calculated by setting the alpha particle heating equal to the rate at which energy is lost from the plasma and is commonly known as triple product or *Lawson's criterion*:

$$nT\tau_E > 3 * 10^{21}\ keV\ m^{-3}\ s^{-1} \qquad (1.2)$$

where

n: plasma density (number of fuel ion per cubic meter);

T: temperature;

τ_E: *confinement time*: measures the rate at which the energy is lost from the plasma.

1.3. Reactor designs

Two different options are been developed to reach these extreme conditions: the *inertial* and the *magnetic confinement system*, following very different lines.

In the *inertial confinement* a small pellet of frozen fusion fuel is flash-irradiated by a number of extremely intense laser beams, and heated so quickly that it reaches the conditions for fusion and burns before it has time to escape. The inertia of the

fuel keeps it from escaping. It uses the same principle of the hydrogen bomb but with smaller fuel quantity (about few milligrams in a few millimetre capsules). A large laser facility National Ignition Facility (NIF) at the Lawrence Livermore National Laboratory in California is experimenting and testing inertial fusion [10].

In the *magnetic confinement* the plasma is controlled by a strong magnetic field. The earliest magnetic-confinement devices were developed in the UK in the late 1940s. These were *toroidal pinches* which attempted to confine plasma with a strong, purely poloidal magnetic field produced by toroidal plasma current but this arrangement resulted seriously unstable.

The second approach to toroidal confinement is the ***stellarator***, invented at Princeton in the early 1950s. This evolved as an attempt to confine fusion plasmas by means of a strong toroidal magnetic field produced by an external toroidal solenoid. It is necessary to twist the magnetic field as it passes around the torus so that each field line is wrapped around the inside as well as the outside of the cross section.

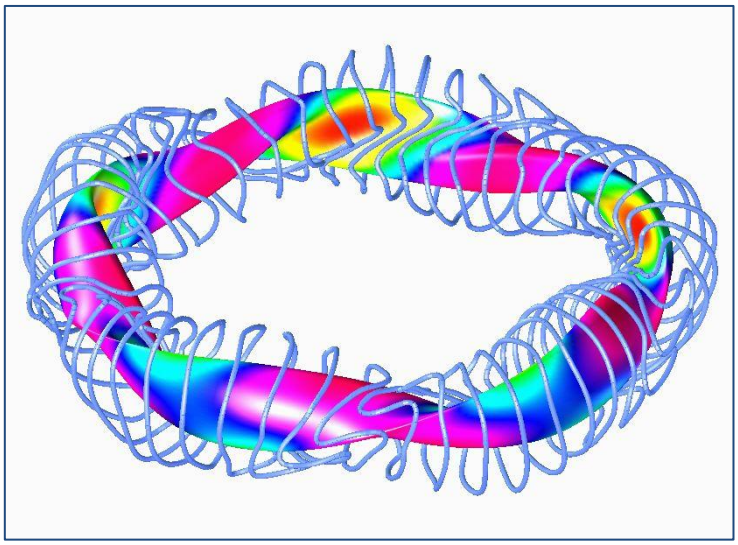

Figure 1.3: Modular coilset and outer magnetic flux surface for the W7-X stellarator.

The advantage of the stallarator is that thanks to the complex shape of the coils, no electrical current is required inside the plasma, implying a number of technical advantages. Although stellarators are very promising as commercial reactors, the research in this direction is still in an earlier phase due to its complex engineering. In Spain since 1997 with the TJ-II machine, in Japan in the largest stellarator, the Large Helical Device since 1998, and in German-Greifswald in the under construction

Wendelstein-7X (see Figure 1.3), the plasma in heliotron configuration is being studied.

The third and most successful, toroidal confinement scheme is the ***tokamak***, developed in Moscow in the 1960s. There are two main magnetic fields. One of these, known as the toroidal field, is produced by a copper coil wound in the shape of a torus. The second magnetic field, the poloidal field, is generated by an electric current that flows in the plasma. The two magnetic fields combine to create a composite magnetic field that twists around the torus in a gentle helix (Figure 1.4). The big problem of this system is that plasma is inherently unstable and always tries to escape from the magnetic field. The plasma extinguishes itself in a sudden manner, known as a disruption: the plasma current abruptly terminates and confinement is lost.

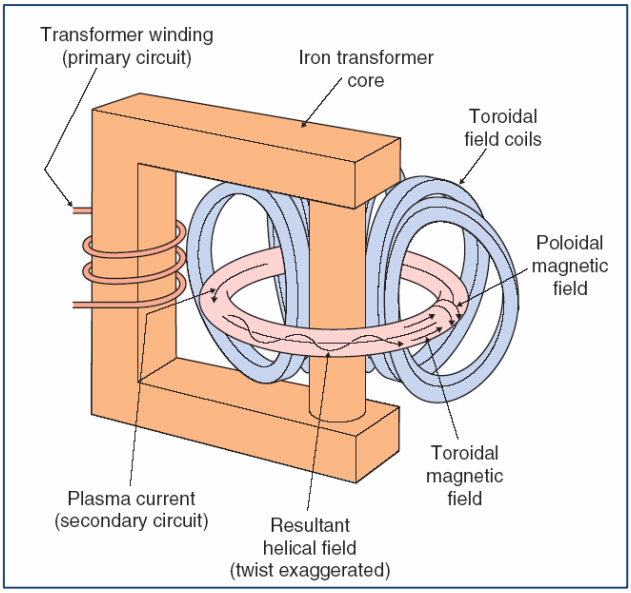

Figure 1.4: A schematic view of a tokamak showing how the current is induced in the plasma by a primary transformer winding. The magnetic fields, due to the external coils and the current flowing in the plasma, combine to produce a helical magnetic field.

Tokamak instabilities are a very complex subject, and very difficult to understand, similar in many aspects to the instabilities in the weather being both controlled by the flow of fluids and a turbulent behaviour. Therefore it is important in fusion experiments to be able to diagnosing the plasma (measuring the properties like temperature, density, impurity concentration, and also particle and energy confinement times). With this porpoise big projects counting with the participation

of Ciemat have been developed since 1970: JET in the Culham Centre for Fusion Energy-UK and JT-60 at the JAEA laboratories in Naka- Japan.

The *ignition* conditions required for the two fusion concepts are a bit different: for inertial-confinement fusion, the time is shorter ($n \uparrow \tau \downarrow$) and for magnetic-confinement plasma density is quite higher ($n \downarrow \tau \uparrow$), thus a really different plasma pressure versus time is required.

Great improvements have been made in the plasma profiles and magnetic control that influence the confinement, but the largest improvement can be made simply by building a bigger tokamak, thereby increasing the plasma volume relative to its surface area (like ITER).

2. Achieving fusion energy: IFMIF facility, ITER and DEMO projects.

A commercial fusion power station will use the energy carried by the neutrons to generate electricity. The neutrons will be slowed down by a blanket of denser material surrounding the machine, and the heat this provides will be converted into steam to drive turbines and put power on to the grid. A fusion power station is conceptually similar to an existing thermal power station but with a different furnace and different fuel (Figure 1.5).

Fusion is expected to become a major part of the energy mix during the second half of this century. With adequate funding, the first fusion power plants could be operating by 2040 as an electrical power station. To achieve this, a series of development steps need to be taken.

IFMIF (International Fusion Materials Irradiation Facility) is a facility with the main objective to provide a sufficiently intense neutron source for testing, selecting and licensing the right materials for fusion reactors.

There is a fundamental need to build an intense high energy neutron source to serve as a tool for calibrating and validating the data generated using fission reactors and particle accelerators, and for qualifying materials up to about full lifetime.

IFMIF concept will work with two intense D+ beams of 40 MeV, each carrying an intensity of 125 mA, and a liquid window of lithium for the generation of high-energy neutrons that will be fired on testing materials identified as suitable for the components of commercial fusion reactors.

The irradiation conditions provided by IFMIF will be very close to the ones expected to occur in DEMO-type reactor, at the level of the first wall, in terms of damage rate and rates of production of helium and hydrogen. Completion of IFMIF's design is now being taken forward as a joint European/Japanese project and a site for the facility is being identified, with operations planned to start in 2019 [11].

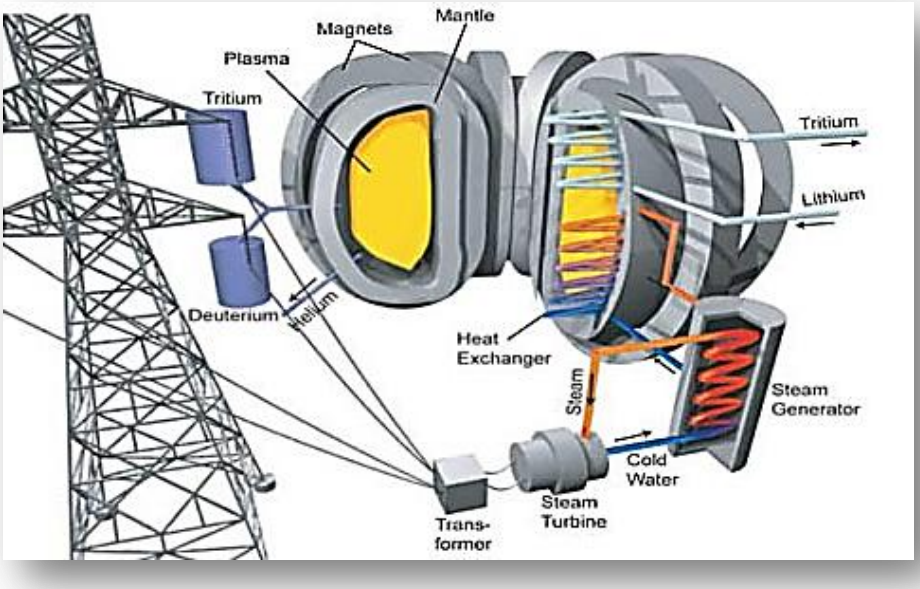

Figure 1.5: Schematic fusion power station, not to scale, explaining how to generate electricity starting from plasma.

ITER (International Thermonuclear Experimental Reactor) is a milestone project in the development of fusion energy. It is the next major international fusion experiment and a crucial step towards commercial fusion energy. Its objective is to prove the feasibility of electricity generation from fusion by releasing some 500 megawatts of fusion power (from a 50 megawatt input) for up to 500 seconds. It will be the first fusion experiment to produce net power – ten times more than the amount required to heat the plasma.

A truly global project, the participants in ITER represent more than half the world's population: China, the European Union, India, Japan, South Korea, Russia, and the United States of America. It is the world's largest international co-operative scientific research and development project, started in 1986 at the Geneva Superpower Summit, where the former Soviet Union General Secretary Gorbachev proposed to U.S. President Reagan the development of fusion energy for peaceful purpose. Thus began an international collaborative project to demonstrate the

potential of nuclear fusion as an energy source, ending on 2007 with the official ITER Organization for the construction of the world's largest and most advanced International Thermonuclear experimental reactor that has been designed to produce 10 times the input power.

The ITER site is next to an existing energy research site at Cadarache in southern France. An international team is now constructing the machine, with the first plasma expected in 2020. This will be followed by a 20-year period of operation that will test essential physics and technologies for the fusion power plants of the future [12].

Once the scientific and engineering systems have been tested, the next stage will be to build a **DEMO**nstration fusion power plant integrating the results. Designs are already advanced for this prototype machine.

DEMO will produce two GW of electrical power to the grid, a similar output to a standard electrical power plant, and could be online in the 2030s. If successful, it will lead to the first generation of commercial fusion power stations [13].
Three important challenges will thus be achieved:

1. Heat a large volume of deuterium and tritium plasma to over 100 million °C temperature — 10 times hotter than the core of the Sun — needed in order to allow the particles to fuse, form a heavier atom and release a comparatively large amount of energy which is will be transformed in electricity. In ITER, a power-station-scale experimental device, steady-state operation should be achieved.
2. Demonstrate that the candidate materials for the walls can endure for years in the harsh conditions of the reactor, which combine bombardment by energetic neutrons very high thermal loads, and intense interactions with deuterium and tritium. This will require tests in an accelerator-driven facility known as the international fusion materials irradiation facility (IFMIF).
3. Ensure reliability of what will be very complex systems building the first DEMOnstration fusion power plant.

3. Fusion materials

Fusion research is developing a big and novel research area related to the materials which should present the following requirements:

- ✓ good performance under stringent operational conditions (support high 14 MeV-neutron fluence, high heat fluxes, high operational temperatures & temperature gradients and thermal stresses, etc.; avoid chemical reactions);
- ✓ low long-term activation (minimizing the production of waste);
- ✓ low short-term activation;
- ✓ low decay heat (facilitating maintenance and cooling).

The high-energy fusion neutrons will produce atomic displacement cascades and transmutation nuclear reactions within the irradiated materials. At the first wall of ITER the primary displacement dose rate will be of the order of 10^{-6} dpa/s and the ionizing dose rate of the order of 10^{4} Gy/s [14]. From the point of view of materials science, atomic displacement cascades induce the formation of point defects (i.e., vacancies, interstitial atoms, vacancy and interstitial clusters) and segregation of alloying element. A second radiation-induced effect is the high rate formation of gaseous species, i.e. helium by (n,α) and hydrogen by (n,p) nuclear reactions, that can form bubbles and blisters modifying physical and mechanical properties of first wall materials.

The microstructure evolution in a fusion reactor environment may bring to the degradation of physical properties, such as a decrease of the thermal and electrical conductivity, as well as degradation of the mechanical properties, leading to strong hardening and/or embrittlement effects. Gas formation can cause a macroscopic swelling of the material, leading to a loss of dimensional stability. These effects are the main factors limiting the choice of candidate materials for fusion power reactors [15]. In addition to a good resistance to radiation damage, materials must show high performance, high thermal stress capacity, compatibility with coolant and other materials, long lifetime, high reliability, adequate resources, easy fabrication with a reasonable cost, good safety and environmental behaviour. The residual radioactivity of a large amount of exposed material is an important concern and will govern the handling methods, dictate the storage periods and the overall waste management and recycling scenarios.

Considering all those requirements and the function of the materials for fusion power reactors, it is possible to classify them in four main groups: structural materials, plasma facing materials, functional materials, Breeding Blanket materials.

3.1. Structural materials

Structural materials will support the basic structure of the reactor. They will be submitted to high temperatures and high levels of neutron irradiation, but also to high mechanical and thermo-mechanical stresses. The challenge is to develop structural materials which should maintain prolonged exposure to high thermal and radiation flux. The materials R&D strategy that takes into account these requirements has led to the development of the so-called 'low activation' or 'reduced activation' materials [16]. In Ciemat several studies on the effect of proton irradiation on Reduced Activation Ferritic Martensitic materials (RAFM) base alloys [17], as the effect of helium implantation of mechanical properties of other structural materials [18], have add important information to the behavior of these material under environmental conditions. In addition they may need chemical compatibility with coolants and be relatively easy to manufacture. Candidate structural materials, as well as candidate plasma facing materials, have a chemical composition that is based on low activation chemical elements (Fe, Cr, V, Ti, W, Si, C).

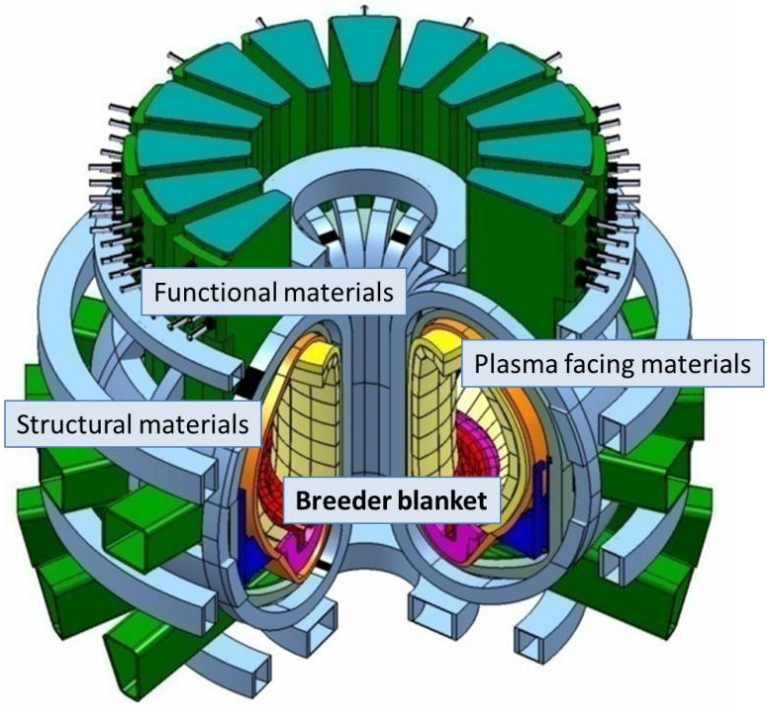

Figure 1.6: Fusion reactor scheme with the four main group's classification.

3.2. Plasma facing materials

Plasma facing materials will be directly exposed to the fusion plasma, which means that will serve as armour for the underlying materials. They will be submitted to a high heat flux of energetic particles (0.1-20 MW/m^2), high temperatures (775-3475 K), electromagnetic radiation, sputtering erosion, blistering and exfoliation, high levels of neutron-irradiation (3-30 dpa/year), and to off-normal events like plasma disruptions and Edge Localized Mode (ELM) events. Key issues relate to hydrogen trapping, erosion and high heat loads are studied in the Ciemat group with different plasma gas discharges together with the use of Li as a plasma-facing component [19]. Selection of plasma facing materials is mainly limited by their capability for absorbing heat and minimizing plasma contamination.

3.3. Functional materials

Functional materials will have one or several specific function (optical, transmission, windows, etc..). Their mechanical resistance under irradiation is presently considered of no primary concern. However, material properties, like the tritium release behaviour, the thermal conductivity or the entire structural integrity after prolonged neutron irradiation, are important concerns. As compared to structural materials orders of magnitude more hydrogen and helium isotopes will be generated in functional materials, e.g., in beryllium-type neutron multipliers and lithium ceramic-type tritium breeders. The irradiation resistance of other functional materials, such as ceramic insulators, dielectric and optical windows, optical fibres or complete sensor assemblies, is also an important concern. Important results have been observed through optical measurements on the defects created in SiO_2 by O, Si and He irradiation [20].

3.4. Breeding Blanket materials

In a fusion power plant, the breeding blanket component is charged of several important functions which result essential for the reactor operation like fuel production (breeding tritium), converting neutron energy into heat and evacuate it for the energy production, removing the first wall surface heat flux without exceeding the stress limit and finally it shall contribute to radio-protect the magnet and the vacuum vessel from radiation.

Tritium, which is hardly present in natural resources, is obtained by the nuclear reaction of a Li-containing medium (breeder), with the fast neutrons (n) coming from the D – T plasma:

$$^{6}Li + n \rightarrow {}^{4}He + {}^{3}T + 4.8\ MeV \qquad (1.3)$$

inside the blanket of the thermonuclear reactor. The Li of this reaction will be proportionate from Li-based breeding blanket which represent, for this reason, a key component of the fusion reactor.

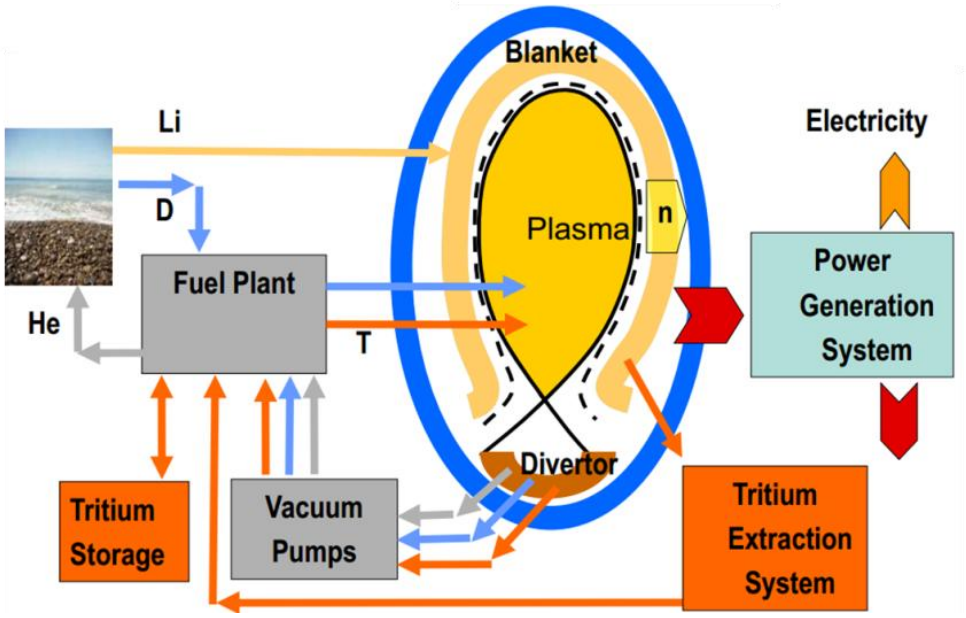

Figure 1.7: Schematic of fusion reactor input/output. The two elements responsible of energy production are evidenced in the reactor scheme: the blanket (where T is produced end extracted) and the divertor (which exhaust alfa, D, T and impurities from the plasma).

Various chemical forms have been considered for the lithium in the blanket. Possible lithium compounds are lithium/lead or lithium/tin alloys, which are liquid at operating temperatures. Lithium and lithium/lead offer the highest breeding ratios without the use of a neutron multiplier such as beryllium. Metallic lithium can be used in principle. The disadvantage in its liquid metallic form is that it is very chemically reactive and it also is easily set on fire in the presence of air or water in the case of an accident. Finally there are some problems in pumping conducting liquid metals at high rates across the magnetic field.

The other breeder possibility is the solid concept in form of ceramics containing lithium. It present the advantage of a little extrapolation of technology, thus near term characteristics for ITER testing. This model will be largely described along the work, being the subject of this thesis work.

Combining the lithium chemical form in the blanket, the type of coolant system and the neutron multiplier,the Breading Blanket (BB) concepts have been developed since 1980 [21]:

- ✓ The ***WCLL*** (Water Cooled Lithium Lead Blanket), with a Li-Pb-cooled divertor acting as both T-breeder and neutron multiplier and SiC_f/SiC as structural material. The coolant temperatures are included between 600°C and 1100 °C. Its advantages are that water is an exceptional coolant, largely available and the PWR cooling technology is well proved and it contributes to neutron shielding in the manifold region. Its disadvantages are the EUROFER embrittlement, the water/PbLi reaction and corrosion effect, apart of Tritium permeation and extraction with possible contamination of the primary coolant (tritiated water)

- ✓ The ***HCLL*** (Helium-cooled Lithium-Lead) blanket concept uses liquid Li-Pb eutectic melt acting as both T-breeder and neutron multiplier and utilises EUROFER and W-alloys as structural materials. The coolant temperatures are between 320°C and 550 °C. The compatibility of W-alloys under irradiation is being studied. Special attention on material integrity and tritium release properties is devoted.

- ✓ The ***DCLL*** (Dual Coolant Lithium Lead Blanket) concept utilize helium only to cool a ferritic steel structure (including the first wall) and slowly flowing PbLi acts as self-cooled breeder in the inner channels. The insulating channels allow reaching outlet temperatures up to 700°C. For an application on an early DEMO a version at about 500°C could be taken into account. Due to the high outlet temperature and the MHD problems, the use of SiC_f/SiC is needed as thermal and electrical insulation.

- ✓ The **WCPB** (Water Cooled Pebble Bed) concept developed mainly by Japan, consider solid breeding materials of Li ceramics, Be multipliers and F82H as structural material. The coolant temperature is required to be about 300 °C as to avoid corrosion. The use of supercritical water can allow heat removal

with a smaller amount of water because of wide operating temperature range, but with serious corrosion problems.

- ✓ The ***HCPB*** (Helium Cooled Pebble Bed) blanket, cooled by helium, uses solid Li-ceramics in pebble bed form as T-breeders, beryllium in pebble bed form as neutron multiplier and EUROFER and W-alloys as structural materials. The coolant temperatures are included between 320°C and 550 °C.

ITER might be the only opportunity to verify and test breeding blankets by test blanket modules (TBMs) that will be a "mock-up" for DEMO, designed in order to allow and validate the measurement relevant for a future power-producing reactor.

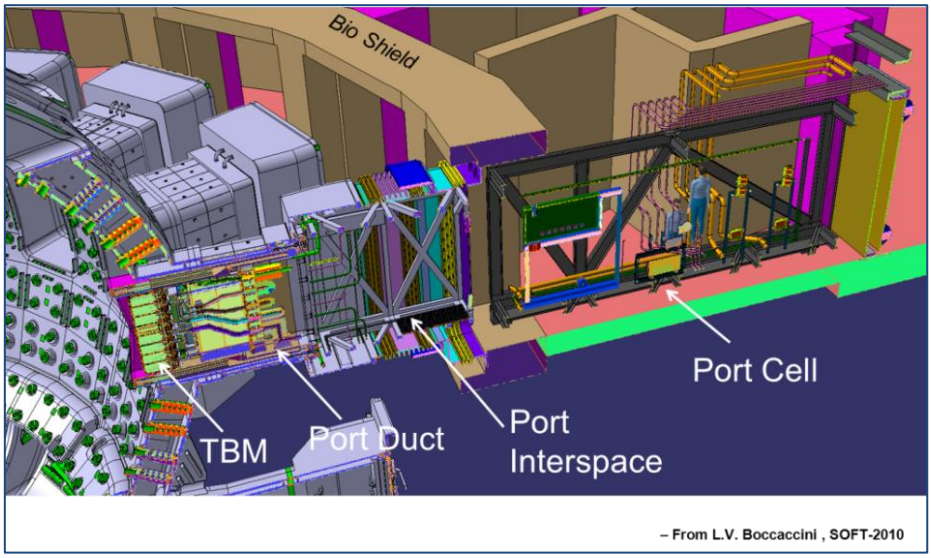

Figure 1.8: The TBM systems extend from Vacuum Vessel to Port Cell and buildings in ITER.

Six TBMs relevant to their respective reactor breeding concepts will be tested in three equatorial ports of ITER. Europe is currently developing two reference breeder blankets concepts for DEMO to be tested in ITER under the form of Test Blanket Modules (TBMs) Systems: HCLL and HCPB [22]. Both blankets use the pressurized He-technology for the power conversion cycle (8 MPa, inlet/outlet temperature 300 °C/500 °C) where the coolant primary circuit exchanges heat through a helium-water steam generator to a Rankine circuit and the 9% CrWVTa Reduced Activation Ferritic Martensitic (RAFM) steel as structural material, the EUROFER. The main difference between the two concepts is the mechanism of T extraction: in the HCPB a low pressure helium purge flow extracts tritium from the ceramic pebble beds; in the HCLL the PbLi re-circulates slowly (~10 PbLi inventories

pro-day) for a tritium extraction outside the vacuum vessel (see Figure1.7). The Test Blanket Modules are developed by several European partners (CIEMAT, CEA, ENEA, KIT, NRI and RMKI) joint together into a Consortium Agreement (TBM-CA), a strategic and organizational cooperation to implement, develop, produce, qualify and install the EU TBM systems in ITER.

In the present work the **HCPB** blanket concept will be analysed in terms of pebble bed breeding unit. Interest in using solid lithium-based materials as tritium breeders has grown since 1970_s. Ceramic lithium compounds present more favourable physical characteristics for the severe operating conditions of high temperatures and intense neutron fluxes.

4. Description of HCPB Blanket

The Helium Cooled Pebble Bed (HCPB) blanket of the European Blanket Programme to be tested during the different ITER experimental phases has been developed in Karlsruhe Institute of Technology (KIT), starting from 1990_s [23,24] and is based on a ceramic breeder (lithium orthosilicate mainly) and beryllium neutron multiplier in form of flat pebble beds, which are inserted into the blanket modules as a series of "breeder units" (BUs), separated each other by radial-toroidal and radial-poloidal stiffening plates. The Vacuum Vessel is covered by blanket modules.

The blanket thermal power, around 3000 MW (DEMO 2003), is extracted by the He primary coolant flowing at high pressure (8 MPa) through the first wall and blanket cooling plates made in RAFM EUROFER 97 steel, derived from the conventional modified 9Cr-1Mo steel eliminating the high activation elements (Mo, Nb, Ni, Cu and N). The inlet and outlet temperatures of the primary coolant are 300 and 500 °C.

In the HCPB system a low pressure purge flow (He loop at few bars pressure with a H addition at 0.1%) is pumped into the pebble beds and the outlet flow containing tritium is sent directly to a dedicate equipment that provides the removal of T from the He carrier, the tritium accountancy and finally the hydrogen isotopes (and impurities) transfer to the ITER Fuel Cycle. The blanket has the role of optimize the process in which neutrons coming from the plasma and multiplied by Be-multiplier can be absorbed in ^{6}Li-medium. This requirement together with that of avoiding inelastic scattering and absorption in iron, imply a small amount of steel structure, thus a thin first wall structure [25].

The breeding unit for the HCPB consists of two "U" shaped EUROFER canisters as indicated in Figure 1.9. The canisters are filled with lithium ceramic in form of pebbles with a typical diameter of 0.6 – 1 mm, used as the breeding material. The space between the canister outside surface and the stiffening grid is filled with beryllium/beryllide in pebble form with a diameter in the range of 1 mm, used as the neutron multiplier material. The canisters are cooled with internal channels in the middle plate of the "U" radial to the plasma, then the coolant splits in an upper and lower portion and returns in the outer branches of the "U" [26]. The canisters are closed at the sides so that contact between beryllium and ceramics is excluded.

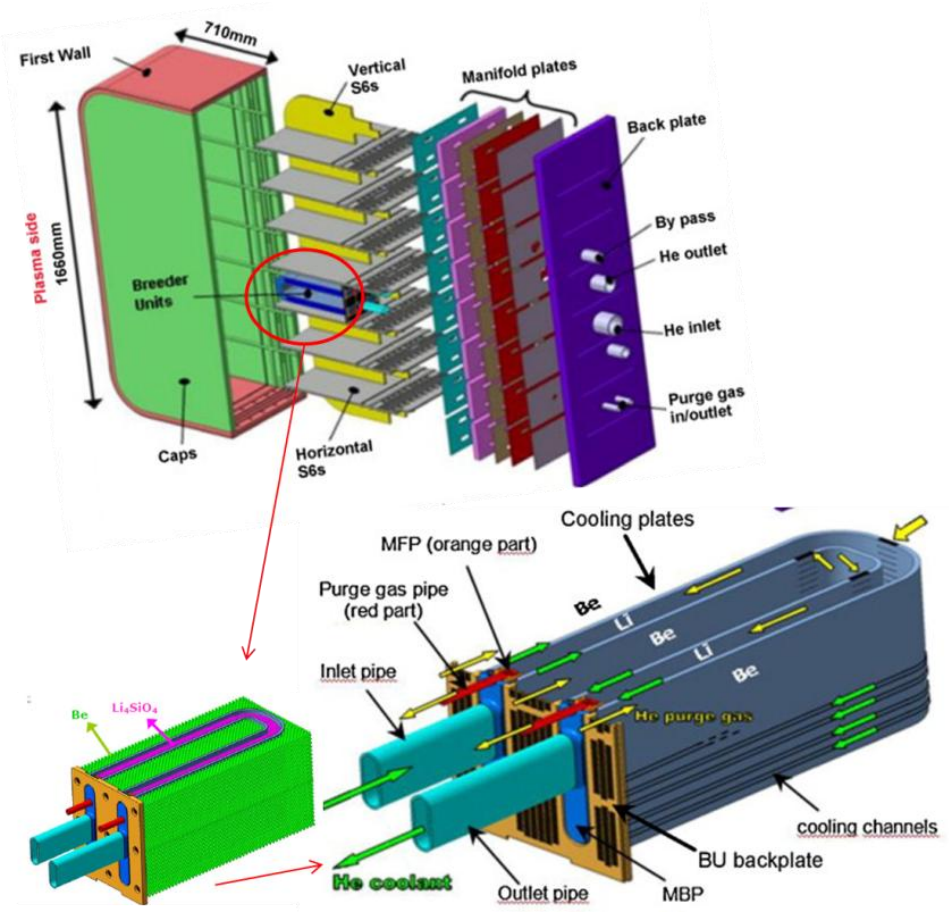

Figure 1.9: HCPB test blanket module (TBM) using lithium ceramics as breeding material. In the lower part, the U-shaped cooling plates (CPs) extracting the heat. The He at 80 bar (green arrow) cools the TBM box components and the BUs CPs, while the He at 4 bar (yellow arrow) purges the breeder zone from tritium.

For tritium removal a purge gas circuit is integrated into the breeding unit. The purge gas is lead in tubes to the plasma side of the breeder unit (BU) and

distributed there in toroidal direction both in the beryllium and in the ceramics. The purge gas leaves the beds via holes in the back plate of the BU.

The advantage of this reference design is its robustness; even if a sudden pressure load with the full operational pressure of ~ 8 MPa in the box could be withstood without a break of the box. This pressure of helium is used to cool the pebble beds indirectly by steel structures. The primary advantage of helium is that it can be operated at high temperature without the need for very high pressure, the second advantage is its chemical inertness; its disadvantage is its low volumetric heat capacity [27].

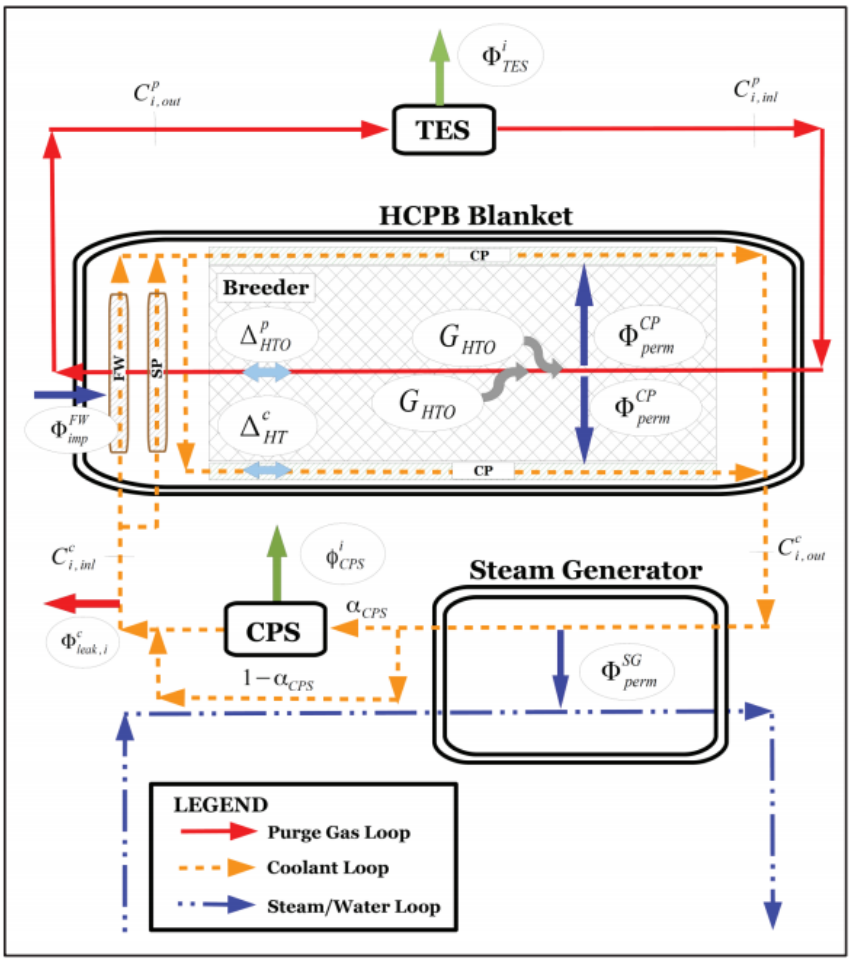

Figure 1.10: Reference Scheme for Tritium Transport in HCPB Blanket.

The extraction of the tritium from the breeder materials is performed by an independent low pressure (0.1 - 0.2 MPa) of Helium purge flow. A simplified flow-diagram of the main tritium transport system for this blanket concept is shown in Figure 1.10. Its first task is to extract tritium from the lithium ceramic and Be

multiplier beds by a low pressure helium plus hydrogen gas stream, removing the tritium in two main chemical forms, HT and HTO. Thus an efficient CPS (Coolant Purification System) must be designed in order to carry out the primary function of tritium removal from He coolant, one of the most important parts in terms of tritium inventory. After getting into the purge gas, tritium is extracted in the Tritium Extraction System (TES) with certain removal efficiency. The analysis demonstrate that tritium assessments for fusion reactors breeding blankets are affected by many uncertainties which are either parametric (e.g. tritium transport properties in materials) and related to models (e.g. surface vs. diffusion-limited permeation models). Despite these problems, the HCPB blanket seems to be quite robust in terms of tritium radiological risk.

The Helium-Cooled Pebble-Bed (HCPB) blanket, featuring lithiated ceramic pebbles (Li_4SiO_4 or Li_2TiO_3) as the breeder and beryllium pebbles as the neutron multiplier one of the EU TBM concepts to be tested in ITER is selected as object of the present work. In the following chapters a detailed characterization of the BB ceramic compositions will be presented together with a detailed analysis on the effect of radiation and light ions behaviour in the material under different conditions.

CHAPTER 2

THE SOLID BREEDER BLANKET CONCEPT

A brief introduction to the main role of this component of the reactor is here presented. Secondly the most important characteristics of both the ceramic material and the pebble bed system are reviewed. The crystalline structure of each ceramic compound is here revised as an important support for the late discussion on the characteristics of the materials obtained along the experimental work.

1. **The role of the solid Breeder Blanket in a fusion reactor**
2. **Main characteristics of lithium-based ceramics**
3. **Phase diagram and structure of the studied ceramics**
   - 3.1. Li_2TiO_3
   - 3.2. Silica-based ceramics

1. The role of the solid Breeder Blanket in a fusion reactor

The breeding blanket is one of the most important components in a fusion reactor. Among the different designs, ceramic pebble bed is a very promising concept, favoured by both the EU and Japan organizations. The role of this component is the generation of tritium by the ^{6}Li (n, α) T and ^{7}Li (n, α n) T nuclear reactions. The ^{6}Li reaction is most probable with a slow neutron; it is exothermic, releasing 4.8 MeV of energy. The ^{7}Li reaction is an endothermic reaction, only occurring with a fast neutron and absorbing 2.5 MeV of energy. Natural lithium is composed 92.6% of ^{7}Li and 6.4% of ^{6}Li thus an enrichment of the chosen breeder material is required. Considering that ^{7}Li reaction works with the high energy neutrons coming from the plasma, the decelerated neutron can still make a tritium atom by the ^{6}Li reaction thus creating two tritium atoms from one neutron (in the next chapter a more complete explication).

Lithium-containing ceramics possess a series of advantages over liquid lithium and lithium-lead alloys. They have a sufficient lithium atom density (up to 540 kg*m^{-3}), high thermo-stability (up to 1300 K), do not create ecological danger in the case of blanket dehermetization. Furthermore, being a non-mobile breeder, the selection of a coolant that avoids problems regarding safety or Magneto Hydro Dynamics (MHD) is possible, and the corrosion is limited only to punctual contacts with the structure of the TBM [7].

Of course there are also disadvantages related to this breeder, like the low thermal conductivity of ceramics which, together with the allowable operating temperature window, results in limits on achievable tritium breeding ratio (TBR, see Chapter 3).

Considering that the temperature in the blanket zone will be included in a range between 300 °C to 900 °C, the radiation rate will be approximately 10^{18} neutrons (m^{-2}s^{-1}) and the intensity of magnetic field up to 7-10 T [28], therefore the material is required to present several important characteristics, as shown in the Table 2.1.

Table 2.1: Main Solid Breeder Blanket functions and key controlling requirements.

Main functions	Materials properties requirements
High tritium breeding properties	High Lithium content for a high T production High tritium release rate to limit the inventory
Optimum temperature maintenance of BB materials	High thermal conductivity
Maintenance of soundness	Good radiation damage resistance High mechanical strength and durability High chemical and composition stability Good compatibility with structural material
Safety	Low induced radioactivity Low reaction with coolant
Implementation potential	Low cost, mass production, easy handling, recycling process, Li-depletion.

All those important functions are related to the position the breeder blanket occupies in the reactor. As can be observed in the Figure 2.1 it is located among the first wall and the magnets, thus a high radiation flux from one side and a magnetic effect from the other side will act on the material. The requirements listed in the Table 2.1 could be satisfied even after long-term operation (the estimated life-time for TMB is of 4-5 years).

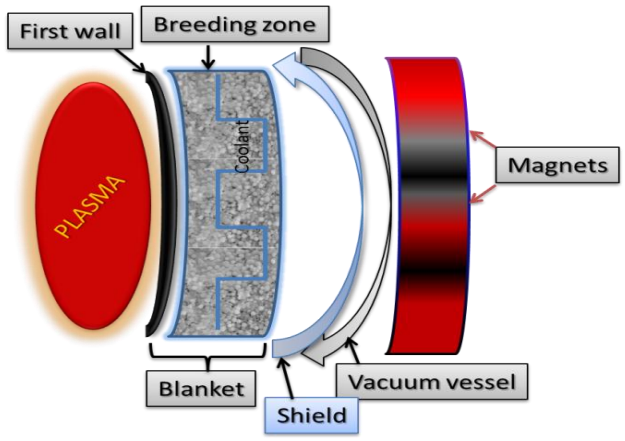

Figure 2.1: Schematic of tritium breeding blanket configuration: the breeding zone is between the first wall and the neutron shield, acting as a heat exchanger, breeding zone of tritium and as shield.

Several ceramics such as Li_2O, Li_4SiO_4 and Li_2TiO_3 with different properties have been considered as candidates for tritium breeders of fusion reactors [29,30] (see Table 2.2). Lithium density in these ceramics is different but it can be be

compensated by a different ^{6}Li-enrichment. It is important to mention that although Li_2O is the only ceramic that may achieve the desired TBR without a neutron multiplier thanks to its high Li-content, it is a highly hygroscopic and corrosive oxide and it presents swelling under radiation. This is the reason why it has not been considered as EU-TBM test modules.

Table 2.2: Main items of the BB ceramic materials. The candidate materials are presented considering their lithium content, an important parameter for tritium breeding rate (see chapter 3).

	Li_2O	Li_4SiO_4	Li_2TiO_3
Li density (g/cm^3)	0.94	0.51	0.43
Thermal conductivity (500 °C)*(W/(m*°C))	4.70	2.40	2.40
Thermal expansion (500 °C)*($\Delta L/L_o$ %)	1.25	1.15	0.80
Crush Load (N)	-	~10	24-33
Min-Max Temp. for Tritium release (°C)	397-795	325-925	600-950
Swelling ($\Delta V/V_o$%)	7.0	1.7	-
Melting point (°C)	1430	1250	1550

The ortosilicate-Li_4SiO_4 and metatitanate-Li_2TiO_3 ceramics are considered as the best options for solid breeder material. After about 30 years of investigations some important characteristics are been detected and compared among all the possible lithium based candidates. Li_4SiO_4 is the selected EU candidate [31] and Li_2TiO_3 the Japan one [31,32]. In the last years a new composition is under study in KIT laboratories with the aim of unify the two materials and take advantage of the best quality of each [33].

The spherical shape of more or less than 1 mm in diameter has been chosen to minimize thermal cracking and volumetric swelling, due to neutron irradiation damage and thermal stress. This configuration, with small pebble size (to avoid mechanical problems) get small thermal gradient and is known as “pebble bed” configuration. Its mechanical degradation is strongly reduced as compared to an equivalent geometric pile of pellets; furthermore small spheres are easy movable and handled in remote plants. Additionally to ensure a facile and homogeneous filling of complicated blanket geometries, a binary packing method by packing microspheres with different sizes has been proposed. The thermal conductivity as the thermal expansion in table 2.2 are thus calculated considering the pebble bed

concept, while the crush load and the swelling are measured on a single pebble sphere.

2. Main characteristics of lithium-based ceramics

Several properties of breeder materials are considered of primary relevance for the reactor right functioning, either in view of the application (thermal and mechanical performances, electrical behaviour) or as a characterisation means during the material development stage (basic structure characteristics). Some properties are more or less fixed while others may be influenced by specific treatments and enable material optimisation. The development of a high quality properties data base is essential for a good design and material selection. The interest resides in keeping any chemical and mechanical interaction with others materials within tolerable limits, establishing the operating temperature regime, testing any relevant change in the physico-chemical properties caused by radiation damage and finally calculating tritium inventory [30]. To distinguish between properties of the lithium based ceramic and properties of the whole pebble bed is thus possible, considering that pebble beds can be described as an intermediate phase between solid and liquid, with properties depending on the fraction of voids present in the bed volume.

To identify some *basic characteristics* for ceramic breeder materials (like composition, density/porosity, purity, cristallinity, grain size) and for pebbles (shape, pebble-size, mechanical and thermal performances, etc.) is possible.

On a *structural level*, ceramics are characterised by features like grains and pores, phase composition, presence of impurities and homogeneity. An important parameter investigated is the crystallisation degree along the fabrication process, which could be followed by thermo-analysis and X-Ray diffraction as well as the microstructure could be observed by electron microscopy. This study allows an optimisation of the heat treatment to obtain material cracks and pores free, improving the mechanical properties of the breeder [34].

The *fracture strength* of a single pebble and of the pebble bed is an important parameter to check, as well as the thermal shock. The fragmentation of pebbles should strongly affect the breeder blanket performances. This characterization is done both in an experimental way [35] and by numerical simulation models [36].

Compression tests on single spheres have permitted to obtain the mechanical properties of the materials [37], having found that the confining pressure is a very important parameter for the determination of the pebble bed mechanical properties. In another study [38] it is evidenced that the pebble bed effective Young's Modulus is 100 times less than that of the individual pebble due to point contacts and uneven stress distribution throughout the pebbles. A smaller size and a spherical shape enable a higher bed packing factor and an optimal configuration for the stress and irradiation effects.

The *thermal performance* of lithium ceramic pebble beds in the TBM plays a key role for the fusion blanket. In order to study the heat transfer, the effective thermal conductivity of the lithium ceramics pebbles has to be measured and characterized, being influenced by many parameters such as thermal conductivity and filling gas, gas pressure, bed deformation and bed packing fraction [39]. In order to establish a reliable design of the blanket system, it is necessary to analyse heat transfer with deformation of the pebble bed, which will result in the deviation of effective thermal conductivity of beds. Results have shown that the thermal conductivity is affected by the density as well as by the microstructure of the ceramic samples [40]. Therefore, variations in the manufacturing procedure have a clear impact on all the previous parameters.

Piazza et al. [41,42] studied microstructure, mechanical properties and Li-losses in Li_4SiO_4 and Li_2TiO_3 ceramics in the case of long-term annealing treatments, simulating the maximum breeder temperature and the lifetime of the HCPB blanket (excluding irradiation effects). After 96 day of annealing experiments, the microstructural changes caused an increase in the roughness of the Li_4SiO_4 pebble surface. Concerning the mechanical and creep behaviour, only the Li_2TiO_3 resulted to be influenced by aging, showing a grain size increase of a factor of 10 and a consequent decrease of the mechanical stability of pebbles.

Thermo-mechanical properties are also studied for the interaction of ceramic breeder with structural materials [43]. The experimental results indicate that high thermal stresses and deformations are present during the first set of thermal cycles, successively accommodated thanks to a combination of pebble rearrangement within the bed and creep induced deformation [44].

The *magnetic effect* is also an important parameter considering the position occupied in the reactor by the breeder blanket. Tiliks et al. [45] have studied the effect of external magnetic field on ceramic pebbles, observing that various physicochemical processes can take place. *Electrical properties* may also reflect

certain characteristics of the physical-chemical processes [46] occurring during reactor operation. These processes can cause compositional and structural changes, which have to be considered a priori to prevent the shielding role of the breeder blanket that may be affected.

Finally there is the important *effect of radiation* which may alter the structure and microstructure of ceramics. To verify the mechanical stability of the pebbles by thermo/mechanical stress, ITER testing have been developed to study the effect of neutron irradiation, like in-pile pebble bed assembly (PBA): HELICA tests and the EXOTIC experiments [47] in the high flux reactor (HFR) [48]. Due to the relevance of a radiation environment on ceramic behaviour, Chapter 4 will be dedicated to deepening in its theory.

3. Phase diagram and structure of the studied ceramics

The micro- and macro-structural properties of solid breeder blanket are really important for the improvement of their performances. The phase stability and the structure are relevant aspect for better understand their behaviour. Here below a summary of the phase diagrams and the crystalline structures is presented. These information will be relevant in the fabrication and characterization process described in Chapter 5, as well as in the study of electrical performances detailed in the Chapter 6 of this work.

3.1. Li_2TiO_3

The phase-diagram given by Kleycamp et al. [49] represented in Figure 2.2 shows the phase equilibrium of the Li_2O-TiO_2 system. The Li_2TiO_3 intermediate compound crystallizes in three phases: α, β and γ [50]. The α-phase is metastable with a monotropic transformation to β by heating above 300 °C. The β-phase is a monoclinic stable phase with space group *C2/c* and crystallizes in the Li_2SnO_3-type structure. At 1200 °C the β to γ phase transformation is reported [50], [51]. This last present a high temperature cubic phase and crystallize in the NaCl-type structure. The temperature of order-disorder transition is found to be of about 950 °C.

It is worth mentioning that exists another intermediate compound ($Li_4Ti_5O_{12}$) with a 72 wt. % of TiO_2, showing a wide coexistence compositional range and a very similar XRD patterns [50] with the monoclinic Li_2TiO_3 compound.

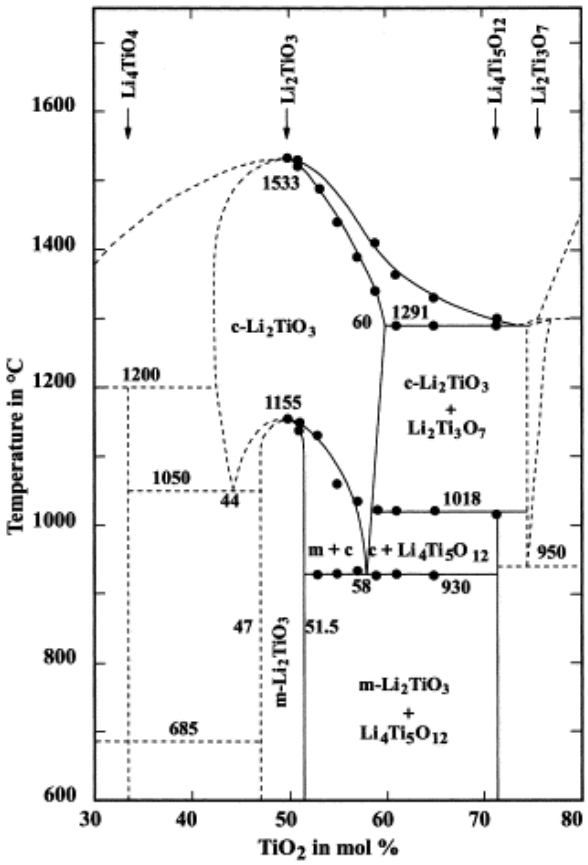

Figure 2.2: Phase diagram of the Li_2O–TiO_2 system; broken lines: from Izquierdo et al.[50] and from Mikkelsen [52]; solid lines from Kleycamp [49].

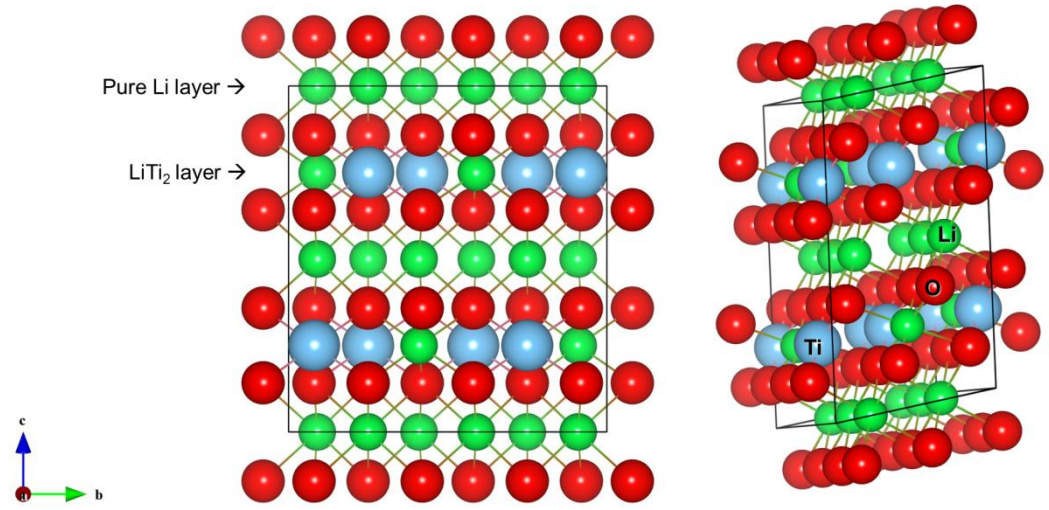

Figure 2.3: Crystal structure of a unit cell of C2/c Li_2TiO_3 compound where the pure Li layer and the Li_2Ti layer can be appreciated.

Regarding the crystal structure, it has been observed that Li and Ti are randomly distributed in the cation sites. It is proposed that in Li_2TiO_3 two types of layer structure exist: one composed by lithium occupying octhaedra and the other composed of lithium and titanium occupying octahedra in a 1:2 ratio [53]. As it can be observed from the crystal structure in the Figure 2.3 the C2/c space group is formed by a distorted rocksalt structure with alternating Li and Li_2Ti planes (111).

3.2. Silica-based ceramics

The Li_2O-SiO_2 system is considered for the fabrication of ceramics with different Li_2O content. Stable Li-Si-O phases can be formed by reaction of Li_2O and SiO_2 as shown in the following reaction:

$$xLi_2O + ySiO_2 \rightarrow Li_{2x}Si_yO_{x+2y} \quad (2.1).$$

The phase diagram in Figure 2.4 shows different phases of lithium silicates (Li_4SiO_4, Li_2SiO_3 and $Li_2Si_2O_5$) for 33.3 mol%, 50 mol% and 66.67 mol% SiO_2 respectively. Li_4SiO_4 decomposes before its melting point, reached at 1255 °C and 33.3 mol % SiO_2 [54]. Li_6SiO_5 is a metastable phase with 25 mol % SiO_2 while Li_8SiO_6 is stable at really low temperatures (<1100 K).

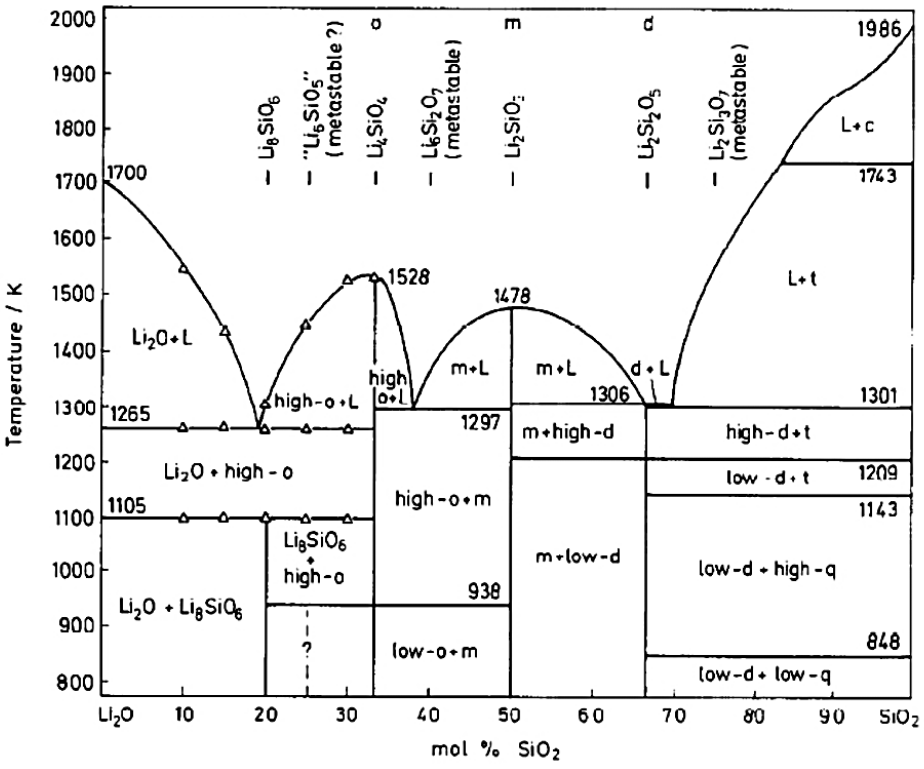

Figure 2.4: The phase diagram of the Li2O-SiO2 system according to ref.[55]

Regarding the crystal structure, the $Li_2Si_2O_5$ (lithium disilicate) structure is monoclinic with a space group of *Cc* with a strong orthorhombic pseudosymmetry *Ccc2*. The lattice parameters are a=5.82 Å b=14.66 Å and c=4.79 Å and the unit cell is composed of a total of 36 atoms with four formula units [56].

The lithium metasilicate (Li_2SiO_3) determined by Hesse [57], has a space group of $Cmc2_1$ and lattice parameters *a*=9.392 Å, *b*=5.397 Å and *c*= 4.660 Å. The structure is a corner sharing LiO_4 and SiO_4 tetrahedra forming parallel chains with lithium ions between the chains (Figure 2.5).

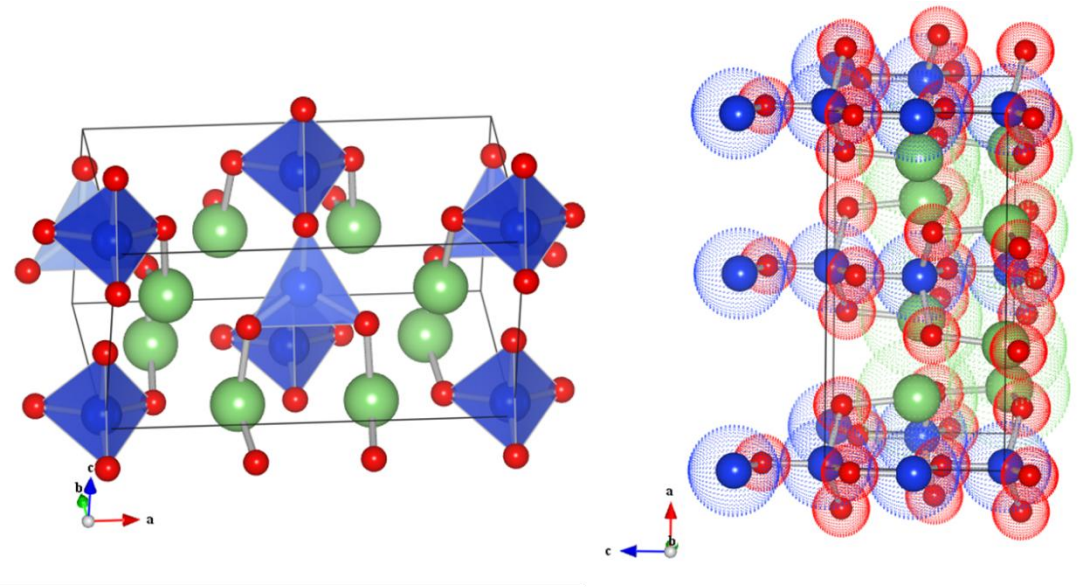

Figure 2.5: Crystal structure of a unit cell of $Cmc2_1$ Li_2SiO_3.

The XRD patterns of the Li_4SiO_4 indicated by Baur [58] identify the monoclinic structure of space group *P21/m* and crystal parameters *a* = 5.140 Å; *b* = 6.094 Å; *c* = 5.293 Å and β = 90°. It corresponds to a tetrahedral anion (SiO^{4-}) structure surrounded by different Li atoms, presenting one type of Si atom, three types of O atoms and six types of Li atoms (Figure 2.6). There are differences between the structures measured by some authors [59,60] given by the occupancy of Li atoms, that in some cases are fixed with full occupancy, whereas in others are half occupied.

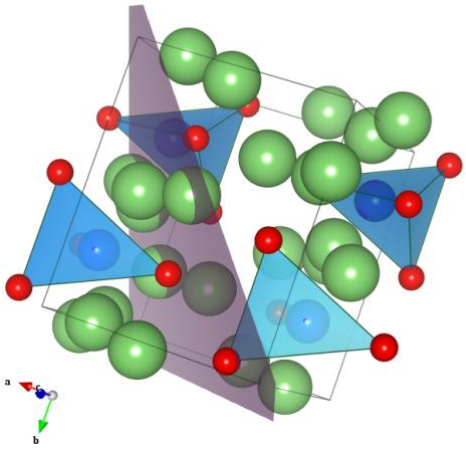

Figure 2.6: A model of the Li_4SiO_4 crystallographic structure where the small red balls of Oxygen, together with the big blue Si ones forms the tetrahedral anion structure while the green Li ones are floating around them. The purple plane represents the 111 direction.

The tetragonal Li_6SiO_5 crystal structure present a metastable phase with a space group *P4-21m* and crystal parameters a=7.67 Å, b=7.67 Å, and c= 4.79 Å respectively. This phase have poor heat resistance owing to its decompositions below 1020°C [54].

The Li_8SiO_6 ceramic has a hexagonal structure with space group $P6_3cm$ and lattice parameters a= 5.458 Å and c = 10.710 Å as found by Hofmann et al. [61], who confirmed that Li_8SiO_6 is isotypic with Li_8CoO_6.

Dubey et al. [62] stated that the crystal structure of Li_4SiO_4 is closely related to the one of Li_4GeO_4 at room temperature with the only difference that in the first case lithium sites, which are 4, 5 and 6- coordinate, are only partially occupied while in the second case there is only one lithium coordination and the sites are fully occupied. The lattice parameters values at low temperature (below 700 °C) are in agreement to that of Völlenkle et al. [63]. The 'superstructure' solved and refined by Tranqui et al. [59] contained 14 formula units, seven times larger than the earlier reported. The Li atoms are ordered and occupy 19 of 42 sites in the sevenfold supercell. The LiO_4, LiO_5 and LiO_6 polyhedra are linked by edge- and corner-sharing. It also had monoclinic structure but the unit cell were a = 11.546 Å, b = 6.09Å, c = 16.645Å and β = 90.5° and space group *P21/m*. The differences in the unit cell parameters may be due to the superposition of crystals.

CHAPTER 3

TRITIUM

An overview on Tritium as the fuel of a thermonuclear fusion reactor is presented. The importance of some parameters (TBR, inventory..) is explained and the steps of production and release inside a breeder blanket are analyzed. Finally the connection between the measurements carried out in this thesis work and the understanding of tritium behavior is shortly explained.

1. **Tritium inventory**
2. **Tritium production**
3. **Tritium release**
4. **Modelling tritium behaviour**
5. **Indirect measurements of tritium diffusion and state of the art**

1. Tritium inventory

A key issue based on economic and safety consideration in a fusion reactor is tritium production and release. The amount of tritium presents in a reactor at a given time is known by the term *tritium inventory*. If the breeder traps too much of the tritium produced, or the cracking/fragmentation of pebbles blocks the purge gas flow line, breeder temperature control may be lost, causing the *tritium inventory* in the blanket to become a threat to safety, which may require an early removal of the blanket module.

Tritium inventory is given by

$$I = \int (G-R)\, dt \quad (3.1),$$

where tritium generation rate (G) and its recovery rate (R) must satisfy self-breeding and start – up, being both parameters controlled by the TBR factor.
The tritium breeding ratio (TBR),

$$TBR = \frac{tritium\ bred}{tritium\ burnt} \quad (3.2),$$

is defined as the average number of tritium atoms bred per tritium atom burnt. We must have TBR > 1.15 [64], for a self-sustained fusion economy.
This factor can mathematically be defined as:

$$TBR - 1 \approx \frac{t_p}{\eta f_b t_d} \quad (3.3),$$

which means that to have the least demanding requirements it is necessary to use the longest possible doubling time t_d, the largest tritium burn fraction f_b, the largest injection efficiency η and the smaller recycling time t_p.

To meet these challenges the breeder should satisfy the following characteristics: high Li content and a low residence time of tritium. The first one can be achieved during fabrication process, while for the latter feature is essential to understand the tritium release dynamics. In a lithium oxide crystal it is a complex process made up of several steps, any of which could be rate controlling: intragranular/intergranular diffusion, boundary grain diffusion, surface adsorption/desorption, pore diffusion, irradiation effect on tritium mobility, purge flow convection [65],[66]. Moreover lithium ceramics are irradiated with thermal or

mixed neutron spectra [67,68]. The accumulation of radiation defects and radiolysis products interacting with tritium species can change the dynamics occurring during tritium diffusion. This knowledge can promote the minimization of the inventory while maximizing the amount of tritium released. Finally tritium is recovered from the surface of the material by a purge gas composed by He + 0.1 % H_2, sweeping the purge gas in a temperature window between 300 and 950 °C. Addition of 0.1% H_2 in the He purge gas enhances tritium release from the ceramics, thus helping to reduce inventory and residence time. The understanding of purge gas role covers another important area of interest for the optimization of Toutgas.

The studies carried on till now in this field are really interesting (better discussed in section 5 of this chapter), quite all referred to the release-rate study, considering different conditions of temperature and radiation. One relevant area with scarce bibliographic data is the one relative to the microscopic effect occurring when the ion bred inside a grain, has to overcome several energetic barriers to find a diffusion path till the surface, where it can desorb and be carried away by the purge gas. Being a radioactive element, it is not possible handling tritium in any type of experiment. An alternative is represented by the use of light ions with similarities features, for extrapolating characteristics of its behaviour inside the ceramic structure. With this aim deuterium and 3-helium ion implantations are proposed as a tool for tritium behaviour understanding.

The stable isotope ^3He, produced by tritium decay (equation 3.4) represents a secondary interesting aspect of fusion power plants. Radioactive tritium spontaneously decays into ^3He, an electron e^- and an electron antineutrino ν_e, with a half-life of 12.3 years in the process of beta-decay described as:

$$T \rightarrow {}^3He + e^- + \nu_e + 18.6\ keV \quad (3.4).$$

Naturally occurring ^3He is rare, so that all the demand is met by the radioactive decay of tritium (from nuclear US weapons or fission reactors). A fusion economy would provide a new peaceful and clear resource of ^3He, and would encourage new applications [69]. The knowledge of its behaviour may cover a special interest in wasted ceramics breeder, considering the problems in the efficiency of tritium total extraction occurring in this solid breeder blanket concept.

2. Tritium production

The main natural source for producing the radioactive hydrogen isotope is the interaction of cosmic radiation with nitrogen and oxygen nuclei in the atmosphere. It is assumed that the transfer of tritium to the oceans by the hydrological system is equal to the total tritium production rate estimated to be of 0.4 kg/year [70].

Most of the industrially produced tritium is obtained by fission generation through various neutron reactions such as ternary fission of heavy nuclei or by neutron reaction with light elements.

The last possibility is given by tritium breeder materials, based on lithium. The engineering data of tritium breeders under neutron irradiation are indispensable to design the fusion blanket. Lithium, composed of two stable isotopes (with isotopic composition ^{6}Li 7.4% and ^{7}Li 92.6%), presents a low nuclear binding energy per nucleon. Tritium is thus produced as a result of the following nuclear reactions:

$$^{6}\text{Li} + n \rightarrow {}^{3}\text{T} + {}^{4}\text{He} + 4.08\ \text{eV} \qquad (3.5),$$

$$^{7}\text{Li} + n \rightarrow {}^{3}\text{T} + {}^{4}\text{He} + n' - 2.5\ \text{MeV} \qquad (3.6).$$

The product neutron *n'* of (3.6) has a smaller energy than the incident neutron *n*. The exothermic reaction (3.5) has a very large cross section, for neutrons with a velocity of 2200 m/s. It represents a substantial contribution to the thermal power output of the fusion reactor since the energy release per reaction, 3.8 MeV, is 27% of the 17.6 MeV energy release of the primary fusion reaction (equation 1.1, Chapter 1). The cross section of the second, endothermic reaction, (3.6) is heavily suppressed because of the Coulomb barrier for charged product particles at energies just above the 2.5 MeV thresholds, but it can be readily driven by the 14 MeV neutrons from the primary fusion reaction, allowing a single neutron to make two or more tritons.

Because thermal neutrons easily penetrate in breeder blanket ceramic crystalline grains, tritium is uniformly generated in these grains under thermal neutron irradiation. A manner to get relatively large tritium breeding ratios is including a neutron multiplier like the beryllium (Be) ($n + {}^{9}\text{Be} + 3\ \text{MeV} \rightarrow 2\alpha + n' + n'$), in the case of the HCPB concept.

The residence time of this gas is defined as:

$$\tau_{res} = \frac{I}{G} \qquad (3.7)$$

where *I* is the current tritium inventory and *G* its generation rate.

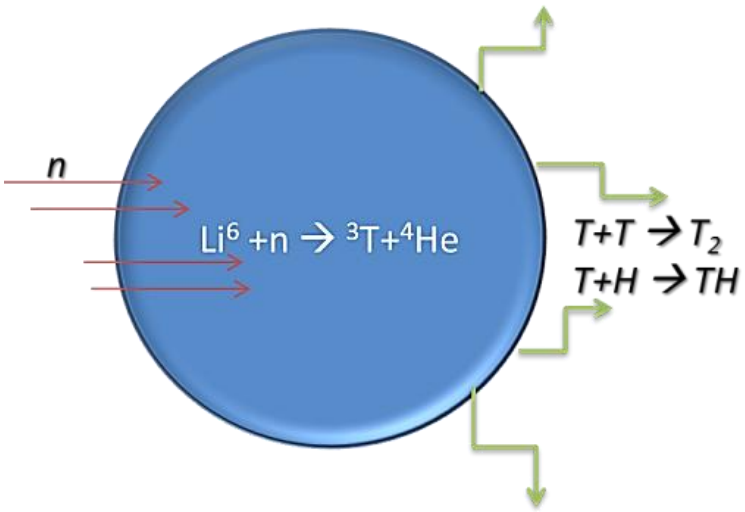

Figure 3.1: Schematic behaviour of tritium production and release from a ceramic pebble. Bred in the lithium based ceramics, it diffuses till the surface where it recombines with purge gas.

3. Tritium release

Tritium release from the surface can be described as a first order chemical reaction according to the chemical decomposition reaction mechanism. The physical processes taking place after tritium bred, are its diffusion along the grain inside the bulk and the recombination with the hydrogen at the grain boundaries, then through the grain boundaries and the interconnected pores, finally reaching the surface where several interactions take place till the desorption and the molecular diffusion in the purge flow convection [71–73]. This last surface-phenomena step such as adsorption from the pore and from the bulk that can be schematized as the desorption to the pore and eventually the dissolution into the bulk, can play an important role in the overall tritium release kinetics, strongly affecting the total amount of gas that reside on the surface of the pebble [74]. Considering a grain as a sphere of radius *a*, the non-stationary equation on the volume of tritium concentration C as a function of time (t) and radial coordinate (r) is:

$$\frac{\partial C}{\partial t} = \frac{1}{r^2}\frac{\partial}{\partial r}\left(r^2 D(T) \frac{\partial C}{\partial r} \right) + S \qquad (3.8),$$

where S is the tritium source and D(T) the diffusion coefficient given by:

$$D(T)=D_0 \exp\left(-\frac{E_m}{kT}\right) \quad (3.9),$$

with E_m being the migration energy.

The boundary conditions for equation 4.8 commonly assumed are:

$$\begin{aligned} &C(r,0)=0 \\ &C(a,t)=0 \qquad (3.10), \\ &\left(\frac{\partial C(a,t)}{\partial r}\right)=0 \end{aligned}$$

where *a* is the sphere radius.

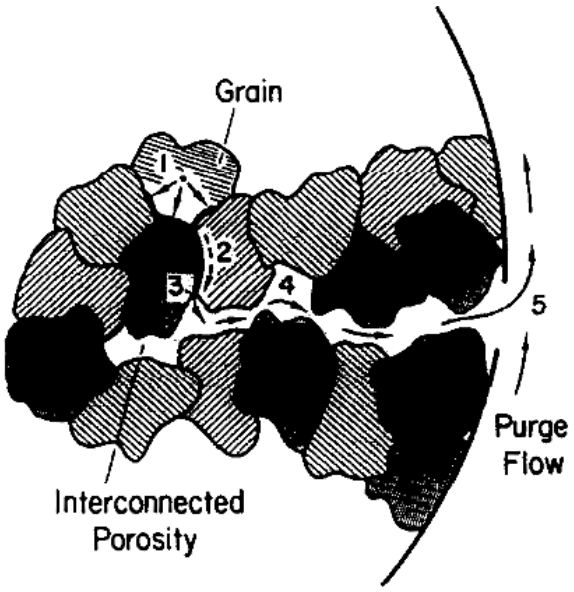

Figure 3.2: Mechanism of tritium transport in ceramic breeder blanket [72], where 5 major steps can be identified: 1) inter-granular diffusion, 2) grain boundary diffusion, 3) surface adsorption/desorption, 4) pore diffusion, 5) purge flow convection.

A diffusion-type model is unable to explain and interpret the results obtained at high temperature, where the light ion is not released by a diffusion-controlled process. It appears to be bond to discrete sites in the solid (maybe defects), or trapped near the surface acting as a barrier, each site being rate constant and characterized by a different binding energy. Thus it is evident that a model with a single mechanism for tritium release, may be limited to really few and unreal cases. Macroscopically the whole mechanisms of tritium transport can be divided into the

following steps (see Figure 3.2): intragranular diffusion; grain boundary diffusion; surface adsorption/desorption; pore diffusion; purge flow convection.

The release kinetic result than very complex and the rate –determining step may be strongly dependent on the ceramic microstructure, the temperature, the purge gas composition and the irradiation history. Tritium transport can be described as a series of dynamics, moving from a regime dominated by only one mechanism (grain boundaries diffusion) to a regime with another mechanism (like diffusion along pores) or to a regime with several contemporary mechanisms. The complex microstructure of polycrystal morphologies like these lithium ceramics, the intricate pore/bulk and surface/bulk interfaces, result in a multiple step tritium release pathways that make difficult the checking and separation of each individual mechanism [75]. This difficult is exacerbated by the presence of so many factors continuously varying the system during its operation (temperature, radiation, the presence and the movement of impurities). The effect of each of this variable cannot be study during in-pile experiments, neither the detailed effect they play in the microstructure, nor the influence in the transport dynamics of the gas. This is the reason why a deeply study and out-of pile experiments are necessary for the determination of fundamental properties to be controlled during the expensive and complex in-pile experiments. The behaviour of implanted light ions is one of the possibilities for recreate similar conditions to the tritium produced via transmutations inside the grains. Their characterization by depth profiling has been identified as a powerful tool for understanding the processes occurring inside the matter.

4. Modelling tritium behaviour

Modelling should be an important help during the experimental design stage as for the interpretation of unexpected results during the experiments. In turn the experiments are necessary to determine the best parameters for the formulation of a simplified modelling theory.

The formulation of a model on tritium behaviour is a complex task. The typical steps to its development are summarized in the Figure 3.3. The starting point is the basic theory on tritium behaviour, from which is possible to plan a series of experiments for studying single effects, the effect of radiation and the multiple effect of different radiation sources, tritium production, diffusion and release all together. At the same time, starting from the relevant processes detected from the basic theory, it is possible to formulate a model, which can finally be compared to

the experiments. From these parallel processes, the design and development of a unique code including experiments results and a theoretical model, should represent an important goal.

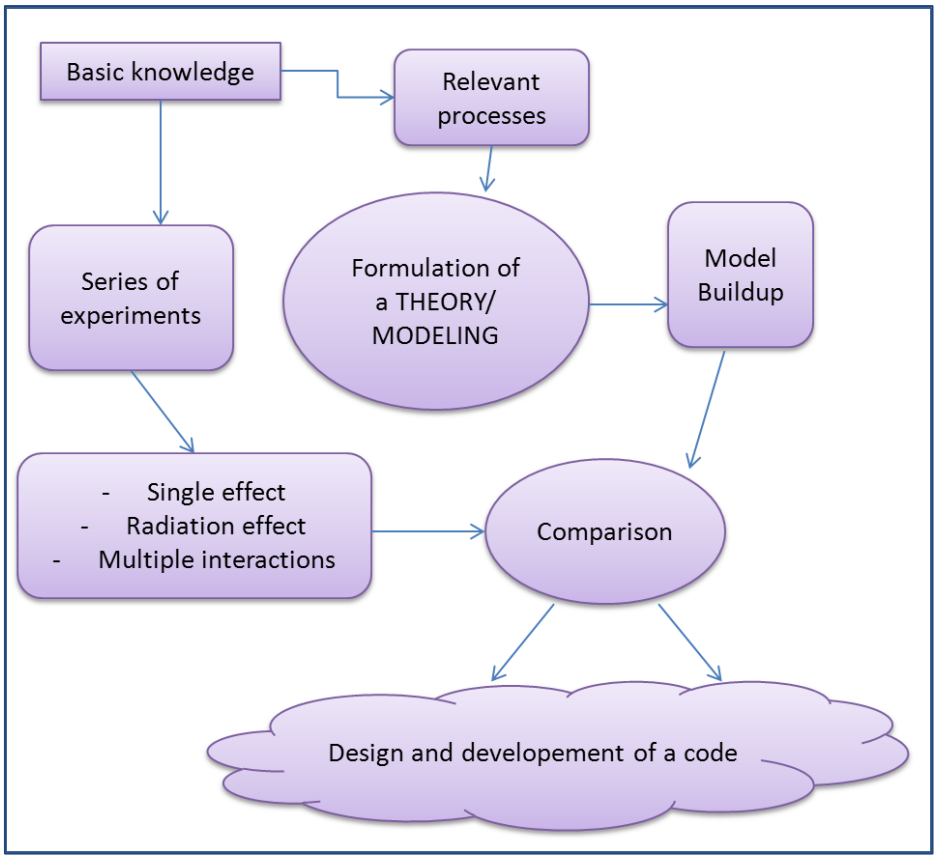

Figure 3.3: Schematization of the main steps to develop a model on tritium transport.

The tritium generated during neutron reaction is assumed to be almost uniformly distributed inside the bulk of the 1 mm pebble. This implies that the main processes controlling tritium release will be the slower: the surface desorption. Thus there are models [76] considering grain as the relevant bulk structure starting from which the diffusion is controlled. TMAP (Tritium Migration & Analysis Program) is one of the first codes improved for understanding the processes involved in atom transport inside fusion materials. Even being a first approximation to this kind of problems, after 7 code-versions it is not still able to work with all the parameters these systems need to consider. By the way it is a first approximation for the validation of the experiments on light ions diffusion, trapping and release [77–79].

The older MISTRAL model (Model for Investigative Studies of Tritium Release in Lithium Ceramics) tried to compare experimental results on how the effects of the

irradiation temperature, the sweep gas flow rate and the hydrogen content in purge gas could affect tritium release [71]. It represents a first approximation to modelling, but quite far from a code-formulation on tritium transport.

In the Fusion reactor the generation/release of tritium inside the breeder blanket represents only a part of the problem. Actually as only a small fraction of the deuterium-tritium fuel is burnt, all the unburnt part has to be removed from the torus to be reused for fuelling. All this part represents the fusion fuel cycle and its understanding is one of the most important requirements for the reactor functioning. With the aim of solve some of these problems, the development and validation of computational tools for describing the H isotopes transport in the breeding zone is being carried on by Ciemat group with the support of Impresarios Agrupados through a new system modelling and simulation software: the Ecosimpro® simulation tool [80,81].

5. Indirect measurements of tritium diffusion and state of the art

An important issue to comprehend is the measurement and the study of the release dynamics followed by tritium from its production in the ceramic pebble to its incorporation into the purge gas. They present a slow tritium release which results in a large tritium inventory, unacceptable from both economic and safety viewpoints. In order to improve it, a precise physical understanding of the relevant mechanisms involved in this critical process is necessary.

Along the years several experiments have been performed, focused on determining the tritium extraction parameters. Some of the most relevant are here reported for identifying the chemical form of the released tritium and for characterizing the rate-limiting process.

During in-reactor experiments like BEATRIX the combined the effect of neutrons, temperature and purge gas chemistry was investigated. The experiment was an IEA-sponsored effort involving the exchange of solid breeder materials and shared irradiation testing among research groups of several countries. The materials were tested in both closed capsules (to evaluate material lifetime) and opened capsules (to evaluate purge-flow tritium recovery) [82]. The results showed interesting data on purge gas composition and on the chemical form of tritium released. The surface role was studied varying the H_2 pressure from an "external" point of view. The surface effect on the release of tritium was observed but not explained.

One of the most important series of experiments on tritium behaviour is represent by the EXOTIC (Extraction of Tritium in Ceramics) EU-programme, where an extensive number of Li ceramics have been in-pile and out-pile analysed after neutron irradiation in the High Flux Reactor (HFR), Petten installation. Several series of this kind of experiment have been performed along the years with some important results on tritium inventory as on the role of the surface in tritium release [47,83]. They represent the only database with in-pile results available nowadays, really expensive and time consuming. The data obtained permitted a comparison of tritium release in ceramics with different porosity and diameter and thus the selection of the best candidate compounds [84]. Also in this case the studies were not able to understand the dynamics occurring inside the material during the release, although some hypothesis were proposed [83].

Finally Munakata et al. [85] investigated techniques that could accelerate the recovery of bred tritium particularly at moderate temperatures. The benefits effects of catalytically active metal additives, such as platinum and palladium were examined [86]. Experimental results indicated that almost all tritium was released as triated water vapour, that slow tritium release took place also at higher temperatures and that a considerably larger amount of tritium was released as the molecular form (HT) from the ceramic deposited with palladium at lower temperatures. Once again this type of studies on the phenomenology of processes occurring once the tritium reaches the pebble surface, did not provide information on how and what is occurring inside the ceramic sphere.

Summarizing it can be suggested that there are six elementary processes from tritium generation to its release: 1) tritium generation by lithium transmutation, 2) thermalization of energetic tritium, 3) tritium trapping at trapping sites, 4) tritium detrapping, 5) tritium diffusion in the bulk, 6) tritium release by recombination or isotope exchange reaction on the surface. The first and the last process have been studied by in –pile reactor experiments. The others have little been investigated so far.

The necessity of deeply understanding the processes occurring inside the ceramic material, all the microstructural features influencing the movement of tritium (defects induced by radiation, material imperfections, impurities, grain size, pores…) and the route it has to follow before reaching the surface are the basic points to study in order to improve tritium release efficiency and the ones that are going to be discussed in this thesis work.

CHAPTER 4

EFFECTS OF RADIATION IN CERAMICS FOR FUSION BREEDER BLANKET

A short review on the effects of irradiation in ceramic materials with a distinction among type of defects and irradiation sources is presented. At the end the state of the art on irradiation effects in breeder blankets ceramic materials is reviewed.

1. Radiation effects in materials

When a particle passes through a material, it changes the matter in a number of ways. These alterations typically cause significant modifications in the physical and mechanical properties of the irradiated material [87]. A charged projectile knock out atomic electrons, causing ionization, which may be followed by a de-excitation as a delayed photon emission [88]; it may collide directly with the atom, causing it to recoil and displace [89]. Furthermore, an energetic neutron or proton may cause a nuclear reaction ejecting other nuclear particles [90]. Finally it is possible to distinguish the *radiation effects,* which include the study of the effects of a particle on the target material, and the *radiation transport*, studying the matter affecting the particle by scattering, slowing down, or absorbing it. Both aspects of the process hold a great interest in the characterization of materials.

A wide range of defects cluster morphologies can be created by particle irradiation [91]. It is possible to define some categories of imperfections or defects in a crystal, as a function of their dimensional extent: *point defects* (vacancies, interstitials and antisite defects), *line defects* (dislocation lines), *planar defects* (dislocation loops), *volume defects* (voids, bubbles). Those associated to radiation damage are the **point defects**, as vacancies and interstitials or clusters of these defects in the crystal lattice [92]. The category of *point defects* includes imperfections localized over a few atomic sites that can be considered as a modification in the stoichiometry of the material. They are stable at room conditions and may be mobile at higher temperatures.

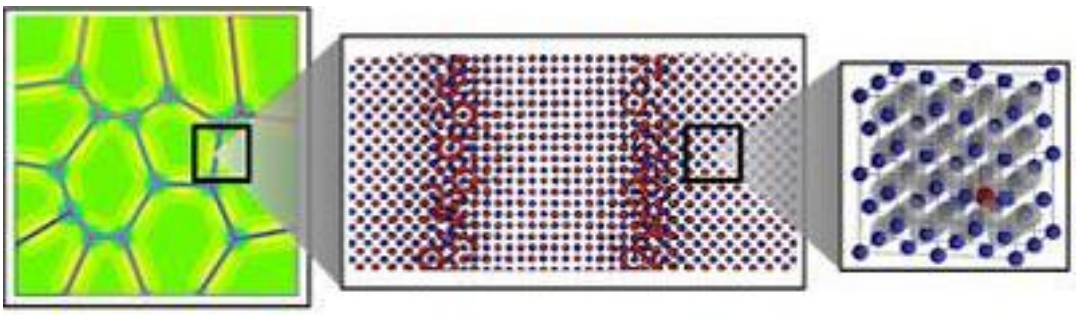

Figure 4.1: A microstructural deepening from the grain boundary to the lattice structure of the lattice change in a material after the creation of a point defect.

It is important to keep in mind that a defect will exert an elastic strain field on the lattice bonds, affecting the mechanical properties of the lattice. In the case of

insulators, electrical neutrality is required and the formation of a simple vacancy may result in a variation of the electronic configuration [93]. Therefore the mechanical and electrical properties of ceramics are affected by defects and their interactions are very important for understanding the behaviour under the mixed effect of irradiation sources [94].

It is important to distinguish a *charged* and a *neutral* particle passing through the matter. The cross section of a *charged* particle (electron, proton, or heavier ion) to interact with an atom is of the order $\sigma \sim 10^{16}$ cm^2, whereas that for a *neutral* one (photon, neutron) is only of the order 10^{24} cm^2 to 10^{20} cm^2. Thus, in matter of number density N~10^{23} cm^3, the mean free path between collisions, $1=N\sigma$, is only a few Angstroms for a charged particle, and microns to centimeters for a neutral one [95]. As a result, a neutral particle interacts infrequently with target atoms, and at each collision it is either absorbed or scattered out of the original beam [96].

The parameter commonly used to correlate the structural damage produced by different irradiation environments is the total number of *displacements per atom* (dpa), which combines the probability for the production of primary knock-on atoms (PKA) and the number of defects created at the end of the cascade process, integrated over the irradiation particle flux spectrum. It is than a correlation between irradiation and resulting material damage. The displacement cross section is a measure of the displacement probability in the material as a function of the incident neutron energy. Kinchin and Pease [97] were the first to attempt the determination of the number of displacements occurring during irradiation. A modified version of their model, known as the Norgett, Robinson, Torrens (NRT) model [98], is generally accepted as the international standard for quantifying the number of atomic displacements in irradiated materials. Integration of the NRT damage function over the recoil spectrum and the time gives the atom concentration of displacements known as the NRT displacements per atom (dpa):

$$dpa = \varphi\sigma_{FP}t = \varphi t\frac{dT(d\sigma(E<T)}{dT}\nu(T) \quad (4.1),$$

where ν(T) is the number of Frenkel pairs generated by a primary knock-on atom of energy E. It provides a measurement of the defects using the damage energy and the threshold energy.

The other important physical parameter for describing radiation damage is the *threshold displacement energy*, which is the minimum amount of transferred kinetic energy to a lattice atom. Depending on the specific displacement energies and ion

masses, it may be possible to induce displacements by one or a two-step displacement sequence [99]. Even electrons, at energies in the range 0.5 – 2.0 MeV should possess a sufficient momentum to displace lattice atoms but not for multiple damage events. Energetic electrons have relativistic mass and their energy is:

$$E_e = (m - m_o)\, c^2 \qquad (4.2)$$

with $m = m_o\,(1 - v^2/c^2)^{-1/2}$ and v the electron velocity.
The maximum energy E_m transferred to an atom of mass M_2 is:

$$E_m = \frac{2\,E_e(E_e + 2m_o c^2)}{M_2 c^2} \qquad (4.3).$$

In order to determine whether an atom will be displaced or not, it is necessary to calculate the *theresold energy* for displacement (E_D) and consequently the cross-section for displacement, obtained by integration from E_D to E_m:

$$\sigma = \frac{\pi Z^2 e^4 (1-\beta^2)}{\beta^2 m_o^2 c^4} \quad \frac{E_m}{E_D} - 1 \qquad (4.4).$$

The cross-section increases rapidly with electron energy and then becomes constant [93]. These damage concepts are used as the base theory for SRIM calculations, but the displacement energy, a crucial parameter for calculating the number of dpa produced, is difficult to measure in the case of polyatomic materials, being strictly related to the mass and nuclear charge of the target nucleus. To overcome this deficiency a binary collision approximation model (BCA) has been developed and implemented using MARLOWE code [100]. It is used to simulate the sequence of atomic displacement generated by a parameterization on a range of *ab-initio* calculation, and used to predict the long term evolution of point defects and clusters [101]. In the present work the parameter used for SRIM calculation was the one reported by Leichtle in lithium based ceramics [100].

2. Radiation defects in breeder blanket ceramics

The components of an operating fusion blanket will tolerate high levels of radiation exposure such as high-energy neutron and γ-fluxes, penetrating till the blanket zone. In the breeding blanket lithium ceramics most of the displacement damage arises from fast neutron reactions such as elastic and inelastic scattering rather than from the lithium transmutation. Although these conditions and lithium

volatility, a solid breeder blanket can achieve significant burn-up level and survive the rigors of the radiation environment [14]. The physical properties modification of ceramic components becomes therefore of great importance regarding the control of some permanent degradation (like electrical properties). The irradiation flux for ITER materials will change as a function of their position in the reactor. In the case of ceramic breeders it is estimated to be of about $<10^{-7}$ dpa/s and $<10^{3}$ Gy/s for of structural and ionizing radiation, respectively [102].

Ceramics are crystalline solids with a highly complex atomic structure. In crystallography they are described as structures with a well-defined planes, but in the practice many are the imperfections present in a lattice [103]. Ceramic radiation responses are similar to those of other well-studied solids, i.e. metals, for both of which the principal considerations are quite the same: point and aggregate defects production and structural, mechanical and physico-chemical properties alterations. The principal distinctions in ceramics lie in the higher bonding energy, the possibility of electrical charge at point defects, and the directionality of bonding in covalent structures [104]. Thus the effects of ionization in insulators are quite marked due to the excitation of electrons from the valence to the conduction band, giving rise to charge transfer mechanisms.

The concentration of radiation defects depends on blanket material preparation conditions, irradiation parameters and impurity content. All these factors can significantly influence tritium localization and release behaviours [105]. Another important phenomenon to consider is the diffusion of host atoms in ceramic materials, a process enabled by defects and controlled by their concentration. Owing to the existence of separate sublattices, cations and anions can diffuse separately with the possible ion movement in one sublattice more pronounced than in the other, an activated process occurring when the ion overcome an energy barrier [106]. As a consequence it is necessary to understand their structure, concentration and interactions. An important role can be played by a doping agent in a crystal lattice, which can have a significant effect on the defect concentration within the material. If it has a different valence state from the host, then a number of alternative strategies are used to accommodate it into the lattice.

These ceramics are mostly ionic crystals and present their own set of rules when speaking about radiation. Among them there is the effect of electronic excitation, the polyatomicity and the charge state of point defects. The interaction of charged particles with matter is based on both Coulomb interaction and elastic collision. The

distinguishing feature about a neutron is that it carries no charge; therefore it suffers no energy loss by Coulomb interaction with the electrons. On the other hand the effect of ionizing radiation can be particularly strong for electron or light ion beam irradiations in oxide ceramics, since the amount of ionization per unit displacement damage is high for these irradiation species, while the ionizing effect per dpa is less pronounced for heavy ion or dual ion beam irradiation [107]. It leads directly on to the problem of surface degradation. For the insulating components, surface degradation is just as serious as volume degradation. It can strongly change if it occurs in vacuum, in air or in helium atmosphere [108], playing a crucial role in tritium release.

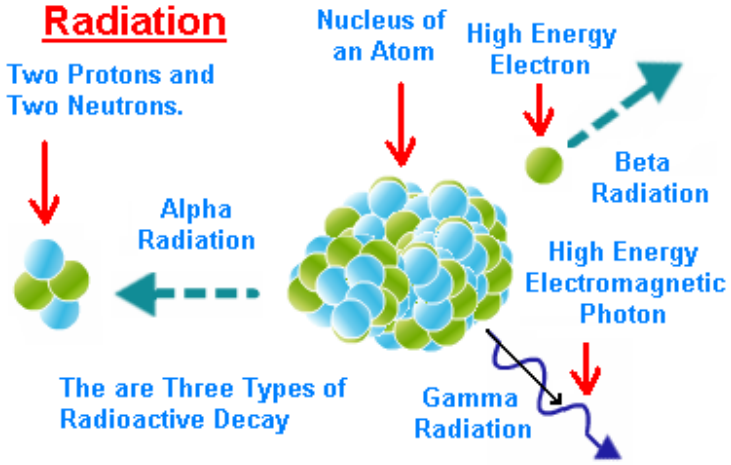

Figure 4.2: On the basis of emitted particles, radioactive decay can be different types: alpha, beta, positron decay and gamma. The first three are charged particles while gamma rays are neutral in nature. Beta particles and positrons are similar in all properties except their charges.

Thus when subjected to radiation, ceramics suffer numerous changes in their structure and properties which can be classified as: 1) electronic defects, with a consequent change in valence state, 2) ionic defects, consisting of a displaced lattice ion, 3) gross imperfections such as dislocations and voids.

2.1. Electronic Defects

Electronic defects are formed when an electron is excited from its ground state configuration into a higher energy state, thus it always involves changes in the valence state. When the excited electron located in a single atomic site is

transferred to another center then there is a change in the ionization state of the atom. The created electronic defect (hole or electron) can then migrate inside the lattice through an activated hopping process. It involves a valence electron and a change in the electrical conductivity depending on the hole or electron moving inside the lattice [93].

These defects can be generated by a thermal input, ion beam damage or γ-radiation.

2.2. Ionic defects

Ionic defects can be distinguished as *vacancies* (the lattice site of a missing lattice ion or atom), *vacancies aggregates*, and *interstitials*, given by a lattice atom or ion occupying an abnormal position [109]. This implies an ionic process type, in which the mobile ions can diffuse because of the presence of intrinsic point defects.

Conduction and diffusion are described in terms of the phenomenological law of steady-state diffusion and the theory of random walk by the Fick's second law of diffusion:

$$\frac{\partial c}{\partial t} = div(D grad\ C) \qquad (4.5)$$

where C is the concentration of diffusing particles, D the diffusing coefficient.

The diffusion in ceramic systems can be distinguished in three main mechanisms. In the interstitial case, ions migrate by jumping between interstitial equivalent positions. This mechanism mostly occurs if the interstitial species are small. The vacancy mechanism is important for the diffusion of substitutional impurities and requires the presence of lattice vacancies whose concentration will influence the kinetics [110]. Finally in the case of interstitialcy mechanism, an interstitial atom displaces an atom from its normal substitutional site, interchanging sites [111]. The collective participation of all the presented mechanisms involves the simultaneous transport of a number of atoms. Of course, there are potential energy barriers hindering the motions of atoms in the lattice, which can be overcome by providing thermal energy to the system. The jump frequency ω to overcome this barrier is given by:

$$\omega = \nu \exp\left(-\frac{\Delta G_m}{kT}\right) \qquad (4.6)$$

where ΔG_m is the free energy barrier which an ion must exceed in order to pass to the adjacent point defect and ν is the effective vibrational frequency of the ion in the initial state [93].

3. Basic effects of radiation in lithium-based ceramics: state of the art

Numerous neutron irradiation experiments have been conducted in fission reactors to observe the effect of damage on tritium release kinetics. Leichtle et al. [112] made a sophisticated damage calculation using an extended version of Marlowe to evaluate the damage correlation parameters in fusion and fission reactor systems. The conclusion is that a thermal fission reactor with a tailored neutron spectrum can provide the best simulation of fusion conditions with regards of the possible dpa accumulation.

It has been suggested [113] that oxygen vacancies or F^+ centers, produced by structural damage, would play an important role on the tritium trapping. Morales et al. [114] characterize lithium silicates by X-ray diffraction (XRD), observing that after neutron and gamma radiation, there are phase transformations in the amounts of different silicates probably due to the radiolysis of silicates. Similar effect have been observed when irradiated with the triple ion beam and with single ion beams of H^+, He^+ and O_2^+ [6]. The experiment shows that the mechanical properties are changed not only because of the structural damage but also because of accumulation of helium and hydrogen in the structure. Alternative measurements like ion implantation are also proposed in the present work with the aim of observe the effect of structural damage on light ion release.

Finally there are the radiation effect caused by photons and electrons. Feldbach [115] demonstrated that low-temperature luminescent methods, based on the investigation of tunnel phosphorescence, TSL and PSL in lithium orthosilicates, are promising for the investigation of e-h processes, identifying the important participation of defects that serve as traps for tritium. The dependence of gamma-ray dose on the formation and annihilation behaviour of irradiation defects is followed by Osuo et al. [116] by means of the electron spin resonance (ESR), observing the evolution of O-related defects. The creation of F^+ and F^0 defects by gamma ray irradiation is related to the irradiation doses, with an increase in 45-75 kGy and a decrease at total dose till 240 Gy.

4. Review of the radiation sources for defects production

The displacement per atom (dpa) is an estimation of the total energy available for creating displacements in a compound, but it is not a direct measurement of the real damage effect due to the high probability of defects recombination. Starting from this assumption, in the present work gamma irradiation and ion implantation are selected for studying the combined effect of radiations. In this way it is possible to test both the ionizing and the structural damage on the ceramics together and for separate. Results and discussion on their effect will be presented in chapters 6 and 7. Here below a brief presentation of the two radiation sources used, with a special focus on the ion beam implantation, used for creating a structural damage, an interesting tool for neutron damage comprehension.

3.1. High energy photons

Gamma radiation is made up of light or high-energy photons which have an extremely small wavelength, no electric charge and no rest mass. There are three mechanisms that can be identified in their interaction with matter: the *photoelectric radiation*, where an electron is emitted from an atom (ionization process) with energy equal the gamma-ray one, so that the gamma ray disappears; the *Compton scattering*, in which the γ-ray interacts with an electron, causing an increase in its energy and the emission of a new gamma ray, which can escape from the matter or be adsorbed through the photoelectric effect; the *pair production* where high energy gamma rays are absorbed and two particles are created (an electron and a positron). The electron interacts with matter while the positron loses its energy through ionization or excitation.

Therefore, although gamma photons cannot themselves displace atoms, the energetic electrons resulting from Compton scattering may be able to do so. The cross sections for displacement under gamma irradiation have been determined for a number of polyatomic ceramics [117]. Small cross section-values are find, indicating that γ-irradiation can poorly contribute to the ion displacement damage and that high energy photons mainly induce electronic excitations in a spatially uniform manner throughout the solids. It should be noted that a beam of gamma photons will transfer energy to electrons in a forward direction thereby leading to charge separation and the build-up of electric fields within an insulator.

In the case of the present work, the gamma–ray emitter is represented for a ^{60}Co source. This is a synthetic radioactive isotope of the cobalt, with a half-life of 5.27

years which decay by beta decay to the stable isotope ^{60}Ni. The activated nickel nucleus emits two gamma rays with energies of 1.17 and 1.33 MeV. The use of this kind of radiation source can be justified as long as the influence of this type of radiation on some physical parameter such as the radiation induced electrical conductivity and ionization effects.

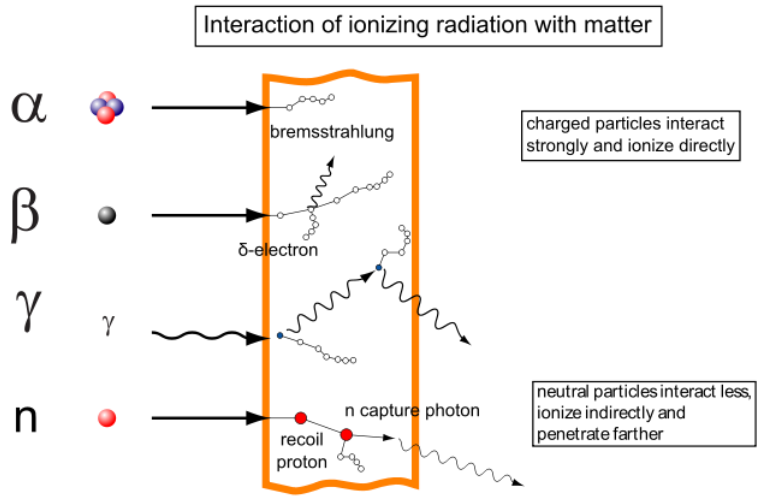

Figure 4.2: Interaction of ionizing radiation with matter. Gamma rays are represented by wavy lines, charged particles and neutrons by straight lines. The small circles show where ionization occurs.

3.2. Ions

When an energetic ion is impinging onto a solid target, there is a rapidly transfer of energy causing several effects: disordering of the original lattice structure (radiation damage), atoms leaving the surface (sputtering), and the structure modification because the implanted ions stop buried at the end of their damage track occupying a crystal site (doping) [118]. The main difference between ions effect and the ionizing radiation lays in the particle energy spectrum. By virtue of their electrically neutrality, electrons can penetrate very large distances producing bulk flat damage profile over a long depth of the material. In the case of ions the energy transfer occurs via several mechanisms with the dominant processes being the excitation of electronic states and the nuclear collision between incident and target ions [119]. These mechanisms had shown energy dependent cross section which varies with the masses. The damage or sputtering will depend on the energy. Along the path of the incident ions, the energy ratio causing displacements and electronic excitation varies. This ratio is reported to be very important for dynamic processes of irradiation damage in ceramics [120].

The literature on the use of ion implantation effects in insulators [120] reports of experiments with light ions used at few MeV where nuclear collision induced damage is almost buried at the end of the ion range, sputtering is negligible and displacements are almost entirely related to the electronic excitation (see Figure 4.5).

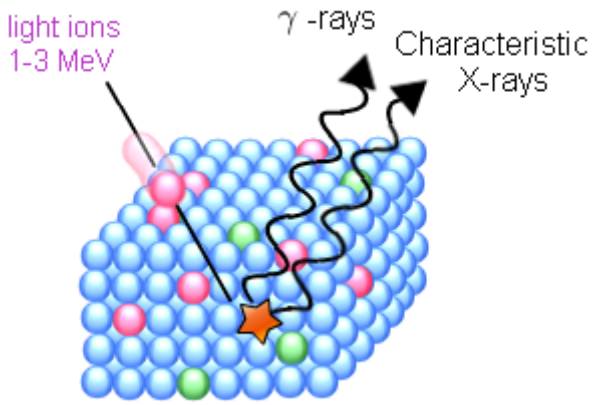

Figure 4.5: A process of emission of gamma rays from excited nuclei. Induced gamma emission is just like fluorescence process in which there is an emission of a photon instead of gamma rays by an excited electron in atom.

In the 1960_s and 1970_s the use of heavy ions for simulating neutron damage in support of the fast breeder reactor program started [121]. The first problem in determining the equivalence between the measurement of radiation with charged particles and with neutrons is the use of a common dose unit. The basic particle dose for neutrons is the fluence unit (n/cm^2), while in the case of charged particles it is important to consider the charge in unit of Q/cm^2. Both measurements can be converted to dose as *dpa* and dose rate as *dpa/s*. taking into account the matter main features (density, atomic number..).

There is a significant interest in using ion irradiation to emulate neutron damage as this technique provides low-cost measurements with a rapid means for elucidating mechanisms of the most important processes, compelling a first important screening of the candidate materials [122]. Furthermore ion irradiations rarely require more than several tens of hours to reach damage levels in the 1–100 dpa range, producing little or no residual radioactivity therefore allowing the handling of samples without the need of special precautions.

Damage state and microstructural variation resulting from irradiation depend upon the particle type and the damage rate [123]. As ion-irradiation can be

conducted at a well-defined energy, dose-rate and temperature, it results in a very well controlled experiment, which should be difficult to match in a fission reactor.

Ion irradiation and simultaneous He-implantation are used to simulate the effect of 14 MeV neutron damage and lithium transmutation effect, saving the residual radioactivity and allowing the handling of the sample without any special need. Thus the challenge is to verify the equivalency between neutron and ion irradiation in term of effect on the microstructure and the properties of the material. The absence of collision cascades effects suggests that in a first approximation, neutron and ion irradiation produce different damage rate and a different ratio of displacement and ionization, but similar damage states. Some fundamental differences are the depth penetration because of the mean free path, and the particle energy spectrum that arise because of the different way in which the particles are produced. Furthermore the cross-section of an ion-atom interaction is greater than for neutron-nuclear, giving rise to a higher damage rate per unit of particle fluence.

The number of displacements per unit volume, per unit time R_d in front of the atom number density N and the particle flux Φ, change for neutrons and ions as:

$$\frac{R_d}{N\varphi} = \frac{\gamma E}{4E_d}\ \sigma_s \qquad (4.7)$$

$$\frac{R_d}{NI} = \frac{\pi Z_1^2 Z_2^2 \varepsilon^4}{4EE_d}\ \frac{M_1}{M_2}\ \sigma_s \qquad (4.8)$$

where the first is for neutron – nuclear interaction (E is the neutron energy γ is the target mass and σ_s the elastic scattering cross-section), described by the hard sphere model and the second is relative to ion-atom interaction, described by Rutherford scattering (with M_1 the mass of the ion, M_2 the mass of the target and $Z_{1,2}$ their atomic numbers). When comparing the damage produced by different atoms and the neutrons for comparable energies, it is possible to observe form the literature (see Figure 4.6) that the damage caused by a 1.3 MeV proton beam is about 100 times more than 1 MeV neutrons per unit fluence, with the big difference that the damage depth is orders of magnitude smaller than that for neutron irradiation. By a simply comparison among the dose rates it is not possible to assess the impact of the two irradiations. The effective dpa correlation between ion and neutron still need to be defined and agreed [123].

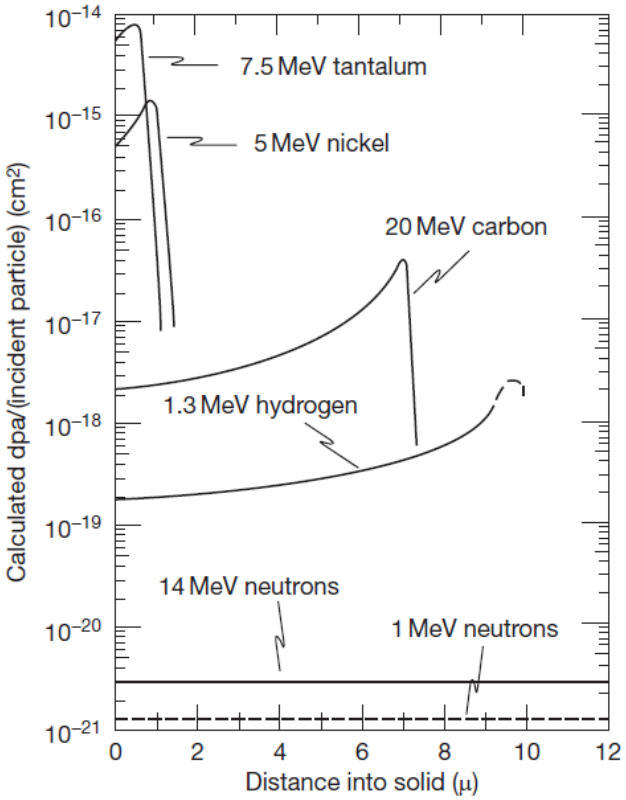

Figure 4.6: Displacement-damage effectiveness for various energetic particles in Ni. Reproduced from Kulcinski et al. [124].

PART II: EXPERIMENTS AND RESULTS

CHAPTER 5

FABRICATION and CHEMICAL CHARACTERIZATION of LITHIUM CERAMICS with DIFFERENT Li-CONTENT

Three different methods followed for the fabrication of spherical ceramics are exposed, presenting the results obtained for two compositions with higher lithium content. Subsequently the basic characterization on dense bodies is presented for all the materials with different matrix and Li-proportion used along the thesis work.

6. **Sintering of Li-ceramics: the effect of Li-content in dense bodies**
    a) X-Ray Diffraction
    b) Secondary ion mass spectrometry
    c) Density and pore distribution
    d) Scanning Electron Microscopy
7. **Discussion**
8. **Conclusions**

5. State of the art

When the ceramic breeder research started around 1970, there were really scarce or irrelevant data for lithium-based ceramics within this kind of application. The initial selection was based on the properties measured for un-irradiated materials. During a large time the development of breeder fabrication technology was only devoted to the manufacturing process based on the achievement of the spherical shape [125] and a good thermo-mechanical behaviour [126].

The pebble configuration was selected as the best option because of its potential advantages in assembly of blankets with complex geometry and in anticipated relief of thermal stress and irradiation cracking [22]. Several methods and ceramics were investigated to produce pebbles with the desired qualities, but only few of these could simultaneously achieve current requirement for basic characteristics [127]. Fabrication processes that have been or are being explored and developed include: solid – state reaction [128–131], sol–gel type process [132,133], precipitation synthesis [134], combustion method [135,136], wet process [137], melting spraying [34] and finally agglomeration/sintering and extrusion/spheronization method [138] for the achievement of the desired spherical shape.

Though a spherical pebble shape is desired, there is no experimental critical evidence in a slight deviation from the spherical form, improving thermal, mechanical and irradiation behaviour. The pebble bed porosity can be adjusted varying the number of pebble sizes and size ratios. In general a smaller size and a spherical shape, enables a higher bed packing factor which represents, together with pebble density, the "smear density" a fitting for the total achievable Li density inside the TBM [139].

The fabrication of these materials needs to take into account the recycling process, not only to recover the expensive ^{6}Li-enrichment for effective resource use, but also for removing radioactive isotopes. Because of the cost involved in the ^{6}Li enrichment, the recovery of tritium from wasted blanket is an important issue that could add interesting economic advantages to the selection of ceramics as breeder best option.

The fraction of lithium-6 burned in the reactor is estimated to be 14.6% after 2.3 years of operation at full power [9]. Hence it is possible to recover a substantial portion of lithium from those ceramics removed from the reactor, which should be used for the preparation of Li carbonate powder as new reprocessed raw material.

The principal methods used for recycling are: humid route [140], wet chemistry [141] and re-melting with an addition of lithium hydroxide hydrate [142]. It was observed that the re-melting process did not deteriorate the properties of the pebbles and that an 83% overall efficiency was achieved for the recovery of lithium carbonate even though it was not possible to remove the activated impurities [142].

It can be stated that the research of the fabrication routes for the achievement of the best shape and mechanical properties have largely been studied and improved [131,143–145]. The next step regards the optimization of solid breeder blankets, taking into account other really important parameters like the effect of radiation and the light ions behaviour for the improvement of its qualities as tritium breeder.

The objective of this part of the work is the fabrication of the material necessary for the radiation effect and the light ions transport. Contemporary a brief study on the achievement of ceramics with higher lithium content and a spherical shape is carried out.

6. Important features for the optimization of BB ceramics

The mechanical and thermal stability cover a special interest considering that pebbles are subjected to neutron flux, thermal shocks, pressure and irradiation that may induce cracking. Their fragmentation may result into the degradation of the heat transfer parameter or a contamination of the purge gas, changing the tritium generation and the release performances but also affecting the shielding role of the breeder blanket module.

The diffusion and the release of tritium, among the major concerns within the reactor operation, are strongly controlled by structural and microstructural features of the breeder blanket materials, being determined by the fabrication route. Tritium production is almost proportional to the lithium atomic density [146]. The interest in increasing tritium inventory makes the fabrication of the over-stoichiometric compounds with higher lithium contents, a very interesting issue. The synthesis of these ceramics was shortly investigated in the past with scarce results [147], prioritizing the optimization of density, mechanical strength, shape and thermal conductivity. The compounds in the Li-Si-O system with different lithium content are proposed in the present work as a tool for the comprehension of lithium effect on some important properties.

Considering its high lithium richness and good physic-chemical stability [143], the Orthosilicate (Li_4SiO_4, OSi or Li4) is selected as the European solid breeder candidate. The lithium metatitanate (Li_2TiO_3) is the candidate material selected by Japanese as the ITER-TBM candidate considering its really good thermo-mechanical behaviour [37,148,149]. EU-KIT group is now working on a new phase compound [33] which combine the advantages of a phase rich in Li-ceramic, as the Li_4SiO_4, with the optimal thermal and mechanical stability of Li_2TiO_3.

The *effect of irradiation and light ions transport* in these breeder blanket candidates (Li_2TiO_3 and Li_4SiO_4) is compared and discussed along all this thesis work with the aim of provide a complete comparative study on the best BB candidates. The fabrication of Li_4SiO_4 (orthosilicate, OSi) is explored in this chapter through different synthesis methods with the idea of achieving a quasi-spherical shape while searching for a higher Li:Si proportion. At the same time the Li_2TiO_3 (metatitanate, MTi), was characterized but not synthetized in our laboratories. Pellets with a starting commercial powder were fabricated and sintered.

7. Powder characterization methods

Throughout this thesis work, several characterization techniques are used. Here the description of the basic theory below each method.

3.1. Thermal analysis

When a ceramic is heated or cooled, its crystalline structure and its chemical composition can be affected by changes that can be studied measuring the variation of some properties as a function of the temperature.

Thermal analysis is formed by a group of techniques studying the properties of materials (like enthalpy, thermal capacity, mass changes..) changing with temperature. They include different methods, distinguished from one another by the property which is measured: thermo-gravimetric analysis (TGA) detects changes in the mass, differential thermal analysis (DTA) studies the temperature differences, differential scanning calorimetry (DSC) is on heat difference, thermo mechanical analysis (TMA) on deformations and dimension, dilatometry (DIL) looks for volume changes and evolved gas analysis (EGA) studies gaseous decomposition products.

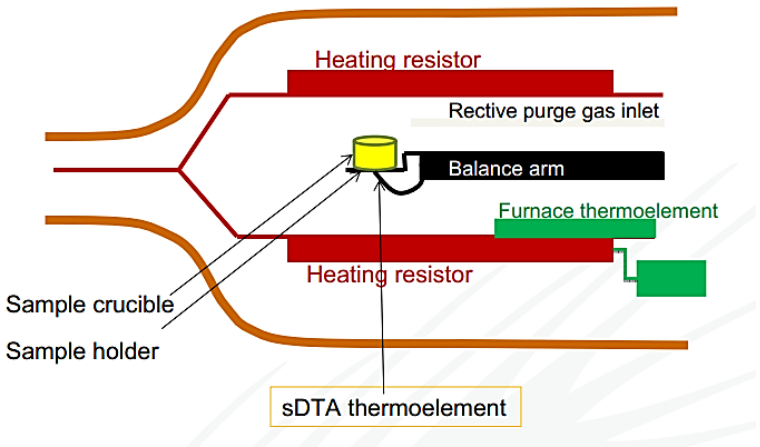

Figure 5.1: Furnace components for thermal analysis.

The methods used for the thermal evolution study on the ceramics fabricated in the present work, are TGA and DTA. *Thermo Gravimetric analysis (TGA)* is basically an analytical technique in which the mass change of a substance is measured as a function of temperature whilst the substance is subjected to a controlled temperature program. Mass loss is only seen if a process occurs when a volatile component is lost. There are, of course, reactions that may take place with no mass loss. As materials are heated, they lose weight due to drying, or from chemical reactions that liberate gases. Some materials can gain weight by reacting with the atmosphere in the testing environment.

During *Differential Thermal Analysis (DTA)* the thermal difference between the sample under investigation and an inert reference material is measured as a function of the temperature. Both samples are treated with the same temperature program and the same heating and cooling rates. During the heating step, the sample receives energy; as a consequence either a phase transition or an internal energy change can occur. From the thermal analysis, peaks are obtained. The peak area (A), which is related to enthalpy changes in the test sample, is that enclosed between the peak and the interpolated baseline and it is given by

$$A = \frac{mq}{gK} \qquad (5.1),$$

where m is the sample mass, q the enthalpy change per unit mass, g a measured shape factor and K the thermal conductivity of the sample. The calibration of the

apparatus is made on standard samples (at least two different), over specified temperature ranges [150].

Often different properties may be measured at the same time, as in the case of TG-DTA analysis as afterwards presented in this work, for the comprehension of ceramics thermal behaviour. In this work only the two described thermal analysis techniques are performed in the "Centro de quìmica" of CIEMAT laboratories. A thermo-gravimetric analyser appending differential thermal analysis (DTA/TG), NETZSCH Instruments, was employed. The study has beewasn performed in air from room temperature to 800 °C with a heating rate of 5 °C/min. For eliminating the error, a baseline was measured at the same experimental conditions prior to the analysis.

3.2. X-Ray Diffraction

About the 95% of all the solid materials can be described as crystalline. When X-rays interact with a crystalline substance a diffraction pattern is obtained, representing like a fingerprint of the material. The powder diffraction method is ideally suited for the characterization and identification of polycrystalline phases [151].

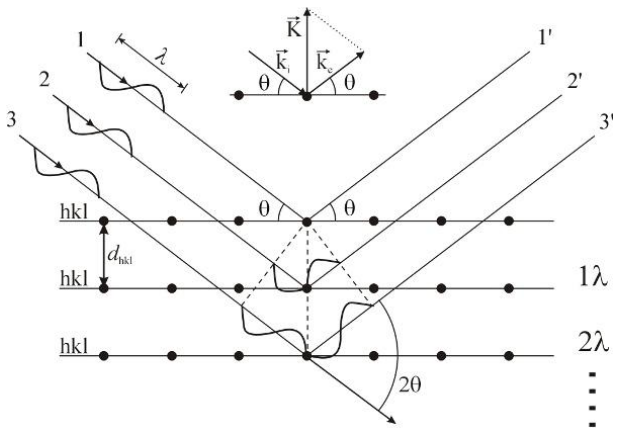

Figure 5.2: A wave diffraction from a set of planes. In the inset the scattering vector $K = k_e - k_i$ as the difference between the wave vector k_e of the scattered wave, and the wave vector k_i of the incident X-ray.

When an X-ray beam hits an atom, the electrons around it starts to oscillate with the same frequency as the incoming beam. In almost all directions there will be a destructive interference, that is, the combining waves are out of phase and there is no resultant energy leaving the solid sample. If the waves are in phase and well

defined X-ray beams leave the sample in various directions, the diffracted beam, a beam composed of a large number of scattered rays mutually reinforcing one another, will be detected. The conditions for constructive interference are easily derived from the simple geometrical picture of the scattering of an X-ray beam by planes of atoms in a crystal, as shown in Figure 5.1. It is possible to talk about X-ray reflections from a series of parallel planes inside the crystal. The orientation and the interplanar spacing of these planes are defined by the three integers *h, k, l* called indices. A given set of planes with indices *h, k , l* cut the a-axis of the unit cell in *h* sections, the b axis in *k* sections and the c axis in *l* sections. A zero indicates that the planes are parallel to the corresponding axis.

Constructive interference is observed for the X-rays reflected from the lattice planes at the specular angle, if the path length difference between X-rays scattered from different *hkl*-planes is an integer time the wavelength number. This condition is summarized in the Bragg law:

$$n\lambda = 2d_{hkl} \sin(\theta) \quad (5.2).$$

Diffraction (i.e. constructive interference of the scattered X-rays) will occur if the Bragg condition (equation 5.1) is fulfilled and the scattering vector K is parallel to the normal of the *hkl*-planes [152].

The XRD measurements of this thesis work were realized in the "Unidad de Microscopía y Análisis de Superficie" of CIEMAT, Spain. In the case of powder analysis the samples suspended in ethanol, were deposited as a uniform film on a glass sample holder. In the case of sintered pellet-samples, there was no need for a previous preparation. The measurements realized through $CuK\alpha_1$ radiation (with a λ=1.54056 Å), were carried out at 40 mA and 45 kV in an angular 2θ range from 10° to 90°.

3.3. Infrared Spectroscopy (IR)

Infrared (IR) spectroscopy is one of the most common spectroscopic techniques used. Its main goal is the structural elucidation and the compound identification. At temperatures above absolute zero, all the atoms in molecules are in continuous vibration with respect to each other. When the frequency of a specific vibration is equal to the frequency of the IR radiation directed on the molecule, the molecule absorbs the radiation. The major types of molecular vibrations are stretching and

bending. Infrared radiation is absorbed and the associated energy converted into different type of motions.

When radiation propagates from an optically denser medium (refractive index n_1) toward an optically rarer medium (refractive index n_2, $n_1 > n_2$), a total internal reflection will occur at the interface of the two media. If the radiation angle of incidence (θ) is exceeding the critical angle (θ_c), than it is defined as a function of the refractive indices of two media:

$$\theta_c = \sin^{-1}\left(\frac{n_1}{n_2}\right) \qquad (5.3).$$

At each reflection, an evanescent field is extending into the adjacent optically rarer medium. If the optically rarer medium is absorbing IR radiation, the attenuated total reflection (ATR) results at characteristic wavelengths corresponding to the vibrational resonant frequency.

IR spectra are obtained by detecting changes in transmittance (or absorption) intensity as a function of frequency. The sample is normally placed in close contact with a more-dense, high-refractive-index crystal. The IR beam is directed onto the bevelled edge of the ATR crystal and internally reflected through the crystal with a single or multiple reflections. Both numbers of reflection and the penetration depth decrease with increasing angle of incidence [153].

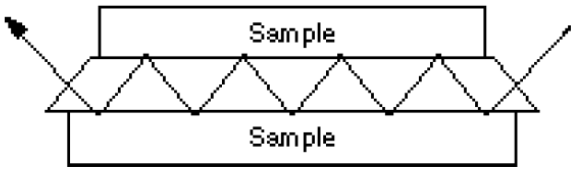

Figure 5.3: Schematic representation of multiple internal reflection effect in Attenuated Total Reflectance (ATR).

The characterization carried out in this work employed a Nicolet 5700 IR spectrometer in the range of 4000-400 cm^{-1}, coupled with a smart performer single-reflection ATR (attenuated total reflectance) accessory that operates by measuring the changes occurring in a totally internally reflected infrared beam when the beam comes in contact with a sample, thus compelling the determination of bond structures and the identification of reaction components.

3.4. Secondary ion mass spectrometry

Secondary ion mass spectrometry (SIMS) can be used to detect atomic ions or ionized molecules which have been sputtered from the sample using a primary beam of either positive (e.g. Cs) or negative (e.g. O) ions. The interaction of the primary ion beam with the sample (under vacuum) provides sufficient energy to ionize many elements. If the primary beam is composed of positively charged ions, the resultant ionization favours production of negative ions; primary beams of negative ions favour generation of positive ions. Although most atoms and molecules removed from the sample by the interaction of the primary beam and the sample surface (referred to as sputtering) are neutral, a percentage of these are ionized. These ions are then accelerated, focused and analysed by a mass spectrometer.

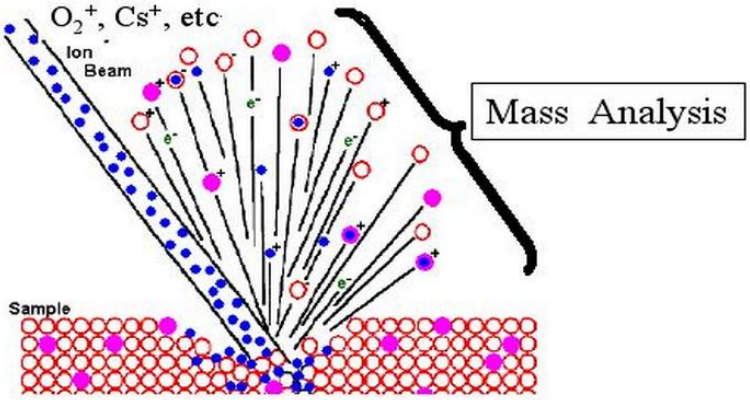

Figure 5.4: Principles of SIMS technique: an ion beam ionizes the elements of a sample, further detected by mass spectroscopy.

This technique uses an ion beam accelerated to energies between 0.5 and 15 keV for the sputtering of the specimen, detecting the secondary ions emitted. The detected ions come from the upper monolayers of the sample. The mass/charge ratios of these secondary ions are measured with a mass spectrometer to determine the elemental, isotopic, or molecular composition of the surface to a depth of 1 to 2 nm. This technique permits the detection of quite all the elements, including hydrogen. Profile concentrations depending on depth, can also be obtained. Due to the large variation in ionization probabilities among different materials, SIMS is generally considered to be a qualitative technique, although quantitation is possible with the use of standards. It is considered as the most rapid and sensitive surface analysis technique, with elemental detection limits ranging

from parts per million to parts per billion. It is capable to furnish information on the impurities with really low concentration in the material. Moreover, the specific character of the mass-spectrometric method entails the optimal mass resolution and sensitivity [154].

The SIMS HIDEN Workstation of the LNF-Ciemat laboratories works in the dynamic mode with a 6 kV, 800 nA O/Ar ion gun as the primary ion source or a 5kV, 150 nA Cs primary ion beam. The chamber vacuum pressure is better than $5*10^{-7}$ mbars and it is provided with a quadrupole mass spectrometer. Thus static SIMS (SSIMS) was used for our measurements, with the aim of obtain sufficient signal for a compositional analysis of the surface, without removing a significant fraction of a monolayer. A very low ion flux was used to ensure that each ion was statically-likely to impact upon the undamaged surface and that the sputtered secondary ions could be representative of the original surface.

3.5. Density and porosimetry

The density ρ is an elementary physical property measuring the "compactness" of matter within a substance defined as the ratio of its mass *m* to its volume *V*:

$$\rho = \frac{m}{V} \qquad (5.4).$$

The density can assume different values depending on the method used to measure the volume of the particle. It is possible to distinguish among three different possibilities: the *true density*, *the pycnometric density* and *the granular density*. The *true density* is the average mass per unit volume, excluded all voids. The true density of a perfect crystal can be determined from the size and composition of the unit cell (theoretical density). The *pycnometric density* uses a gas pycnometer and the volume occupied is determined by measuring the volume of gas displaced. It is quite equal to the true density unless if the material contains impenetrable voids or pores, inaccessible to the gas.

It is possible to distinguish a density value related to the open and closed porosity. A common measurement is mercury porosimetry, where the limiting pore size depends upon the maximum intrusion pressure. It is a useful technique providing a wide range of information as the pore size distribution, the total pore volume, the apparent density and the specific surface area of the sample [155]. Its

limitation consists in the fact that it measures the largest entrance towards a pore but not the inner size of a pore, a part of not being able to analyse closed pores (see Figure 5.4) since mercury has no way of entering. For the measurement of pore shape the Washburn equation is used:

$$\Delta P = \gamma\left(\frac{1}{r_1}+\frac{1}{r_2}\right)=\frac{2\gamma\cos\theta}{r_{pore}} \qquad (5.5).$$

It relates the pressure difference across the curved mercury interface (r_1 and r_2 describe the curvature of that interface), to the corresponding pore size (r_{pore}) using the surface tension of mercury (γ) and the contact angle between the sample and the mercury (θ). The parameter most affecting the real results has been proved to be the contact angle [156]. The pore diameter thus varies along the path of the pore, and consequently the pressure. It presents a maximum value at the most constricted part, thus the size of the smallest pore is limited by the maximum pressure. Blind pores, cross-limited pores and through pores (see Figure 5.5) can be measured.

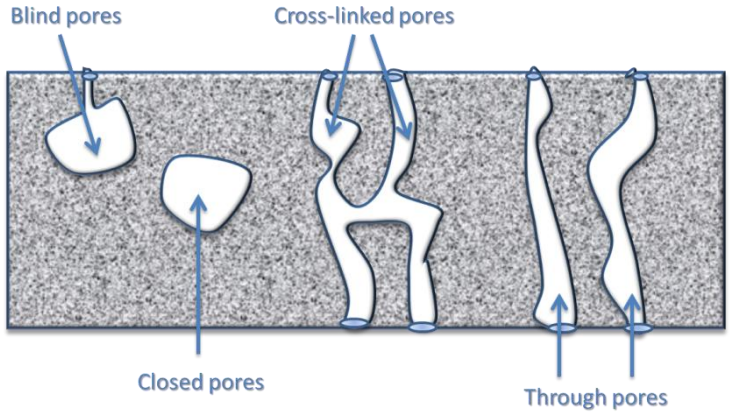

Figure 5.5: Schematic representation of the different kind of pores.

Ceramics are generally porous materials with several degrees of porosity. Along this thesis work the open porosity will refer to the network of pores that is open to the surface and into which a liquid can penetrate if the part is submerged in it; the closed porosity will refer to those pores that have become sealed with the grain structure. The measurements were carried out in the ICV-CSIC centre in Madrid with a Quantachrome poremaster 5.10, being the Hg surface tension 480 erg/cm^2 and the Hg contact angle of 140°.

3.6. Electron Microscopy

Electrical microscopy is a technique which provides "local" information of the studied material. The resolution scale depends on the microscopy and the technique used.

In *SEM (Scanning Electron Microscopy)* a source of electrons is focused into a fine probe that is rastered over the surface of the specimen. As the electrons strikes the surface, a number of interactions occur that can result in the emission of electrons or photons from the surface. A reasonable fraction of the electrons emitted are collected by appropriate detectors [157]. New SEM microscope as a field emission gun (FEG-SEM), works using as electron source, electron beams with high and low energy better focused. This permits a better spatial resolution, a charge minimization on the sample and thus less damage on the surface achieving a final better image.

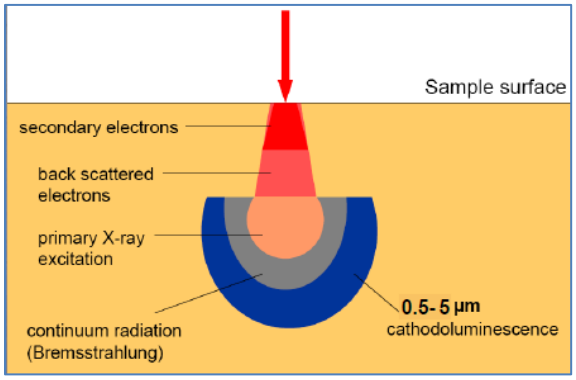

Figure 5.6: Scheme of the interactions among the electron beam and the matter, where the different scattered particles are evidenced.

Primary electrons enter through the surface with an energy of 0.5 – 30 kV and generate many low energy secondary electrons. An image of the sample surface can thus be constructed by registering secondary electron intensity as a function of the position of the scanning primary electron beam. In addition to low energy secondary electrons, backscattered electrons and X-rays are generated by primary electron bombardment. The intensity of backscattered electrons can be correlated to the atomic number of the element within the sampling volume. Hence, some qualitative elemental information can be obtained. The analysis of characteristic X-rays (EDX or EDS analysis) emitted from the sample gives more quantitative elemental information.

The Zeiss Auriga Compact focused ion beam-scanning electron microscope (FIB-SEM) present in LNF-CIEMAT laboratory offers very high resolution of up to 2.5 nm

also at low acceleration voltage of 1 kV and was successfully used to image and analyse the composition of samples studied along this work.

In a *transmission electron microscope (TEM)*, the sample is illuminated by an electron beam, produced by a thermionic or field emission gun. When the electrons are emitted from the filament they are accelerated by an electrical potential. The electrons are then focused by electrostatic and electromagnetic lenses onto the sample and the transmitted beam is used to form an image [158].

TEM specimen preparation can be a complex procedure. Samples are required to have a thickness almost comparable to the mean free path of the electrons that travel through the samples, which may be only a few tens of nanometers [159]. Mechanical polishing is used to prepare samples, even if additional fine methods such as ion etching may be required to perform final stage thinning. Polishing needs to be done with high quality, to ensure constant sample thickness across the region of interest. More recently, focused ion beam (FIB) has been used to prepare thin samples. Unlike inert gas ion sputtering, FIB makes use of significantly more energetic gallium ions and may alter the composition or structure of the material through gallium implantation [160].

Cross section TEM specimens of lithium based ceramics were prepared after thermal evaporating a W thin layer (about 6 nm) to protect the implanted alumina surface grains from a severe and quick ion thinning. Then the W-coated implanted surfaces were face-to-face glued, sectioned perpendicular to the irradiation surface and thinned by means of mechanical dimpling and cooled ion milling (Ar+ ions, 5-8° milling angle). Preparations were finished until perforation occurred at the W-W interface [161] (see Figure 5.7).

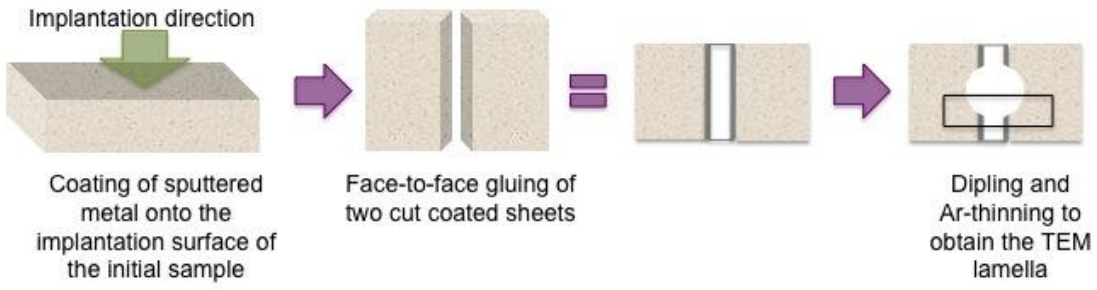

Figure 5.7: Cross section preparation of specimens for TEM characterization.

Specimens were examined using a TEM (Philips TECNAI 20T) operating at 200 kV and equipped with a x-ray energy dispersive spectrometer (EDS) in the "Centro Nacional de Microscopía Electrónica" of UCM-Madrid.

4. Synthesis processes of Li-Si powders

The main line of ceramic breeder materials research and development is based on the production of quasi-spheroid pebbles with small diameter (Ø < 1 mm) [162,163], synthesized by different methods [29].

The attainment of lithium silicates is given by the reaction between silica and lithium oxide in the correct molar ratio to obtain:

$$xSiO_2 + xLi_2O \rightarrow Li_xSi_xO_x \qquad (5.6)$$

where in the case of increasing temperatures (up to 800 °C) or in presence of impurities, the compounds can decompose into:

$$Li_4SiO_4 \rightarrow Li_2SiO_3 + Li_2O \qquad (5.7)$$
$$Li_6SiO_5 \rightarrow Li_4SiO_4 + Li_2O \qquad (5.8)$$
$$Li_8SiO_6 \rightarrow Li_4SiO_4 + 2LiO_2 \qquad (5.9)$$

and their mixture, hindering the achievement of a unique phase [164].

Along the thesis work, three different routes are experimented for the achievement of spherical shapes. The final characterization and results are shown only for the two compositions with high Li-content: Li_4SiO_4 and Li_8SiO_6.

I. Solid-state method (SS)

The conventional solid-state method is the dominating way for ceramic synthesis according to the literature, due to its simplicity (there are no special needs for experimental conditions) [130]. Varying the lithium carbonate molar content (x):

$$xLi_2CO_3 + xSiO_2 \rightarrow Li_nSiO_n \qquad (5.10),$$

with x = 1 for the Li_2SiO_3 composition, x = 2 for the Li_4SiO_4 composition, x = 3 for the Li_6SiO_5 composition, x = 4 for the Li_8SiO_6 composition, the different phases are than obtained.

The raw materials, Silica (Davisil- Scharlau 100-200 mesh, > 99%) and Li_2CO_3 (Aldrich > 99%) were manually mixed in an agatha mortar during 30 minutes. The mixture was put in a Al-crucible and heated in an Ar-atmosphere oven during 24 h (Figure 5.8, Flux diagram I). The calcination temperature varied between 650 and 950 °C depending on the composition.

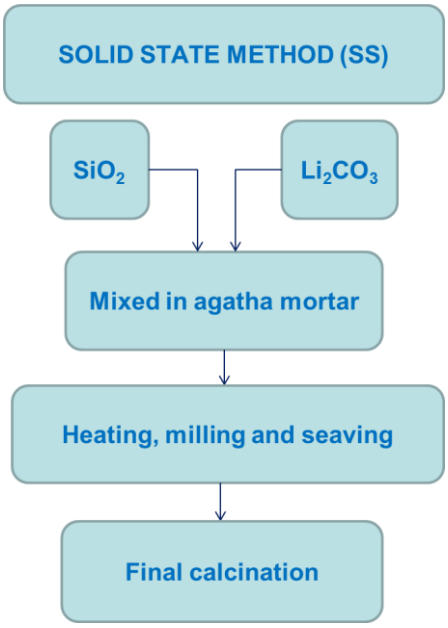

Figure 5.8: Flux diagram of solid state (SS) method.

II. *Suspension dried in a Rotary Evaporator (RV)*

The compounds were prepared starting from amorphous silica gel (suspension of Ludox TMA colloidal silica 34%) and a water solution of lithium citrate (Aldrich hydrated $Li_3C_6H_5O_7$, 99%) (Figure 5.9, Flux diagram II) reacting as:

$$xLi_3C_6H_5O_7 + xSiO_2 + xO_2 \rightarrow xLi_xSiO_x + xH_2O + xCO_2 \qquad (5.11).$$

After mixing the raw material during 15 minutes, it was fired in an open oven at 250 °C during 12h for the organic residue elimination. The ceramic was then smashed manually in an agatha mortar and subsequently milled in alcoholic media through a

ball milling during 1 h. The fine powder obtained in ethanol media, was dried during 30 minutes in a rotary evaporator using a 50 °C water bath and a pressure of 102 mbar, at a constant rotary velocity. The powder obtained was heated at 750 °C during 10 h in air, thus smashed, milled and dried again till a final thermal treatment at 950 °C during 10 h in air.

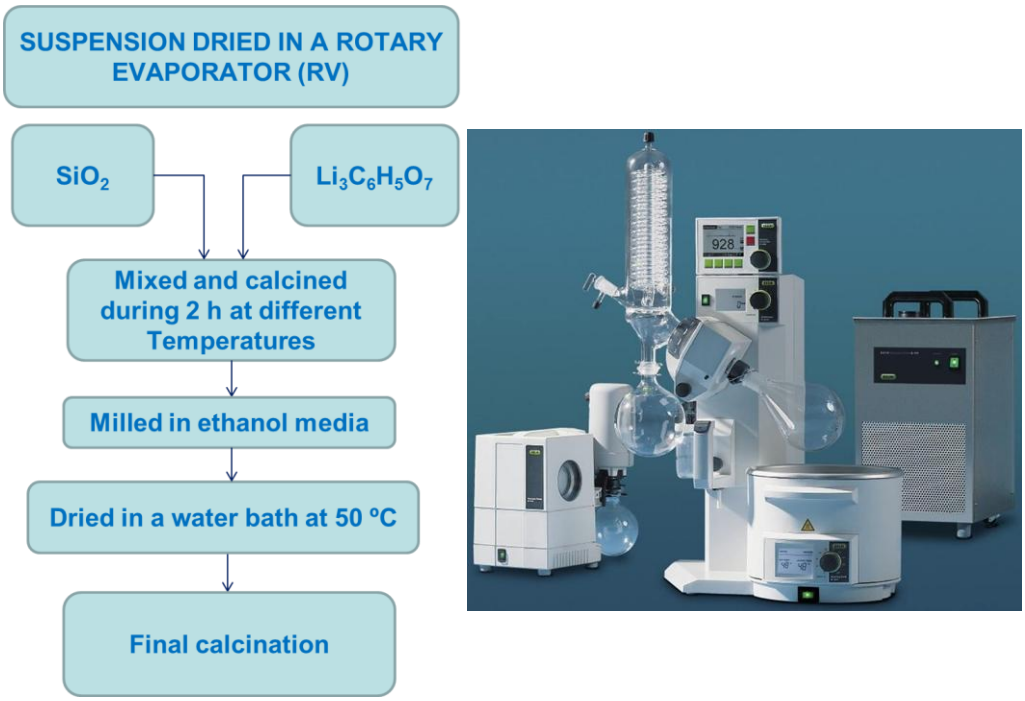

Figure 5.9: Flux diagram for rotary evaporator method (left) and rotary evaporator instrumentation (right).

III. Spray Drying Technique (SD)

The spray-drying technique is a solvent vaporization method widely used in the ceramic industry for converting a sol in spherical dry powders.

Silicon tetracetate was suspended in water and mixed with a magnetic stirrer, while a stoichiometric amount of lithium acetate powder was slowly added to the suspension inducing the following chemical reactions (Figure 5.10, Flux diagram III):

$$xC_8H_{12}O_8Si + xC_2H_3O_2Li + xO_2 \rightarrow \mathbf{Li_xSi_xO_x} + xCO_2 + xH_2O \qquad (5.12).$$

After a rather extensive stirring (about 2-3 h), the uniform milky suspension was connected to the Mini spray-drier Buchi B-290 and the parameters adjusted, like the

molar concentration of the suspension (0.4 Mol) and the outer temperature of the vapour steam (170 °C), for obtaining of rounded-shaped final products [165].

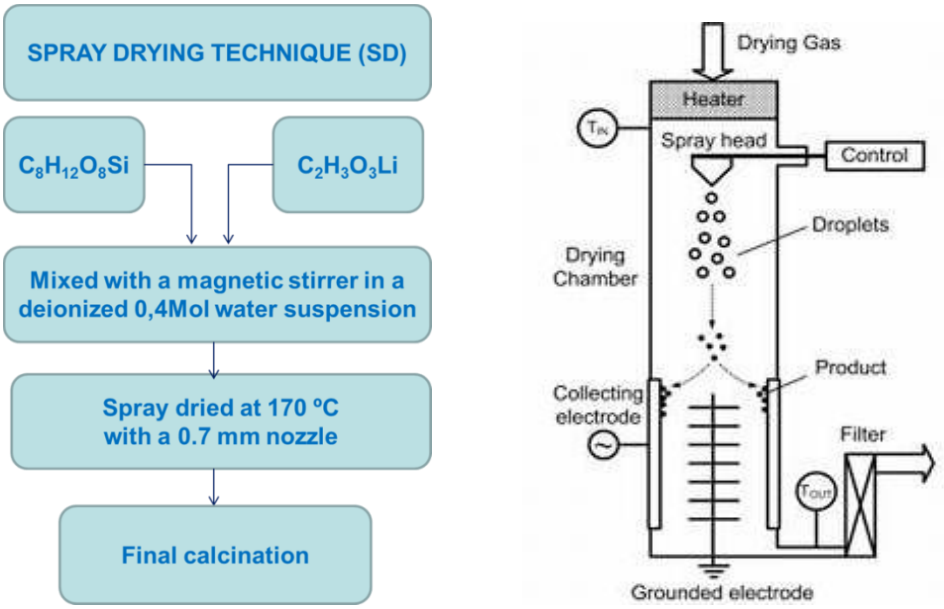

Figure 5.10: Flux diagram of spray drying (SD) technique (left) and a schematic representation of the Spray drier machine.

The suspension was sprayed through a nozzle of 2 mm diameter (for the control of the droplet size) into a hot vapour stream and separated into solid droplets and vapour [166]. The solid was collected in a cyclone. All the process was able to provide about 0.45 gr of material in 3 h.

The material obtained was calcined at temperatures varying from 600 to 800 °C.

5. Characterization of Li_4SiO_4 and Li_8SiO_6 ceramics

All the powdered compositions obtained from the described methods were processed as pellet discs and sintered.

Powders were sieved through a 100 μm mesh and inserted in a plastic smooth cylinder, avoiding air bubbles. Once closed, the cylinder was pressed in an isostatic press at 250 MPa during 15 minutes. The compacted rod obtained was cut into 2mm discs, using acetone as medium for cooling and minimizing secondary effects caused by friction.

The discs obtained, dried in air during 10 minutes, were thus ready for sintering. In order to increase the density of the ceramic compounds, a study on the heating/ cooling ramp and the maximum sintering temperature was required for the pellets obtained from each fabricated powder.

Finally the best sintering temperature for the achievement of a crystalline compound with the highest density was researched, working in an air atmosphere with heating and cooling ramps of 5 °C / min and an annealing time of 2 hours.

A comparison of the analytical characterization results in ceramics synthesized by different fabrication routes described in the preceding section is presented. The objective is the evaluation and the selection of the best manufacturing process, able to provide a quasi-spherical shape preserving the physic-chemical stability and besides the possibility of achieve a material with higher lithium density [167]. For practical reasons only the results obtained in two materials are presented: the BB candidate composition (Li_4SiO_4) and the silica-based compound with the highest Li:Si proportion (Li_8SiO_6) (see the phase diagram of Figure 2.4 in the Chapter 2). The interest in a ceramic with higher Li-content, strictly related to the TBR factor improvement, was one of the objectives to be pursued when this work started.

Therefore, several characterization techniques have been applied. The results on the two selected compositions will be discussed herein.

5.1. Differential thermal analysis + Thermo gravimetry

Figures 5.11 a, b, c, show the DTA diagrams registered in the powders obtained in the final step of synthesis process in the case of all methods used.

Endothermic peaks at quite low temperatures (around 100 °C), are observed. They are associated to the loss of organic material given by some volatile precursor. The peaks appear in correspondence of weight losses detected by thermo-gravimetric (TG) analysis.

In solid state synthesis (figure 5.11 a) the first endothermic peak at 65 °C can be assigned to the ethanol evaporation used during mechanical homogenization. Subsequently two exothermic peaks very close in temperature (425 and 465 °C), are associated to a weight increase in the TG curves. They are ascribed to the chemical reactions between SiO_2 and Li_2CO_3. The small endothermic peak observed above 700 °C could be related to the volatilization of lithium or lithium -oxides.

The thermal characterization of powders produced by RV and SD synthesis (Figures 5.11 b and c) highlights the combustion process of the organic species, after water loss, at low temperatures (Figure 5.11 b, RV method).

In the case of the RV process, the formation of an intermediate compound around 300 °C and its sudden combustion at about 350 °C corresponding to a weight loss of the 20% for the Li_8SiO_6 or the 30% in the case of Li_4SiO_4, is observed. A final nucleation at about 450 °C without any weight loss is observed in the Li_8SiO_6 curve.

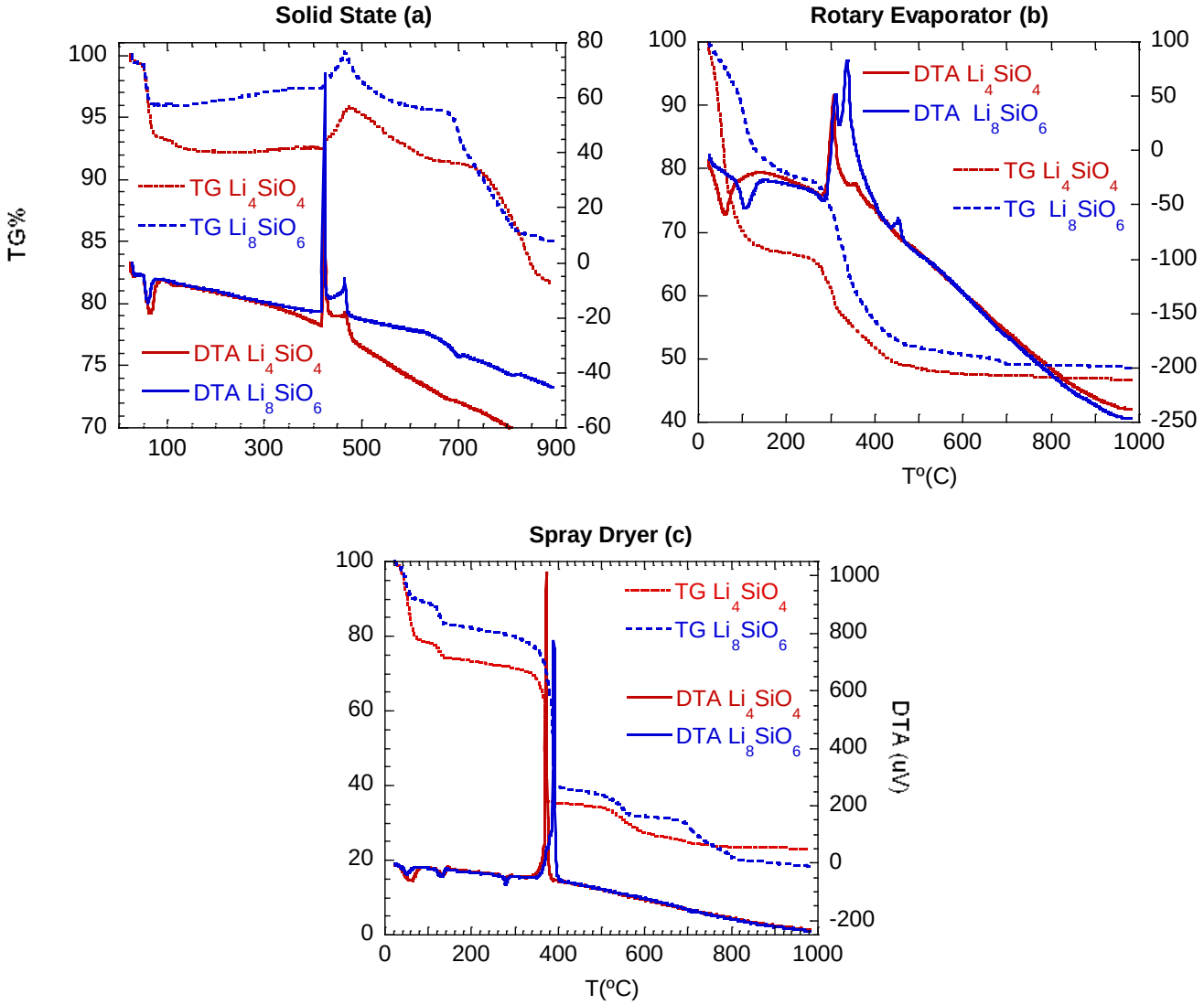

Figure 5.11: DTA (lines) and TG (dots) diagrams of the routes: a) Solid State, b) Rotary Evaporator, c) Spray Dryer, d) Reflux, for the ortosilicate (Li_4SiO_4 red lines) and oxosilicate (Li_8SiO_6 blue dot-lines) ceramic powders, obtained in the final step of the synthesis processes.

Above this temperature the peaks indicates the completion of the reaction and the final formation of the compounds.

The situation is similar for the SD (Figure 5.11 c) route with the exception that the acetates combustion occurs in one single step, in the temperature range between 370 °C and 400 °C and a weight variation of about 40 % is registered, as expected by the chemical reaction.

Finally it is interesting to note that the thermal diagrams of the materials are similar within each synthesis method, with a pronounced weight loss in the case of the lower lithium-content ceramic.

5.2. Study of crystalline phases: X-Ray Diffraction

The Figures 5.12 a, b, c, and d show the XRD patterns of Li_4SiO_4 sample obtained after the last calcination process in the three fabrication methods here studied. The SD and RV methods provide a single and highly crystalline orthosilicate phase (figure 5.12 b and c), while the SS route lead to the synthesis of a highly crystalline material always associate to the metasilicate phase (Li_2SiO_3).

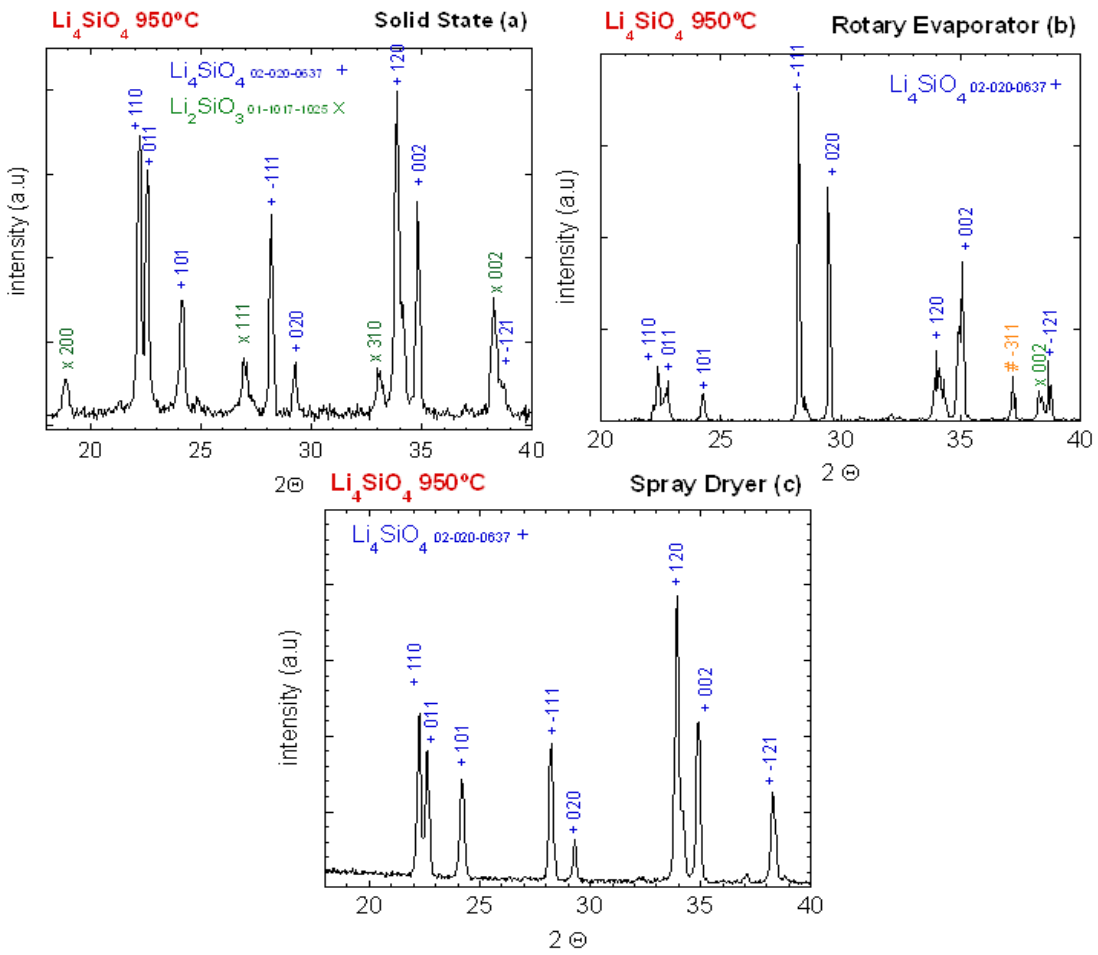

Figure 5.12: XRD patterns found in the Li_4SiO_4 calcined powder obtained following the three fabrication routes: a) Solid State, b) Rotary Evaporator, c) Spray Dryer(Li_4SiO_4 peaks (+) and Li_2SiO_3 peaks (x)).

The figures 5.13 a, b, c, show the XRD patterns obtained in the case of the SS, RV and SD methods respectively for the Li_8SiO_6 sample after the calcination treatment at 650 °C / 2 hours. As reported in literature [147] the achievement of this phase is quite complex except for the solid state reaction (SS, figure 5.13 a), able to provide the compound together with orthosilicate and other minority phases. With the spray dryer (SD) process (figures 5.13 c), a small amount of this phase is detected while with the rotary drying route (RV, figure 5.13 c) it is completely non-existent.

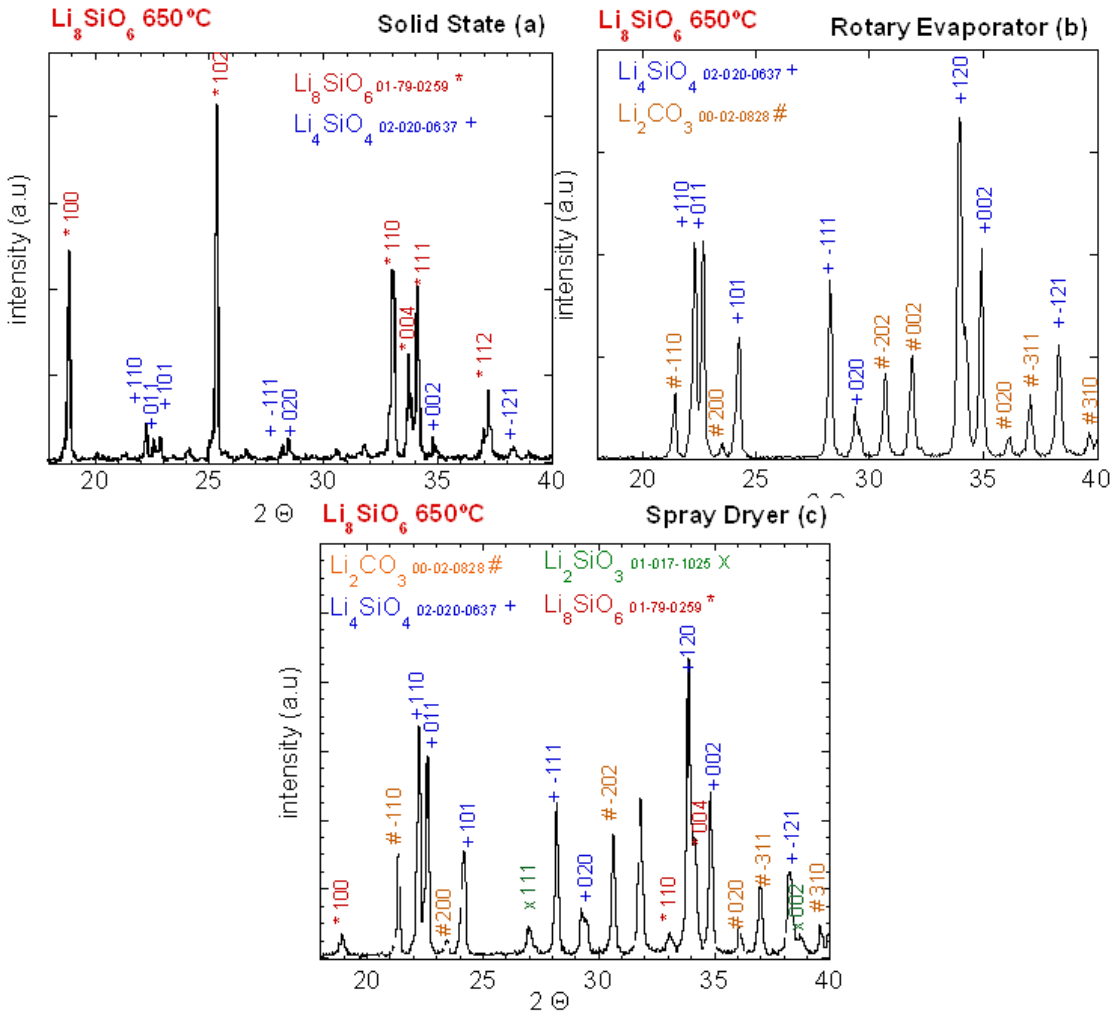

Figure 5.13: XRD patterns for the Li_8SiO_6 calcined powders obtained following the three methods: a) Solid State, b) Rotary Evaporator and c) Spray Dryer (Li_4SiO_4 (+), Li_2SiO_3 (x), Li_8SiO_6 (*), Li_2CO_3 (#)).

Nonetheless these results in ceramics with high lithium content are interesting for fusion objectives considering that the interest lies in the achievement of a material with good crystallinity and high Li-proportion, relevant features for breeder blanket application.

5.3. Attenuated Total Reflectance - Infra Red Spectroscopy

In the figures 5.14 a, b and c the results of ATR-IR spectroscopy for the mid-IR region applied to calcined powders obtained by using the three different fabrication routes, are presented.

The first intense bands appear in the range of 1400-1500 cm^{-1} for the materials prepared by RV and SD methods, being almost absent in the ceramic synthesized by mixing oxides (SS). The 1430-1460 cm-1 peaks are probably caused by the Li_2CO_3 present as raw material, considering the results reported in previous studies on the CO_3 vibrational modes [89,168].

Several studies [169,170] report that the isolated SiO_4 structure presents a strong absorption band around 900 cm^{-1} caused by the Si-O asymmetric stretching vibration, while the absorption band near 800 cm^{-1} is due to the Si-O holosymmetric stretching vibration. The vibration due to the SiO_4 structure is a triple degenerative splitting in three vibrations in the case of the Li_4SiO_4 structure. Bands at 1080, 740 and 847 cm^{-1} are attributed to the Si-O stretching bond in the silica tetrahedra, while the bands at 600 and 580 cm^{-1} are related to the bending vibrations. The band at 475 cm^{-1} is attributed to the deformation mode of Si–O–Si. Likewise in the Li_4SiO_4 structure, the band at 565 cm^{-1} is associated to the stretching vibration of the Si-O-Li bond, and the absorption bands in the range between 465 and 395 cm^{-1} are due to symmetric and asymmetric stretching vibrations of the Li-O bonds in the LiO_4 tetrahedra [171].

The identification of those bands corresponding to the SiO_4 tetrahedral structure is clear in all the materials. In the case of the Li_8SiO_6 ceramics the bands overlap appearing wider and shifted to lower wavenumbers. When different types of compounds (such as Li_2SiO_3 and Li_4SiO_4) coexist, the IR-spectra are complex to interpret and the bands corresponding to the different phases tend to overlap being close in wavelength. In the Li_8SiO_6 case it is especially evident: the single chain structure of the Li_2SiO_3 has three strong absorption bands in the region of 850-1100 cm^{-1} coexisting with the isolated SiO_4 tetrahedral structure of the orthosilicate which exhibits strong bands between 800 and 1040 cm^{-1}.

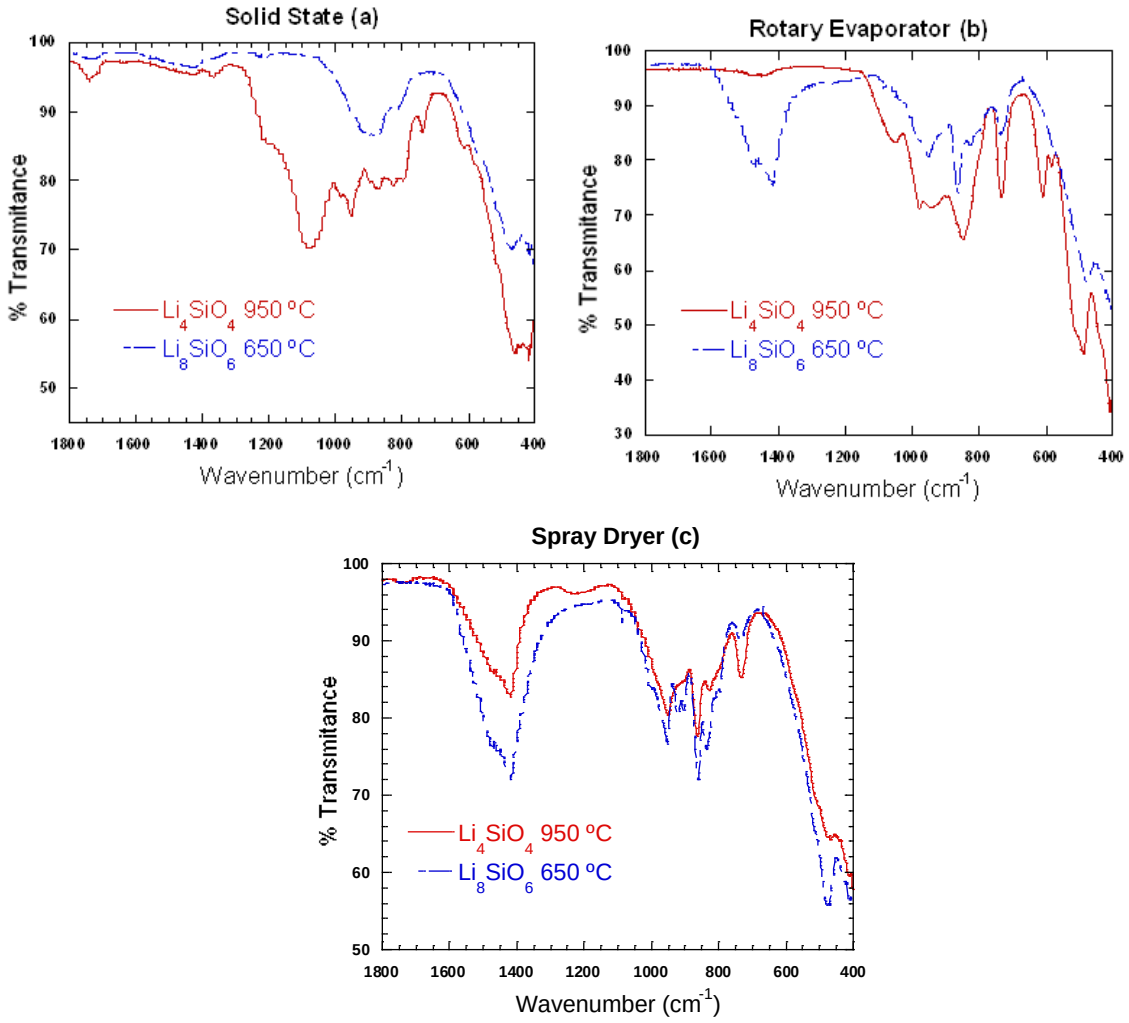

Figure 5.14: IR spectra of the final phases found in the Li_4SiO_4 (line) and Li_8SiO_6 (dot-line) materials for the methods: a) Solid State, b) Rotary Evaporator, c) Spray Dryer.

5.4. Microstructure of powders by SEM

Figure 5.15 (a to c) shows the morphology characterization of the two selected powders fabricated by the three synthesis methods. The SEM images evidence that only the SD-method is able to provide perfectly spherical powders (Figures 5.15 c). The size distribution of particles varies between 1 and 12 microns without signs of coalescence. The ceramics specimens obtained by the SS reaction are large rounded aggregates formed by the coalescence of very small primary particles of few nanometers (Figure 5.15-5.16 a). The RV method provides particles with rounded

appearance and small homogeneous size of about one micron agglomerated after sintering (Figure 5.15-5.16 b).

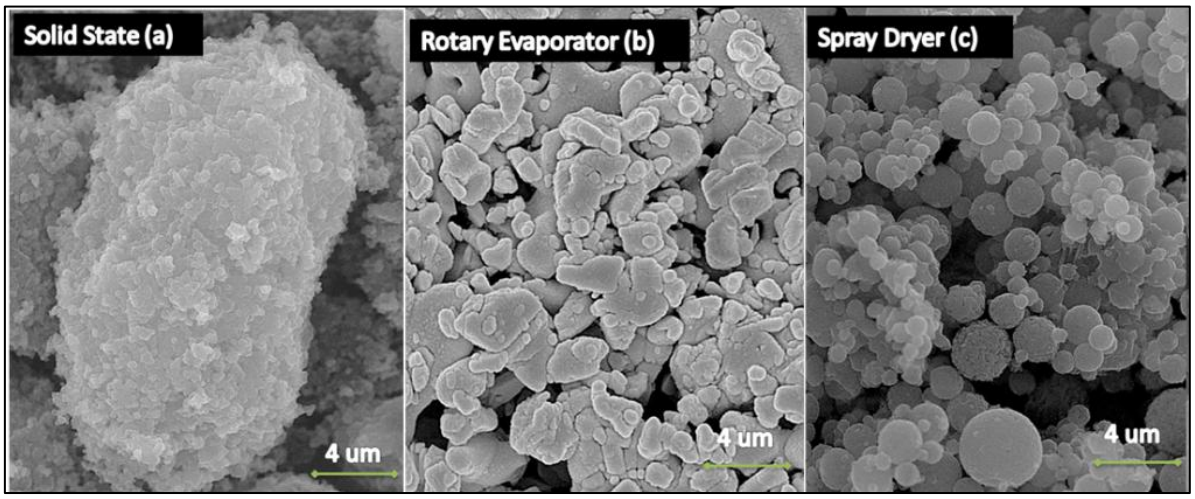

Figure 5.15: SEM captures of the particles of Li_4SiO_4 material obtained by Solid State (a), Rotary Evaporator (b) and Spray Dryer (c) synthesis route.

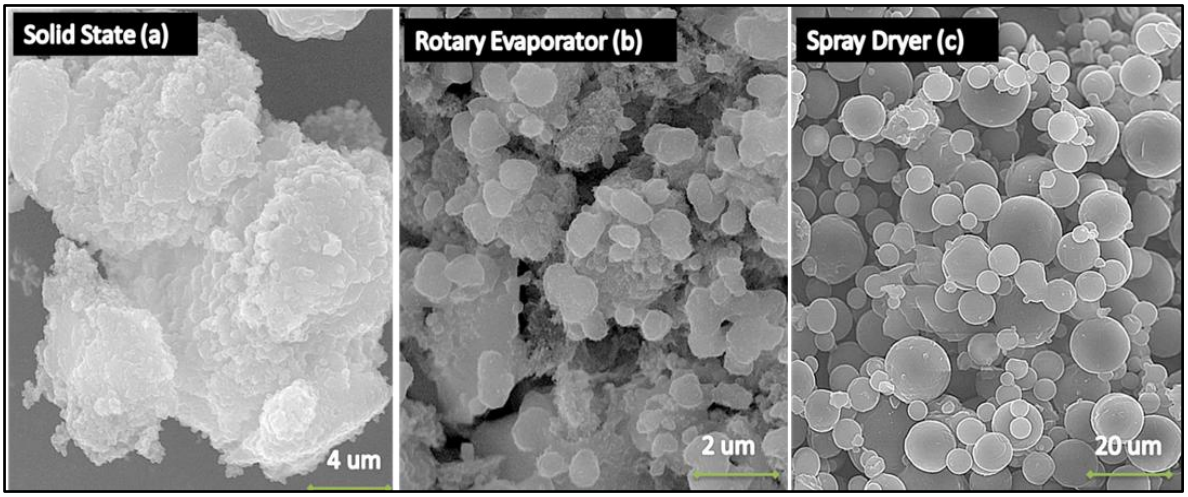

Figure 5.16: SEM captures of the particles of Li_8SiO_6 material obtained by Solid State (a), Rotary Evaporator (b) and Spray Dryer (c) synthesis route.

5.5. Primary conclusions

The achievement of the spherical form by Spray drier method is really slow (0.45 gr/180 min), thus considering the quantity of material necessary for all the others experiments, the ceramics used in the thesis are obtained by rotary evaporator method, which results to be a good compromise among the three methods. The synthesis with other fabrication routes has not been applied to all the compositions not being the fabrication of breeder blanket ceramics the principal focus of this work.

6. Sintering of Li-ceramics: the effect of Li-content in dense bodies

Once selected the method, several compositions in the Li_2O-SiO_2 system have been synthesized following the intermediate rotary evaporator route till the sintering of compressed powders listed in Table 5.1. The pellet form is selected as the best one for the studies of volume electrical behaviour, irradiation effect and light ion transport.

Table 5.1: Best sintering temperatures for all the ceramic compositions studied.

Compositions	$Li_2Si_2O_5$	Li_2SiO_3	Li_4SiO_4	Li_6SiO_5	Li_8SiO_6	Li_2TiO_3
Li:Si proportion	**1:2**	**1:1**	**2:1**	**3:1**	**4:1**	
Sintering conditions	950 °C / 2 h	1000 °C / 2h	950 °C /2h	1000 °C /2h	650 °C /2h	1150 °C / 2h

In the last column, the metatitanate material, sintered from commercial powders is added. It is largely used along the thesis and its main characteristics are presented afterwards.

a) X-Ray Diffraction

In the Table 5.2 a list of the phases obtained for ceramics and the Li:Si proportion, variable from 1:2 to 4:1, used.

In the last column, the titanium-based material is added. This material is sintered from a commercial powder (99.9 % Alfa Aesar).

Table 5.2: Phases identified by XRD for each Li-based ceramics prepared in CIEMAT-LNF laboratory.

Compositions	$Li_2Si_2O_5$	Li_2SiO_3	Li_4SiO_4	Li_6SiO_5	Li_8SiO_6	Li_2TiO_3
New nomenclature	**Li1**	**Li2**	**Li4 (OSi)**	**Li6**	**Li8**	**(MTi)**
Phases	$Li_2Si_2O_5$ SiO_2	Li_2SiO_3 $Li_2Si_2O_5$	Li_2SiO_3 $Li_2(CO_3)$ Li_4SiO_4	Li_4SiO_4 Li_2SiO_3	Li_4SiO_4 Li_2CO_3	Li_2TiO_3

b) Secondary ion mass spectrometry

SIMS technique is here used as elemental analyses with the aim of identify all the impurities present in each compound. In this form the following information (see Figure 5.17) about all the elements present in the surface, is obtained.

Sample handling and its storage are the responsible of some of the impurities find (K, P, Na, Cl).

Main of them are derived from the raw material used (Aldrich hydrated $Li_3C_6H_5O_7$, 99%), both because a part has not react (as in the case of C element), and because some metal in trace quantity is present (Al, Fe).

The possibility to have a detailed knowledge of the trace impurities in these ceramics is important when studies related to the electrical properties are preformed, considering that the presence of defects in an insulating material can lead to the creation of intermediate levels in the energy gap facilitating the process of conduction of the electric charge.

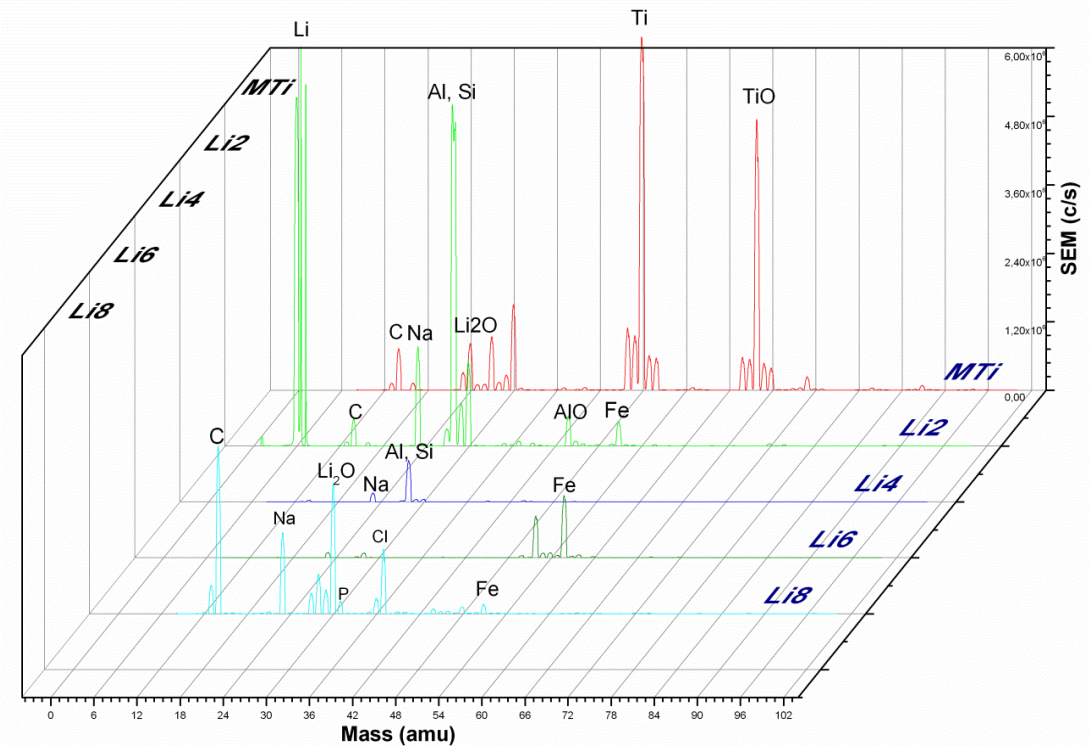

Figure 5.17: Static SIMS spectra for the elemental analysis of the ceramics fabricated.

c) Density and pore distribution

Pore size distribution data generated by mercury porosimetry cover a great interest in the comparative studies of these materials. Actually all the characterizations carried on in this work (both electrical conductivity and light ion diffusion), are affected by material porosity.

Table 5.3: Main density and porosity characteristics for all the ceramic specimens.

Compositions	Li1	Li2	Li4	Li6	Li8	MTi
$Density_{th}$ (gr/cm^3)	2.48	2.33	2.22	2.17	2.13	3.43
$Density_{exp}$(gr/cm^3)	1.225	1.95	1.64	1.41	0.84	2.7
Mean pore diam. (µm)	2.353	1.557	2 – 0.6	0.1;0.025	5.850E+01	3.5
Opened porosity (%)	24.5 %	42 %	34.8 %	5.3 %	17.1 %	16.3 %

From the analysis of the Table 5.3 many interesting differences can be observed among the different silicare-compositions first and the MTi after. The materials with higher lithium content result to be the ones with lower opened porosity percentage

(Li6 and Li8). At the same timeLi8 compositions the one with the bigger mean pore diameter, meaning that it only have big pores.

d) Scanning Electron Microscopy

Microscopy is used to check the formation of rounded particles, to measure the size of grains and to observe the presence of amorphous phases.

Prior to SEM observation, sintered specimens are embedded in a resin and let dry during 12 hours; then it is polished using sandpaper and finally a diamond medium of different grain (from 220 to 1 μm) achieving a mirror like polished surface. Finally it is thermally etched during 30 min at temperatures slightly lower than the sintering one to reveal the grain boundaries. Being samples electrical insulators, their surfaces are covered by an e-beam deposited carbon layer, which prevents the material get charged.

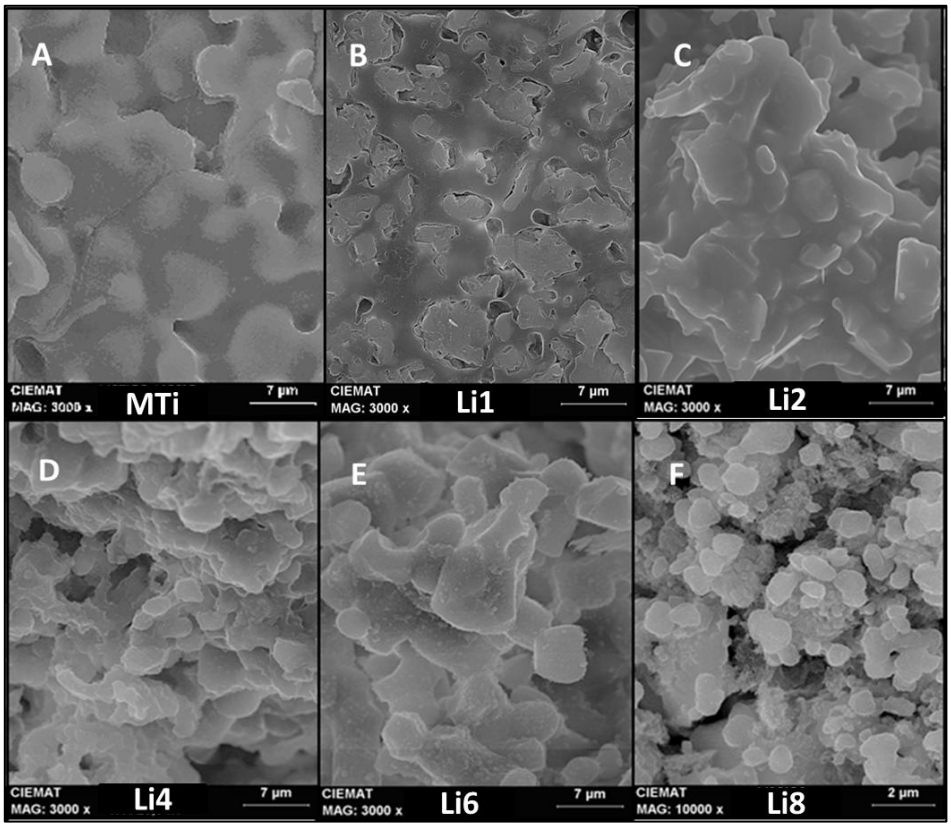

Figure 5.18: SEM images of the polished surface obtained after the last sintering pellets process for the following compositions: MTi(A), Li1(B), Li2(C), Li4(D), Li6(E), Li8(F).

After sintering (see Figure 5.18), the microstructural differences among the polished surfaces of the compositions fabricated following the rotary evaporator route is shown.

The MTi sample presents a rather compact surface, data confirmed by the really low open porosity. In the case of samples Li1 and Li2, an amorphous phase (white ring) acting as grain compact can be detected. The Li4 and Li8 surfaces show a lot of cavities and quite small grains, being the Li8 the one with the smaller size (<2 μm). The last three compositions (Li4, Li6 and Li8), all multi-phasic, present several sized grains. In the case of Li6 (E) the bimodal microstructure is marked by a strong difference between the bigger (6 μm) and the smaller grain (0.15 μm).

In the case of the MTi specimens, a SEM study reveals the high degree of crystalline orientation visible through pores (see Figure 5.19).

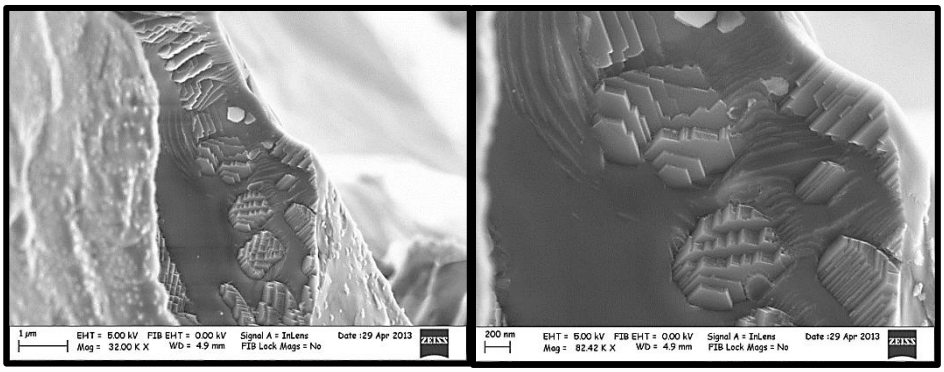

Figure 5.19: SEM image of the MTi pores. A laminar structure is observed in the fracture of the sample.

7. Discussion

Different experimental techniques have been investigated for the fabrication of two lithium-based silica ceramics: the orthosilicate (Li4) and the oxosilicate (Li8) as possible candidates with high Li-content for fusion breeder blanket application.

The synthesis of orthosilicate is easy to follow regardless the method used. The crystalline lithium orthosilicate is built up from isolated SiO_4 tetrahedrons connected by LiO-polyhedra. The SiO_4 tetrahedron is very irregular and so lithium ions can be coordinated by 4, 5, or even 6 oxygen ions [172,173]. The IR spectroscopy is very sensitive to the morphological and structural changes of the matrix originated by the variations in the sample composition [174]. This is the case of the typical transverse optical modes for glassy silica at 1085 cm^{-1} and the shoulder

around 1200 cm^{-1}, perfectly identified in the Li_4SiO_4 composition obtained by the solid state synthesis, probably displaced to lower wavelengths in the case of the other two fabrication processes (RV and SD) because of the different crystallization degree.

The oxosilicate-phase is obtained only by solid state synthesis in small proportions, the other processes giving rise to intermediate stages probably because lithium volatilization or a not fully reaction of the raw materials. The Li_8SiO_6 lattice structure is isotypic to the Li_8CoO_6 or Li_8GeO_6 crystals [61]: near the SiO_4 tetrahedrons the Li-atoms can be positioned at the vertices of LiO_4 pyramids, creating trigonal bi-pyramids, or in the centre of Si tetrahedrons in a tetrahedral coordination. As state by the theory of cluster self-organization for crystal-forming systems [175], the nanoclusters are self-assembly of primary chains. Thus the shift to a lower wavenumber of the Si-O-Si stretching vibration found in IR spectra is related to the degree of polymerization and the connection of Li atoms [176], considering that impurities and secondary phases are present. This complex structure gives rise to an overlapping of the vibrational bands in the range of 750-950 cm^{-1} resulting in the spectra shown in Figure 5.14.

In the second part of the work, the fabrication of several Li-Si compositions with different Li:Si proportion is presented. The achievement of the spherical form by Spray drier method is really slow (0.45 gr in 180 minutes), thus considering the quantity of material necessary for all the others experiments, the ceramics used in the thesis are obtained by rotary evaporator method, which results to be a good compromise among the three methods. The synthesis with the other fabrication routes has been applied only to some of the compositions not being the fabrication of breeder blanket ceramics the principal focus of this work.

The difficulty of working with over-stoichiometric materials for achieving the desired phase is confirmed by the weight loss in the DTA/TG analysis as well as by the literature [144] and justified by the high lithium volatility [55]. The loss of lithium would avoid the evolution of the reaction, so for an assured achievement of the over-lithium phases, working with an excess of lithium is recommendable. It is worthwhile to mention that the low carbonate melting point, strongly reduce the sintering temperature of the material with the highest lithium content (Li8). The Li_2O-SiO_2 diagram (Chapter 2, Figure 2.4) shows a narrow range of thermal stability for over-stoichiometric ceramics. Anyhow, considering that the interest in the preparation of a ceramic with higher lithium reside in the upgrading of the TBR

factor [177], the achievement of a single phase is not the primary aim. Other authors have tried out the synthesis of these phases, with no good results [147].

Finally the observed double-phase structure in the Li6 high Li-content ceramic together with the bi-modality of grain size found for some fabrication route represents an interesting morphological characteristic. It is worthwhile mentioning that the presence of two coexisting phases is the basic idea for the development of a new solid BB concept [33] with improved features.

8. Conclusions

The principal objective of this part is the fabrication of a rounded-shaped powder with good crystallinity. Only the *Spray Dryer route* provides homogeneous in phase particles, satisfying the requirement for a soft, spherical powder but it results to have a really slow fabrication rate (0.15 gr/h). At the same time the rotary evaporator method offers rounded polycrystalline aggregates and a faster rate production. Thus this method was the one selected for the fabrication of the ceramics characterized along the work.

The fabrication of a high-Li-content ceramic has been attempted. The results show that the synthesis of Li_4SiO_4 is easy to achieve regardless the method used, while the Li_8SiO_6 is obtained only by solid state route and in small proportion. This last composition presents a really low sintering point (650 °C), which makes it not considerable for several characterization studies.

Several ceramics with varying lithium content presenting a double phase (Li_4SiO_4 and Li_2SiO_3) in different proportion, were fabricated. Working with ceramics presenting a different Li-content, plays a special interest in relation to the Lithium burn-up factor regardless the purity-in-phase.

Starting from all these considerations, the experiments on light ion behaviour presented in Chapter 7 are performed only on the two main candidates (MTi and Li4), plus a third composition with higher lithium content (Li6). This last composition was selected because of its peculiar bimodal grain microstructure, really low open porosity, for its high lithium content and because of its better thermal qualities.

CHAPTER 6

ELECTRICAL MEASUREMENTS AND γ - RADIATION EFFECT

The electrical measurements in insulators materials provide important information on the creation of defects. Varying the lithium content and the gamma irradiation dose, a study on the electrical changes in breeder ceramics is here proposed. The results are used as an indirect measurement for getting information on tritium mobility and ceramic behaviour during Li-burn up.

1. The effect of radiation on electrical properties

The breeder blanket materials will be exposed to several types of irradiations: neutrons with energies up to 14.1 MeV, γ-rays, tritons of 2.7 MeV and helium of 2.1 MeV produced by lithium transmutation. For insulators in general, radiation fields deposit far more energy in the materials through electronic excitation process than through an atomic displacement process. Hence if radiolysis takes place efficiently, permanent structural changes will proceed far more quickly [178].

Among the variations created by the radiation, the ones on the electrical properties are extremely important: if the blanket zone forms a close circuit because of changes in the electrical configuration then also the magnetic field of the near magnets may be affected [179]. At the same time these properties reflect important features of the structure, providing information on the creation of defects, the presence of impurities or the ion movement in the lattice [74].

Several types of electrical degradation have been recognized and investigated, among them it is noteworthy the Radiation Induced Conductivity (RIC) effect and the Radiation Induced Electrical Degradation (RIED) [180].

The radiation-induced electrical conductivity (RIC) cause the excitation of electrons from the valence to the conduction band, inducing a large electrical conductivity and the degradation of the electrical insulating ability [181]. Among the degradation mechanisms observed during the study of radiation effects in nuclear ceramics, this is undoubtedly one of the most important [182].

The phenomenon of radiation induced electrical degradation (RIED), which implies a permanent increase in electrical conductivity, is potentially one of the most crucial problems for insulating ceramics not only from the point of increasing the electrical conductivity through a degradation of σ_0 (conductivity), but also because it has been still not fully understood.

Among the different ionization sources responsible of changes in electrical properties, the present work is based on the gamma-radiation effect in breeder blanket ceramic. Gamma-radiation presents three modes of physical interaction with the matter: (a) photoelectric effect – from 0.01 to about 0.5 MeV, (b) Compton scattering – from about 0.3 MeV to 8 MeV, and (c) pair formation (electron/positron), 5 MeV to 100 MeV [183]. Ionization is a secondary effect which results to be quite important in the case of insulators: when ceramics are subjected to gamma-rays, the electronic defects created involve changes in valence states of the whole crystal. This irradiation suppresses the polarization properties of ceramics, helps the migration of defects and changes the mobility of domain walls

and Curie temperature [184]. Thus its effect on the electrical properties of insulating materials may provide interesting results on material durability.

The measurement of electrical resistivity versus thermal annealing treatments is one of the most used techniques to study *ionic* defects and their transport properties in a material. The Electrochemical Impedance Spectroscopy (EIS) analysis is a non-destructive tool which can elucidate transfer mechanisms and dynamics of the principal charge carrier along the entire volume of the material [149,185].

As a support and with the aim of identify the nature of the defects created by gamma irradiation, Positron Annihilation Spectroscopy technique (PAS) is used in this thesis. The measurements in the as-prepared conditions are compared with the ones after irradiation and after thermal treatments, identifying the nature of some defects.

The aim of these experiments is not only the study of radiation effect on the electrical configuration of the selected compounds. De facto it has been reported that irradiation defects could affect tritium recovery process [186,187] through degrading mechanical and electrical properties of tritium blanket material (TBM) [188,189]. Moreover ionic conductivity studies suggest that the mechanism of tritium diffusion is intimately associated to the Li^+-ion one [16,17]. The places occupied by tritium in the crystal network are supposed to be related to those left empty by the transmutation of lithium, and from those created by the irradiation defects. Therefore one can theorize that the mobility of tritium will be strongly related to the places that lithium occupies in the crystal structures and to its mobility through the lattice [18].

Electrical measurements are used as a tool for understanding the effect of γ-radiation in ceramic breeders and contemporary to comprehend the ion mobility dynamics, related to tritium diffusion.

2. Electronic structure of breeder blanket ceramics

The knowledge of the electrical structure of the studied materials is very important for being able to detect all the possible changes caused by radiation.

The electron state of Li_4SiO_4 crystal has been examined in the literature by *ab-initio* calculation with CRYSTAL98 program [7, 6]. The crystal structure of Li_4SiO_4 contains 126 atoms (14 Si, 56 O and 56 Li) per unit cell, formed by isolated SiO_4 tetrahedra with Li atoms floating around them. Using *ab–initio* calculation with Density Functional Theory (DFT) various atomic fractional coordination of Li_4SiO_4 are found [190]. The electronic band energy calculations show that Li_2SiO_3 and

Li_4SiO_4 are insulators with a band gap of about 5.36 and 5.53 eV respectively. Their valence band properties are mainly determined by the oxygen 2*p* orbital electron [8].

Li_2TiO_3 material presents an indirect band-gap of 3.49 eV [191], indicating its non-metallic nature. *Padilla-Campos* [192] studied two octahedral sites for tritium atoms and two possible substitutional sites in the positions occupied by lithium, using *ab-initio Hartree-Fock* method. Potential-based molecular dynamics (MD) has been used for lithium-metatitanate characterization, founding that in the pure Li layer lithium diffusion is equally probable [193]. The model foresees that lithium can occupy a tetrahedral site when two or more vacancies are in the vicinity. Wan et al. [191] deeply investigates the electronic and dynamical properties of this material, suggesting that interactions between Ti and O are mainly covalent, while between Li and TiO_3 are mostly of ionic-type.

The characterization of the electronic structure and the nature of the chemical bonds, can lead to a better understanding of structure-properties relationships, mainly determined by the stability of chemical bonds that can be characterized by the degree of ionicity. In ceramics, which are generally insulators and have very few free electrons, ionic conduction can be a significant component in the total conductivity.

3. Fundamentals of Impedance Spectroscopy

Impedance spectroscopy is a powerful technique for studying both the transport properties of charge in the volume and the electrochemical reactions at interfaces. Typically, AC impedance experiments are carried out over a wide range of frequencies (several milli-hertz to several megahertz), and the interpretation of the resulting spectra is aided by analogy to equivalent circuits involving simple components such as resistors and capacitors. In general, such equivalent circuits are not unique; indeed there exists an infinite set of circuits that can represent any given impedance.

As shown in Figure 6.1, the fundamental approach of the impedance spectroscopy is the application of a small amplitude sinusoidal current excitation to the system under the steady-state and the measurement of the voltage response.

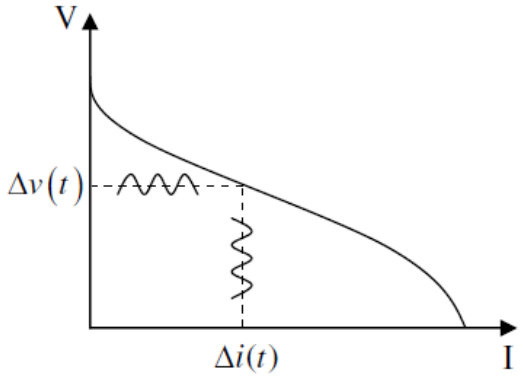

Figure 6.1: The application of a sinusoidal current, measuring the voltage response.

The excitation signal, expressed as a function of time, has the form:

$$E_t = E_o \sin(\omega t) \qquad (6.1),$$

where E_t is the potential at time t, E_o the amplitude of the signal and ω the radial frequency, whose relationship with the frequency f (in hertz) is:

$$\omega = 2\pi f \qquad (6.2).$$

In a linear system the response signal I_t is shifted in phase (Φ) with an amplitude I_o:

$$I_t = I_o \sin(\omega t + \Phi) \qquad (6.3).$$

The ratio between the perturbation and the answer is a frequency-dependent complex number, called impedance. The value of the impedance is equal to:

$$Z = \frac{E_t}{I_t} = \frac{E_0 \sin \omega t}{I_{0 \sin\ \omega t + \Phi}} = Z_0 \frac{\sin \omega t}{\sin\ \omega t + \Phi} \qquad (6.4),$$

where the impedance is expressed in terms of amplitude Z_o and phase shift Φ.
Using Euler relation:

$$\text{Exp}(j\Phi) = \cos\Phi + j \sin\Phi \qquad (6.5),$$

It is possible to express the impedance as a complex function in function of the angular frequency ω:

$$Z(\omega)= Z_o \exp(j\Phi) = Z_o (\cos\Phi + j\sin\Phi) \qquad (6.6).$$

The plot of modulus |Z(ω)| and phase angle μ(ω) vs. frequency ω or f = ω=2¼ is called the Bode-Bode plot. The expression for Z(ω) is composed of a real and an imaginary part. If the real part is plotted on the X-axis and the imaginary part is plotted on the Y-axis of a chart, we get a "Nyquist Plot" (see Figure 6.2). In this case, the frequency is implicit. It is worth mentioning that the plot of Im(jω) vs. Re(jω) sometimes in the literature is called the Cole-Cole plot. Unless specified, both the Nyquist plot and Bode-Bode plot are called impedance spectra.

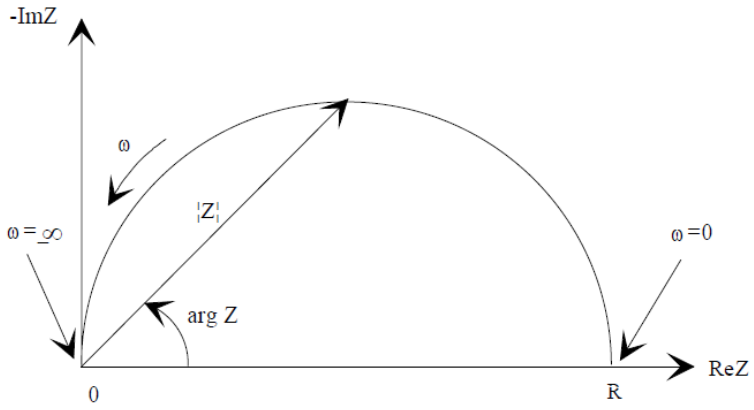

Figure 6.2: Nyquist plot with impedance vectors indicating the main variables.

Notice that in Figure 6.2, the Y-axis is negative and that each point on the Nyquist Plot is the impedance at one frequency; at low frequency data are on the right side of the plot and at higher frequencies are on the left. On the Nyquist Plot the impedance can be represented as a vector (arrow) of length |Z|. The angle between this vector and the X-axis, commonly called the "phase angle", is φ (=arg Z). Nyquist Plots have one major shortcoming: when you look at any data point on the plot, you cannot tell what frequency has been used to record that point.

One of the most attractive aspects of impedance spectroscopy is the direct connection that exists between the behaviour of a real system and that of an idealized model circuit consisting of discrete electrical components. This circuit is called the *equivalent circuit* of the impedance function.

The Nyquist Plot of Figure 6.2 results from the electrical circuit of Figure 6.3, considering that the semicircle is characteristic of a single "time constant". Electrochemical Impedance plots usually contain several semicircles but often only a portion of a semicircle is seen.

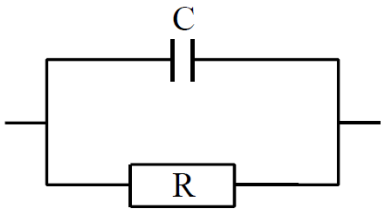

Figure 6.3: Equivalent circuit with one capacitor and one resistor element. EIS plots can contain several elements in series or in parallel configuration.

The analysis of impedance data is the most challenging part of the EIS technique. The Kramers-Kronig (K-K) relations can be used to evaluate data quality, relating the imaginary part of the impedance, Z_{Im}, at a single frequency with the complete set of real values of impedance, Z_{Re}, and vice versa. It individuates and eliminates the non-linear, instable and stochastic effects from the set of measured impedance data. If measured real and imaginary spectral data to not comply with the K-K relations, the data must violate one of these conditions. In practice, K-K analysis is performed by fitting a generalized model to spectral data. Agarwal et al. [194] proposed the use of a model consisting of *m* series connected by Voigt elements: -R-$(RC)_m$-. A Voigt element is a resistor and a capacitor connected in parallel (like in Figure 6.3). The parameter *m* is generally equal to the number of complex plane data points in the spectrum. This model is by definition K-K compliant.

The EIS method is here used to observe in an indirect way the volume conductivity variations. Impedance spectra shape and evolution with temperature are mainly determined by grain boundary (GB) contributions to ionic conductivity. It has to be pointed out that, particularly when dealing with materials with a densification level at boundaries, between fully opened and partially closed pores, a small density variation might mean a significant change in the electrical conductivity.

According to Bauerle [195], the intercepts of the semicircle with the real axis correspond to the grain interior resistance and the bulk resistance respectively and the low frequency spike represents the polarization resistance of the sample-electrode interface (see Figure 6.4). In general it is possible to distinguish two main contributions: one related to the movement of the charge carriers along the grain, the other relative to its movement along the grain boundary. By the way it is important to consider the influence of "imperfect" contacts, because of nanopores between two grains, or for the presence of an amorphous phase. These

imperfections give rise to low frequency semicircles in the complex impedance plane [196].

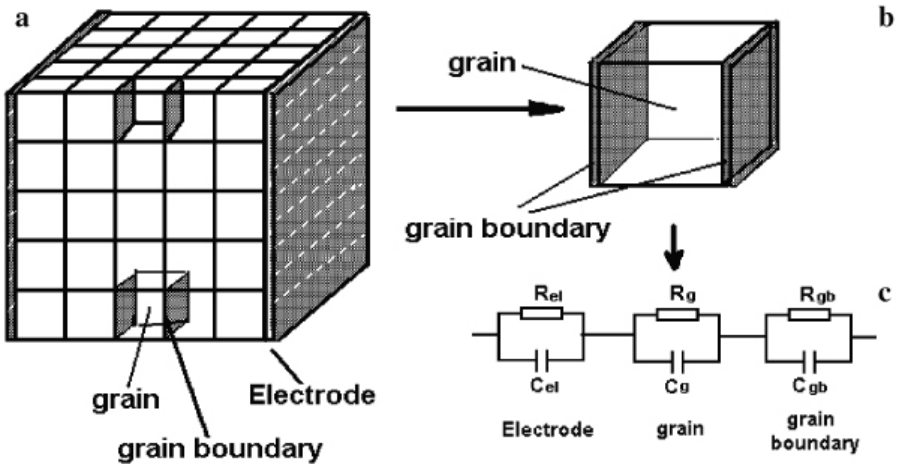

Figure 6.4: Simplified model of a material where grain and grain boundaries play an important role in ionic conduction. Electrode contribution is also added in the equivalent circuit, considering the polarization resistance of the electrode-sample interface.

In the majority of electroceramics the grain boundaries represents a really important contribution, presenting a different behaviour than the interior of the grain and being strongly involved in the total charge transport. The model known as *brick layer* is frequently used to explain the polycrystalline ceramics behaviour, including ionic and electronic conduction. In the image 6.5 it has been represented an ideal and a real case of the equivalent circuit corresponding to the brick layer model, where R_b and R_{gb} represent the bulk and grain boundary resistance.

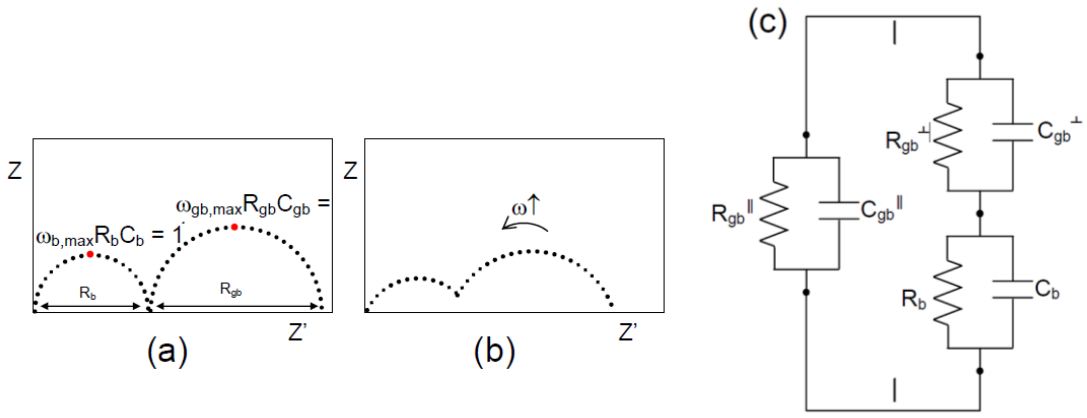

Figure 6.5: Semicircles ideal (a) and real (b) of the equivalent circuit schematically representing (c) the brick layer model.

Generally the arc with mayor frequency is assigned to the grain interior conductivity, while the one at low frequency corresponds to the processes happening on the grain boundaries. The signals at lower frequencies are generated by processes on the electrodes, which are normally neglected.

The value of A.C. impedance spectroscopy derives from the effectiveness of the technique in isolating individual reaction/migration steps of a multistep process. That is, because each reaction or migration step has, ideally, a unique time constant associated with it, these steps can be separated in the frequency domain. In recent years, impedance spectroscopy has found widespread applications in the field of characterization of materials. It is routinely used in the characterization of coatings, batteries, fuel cells, etc. [197,198].

In a polycrystalline crystal, where grains have a chaotic orientation, the electrical process can be treated in the following way. Firstly Ohm ley has to be respected:

$$V = IR\,; \quad I = \frac{V}{R} \qquad (6.8)$$

Then, considering the movement of ion vacancies, conductivity is given by:

$$\sigma_0 = n_V \frac{N}{E} q v_0 \qquad (6.9),$$

where n_v is the fraction of vacancies, N the number of positions per unit volume, q the charge and v_o the velocity of the charge carriers. Knowing that mobility is defined as:

$$u_0 = \frac{v_0}{E} \qquad (6.10),$$

than the conductivity equation is:

$$\sigma_0 = n_V N q u_0 \qquad (6.11).$$

If diffusion D and its relation with mobility are considered, the relation:

$$u_0 = \frac{q}{kT} D_0 \exp\left(\frac{-\Delta G_m}{kT}\right) \qquad (6.12),$$

is obtained.

In the case of the conductivity, when searching for the same relation, the following equation is obtained:

$$\sigma_0 = \frac{n_v Nqq}{kT} D_0 \exp\left(\frac{-\Delta G_m}{kT}\right) \quad (6.13).$$

Considering that $\Delta G_m = \Delta H_m - T\Delta S_m$, and that $-\Delta H_m = E_A$ (representing the activation energy of the conduction process), and defining:

$$A = \frac{n_v Nqq}{k} D_0 \exp\left(\frac{-\Delta S_m}{k}\right) \quad (6.14),$$

ionic conductivity will be governed by the relation:

$$\sigma_0 = \frac{A}{T} \exp\left(\frac{-E_A}{kT}\right) \quad (6.15),$$

which, in logarithm form, and transforming the *ln* in *log* is:

$$\log \sigma_0 T = A' - \left(\frac{E_A}{2.303kT}\right)\frac{1000}{T} \quad (6.16).$$

Its representation corresponds to an Arrhenius plot, where the slope of the curve represents the activation energy of the studied process (E_A), k the Boltzman constant, T the temperature in Kelvin and σ_o a pre-exponential factor. These graphs, called Arrhenius type, are the one used in our study starting from electrical impedance spectroscopy analysis.

4. Experimental procedure

The samples used for the electrical characterization are the ones characterized in Chapter 5, section 6 and present a pellet shape. After the last sintering process, ceramic discs were roughly polished for the achievement of good plane-parallel faces and its dimensions (10 mm-diameter and 2 mm-thickness approximately) measured.

The samples were thus wrapped in aluminium paper and located in a cylindrical sample holder with dry nitrogen. The sample holder was immersed in the Nayade pool irradiation facility and γ-irradiated by a ^{60}Co source in the CIEMAT installation (Madrid, Spain). The gamma radiation source was contained in small cylinders of stainless steel, introduced in a sheath stainless steel and the irradiation dose-rate was of 6 Gy/sec.

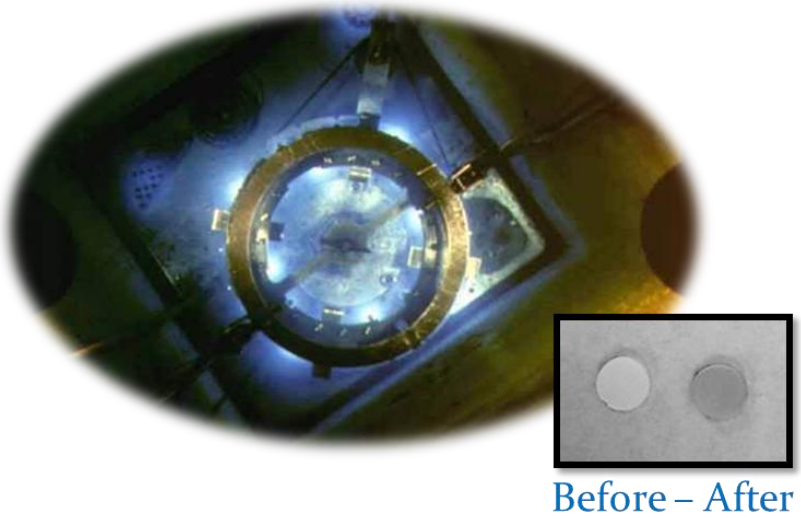

Figure 6.6: Nayade installation pool. In the inset an example of all the pellet compositions analysed by EIS before (left) and after (right) gamma irradiation.

The irradiation treatments were performed in nitrogen atmosphere (27 °C +/- 2 °C) or, only in one case, at 250 °C using a thermocouple controlled oven. When the desired irradiation dose was reached, the samples were removed. The colour of the samples was slightly changed after irradiation (see the inset in Figure 6.6), becoming darker, probably due to the creation of defects or the material reduction [199].

After this step, electrodes were provided onto both faces, painting the surface with a high conductivity silver paste chosen as the best option for porous and rough materials. Samples were dried in air at 130 °C during 15 min for eliminating all the paste organic components. The R value of the deposited film was revised with a digital tester.

The conductivity behaviour was examined by EIS (Electrochemical Impedance Spectroscopy) analysis. Impedance measurements were performed using a Solartron model 1255B Frequency Response Analyser with platinum as blocking electrodes (see the sample holder in the Figure 6.7 right), all inserted in a tubular

oven varying the temperature between 26 °C and 800 °C for the bulk conductivity measurement, over a frequency range from 40 Hz to 100 MHz. All experiments were performed in dry air.

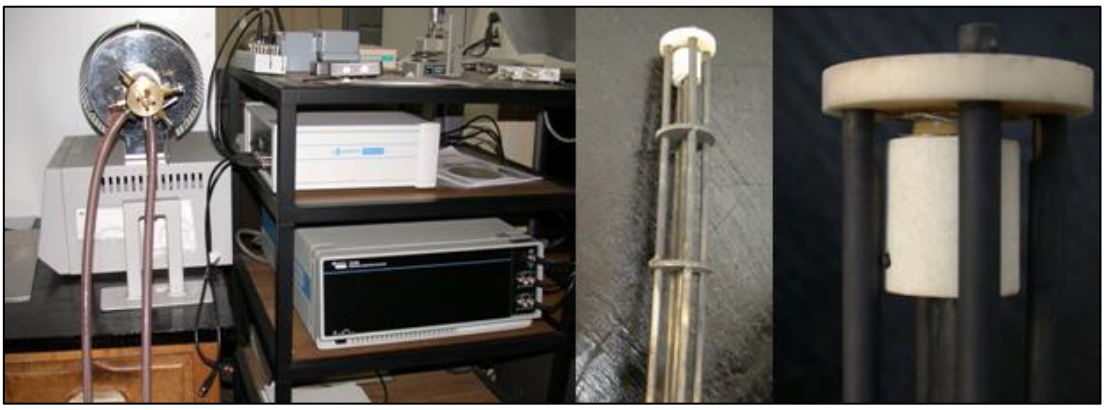

Figure 6.7: Experimental set-up for EIS measurements. From left to right: the whole set-up, the sample holder, a magnification of the sample holder where the pellet is inserted among the electrodes.

Electrical Impedance Spectroscopy method registered the overall impedance of the sample as a function of temperature and frequency, usually a combination of the ionic and the electronic contribution. The spectra were acquired using the "EQUIVCRT" (Equivalent Circuit Programme [200]) software. Impedance values as a function of temperature were obtained in the Nyquist diagrams. The software required the knowledge of the sample geometry for the precise calculation of the resistance. Starting from the parameters relative to the geometry of the material (surface area (A) and thickness (e)), and calculated the resistance value (R) from EIS measurements, it was possible to calculate the conductivity as:

$$\sigma (T) = e/(A*R) \qquad (6.17).$$

Finally from the equation 6.16 previously reported, the Arrhenius plot for studying the thermal induced electrical behaviour of the ceramic breeder candidates was obtained.

5. Li-content variation versus electrical conductivity

The study of changing physical properties with lithium-content covers a special interest, representing an indirect measurement of Li-burn up. With this aim several

Li-based ceramics were fabricated in our lab for observing the effect of γ-radiation on their electrical properties.

Table 6.1: Li-based ceramics prepared in CIEMAT-LNF laboratory.

Compositions (new nomenclature)	**Li1**	**Li2**	**Li4 (OSi)**	**Li6**	**Li8**
Li:Si proportion	**1:2**	**1:1**	**2:1**	**3:1**	**4:1**
Phases	$Li_2Si_2O_5$(98 %) SiO_2(2 %)	Li_2SiO_3(77 %) $Li_2Si_2O_5$(23 %)	Li_4SiO_4(43 %) Li_2SiO_3(47 %) Li_2CO_3(8%) SiO_2(2 %)	Li_4SiO_4(62 %) Li_2SiO_3(36 %) SiO_2(2 %)	Li_4SiO_4(70 %) Li_2CO_3(18 %) Li_2SiO_3(12 %)

In table 6.1 all the compounds used in the next experimental study, obtained by the rotary evaporator method as described in Chapter 5. The relevant data to evidence is the different Li:Si proportion as if Li-burn up is occurring. Considering the phase transformation of lithium silicates under irradiation [199], and the Li burn-up occurring after lithium transmutation, a change of the compound phase, contemporary to a lithium-content decrease, is expected. Thus the aim of the work is to study the effects of γ-ray radiation in silica-based ceramic compounds with different Li-content. The phases present in our compounds are Li_4SiO_4, Li_2SiO_3 and $Li_2Si_2O_5$, varying their percentage together with lithium proportion.

The electrical conductivity is indirectly measured starting from EIS analysis in pellet ceramics.

In some of them a good fit between experimental data (symbols) and the fitting line (dot arcs) is found, confirming the suitability of the equivalent circuit proposed in the section 5 (see Figure 6.8). In general some difficult in the analysis are found when modelling with brick layer model. The explication is extensively and very clearly furnished by Fleig [25], who finds in the imperfect contact between grains, the presence of porosity, the agglomerate of small grains or a bimodal grain distribution, the reason of considerable errors. Grain boundary arcs deviating from ideal semicircles are found, with a distortion of the real activation energy value.

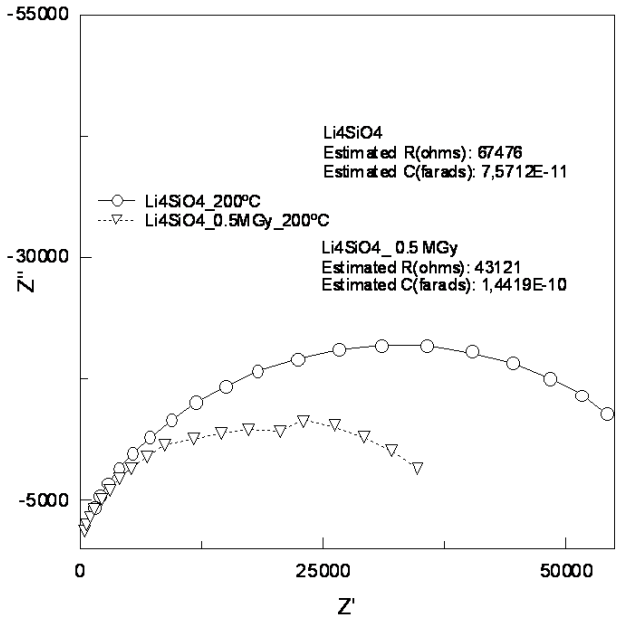

Figure 6.8: Complex impedance plot (plotted by ZView program [201]) of an as-prepared and irradiated pellet measured at 200 °C. The estimated resistive terms corresponds to the total resistance.

Here below, some of the measurements performed on all the compounds of Table 6.1. In Figure 6.9 the conductivity values of 5 MGy-irradiated materials, are reported. This radiation-dose was selected as a representation of the total electrical conduction behaviour, because it is the one providing more pronounced changes in comparison with the AP electrical behaviour, in almost all the materials. Pure silica measurements are included as reference. At the left of Figure 6.9 the Arrhenius trend of conductivity is represented while in the right part the electrical conductivity at 500 °C in as-prepared and damaged conditions, in function of Li:Si proportion is graphed.

From the Arrhenius plot in Figure 6.9 (left), the rise of conductivity with increasing Li:Si proportion is evident. Then, focusing on the electrical conductivity at 500 °C in function of the Li-content (see Figure 6.9 right), a quite similar behaviour is observed among the Li4, Li6 and Li8 ceramics as in the AP-damages case. This result is especially interesting considering that 500 °C is in the range of working temperatures selected for solid BB, thus a good stability in the electrical behaviour of burned ceramics can be stated in the first life-time of pebble bed. In the most interesting case, such as the 5 MG irradiated ceramics, a really different behaviour for Li2 composition is observed, when comparing it to the AP case. Then,

considering the low Li-content of Li2, it is possible to suppose that it is caused by the effect of defects generated by γ-radiation. The effect is more pronounced in this compound than in the others, where Li-ion mobility dominates the electrical conduction process.

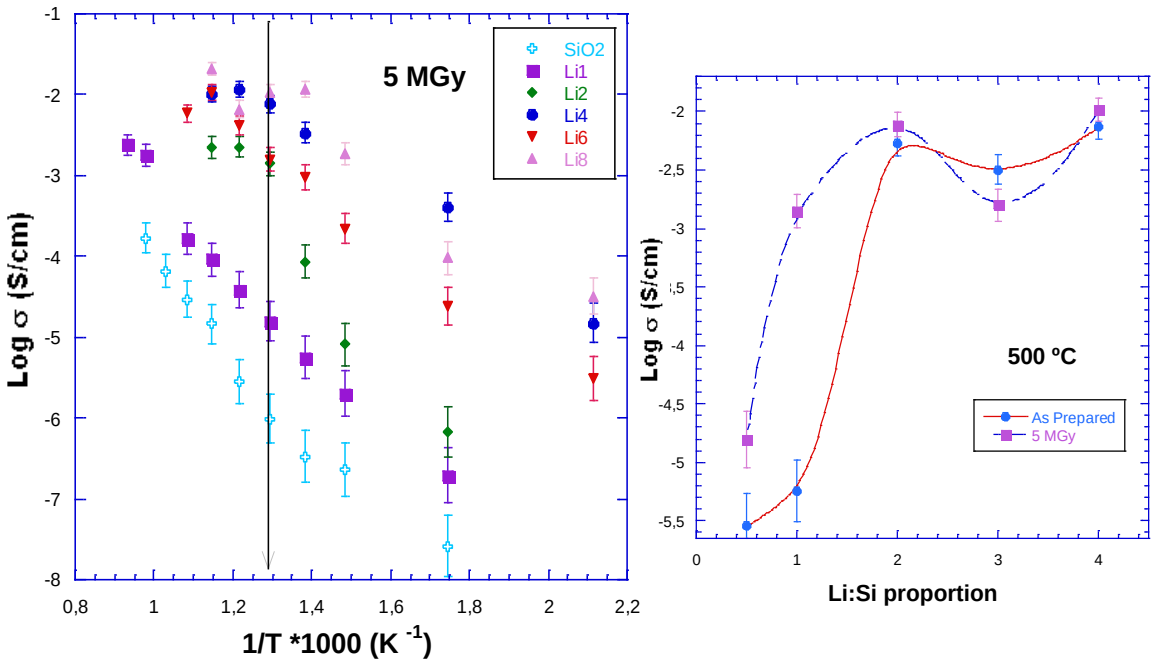

Figure 6.9: Arrhenius plot of Li-based ceramics with Silica matrix and different Li-content irradiated till 5 MGy by γ-irradiation. The black line marks the values at 500 °C. In the right a comparison among the conductivity values varying Li:Si proportion.

The study is repeated with different doses of gamma irradiation. Considering the high quantity of Arrhenius graphs to represent, the analysis is limited to a comparison among the activation energies of each composition at different radiation doses. The activation energy variation is represented in Figure 6.10, where the different compositions are indicated as a function of the Li:Si proportion near each point.

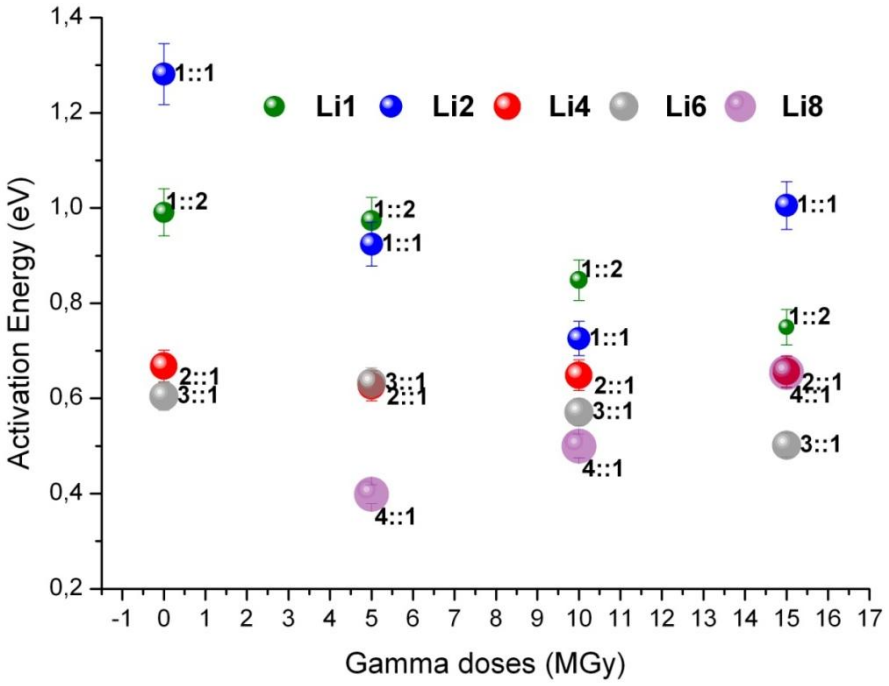

Figure 6.10: Comparison of the activation energies found for silica-based materials with varying lithium content, at the irradiation doses selected for this study.

It is interesting to observe that the gamma dose does not have the same effect in all the samples. As expected the energy necessary for the activation of electrical conduction in compounds with less Li and O ions, is higher. The creation of defects facilitates the conduction process in the materials with low Li-content, being the major contribution to charge movement. The low activation energy value found in the case of higher lithium content reveals the important role of lithium ions as charge carriers.

The trend of electrical conductivity between materials with different Li content is primarily ionic as confirmed in literature [6, 31]. Lithium ions are responsible of impedance variation: the material with the highest Li content (4:1) is the one with the lowest activation energy value.

All these considerations will be especially relevant in the discussion on the hypothetical similarities with Li- burn-up effect. In general it is possible to state that the electrical characterization shows a slight increase at a total dose of 5 MGy and a quite stable behaviour of the majority of compounds after different irradiation treatments. On the other hand when varying lithium content a different behaviour is observed for ceramics with low Li-proportion which notably increase the charge movement and thus the electrical conductivity in the volume.

6. The electrical behaviour of Li-orthosilicate

The orthosilicate is a really eclectic material with multiple and powerful applications, presenting an interesting bibliography on electrical properties [197,198]. Its electrical behaviour is here studied and discussed in ceramic pellets fabricated in the Ciemat-laboratory (the Li4 composition of Table 6.1). The pellets were gamma irradiated by a ^{60}Co source in the Nayade-installation at different doses, following the experimental procedure described in section 6. Several studies with slight variations in the experimental parameters were effectuated and here presented.

6.1. Results

The samples irradiated at different doses between 5 and 15 MGy are subjected to a thermal ramp between 26 and 800 °C with a step of 50 °C for each measurement for the volume conductivity measure.

Lithium Orthosilicate specimens irradiated at different doses are then compared with an "as-prepared" sample. In Figure 6.12 the indirect measure of electrical conductivity obtained from impedance measurements, is shown in an Arrhenius plot. The highest increase in electrical conductivity is obtained for a 5 MGy dose with a maximum value of $1.17*10^{-2}$ S/cm (at 550 °C). For increasing gamma doses a recombination process seems to occur, with a decrease in conductivity till values lower than those found for the un-irradiated sample. Regarding the E_A calculation, the impedance data used correspond to the temperature ramp between 200 and 800 °C, avoiding the dependence from electrodes polarization affecting the low temperature measurements.

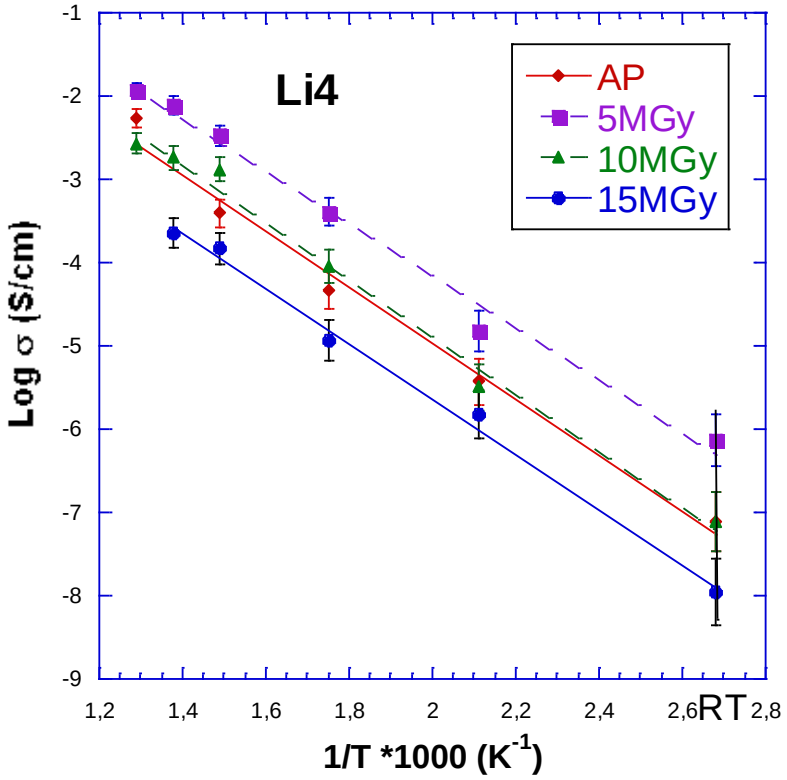

Figure 6.12: Comparison between the Arrhenius plots obtained for the Li_4SiO_4 samples irradiated to different doses: As-prepared (red rumble), 5MGy (purple square), 10 MGy (green triangle) and 15 MGy (blue circle), irradiated by a ^{60} Co source.

The volume conductivity at room temperature in as-prepared conditions is of $3.16*10^{-8}$ S/cm and it slightly increases with irradiation damage (i.e.: $2.24*10^{-7}$ S/cm for 15 MGy of irradiation-doses, see Table I). The conductivity rises with temperature, as expected when phonon lattice movements together with point defects are considered [202].

Figure 6.13 summarizes the results of the conductivity variation with irradiation at some selected temperature. The values can be considered quite constant. Only a slight decrease with irradiation dose is observed, thus confirming that ionizing radiation is not affecting the activation of charge carriers for the conduction process.

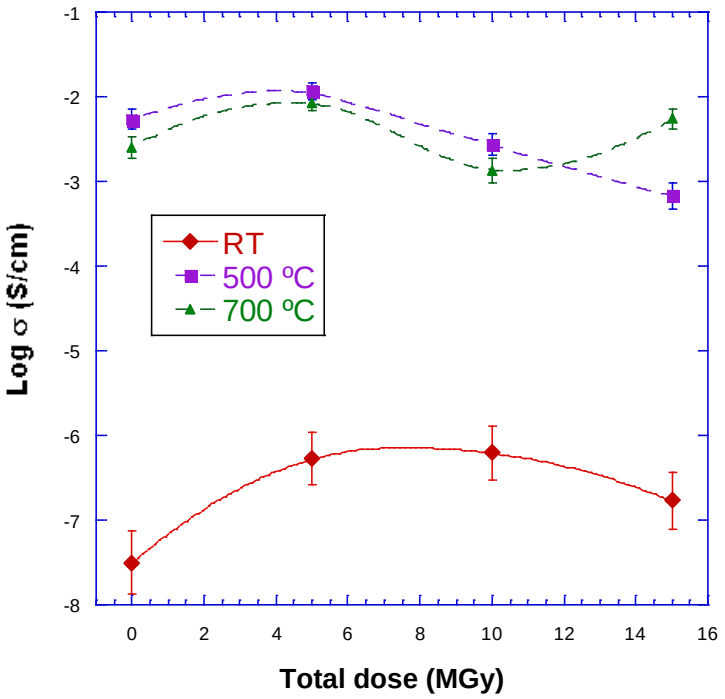

Figure 6.13: Comparison between the conductivity under different irradiation doses in correspondence of some temperatures: room temperature (red rhombus), 500 °C (purple square) and 700 °C (green triangle).

In Figure 6.14 a comparison of the electrical conductivity behaviour in SiO_2 and Li_4SiO_4 is presented. The measurement is performed on "as-prepared" and 5 MGy γ-damaged samples under the usual temperature ramp variation. The SiO_2 pellets are fabricated in our laboratory from a starting colloidal silica (Ludox TMA 34% wt.), following the same rotary evaporator described in Chapter 5, with a final sintering treatment at 1600 °C during 2 hours. From the SiO_2 bulk conductivity it is evident that it presents an almost insulating behaviour at room temperature with a conductivity of 6.8 x 10^{-8} S/cm. The presence of two different processes is observed before and after the measurement at 200 °C, confirming the charge role of O ions. The activation energy of SiO_2 (0.89 eV) is twice the one of Li_4SiO_4 (0.48 eV) confirming the charge carrier role of Li^+ (and possibly Li^{2+}) ions in BB ceramic compounds. It is interesting to observe the different behaviour on the total conductivity for the two materials under the same gamma irradiation dose: if in Li_4SiO_4 it causes a soft increase in the electrical conductivity, in the SiO_2 case it causes a more pronounced decrease. This may be provoked by the mayor number of starting defects present in the Li4 material, whose effect is enhanced by radiation.

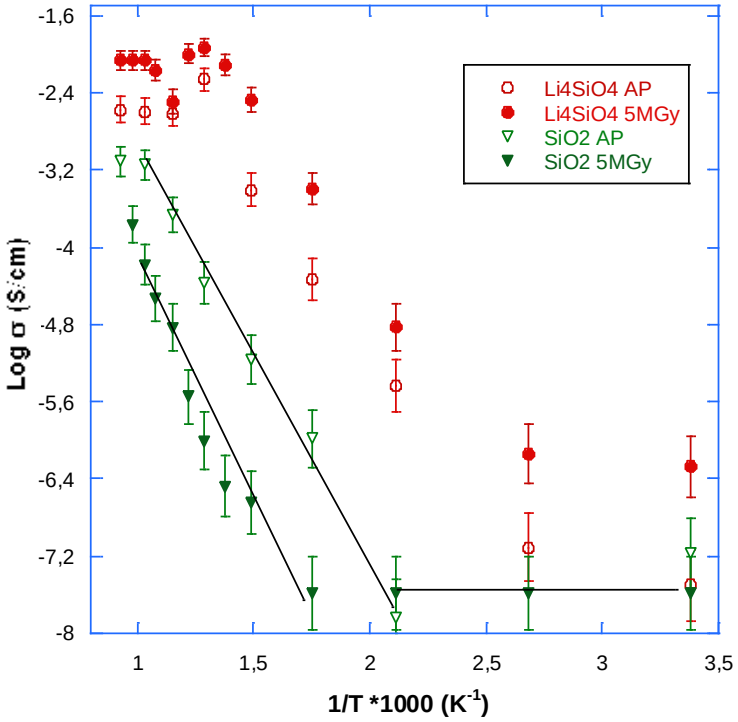

Figure 6.14: Arrhenius plot of the bulk conductivity for a SiO_2 as-prepared sample (pink rhombus) and 5 MGy irradiated SiO_2 (green triangle), compared to Li_4SiO_4 as prepared (red circles) and irradiated up to 5 MGy (blue squared) at 22 °C.

With the aim of extrapolate truthful results under reactor conditions, samples are than irradiated at 250 °C (temperature selected for experimental limitations), to a total dose of 5 MGy. Figure 6.15 shows the evolution of conductivity as a function of temperature, compared to the room temperature irradiated specimen. The results show the same trend for measurements, with slightly lower values in the conductivity for the irradiation performed at 250 °C, confirming the recombination role of temperature in charge carriers, as may be defects and impurities.

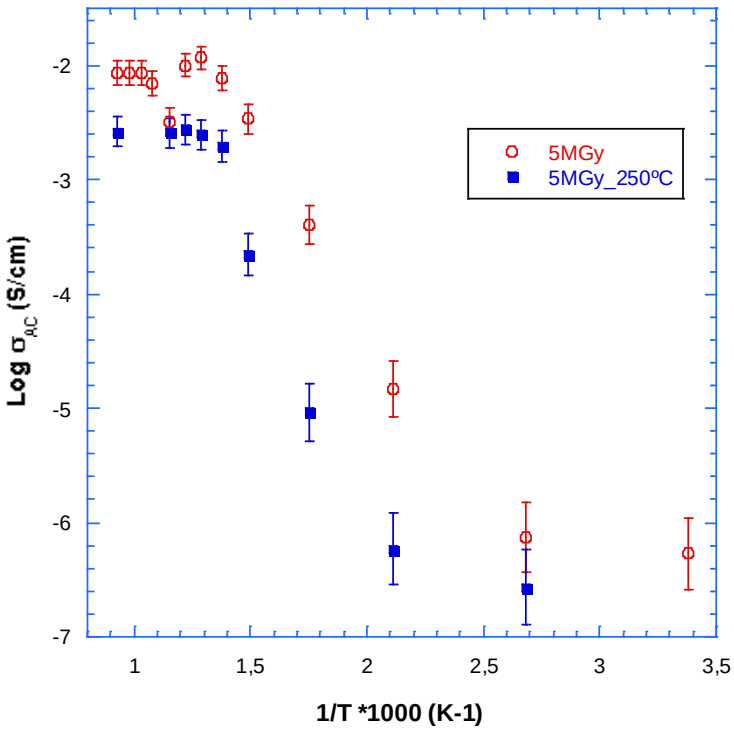

Figure 6.15: Arrhenius plot of the bulk conductivity for a Li_4SiO_4 sample irradiated up to 5 MGy at 26 °C (red circles) and at 250 °C (blue squared).

A plateau in the temperature range between 600 and 800 °C is observed in both cases. It represents a "saturation level" for electrical defects above which the electrical conductivity becomes stable. It is worthwhile mentioning the insulating character of these ceramics, which must be conserved under operational conditions.

Finally, to corroborate the effectiveness and accuracy of the experimental data collected, a comparison between the electrical behaviour of a sample irradiated continuously up to 15 MGy and one irradiated in two different steps (firstly to 10 MGy and then to 5 MGy), is proposed. As shown in Figure 6.16, no difference between the two electrical conduction behaviours is found. A good reliability of the measurements and the permanent effect of ionization defects on insulating materials after their irradiation are thus demonstrated.

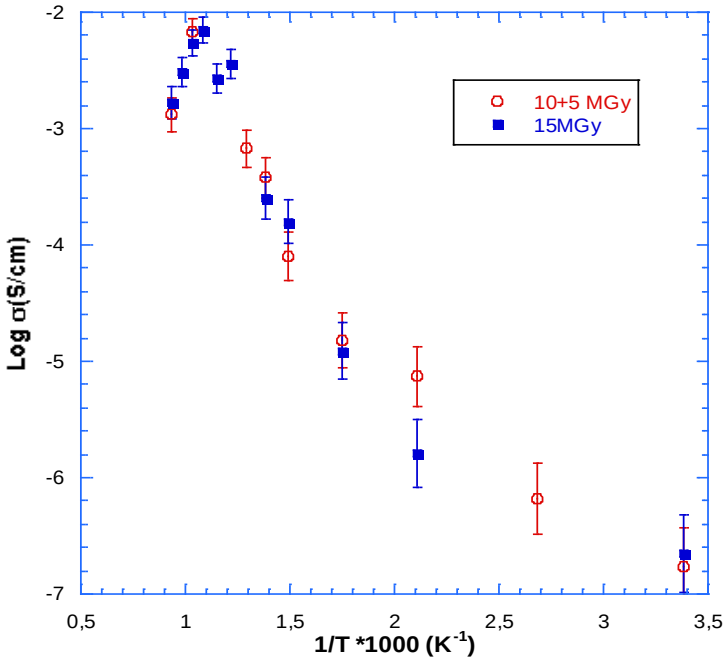

Figure 6.16: Electrical conduction behaviour for a Li_4SiO_4 sample irradiated up to 15 MGy continuously (blue squares) and in two different steps: till 10 MGy and then adding other 5 MGy-doses of gamma-irradiation (red dots).

Scanning electron microscopy is here presented for observing the microstructure and the grain boundaries structure.

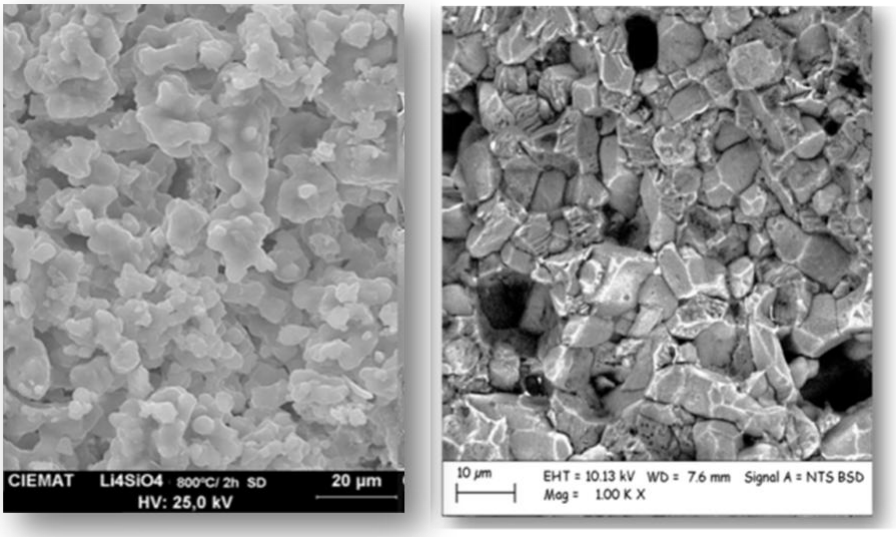

Figure 6.17: SEM images of Li_4SiO_4: surface (left) and fresh fractured (right) of the sintered ceramic.

The main grain size is captured on the polished surface (Figure 6.17 left) and along the fresh fractured (Fig 6.17 right) of Li_4SiO_4 pellet ceramic. The

microstructure shows a material formed by the incomplete coalescence of the grains, with a mean grain size of 5-8 μm, the surface looking quite porous and rough. In the case of the fresh fracture image (Figure 6.17 right), it can be observed that cracking occurs mainly intra-granularly and that closed porosity is present. These results will be helpful in the discussion part here below.

6.2. Discussion

Electrical conductivity is a thermally activated process and follows the Arrhenius law. In a polycrystalline material it depends on structural factors as ordering, microstructural factors like porosity, grain size, grain boundary and extrinsical factors like impurities [36].

The detailed diffusion pathways of Li in the bulk and the occupancy of the ion in the lattice as well as the influence of the defects are critically important for understanding the electrical behaviour of Li_4SiO_4 ceramics. Duan et al. [60] found that the band structure of both monoclinic and triclinic phases of Li_4SiO_4 have mainly two valence bands, presenting the first a direct and the second an indirect and smaller band gap. Munakata et al. [203] found that in a Li_4SiO_4 crystal studied by *ab-initio* calculation, more electrons are concentrated in the *3sp* shell of the oxygen, the outer shell, and that Li^+ ions play an important "bridge" role for the movement of the electrical charge in lithium based-ceramics. Following Mott predictions [204] it is possible to propose a model in which Li^+ charge is transported by the thermally assisted hopping of electrons between electron traps randomly distributed, created by the introduction of impurities during fabrication process as by the electrical damage.

Regarding the soft decrease in the conductivity with the gamma dose, it could be attributed to the release of trapped charges and a subsequent quenching of the conductivity through its recombination. The effect of irradiation is attenuated by the recombination effect of temperature, as observed when irradiating at 250 °C. This result is of special interest in the BBs field. Actually the defects created by radiation can act as traps for the tritium bred in those ceramics hindering its quickly release, as desirable for maintaining the Tritium Breeder Ratio value > 1.15 [64]. Considering the working operational temperature of this part of the reactor (around 400 °C), the result confirms the kinetic effect of recombination due to the lattice vibration under thermal stimulation.

The microstructure in Figure 6.17 shows a not homogeneous grain size, open porosity and a small close porosity, which can lead to the anisotropy of the electrical conductivity and to a kinetic of the overall process mainly determined by the transport across grain boundaries [205].

In the microcrystalline regime, the electrical behaviour of grain boundary-controlled electroceramics can be described by the "brick-layer model" [206]. Fleig and Maier [207] have predicted that some microstructural features might exert additional effects on the impedance spectra, causing deviations from the model. Some examples of such deviations are given by a bimodal distribution of small and large grains, or by an imperfect contact between grains. The effect is that the current path might make detours across larger grains to minimise the number of boundaries effectively crossed, leading to a depression in the semicircle of the grain boundary. This is the case of the Li_4SiO_4 presented in this work whose microstructure presents micropores along the grain boundaries as an inhomogeneous spatial distribution of grain size, confirmed in EIS analysis by highly depressed arcs.

The effect of the gamma irradiation on the electrical conductivity for lithium glasses has been studied to assess the accumulation of radiation [208]. Gamma rays interact with the electronic structure of the material, generating electron-hole pairs that can recombine or be trapped at specific defect sites. This implies the creation of charge compensation in the electrical state of the crystal. This is the direct cause of the distortion of the tetrahedral LiO_4 coordination with a consequent total conductivity value modified by the Li^+ ions movement.

7. The electrical behaviour of Li- metatitanate

Several studies [193,209] show empirical models for the generation of a complete database on the relevant properties of lithium-metatitanate ceramics, thus an experimental validation is necessary. In this part of the work pellet samples, pressed, cut and sintered in our laboratory starting from a commercial powder (Alfa Aesar 99.9 % purity) as described in Chapter 5, are used. The pellets were gamma irradiated by a ^{60}Co source in the Nayade-installation at different doses, varying their residence time in the pool.

7.1. Results

Lithium-metatitanate (MTi) ceramics were irradiated at different gamma-radiation doses at room temperature, and analysed by EIS spectroscopy with thermal ramps of 50 ºC between RT and 800 ºC. Figure 6.18 evidences the logarithmic trend of conduction versus the inverse of Temperature. The metatinate trend is characterized by two well separate trends (marked by a black line) changing at 300 ºC. The same change in slope has been observed in literature [49] and attributed to a first-order phase transition associated probably with order-disorder effects.

It is interesting to notice that the variation of electrical conductivity with irradiation does not suffer relevant changes, confirming the really good electrical stability of this material. The variation in electrical conductvity with the γ-ray dose is different compared to silica-ceramics trend. In the MTi ceramic quite no increase is found in electrical conductivity after irradiation, nor at 5 MGy, being in general its behaviour rather similar to the no irradiated material.

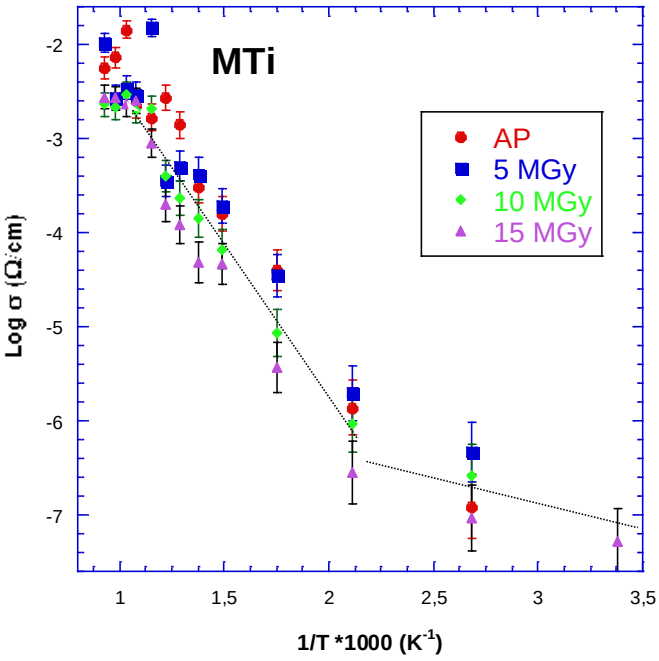

Figure 6.18: Comparison between the Arrhenius plots obtained for the MTi samples irradiated with different doses: As-prepared (red circle), 5MGy (blue square), 10 MGy (green rhombus) and 15 MGy (purple triangle), irradiated by a ^{60} Co source.

Considering that charge transport is presumed to be caused by Li^+ ions, one can guess that the lower Li content provokes this sort of homogeneity in the MTi behaviour even under gamma irradiation. Thus a comparative with metasilicate (Li2,

Li_2SiO_3) ceramic is proposed for understanding the role played by the matrix. In Figure 6.19 the difference between Metasilicate (Li2, Li_2SiO_3) and Metatitanate (MTi, Li_2TiO_3) ceramics with 1 to 1 Li:Si proportion is shown. The study is carried on as-prepared and gamma-irradiated up to 5 MGy materials.

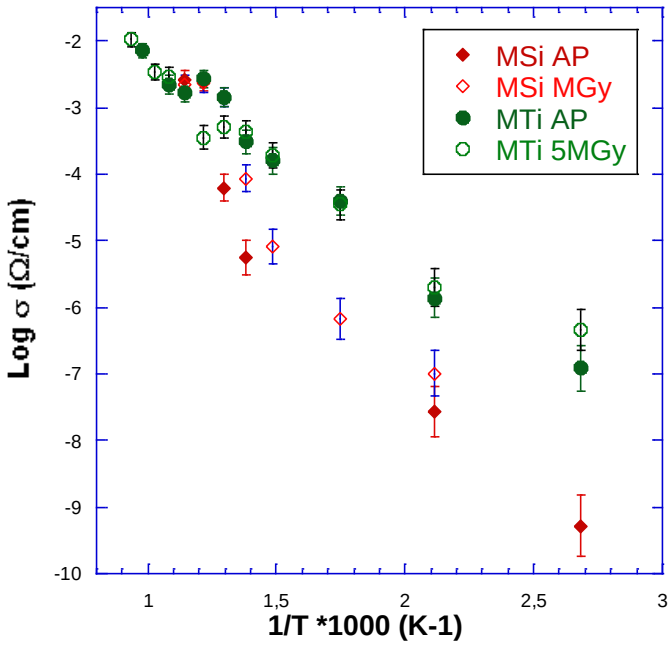

Figure 6.19: Comparison of the conductivity trend between two materials with the same Li content but different matrix (MTi and Li2) in the case of as prepared (AP) and irradiated samples to a total dose of 5 MGy.

The Arrhenius plot indicates a slight difference between the two materials. The best difference can be found in the activation energy value (see table 6.3). While in the MTi case it presents a quite constant value in the AP and damaged case, in the Li2 ceramic the electrical conduction process after irradiation requires a higher energy value for its activation. This is a confirmation of the electrical stability of MTi matrix in comparison with lithium-silicate ceramic, although the same lithium content.

Table 6.3: Activation energy values for the conduction process in two different BB ceramics with the same Li content.

Activation Energy		
	As prepared	5 MGy
Li2	0.81±0.04 eV	1.1± 0.05 eV
MTi	0.57± 0.02 eV	0.51±0.02 eV

The main differences among the selected ceramics can be observed in their crystallographic structure (Figure 6.20) as the chemical bonds, which strongly affect the charge movement.

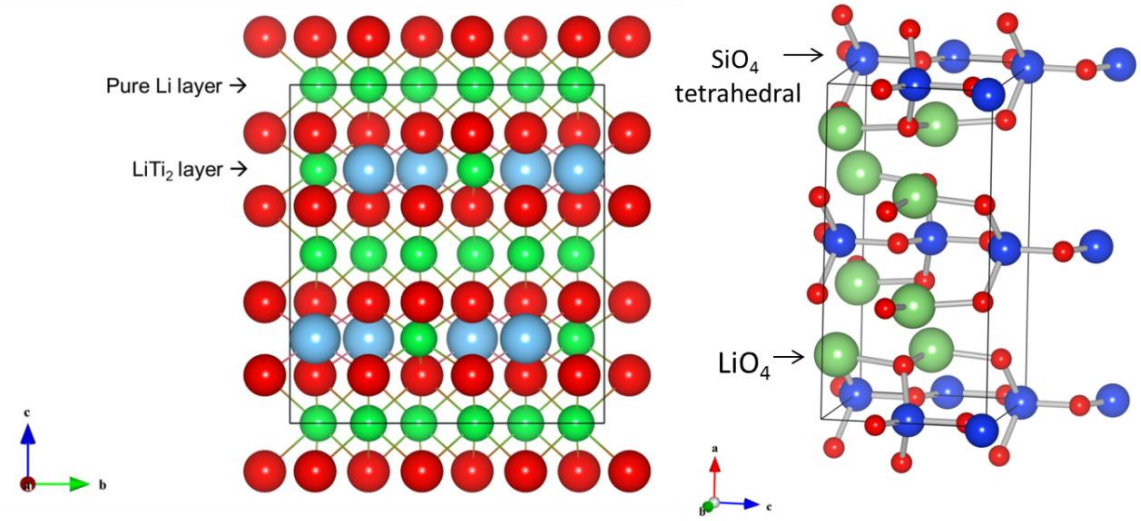

Figure 6.20: Crystallographic structure of the two ceramic compounds compared in the study. At the left the Li_2TiO_3 crystal structure, at the right the Li_2SiO_3 orthorhombic structure.

Li_2TiO_3 ceramic present a monoclinic structure with space group *C*2/*c* formed by an ordered rock-salt super-structure with cationic (111) planes alternately occupied by pure Li and $LiTi_2$ layers [191]. Li_2SiO_3 ceramic has an orthorhombic structure, a space group of Cmc_2 with 4 formula units comprised of 24 atoms per unit cell. It can be considered as a framework of corner-sharing [LiO_4] and [SiO_4] tetrahedral. In general in silicates, the Si-O bonds are considered to be of half covalent and half ionic character [210], while in MTi case Ti-O is a covalent bond. The presence of a pure Li-layer in MTi structure may explain the easiest activation for electrical conduction (lower E_A values).

7.2. Discussion

Starting from the theory on Li_2TiO_3 electronic structure, it is important to remember the non-metallic nature of this material, presenting a band gap value of 3.49 eV. When the density of states is studied [8], some important considerations can be made: the interaction between Ti and O is mainly covalent and between Li and TiO_3 is mostly ionic; the interaction between Li and $LiTi_2$ layers is much weaker than the one between O and Ti atoms in $LiTi_2$ layers. Thus starting from these

considerations, it is possible to suggest that the charge carriers responsible of the electrical conduction are Li^+ ions.

Following Fehr suggestions [149] Li^+ migration is thought to occur firstly in (001) planes, associated to the presence of lattice. On the other hand the octahedrally coordinated Li^+ positions in a stoichiometric β-Li_2TiO_3 are all occupied, thus Li vacancies transferred by adjacent sites or caused by some deficiency during sample preparation.

Taking into account the metatitanate structure described in Chapter 2, it is possible to suppose that in the presence of defects created by gamma irradiation, two directions for lithium diffusion are possible: one among lithium sites in the pure Li layer, the other considering lithium jumps between the pure Li and $LiTi_2$ layers.

According to some thermo-luminescence studies effectuated on this material from other authors [88] after gamma-irradiation experiments on lithium MTi, a consecutive breaking and linking of bonds is observed. Moreover the redox reduction occurring with thermal variation induces an increase of traps and recombination centers. Further explanations are searched by Position Annihilation spectroscopy analysis in materials damaged by gamma-ray.

8. Positron annihilation spectroscopy on gamma irradiated ceramics

Positron annihilation spectroscopy (PAS) was used in some of the studied ceramics with the aim of identifying the nature of the defects present in these crystal structures and those created after gamma-radiation. It is a non-destructive method based on the interaction of positron, emitted from radio-nuclide sources (^{22}Na, ^{64}Cu, etc.) with matter. The interaction of the positron with the trapped electron, bring to its annihilation as a photon. The time delay between the injection of positrons and the detection of photon provides a time distribution, from which one can deduce the decay rate of positron [211]. The injected positrons are annihilated in the medium in various possible ways: with free electrons, at point defects or capturing an electron to form a positronium (a hydrogenic two body e^+ - e^- system). For ionic solids generally three components are considered: the fast τ_1, the medium one τ_2 and the longer τ_3.

Positron interacts with more than one electron in different energy states in many particle systems, providing information on the electron density and on the distribution of electrons in momentum space. Thus different measurements can be

performed such as a study on positron decay spectrum (its lifetime is obtained) and a Doppler shift of the non-zero momentum of the electron-positron pair.

It is important to consider that this technique in non-metals is more complex and the life time of the first two components can be influenced by particle size. PAS measurements can help the understanding of the dynamic occurring after the damage, when irradiation defects are annihilated. The sensitivity of positrons towards micro-defects domains makes it an attractive toll for many material science problems.

The interest of the technique in this thesis work is related to the nature of the materials used. Being novel and polycrystalline complex atomic structures, really scarce information on the nature of their defects is present in the bibliography. The measurements are performed on the two different matrixes, MTi and Li4 before and after a gamma-ray radiation at 5 MGy, with the aim of elucidate the defects nature and variation.

In Figure 6.21 the positron decay spectrum in the form of three lifetime components is presented. The last graph represents an average behaviour of positron lifetime in MTi and Li4 ceramics.

The MTi material presents a first component with high intensity, with about the same I(%) value in all the cases. Only for the gamma-irradiated sample, a first component decrease, a second component with low intensity and a third component with really high intensity are found. It means a high purity of the as-prepared material, with a consequent annihilation of positrons with free electrons in the first lifetime component range. After gamma-radiation the small second component indicate the appearance of defects and the large third component indicates the interaction among positron and ionizing tramps associated to vacancies. The thermal treatments after irradiation are able to restore the starting configuration, which means that the defects induced by gamma radiation do not produce any irreversible change in the material structure.

Considering the life-time of the third component in the gamma irradiated sample, it is possible to suppose that F^+ (Oxygen with 1 trapped electron) defects are present. In the Doppler analysis a really small variation in the energy range (25 keV) relative to the positron annihilation with the electrons of O or Li is observed. Thus it may confirm the creation of F^+ defects, restored by charge movement in the lattice after thermal treatments.

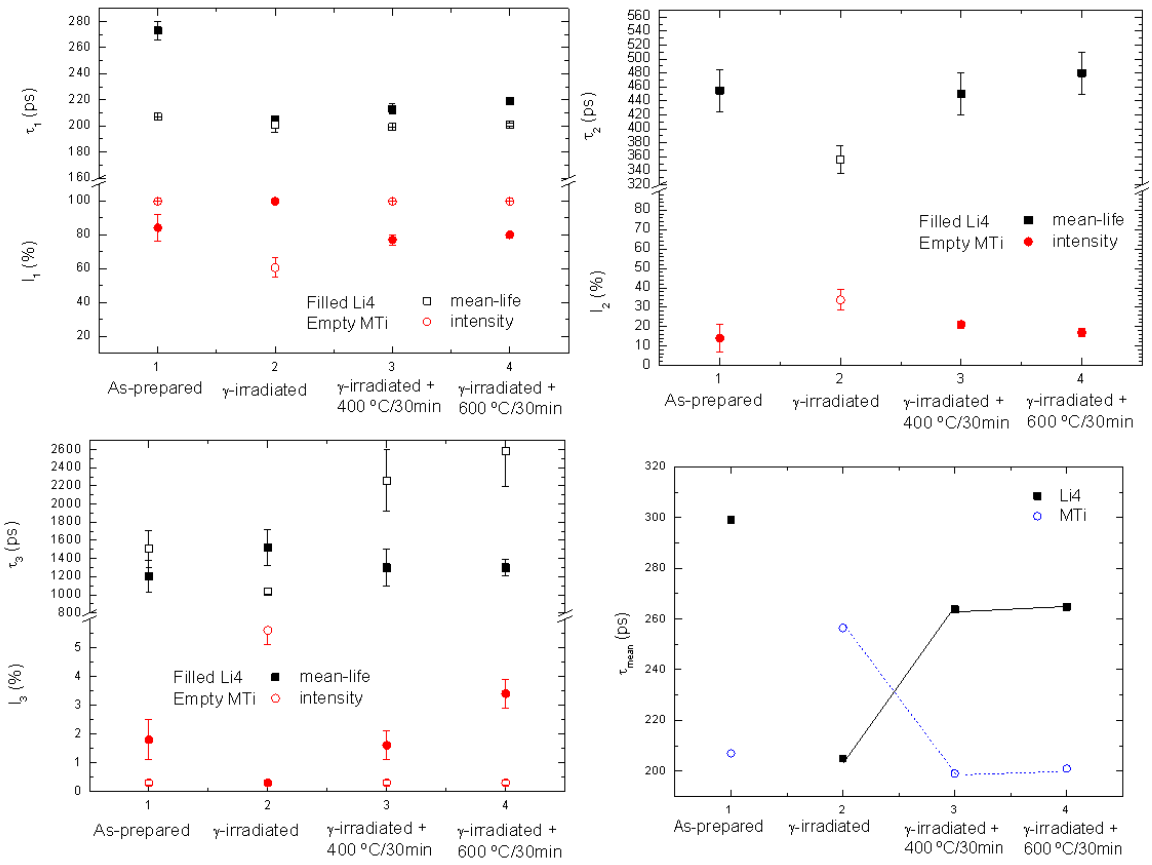

Figure 6.21: Representation of the three PAS components calculated for Li4 (filled dots) and MTi (empty dots) ceramic pellets. The graphs represent the Intensity (red circles) and the mean-life (black square) of the three components measured in samples (1) as-prepared (2) γ-irradiated (3) irradiated and then heated for 30 minutes at 400 °C, (4) irradiated and then heated at 600 °C during 30 min. The last graph (bottom right) represents an average of the mean-life for the two ceramics.

The Li4 as-prepared material presents a first high component and second and third small components. It can be explained by a higher quantity of structural defects deriving from the fabrication process. After irradiation only one component appears, indicating saturation in the trapping centres for positrons. Thermal treatments do not totally restore the starting situation and a slightly higher third component appears. Doppler analysis does not provide any interesting information.

Finally comparing the average mean life in the two materials, it is possible to state that gamma-radiation act in an inverse manner in the two materials: while in the MTi material it facilitates the creation of defects and the annihilation as

positronium, in the Li4 case the trapping as free electrons is favoured and the positron average mean-life drops. The thermal treatments after irradiation quite totally restore the starting configuration in the case of MTi ceramic but not same happens in the case of Li4.

The difference in starting purity of the two materials (one sintered starting from commercial powders, the other totally fabricated in our laboratories), may explain the differences found in the defect configuration.

When relating PAS study on defect identification with the electrical measurements, it is possible to confirm the hypothesis made for charge transport carriers in the two different materials. In the case of MTi, a better stability with radiation-dose is observed: the impedance variation is mainly caused by the defects produced by gamma-radiation and the thermal treatment help to restoring the starting electrical configuration.

In the case of Li4, assuming that the material has some impurities (like the ones find by SIMS analysis in Chapter 5), a major density level of defects in the as-prepared condition is found by PAS. This causes a difficulty in the recovery of the damaged samples after their heating and a different nature of defects as indicated by the three positron components.

Assuming that the radiation can cause electron defects, changes in the valence state of lattice are expected. Such charged induced defects are related to defects present in the material after its fabrication (Li4 case) or are induced by γ-irradiation (like in the case of MTi) implying different levels of variation in the electrical conductivity behaviour, like observed.

9. Indirect measurements: T mobility and Li-burn up effect

Considering the difficulty in handling Tritium, several indirect methods to understand its behaviour have been searched. Among others, *ab-initio* simulation (Dynamical Functional Theory) [190] or the study of some microstructural properties have been proposed [149]. Starting from them, ionic conductivity studies [212] suggest that the mechanism of tritium diffusion is intimately associated to the Li^+-ion movement.

It is assumed that the places occupied by tritium in the crystal network are related to those left free by the transmutation of Lithium, and from those related to the defects created by irradiation. Therefore, one can theorize that the mobility of

tritium will be strongly related to the mobility of lithium through the lattice. The rate of occurrence of such vacancies determines the diffusion of the already formed tritium. Meanwhile blanket materials are exposed to different kind of radiation (neutron, heavy ions, γ-ray..) creating defects in the crystal structure (vacancy, interstitial, small clusters) that affect the microstructure of lithium ceramics and tritium release performance.

Tritium release is associated to oxygen vacancies creation: Tritium ion is in the valence state of T^+ and is assumed to be bounded with the oxygen ions, thus its migration is assumed to occur by hopping from oxygen to oxygen ion in the lattice. In such migration the tritium must overcome the barrier of electrostatic repulsion due to lithium ions. Since the lithium ion is consider to migrate through vacancy mechanism, and considering that its transmutation creates vacancies, the repulsive force decreases and the tritium can easily diffuse.

The sum of these mechanisms may then cause Li_2O evaporation, a common effect in Li-oxide ceramics during heating. The activation of Li2O represents another thermodynamic variable influencing the disorder status.

Li-ion inter-grain transport, similarly to tritium desorption, is a thermally activated process, starting from 400 °C and hopping among randomly distributed electrical states, allowing the diffusion process inside the material. Its movement is favoured by the presence of defects, but not strictly related to it (as confirmed by the activation energy constant value in some lithium-ceramics after different total irradiation doses).

As observed in next chapter and confirmed by literature [213], gamma-radiation facilitate the recovering of some kind of defects (as the V_o created for preferential sputtering).

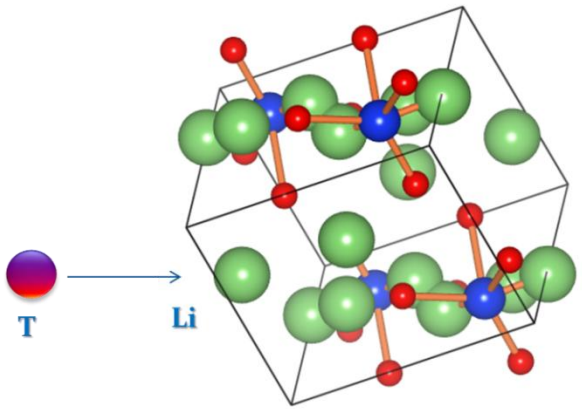

Figure 6.22: Scheme representing tritium atom occupying Li site in a lithium-orthosilicate crystal structure.

Another important aspect to consider is that lithium atoms in a breeding blanket are burned up through neutron, transforming into helium and tritium atoms. The effects of lithium burning on the tritium breeding ratio variation with time and on tritium behavior are not easy to calculate. The tritium production is almost proportional to the atomic density of the lithium; consequently it might be changed by the lithium burn-up factor as by the effect of the damage due to irradiation during Li-transmutation [214]. Some studies have been performed to model the lithium burn-up versus TBR relation, taking into account the operation-years and the position of the ceramic pebble bed, but not other factors like the material degradation or the Li-movement changed by irradiation defects [112]. Therefore more irradiation experiments to investigate the behaviour of these materials under irradiation focused on burn-up values are required.

The measurements here proposed are only a hypothetical approximation to the real effect that burning lithium will have in a ceramic pebble during reactor functioning. The proposal is the possibility of observe the effect of gamma-radiation on the electrical properties, when lithium content is varying. The use of ceramics fabricated all following the same route, in which only the Li to Si content is modified, makes comparable the results obtained. These show that electrical conduction at the working temperature of a breeder (around 500 °C), does not present drastic changes, mostly decreasing when Li:Si is in a 1 to 1 proportion. Similarly the energy value necessary for the activation of the conduction process is quite constant in the materials with higher lithium content, also after different irradiation treatments. The changing behavior is observable for really poor-in-lithium ceramics. The results obtained cover a special interest because confirm the electrical stability of these ceramics (which have an important shielding role in the reactor). Secondly the behavior after irradiation and the quite low activation energy value, mean a facility in ionic movement which is not lost neither when lithium content decrease nor when radiation total dose increase. This represents an interesting result as an indirect measure for tritium behavior understanding.

10. Conclusions

Lithium – MTi and –Li4 are rather durable materials under different doses of gamma-irradiation. It has not been observed any drastic change in their electrical properties, confirming the good electrical stability and durability as breeder blanket ceramics for future ITER reactor.

The conductivity of sintered bodies is slightly promoted by γ-ray. During irradiation process defects associated to charge transfer are anticipated, encouraging Li^+ ion mobility and conductivity process in the Breeder Blanket candidate material. A model based on ionic conductivity by hopping process is proposed. The charge is transported via point-defects through an ion migration between vacancies or interstitial states, mainly distributed along grain boundaries. In terms of T mobility it means that γ-radiation could help the ion hopping between vacant sites: the ones created by Li transmutation and defect sites created by radiation.

The study on silica-based ceramics with different lithium content permits an analogy with lithium burn-up effect. The results show good electrical stability when lithium content and the total dose-rate are changed. The formulation of a mathematical model relating the content of lithium, the burn-up factor and the ion movement could be an interesting tool to work out in the future.

CHAPTER 7

LIGHT IONS TRANSPORT

The study of light ions behaviour in solid breeder blanket covers a special interest as the transmutation products of lithium (tritium and helium). The study of their diffusion behaviour with temperature and in damaged materials represents a novel study that will be here present and discussed with the support of several techniques. From the results obtained on D and ^{3}He behaviour it is possible to deduce information on tritium transport behaviour in different microstructures.

1. A big deal: understanding tritium behaviour

One of the main parameters to be considered when designing a nuclear fusion reactor is the supply of tritium (T) from the following nuclear reactions ^{6}Li (n, α) T or ^{7}Li (n, n α) T [215], taking place when the breeder blanket is irradiated with neutrons.

The understanding of tritium behaviour (retention and release) in the bulk and at the surface of breeding materials is crucial in order to achieve a self-sustainable operation reactor (Tritium Breeder Ratio, TBR higher than 1.15 [64]). Previous experimental and simulated results evidence that both tritium transport and release are complex processes involving, among others: grain boundary and inter-granular diffusion, absorption and desorption at the gas/solid interfaces, diffusion along the interconnected porous, surface reactions, etc [76,216,217]. Moreover an additional factor to be considered on T behaviour is the microstructural evolution during irradiation with ions, neutrons and electrons [125]. A good number of *in-situ* tritium release experiments have been carried out at different laboratories [47,90,218], the conclusions being that processes involved in the annihilation of radiation defects seem to play an important role to establish the tritium recovering system and its release behaviour. See Chapter 3 for complementary information.

Because of the high tritium activity, its volatile and its long decay time which lead to complex and rigid safety procedures, breeder irradiation tests can be simulated by ion implantation of other light species such as H, D or ^{3}He [219] which are easier to handle. Owing to the nature of the injected fuel, fusion research is particularly interested in the light elements interaction with materials [220]. Few are the publications studying hydrogen isotopes behaviour in ceramics for fusion breeder applications [71,213,221,222], reporting that tritium release is limited by the materials composition or microstructure [223], or the improvement obtained by using argon or helium mixtures with low concentration of hydrogen in the purge gas [224].

The objective of this work is to confirm previous theories and add new information on the tritium behaviour in ceramics, through the use of implanted deuterium (as another hydrogen isotope) and helium-3 (presenting the same mass and spin of T). This is done firstly with a migration study in different microstructures, to reach some significant evidence of its role in the transport of light elements, and secondly with a comprehensive study on the temperature effect on ion diffusion. Furthermore an analysis of the irradiation effect on light ion transportation is here proposed. The joint study of the thermal and irradiation

effects will help to better simulate the reactor working conditions.

2. Light ion detection

The analytical study of light elements is challenging for several reasons. Hydrogen and its isotopes are very volatile, which can easily distort measurements. Hydrogen is usually the main component for the residual gas in vacuum chambers. Most of the detectors used in extended techniques for the chemical analysis are blind to low Z elements (lower than B or Be). Added to this, the quantitative analysis of H, the main impurity in fusion materials, requires ultra-high vacuum and high sensitive analytical techniques to avoid the noise signals. As a consequence of its very low ionization potential, He determination is restrictive to a couple of techniques. The result is that there are few compositional characterization techniques for light ions detection which can be divided in four main groups:

1. mass spectrometry-based techniques (SIMS, TDS, EELS, ...),
2. resonance - based methods (NMR, absorption spectroscopy, ...),
3. accelerator – based methods (ERDA, p-RBS, NRA),
4. indirect methods (neutron scattering, small-angle X-ray..).

The number of these techniques is reduced when considering those able to perform in-depth compositional profiles. The Ion Beam Analysis (IBA), Secondary Ion Mass Spectrometry (SIMS) and Glow Discharge Emission Spectrometry (GDOES) are considered the best techniques for the surface and depth analysis of light ions in fusion materials [225].

This work is focused on the detection and the profile examination of light ions accumulated in solid BB, especially deuterium and helium, focusing on their retention and migration. The objective is to study the dependence with temperature and radiation of light ion diffusion taking into account the physico-chemical characteristics of the host ceramics. With this aim the results of different ion implantation experiments are here discussed through depth-profiling studies and conclusions on tritium transport in the breeder structure will be proposed.

2.1. Ion implantation

The first basic tool for the development of experiments on light ion transport is the ionic implantation. Through this method it is possible to introduce any kind of foreign element inside the lattice, controlling its quantity and depth penetration [119]. The depth implantation provides a method to understand the kinetics and dynamics of the ion before its release from the surface. The implantation technique is based on the acceleration of ions which, impacting in a target surface can enter to a determined depth, remaining there trapped meanwhile a number of physical phenomena happens in the interaction with the crystal lattice. This is especially important when simulating tritium behaviour, considering that it is formed inside the grain.

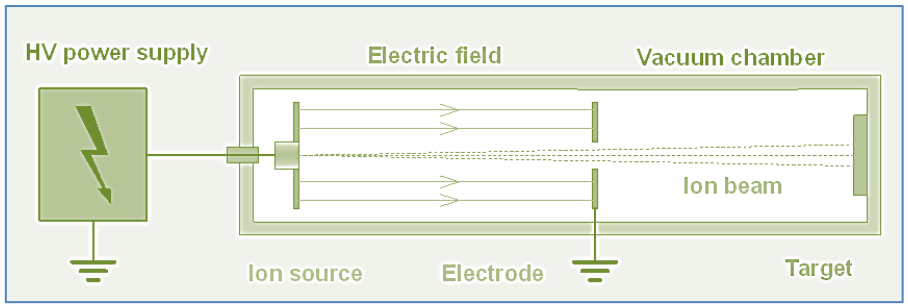

Figure 7.1: Schematic representation of an ion source system including the principal elements necessary for the implantation.

One of the important aspects of ionic implantation is that it is a doping method isotopically pure. It means that the implanter can discard the ions different to the one object of the study, through the application of a calibrated magnetic field (see Figure 7.1).

The basic physical principles can be summarized as:

$$\vec{F}_L = q \cdot (\vec{v} \times \vec{B} + \vec{E}) \quad (7.1),$$

$$\vec{F}_{MD} = \mu \cdot \frac{d\vec{B}}{dz} \quad (7.2),$$

$$\vec{F}_{ED} = d \cdot \frac{d\vec{E}}{dz} \quad (7.3),$$

where q is the electric charge, Ē is the electric and B the magnetic field, μ the magnetic dipole moment and *d* the electric dipole moment, F_L, F_{MD} and F_{ED} *are* the forces modifying the direction and the velocity of the projectile charge. In this way, ions with a different mass from the one of the selected element will describe curves with different angles and will end up hitting the walls of the chamber. It is thus possible to calculate the kinetic energy change for ions as:

$$\Delta W = \int_{r_1}^{r_2} \vec{F} \cdot d\vec{r} = q \int_{r_1}^{r_2} \vec{E} \cdot d\vec{r} \quad (7.4).$$

In general to implant charged particles, the acceleration by an electric field is necessary. The ion beam emerging from the accelerator contains a range of energies and species that have to be selected. This is done by magnets that filter the ions by momentum per unit charge. Then, by placing a series of viewers along the beam, it is possible to propagate an image of the aperture from which the ion source emits the beam. The final size of the beam on the target can be modified by a lens system. The quantity of ion beam on the target is carefully measured by the electrical current.

2.2. Ion Beam Analysis (IBA)

IBA provides several different techniques (see Figure 7.2) useful for the analysis of fusion materials [226,227], allowing the study of materials basic properties, the plasma–material interactions, the retention/release/permeation of hydrogen, the isotope exchange and the species sputtering. The techniques, based on the interaction among a charged particle and the atoms of the matrix to study, are able to characterize the materials in a compositional way, determining the elemental composition with the depth resolution, and in a structural way, determining the elements inside the lattice and the heterostructural stresses.

When an ion from an accelerator interacts with atoms of a solid matrix, energy is transferred to the solid causing a slowing down of the incoming beam. In its way through matter, the ion interacts with the atomic electrons and/or nuclei. The first interaction is purely Coulomb and will result in the *ionization* if the electron is ejected from its atomic orbit or an *atom excitation* if the electron is raised to an outer orbit [228]. An electron ejected is called a secondary electron. It may further ionize or excite another atom, resulting in the emission of more x-rays/photons. A

secondary electron may also be decelerated by the coulomb field of a nucleus, losing part or all its energy in form of bremsstrahlung (braking radiation).

In the case of an ion interacting with an atomic nucleus, it can result in a coulomb elastic scattering (with change of the direction and reduction in energy), a coulomb inelastic collision (decelerated the particle lost part or all of its energy in the form of bremsstrahlung), a coulomb excitation (with a consequent change of direction and reduction of energy), a nuclear inelastic scattering (as for coulomb excitation) or a nuclear transformation (where the particle is transmuted or absorbed). An excited nucleus will eventually return to its ground state accompanied by the emission of one or more γ rays. For ions with incident energy of few MeV, radiations emitted from nuclear reactions are usually protons, neutrons , α-particles and/or γ-rays [229].

The energy transferred via electronic excitations is quantified by the electronic stopping power that describes the energy loss per unit path length. The energy loss by interaction with the nuclei of the solid is consequently referred to as nuclear stopping and dominates at low velocities. For the fast ions used in ion beam analysis the electronic stopping power is dominant and can be seen as a friction force, gradually slowing down the particle. If the incoming ion and a nucleus of the sample collide, information about the sample can be obtained by analysing the mass and energy spectra of the resulting particles.

The importance of the various interaction processes depends on the ion velocity and on the charges of the ion and the target atoms. When the velocity of the ion (v) is significantly lower than the Bohr velocity of the atomic electrons (v_o), the ion tends to be neutralized by the target electron capture, thus elastic collisions with target nuclei dominates. When the ion velocity increases, the nuclear energy loss diminishes and the electronic energy loss becomes the main interaction. Being surrounded by an electron cloud, the nuclear stopping power is usually much smaller than the electronic stopping power, and can be ignored. The stopping power of a material depends on what charged particle is travelling through it, and the energy of that particle. Usually two major simplifications in stopping theory are made: (1) the ion is moving much faster than the target electrons and is fully stripped of its electrons; (2) the ion is much heavier than the target electrons.

The total energy loss is the sum of nuclear and electronic contributions. At velocities v >> v0, the energy loss is proportional to the square of ion charge and is given by the Bethe-Bloch formula:

$$\frac{dE}{dx} = NZ_2(Z_1e^2)^2 \, f\,(\frac{E}{M_1}) \qquad (7.6),$$

with $f(E/M_1)$ being a function depending on the target, Z_1 the particle atomic number, Z_2 the target atomic number, N the density of target atoms per unit volume, and *e* the electron charge. It describes the energy loss per distance travelled of particles traversing the matter and, as evident, it is Z dependent [230].

The principal techniques can be distinguished for the particle or radiation measured: Nuclear Reaction Analysis (NRA) measures prompt product particles, the Particle Induced Gamma Emission (PIGE) captures prompt gamma-rays, Particle Induced X-Ray Emission (PIXE) detects the characteristics X-rays, Elastic Recoil Detection (ERDA) recoils target nuclei and Rutherford Backscattering Scattering (RBS) the elastically scattered ions in backward angles (see Figure 7.2). Often two or more of these techniques can be used simultaneously in order to obtain complementary information. The development of detectors, their position and their properties represent one of the most important parts of the analysis system.

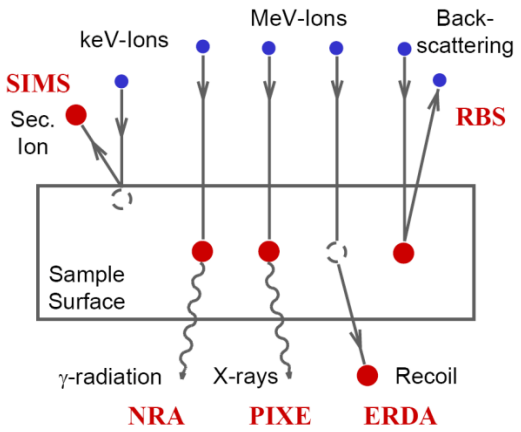

Figure 7.2: Interaction of ion beams with matter. IBA techniques are indicated and related to the kind of particle impinging and the one to be detected.

The advantage of ion beam analytical methods is the non-destructiveness, the straightforward and the quantitative interpretation of the experimental results. The high accuracy of the techniques is mainly due to the precision with which cross-sections of the involved atomic and nuclear processes are known. The Nuclear Reaction Analysis (NRA) is the most effective method in the field of light ion detection compared with other representative nondestructive analysis with ion beam, such as RBS (Rutherford backscattering) and the elastic recoil method

(ERDA). Several authors [229,231,232] emphasized the sensitivity of Nuclear Reaction Analysis (NRA) for its depth resolution: a very sensitive, quantitative and non-destructive method in the field of light elements detection. The sensitivity of this analysis is due to the large nuclear reaction cross sections for lower energies than light elements posses [233].

2.3. Nuclear Reaction Analysis

Remembering the challenges in measuring light ions profiles in material composites, one method which overcome these difficulties is the Nuclear Reaction Analysis (NRA), a specific and sensitive method with a sufficient analysis depth resolution. When the target nuclear structure is reached with high-energy ions, the interaction may become inelastic (changes in mass in the reaction) and nuclear reactions may occur. This is the principle for nuclear reaction analysis.

NRA is an analytical method that investigates products collected by a detector as a result of a nuclear reaction within the incoming ion and the target nuclei (see Figure 7.3). This means that different nuclear reactions have to be used depending on the elements investigated. The yield of the peaks in the spectrum can be used to determine the density of distinct particles within the target sample. The width of the peaks provides information on the depth of the target sample.

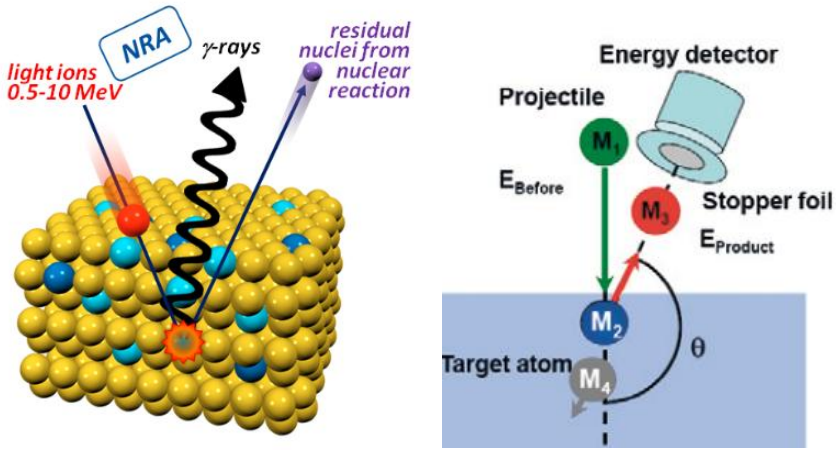

Figure 7.3: Nuclear reaction occurring between light ions and matter. The emission of γ-rays and residual nuclei is indicated. On the right the principal sketch of a NRA measurement.

Considering that the cross sections of nuclear reactions vary rather irregularly when light ion beams of only few MeV are used, nuclear reaction cross sections result better enough for the analysis of only low- and medium-Z elements.

There are two ways for NR analysis: prompt radiation and delayed analysis. When using the prompt radiation analysis method, the radiation given off instantaneously from each reaction is measured. The detected particles in this method are the smaller products of nuclear reaction, usually protons or alpha particles. With the delayed analysis, the detector makes measurements with a delayed time from irradiation. It measures the particles emitted from the decay of nuclei that the impinging ion beam made unstable. These are beta particles or gamma rays. Another important difference resides in the geometry in NRA, which can be backward or forward and the filtering of the detector. In the present work the absorber foil technique and the coincidence technique are used.

The incident particles strike the material to be studied and lose their energy while penetrating. This stopping process is mainly due to the interaction of the beam with the atomic electron shells (electronic stopping power). In a certain depth, the incoming particle can undergo a nuclear reaction with target atoms leading to products with different kinetic energies. If the kinetic energies of these particles are sufficiently high, they will be recoiled out of the sample with different energies depending on the depth from which they were emitted. The energy of the reaction product is a function of the energy of the incoming ions. By simple detection of the particles emitted from nuclear reaction, it is possible to obtain concentration vs. depth distributions for certain target chemical elements in a solid thin film.

It is worth mentioning that nuclear reactions can generate fair amount of neutrons. Deuteron-induced nuclear reactions in Li-based materials are more hazardous than those by usual H or He beam and the number of generated neutrons increase exponentially with the deuteron energy. Therefore the presence of really strict legal procedure, essential for this kind of measurements, has impeded the experimental analysis by NRA of lithium based ceramics in a Spanish installation. Thanks to the support of two different projects, the experiments were performed in different European facilities (KUL-Leuven and CEMTHI-Orleans), which fulfil all the radiation safety requirements. The Deuterium-profiling experiments were performed in the frame of SPIRIT-project, representing an Integrated Infrastructure Initiative (I3) funded by the European Commission whose main goal is to grant public and industrial researchers from Europe for free access to leading European ion beam facilities. In the case of ^{3}He experiments, CNRS and CEA, in

agreement with the French Ministry of Higher Education and Research, have set up a national network (EMIR) of accelerators dedicated to material irradiation, providing a free access to their irradiation facilities.

3. D-depth profiling experiments in as-implanted and annealed ceramic breeders

In an attempt to better understand tritium transport in fusion breeding blankets during operation, this part of the work has studied the hydrogenic ion (D) thermal ion behaviour with the help of a comparable H isotope as a trace.

Deuterium is implanted in the selected ceramics and its depth profile characterized by NRA before, during and after thermal annealing treatments. A set of porous lithium ceramics with different chemical compositions (MTi, Li4 and Li6) and microstructures (porosities and grain sizes) are selected and implanted with a D^+ constant concentration. Since the operational temperature of a solid breeding material has been estimated to be in the range 300°C - 900°C [65], the D profiles are studied as a function of temperature by Resonance Nuclear Reaction Analysis (RNRA), using the following nuclear reaction[234]:

$$^2H + ^3He \rightarrow ^1H + ^4He \quad \equiv \quad D\,(^3He, p)\,^4He \quad (7.7)$$

till the total D outgas. Considering fusion interests towards the development of solid breeders with the highest possible lithium contents, the D thermal diffusion is discussed comparatively in terms of material composition and microstructure. In the second part, a detailed study on deuterium transportation under thermal variation and a first approach to the effects of ceramic irradiation are presented. Therefore D^+- implanted samples of a selected compound (MTi) were previously damaged by γ-rays and Ti^{4+} ions and the deuterium thermal profile compared.

The reaction of ^3He ion with deuterium (see equation 7.7) gives rise to a proton and a ^4He particle. The total cross section of this interaction (in Figure 7.4) shows a broad resonance with a maximum around 0.64 MeV. By using higher beam energies the deuterium content can be probed at higher depths, thus the incident ^3He energies close to 0.63 MeV (the maximum of the reaction cross-section) and up to 1.5 MeV are used to probe depth up to several microns. At ^3He energies below 1 MeV the differential cross-section is almost angle independent in the centre-of-mass system, while at higher energies the angle dependence has to be taken into account [234].

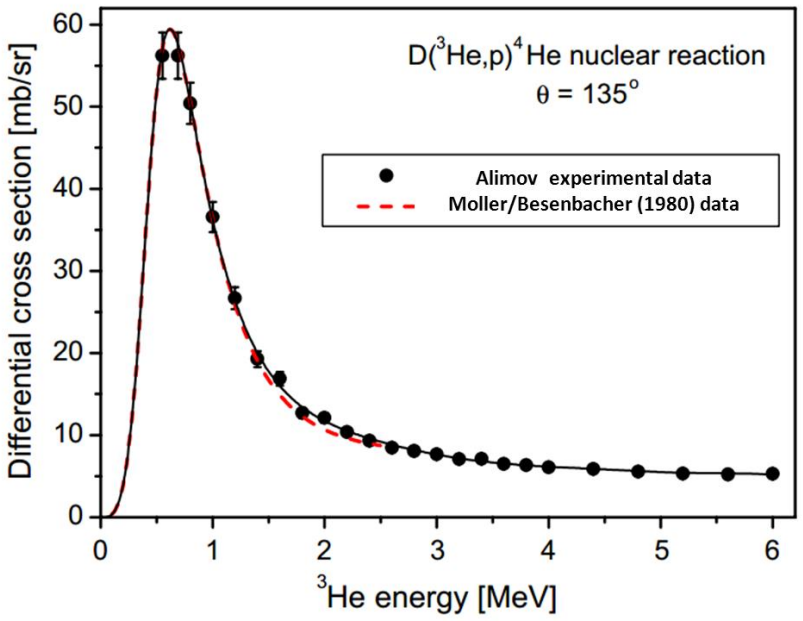

Figure 7.4: Differential cross-section of the D (^{3}He,p)^{4}He nuclear reaction at detector angle of 135°. Dots: experimental data from Alimov work [234]. Dashed line: differential cross-section from the fit function of Moller and Besenbacher [235] to the total cross-section, assuming angle independence in the centre-of-mass system.

This resonance structure can be applied to measure deuterium depth profiles to larger depths by means of the resonance method, in which the proton yield is determined as a function of the incident energy [236,237]. The total number of detected protons $Y_P(E_0)$ generated by the nuclear reaction, is given by:

$$Y_P(E_0) = \frac{Q_{He}}{\cos\alpha} \int_{\Omega_L \text{ det}} \int_0^x C_D(x) \frac{d\sigma_L(E(E_0,x)}{d\Omega_L} d\Omega_L^{\text{det}} dx \quad (7.8),$$

Where E_0 is the incident ^{3}He energy, $d\Omega_L(E)/d\Omega_L$ the differential cross section at a determined angle θ_L and ^{3}He energy, $C_D(x)$ the deuterium concentration in depth x, Q^3_{He} the analysing beam dose on the target, α the angle between the analysing beam and the surface and $\Omega^{\text{det}}_{\ L}$ the solid angle of the detector. Increasing the incident beam energy, the maximum of the differential cross-section curve is shifted to larger depths according to the energy loss of the ^{3}He ions in the material.

3.1. Experimental details

Li4 and Li6 ceramics were synthesized following the rotary evaporator route as

described in Chapter 5, while the MTi is fabricated starting from commercial 99% purity Alfa Aesar powders. The sintering conditions and the crystalline phases achieved for the three ceramics are indicated in Table 7.1.

Table 7.1: Sintering condition and main phases for the studied samples.

Compositions	**MTi**	**Li4**	**Li6**
Sintering temperature/dwell time (°C/h)	1150/2	950/2	1000/2
Present phases	(100%) Li_2TiO_3	(47.8%) Li_2SiO_3, (23.4%) Li_4SiO_4, (3%) SiO_2	(59.4%) Li_4SiO_4, (38.8%) Li_2SiO_3 and (1.8%) SiO_2
Experimental density (g/cc)	2.7	1.6	1.41

The above described sintered ceramic bodies were used as targets for the deuterium implantation. The ionic implantation was performed in the "Centro de Asistencia a la Investigación" (CAI) of Universidad Complutense de Madrid (UCM). The implanter used is a VARIAN CF3000 with a minimum energy of 200 keV, a voltage of 32 keV and a mobile sample holder. Roughly polished and previously characterized pellets were room temperature implanted at energy of 100 keV using the D_2^+ beam to a total fluence of about $3x10^{17}$ cm^{-2}. Using the experimental densities, the maximum depths for the implanted ions were calculated by the SRIM Monte Carlo code [238] to be 0.96 µm for MTi, 1.32 µm for Li4 and 1.1 µm for Li6. After implantation samples were stored for three days under environmental conditions (about 30% of relative humidity in autumn months in Madrid, Spain) before D depth profiling analysis (see a scheme of the measurements in the upper part of figure 7.5).

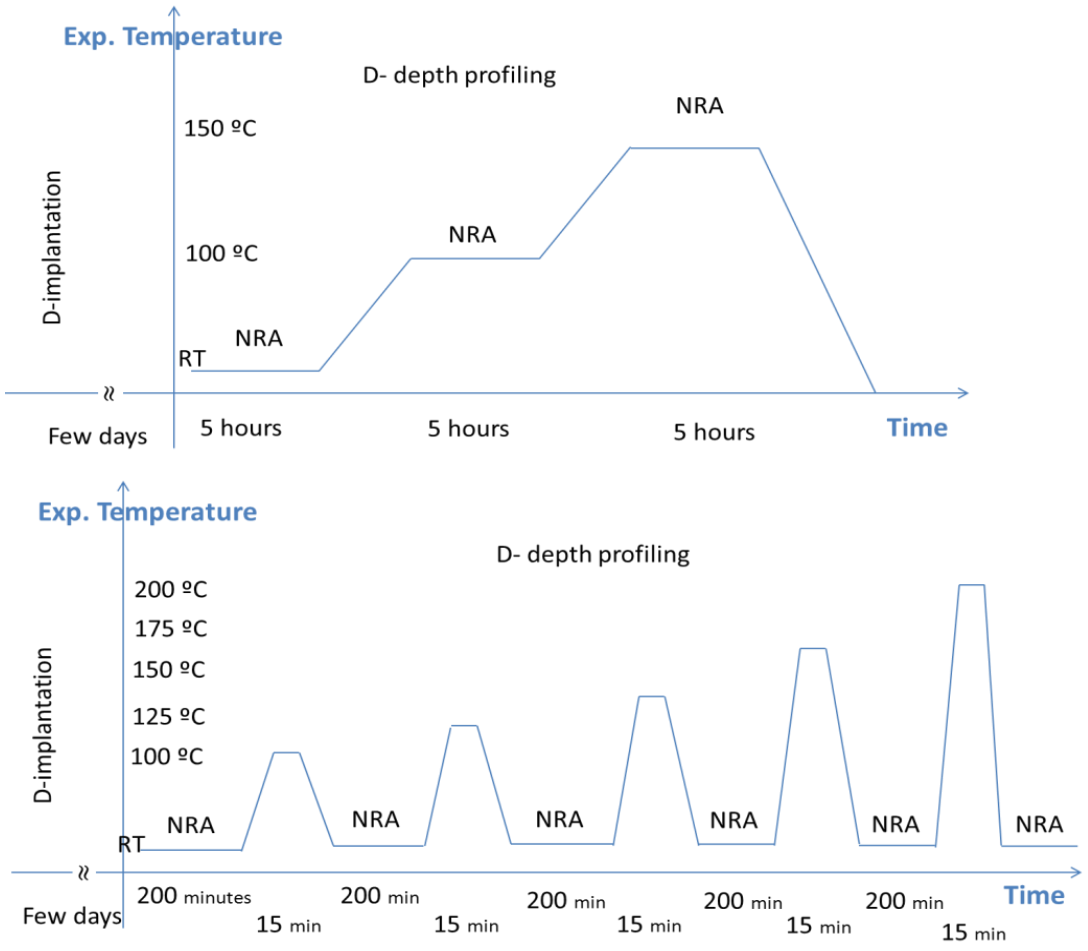

Figure 7.5: Experimental scheme of the two set of measurements carried on D-implanted samples for the characterization of their depth profile. In the upper part the first set where NRA profiles are calculated during thermal treatments, in the bottom one of the experiments of the second set, where NRA measurements are taken after the thermal treatment.

In a second set of measurements only MTi compound was selected for the experiments. Firstly the samples were γ - irradiated by a ^{60}Co source in the Nayade-pool facility at 6 Gy/sec to a total dose of 7.3 MGy. After that some samples were implanted in CAI-UCM facility with a 150 keV Ti^{4+} beam to a fluence of 10^{15} ions/cm^2 corresponding to an implantation depth of 500 nm. Deuterium was then implanted in the same facility with a 70 keV beam, to a total fluence of 10^{17} at/cm^2 into a depth of 750 nm (for SRIM calculations).

The D depth profiles were characterised by means of Resonance Nuclear Reaction Analysis (RNRA) at the Nuclear and Radiation Physics Department, KUL-Leuven, tandem accelerator facility by using the D (^{3}He, p) ^{4}He nuclear reaction.

Measurements were carried out with a ^{3}He ion beam impinging the sample surface at normal incidence. This reaction presents a broad resonant peak at 0.63 MeV; therefore the beam energy is varied in the range from 0.64 to 1.5 MeV in order to cover the whole projected range. Protons were detected by a glancing PIPS (Passivated Implanted Planar Silicon) Canberra detector with an active area of 50 mm^2 located at 142° from the beam direction. A 13 µm Mylar foil was placed in front of the detector in order to stop other light elements (i.e. α particles) arising from the nuclear reaction.

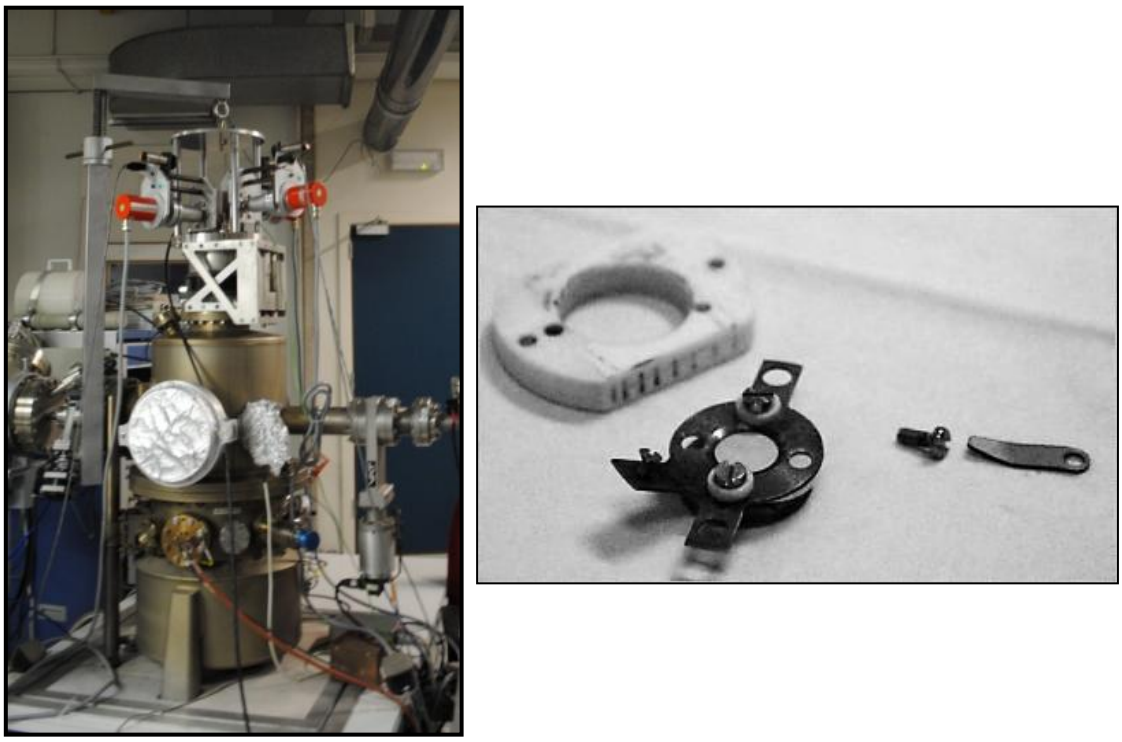

Figure 7.6: Experimental chamber (left) and sample-holder (right) for NRA experiments, mounted on a base for a homogeneous heat transfer during thermal treatments.

The total accumulated dose for each spectrum was 5 µC. The beam spot and the current were selected to be 1 mm^2 and ~ 10 nA, respectively, with a fluence of $3x10^{17}$ cm^{-2}. Previous tests were performed to assure reliable depth profiling measurements. D depth profiles were registered during heating, at increasing temperatures (27 °C, 100°C, 150°C and 200°C). Temperature was measured and controlled using a K-type thermocouple fixed to the furnace located at the back of the sample-holder, an experimental set-up designed at the KUL laboratories (see Figure 7.6). This configuration allows *in-situ* measuring the spectra of nuclear reactions, while the annealing treatments are carried out. The time for each NRA

measurement at the selected energy is of about 20 minutes, being 15 the total points for each curve.

Deuterium concentration as a function of depth was determined by comparing measured and simulated RNRA spectra. For simulations of any ion-target combination geometry and the presence of foils in front of the detector, the commercial computer code SIMNRA (a Microsoft Windows program) was used [239]. The selected cross section for the calculations is that reported by Alimov et al. [234] whose measurements were performed at a scattering angle of 135°. In this experiment, the angle is set at 142°, because according to Möller et al. [235] within ^{3}He energy range 0.64 - 1.2 MeV the nuclear reaction is almost angle independent. A tailor-made program implemented in the Nuclear and Radiation Physics Department at the KUL- centre was used to calculate the recorded proton yield.

3.2. Results and discussion

3.2.1. Microstructural features

Pointing their final application as fusion breeder blankets, the sintering conditions used for the fabricated ceramic bodies were established to achieve porous ceramics with stable crystalline structures. Crystalline phases, experimental densities, open porosity and pore size distributions are here recalled in order to properly discuss D transport processes.

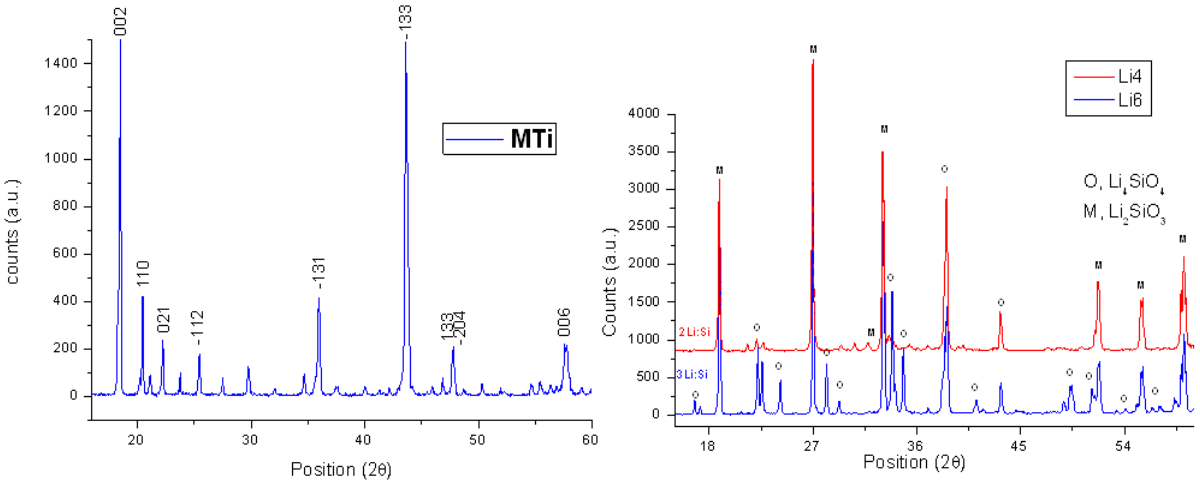

Figure 7.7: X-ray diffraction patterns for the titanate (left) and the silicates (Li4 and Li6)

(right) of as-sintered ceramic samples. In the Silica-based samples the peaks of the two main phases are identified as O (Orthosilicate) and M (Metasilicate).

As determined by XRD analysis (see Figure 7.7), MTi presents the metatitanate as a unique phase (MTi: Li_2TiO_3) with high crystallinity. For the Li4 ceramic, Li_2SiO_3 (MSi) and Li_4SiO_4 (OSi) crystallographic phases are observed to co-exist with a mixture of SiO_2 and Li_2CO_3 phases (reaction precursors). In the case of the Li6 ceramic, Li_4SiO_4 and Li_2SiO_3 phases are detected, as discussed in Chapter 5. The effect of Li excess seems to be the explanation for the precipitation of the new orthosilicate phase in higher proportions.

The pore size distribution for the three sintered materials was estimated by using the mercury intrusion method and corresponds to the microstructures shown on Figure 7.8. Since the bulk sample volume is an experimental data obtained from porosimetry, the experimental density and porosity values could be calculated with high accuracy (see Table 7.2). The porosity distribution curves as a function of the apparent size of the accessed pores under increasing Hg pressure [240] were obtained and compared in Figure 7.8.

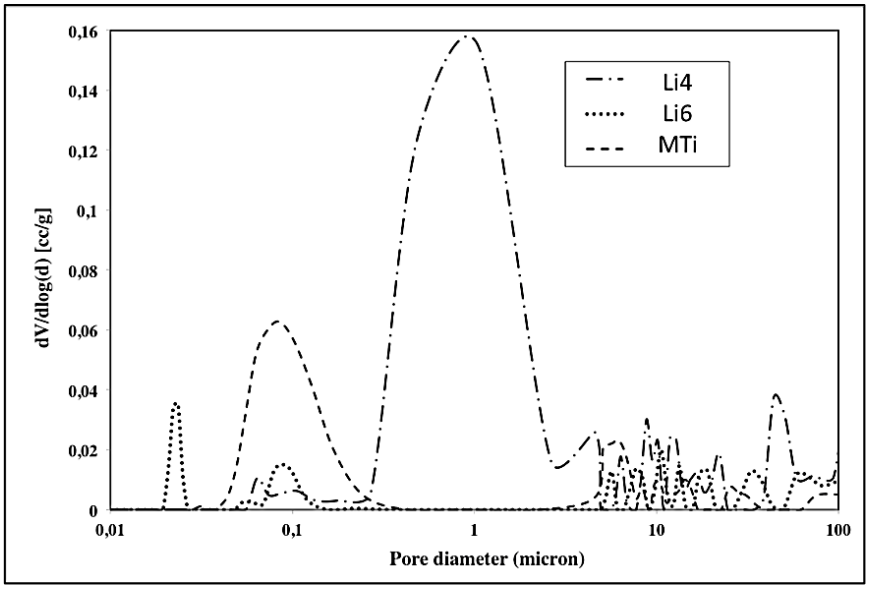

Figure 7.8: Comparative pore distribution curves experimentally obtained for the three studied lithium ceramics by using Hg inclusion porosimetry.

A wide range of open-pore diameters is identified for the samples after sintering (see Table 7.2). All compositions show narrow pore distributions where the majority

of pores have diameters below the micron size. The Li6 composition shows a distribution curve where two more frequent pore diameters of nanometer size are detected. The presence of a narrower pore size distribution of smaller pore diameter is the explanation for a better-densified material.

Table 7.2: Main microstructure characteristics of the ceramic specimens.

Material	MTi	Li4	Li6
D_{exp}: experimental density (gr/cc)	2.7	1.6	2.05
Density (% T.D.)	78	73	94.5
Porosity (%)	22	27	5.5
Main open pore diameters (µm)	0.08	0.9	0.1 & 0.025
Grain size (µm)	3	2	0.15 & 6 (bimodal)

Sample morphology was studied by scanning electron microscopy (SEM). When comparing SEM images of the as-sintered polished surfaces (polishing procedure described in Chapter 5, section 6.d) morphological differences is appreciated between the samples (Figure 7.9). Mean grain sizes are estimated to be about 1.5 and 2 µm for the MTi and the Li4 ceramics, respectively. The observed microstructures are in agreement with those reported in the literature for similar sintering conditions [35], [36].

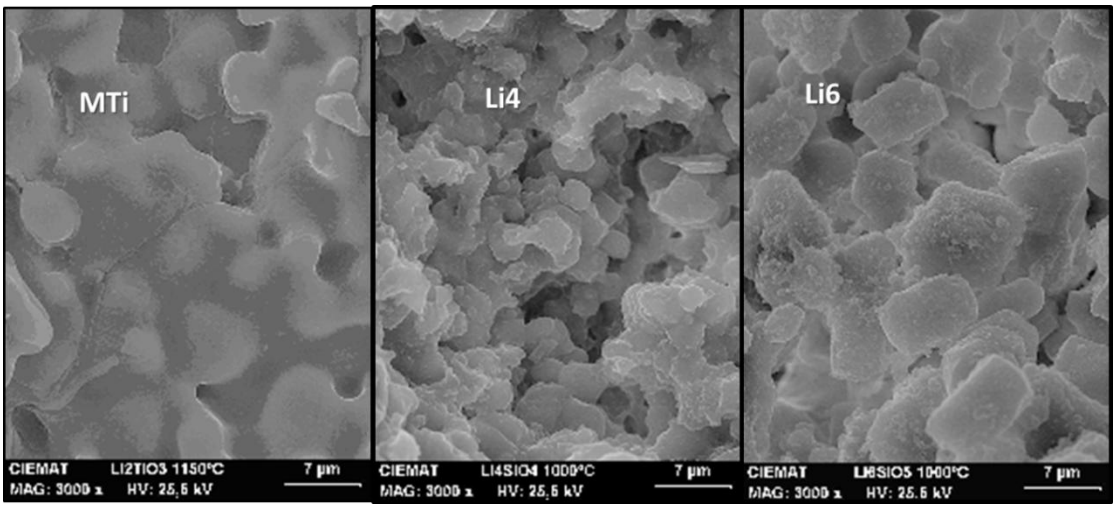

Figure 7.9: SEM micrographs of the polished and thermally etched surfaces of Li-based ceramic pellets (left-MTi; center-Li4; right-Li6). See table II for the calculated mean grain sizes.

On the other hand, a bimodal grain size distribution is observed for the Li6 sample, where grains with an average grain size of 0.15 μm are shown decorating the 6 μm sized grains. Following Knitter suggestions [34,142] it is assumed that smaller grains correspond to the Li_2SiO_3 phase, located at pores and grain boundaries of the bigger grains of Li_4SiO_4 phase. As expected from the phase diagram [55], the explanation of a higher amount of orthosilicate phase in the Li6 composition can be found in the excess of lithium carbonate as reactant and due to the slightly superior temperature during sintering. The crystallization of the Li_2SiO_3 phase in the Li6 composition in submicron grains may be explained by the sintering temperature, since the grain size is still reported to be very small (2 - 3 μm) for sintering temperatures of 1020°C [241,242]. As a consequence the very high density (94.5% D_{th}) in case of Li6 composition is also better described by the presence of these very small particles. As is here experimentally observed, the existence of so-small sized grains allows a better packing resulting in a sintered matrix with reduced porosity. The existence of nanograins accompanying the main crystalline structure is then a definitive method to reduce porosity.

For Tritium recovery purposes, ceramic breeders having the 85-90% of true density and open porosity are required. Moreover, a uniform small grain size distribution (having diameters smaller than 10 μm) should be achievable since the activation energy for grains diffusion is higher compared to that along grain boundaries [71]. After sintering, all samples here studied exhibit the interconnected porous network expected for breeder applications. Therefore the achieved microstructures as fitting these fusion breeder requirements could be considered optima for the easy transport of the implanted ion.

3.2.2. Deuterium analytical determination by NRA

Implanted deuterium depth-profiles were characterized by means of Resonant-NRA analytical technique. It is worthwhile mentioning that in order to determine D concentration in a reliable way, background spectra were measured deep into the sample (corresponding approximately to 1.5 MeV ~ 3.27 μm) where no implanted D was expected to be.

Protons in the MeV range can also arise from nuclear reactions between the ^3He analytical beam and Li, Si and O atoms in the target, contributing and increasing the measured proton counting rate. Therefore the proton yield measured at depths higher than 4 micron was subtracted from the total proton yields measured for the

deuterium concentration in the implanted zone.

After background subtraction, the deuterium concentration curves as a function of depth and temperature calculated by SIMNRA are shown in Figure 7.10 where the dot line represents the expected SRIM maxima at Room Temperature for the material at the implantation ion energy. Clear differences between the measured and the simulated implantation maxima are observed. These differences might be mainly due to both the deuterium diffusion taking place at room temperature and the presence of residual D in the chamber. The chemical reactivity of Deuterium with the structure has to be also taken into account to understand the different profile shape between the simulated and the measured one.

The Nuclear Reaction Analysis was carried out during the annealing, once stability in temperature was reached. At room temperature (see Figure 7.10), D concentration is significantly higher in the surface region than deeper into the samples, which indicates the influence of surface on D retention for all the samples. The deuterium retention in Li6 is quite lower than the other two ceramics even at RT. From depth profiles, the RNRA measured total amount of deuterium in as-implanted samples is almost the same of the estimated from the implantation fluence. It indicates that, even when D diffusion is observed to occur at RT, D does not significantly release from the samples when storing them three days under environmental conditions. The storing process was necessary, considering that the implantation was made in Madrid (CAI-UCM) and the NRA characterization in KUL-Leuven laboratories (see Figure 7.5).

It must be stressed that thermal annealing as low as 100°C promotes D release, being its outgas more evident in the case of MTi, which presents higher initial D concentration. For annealing temperatures ≥ 150°C, the D atomic percentage detected in the material is negligible, indicating that at these temperatures the light ion is completely outgassed.

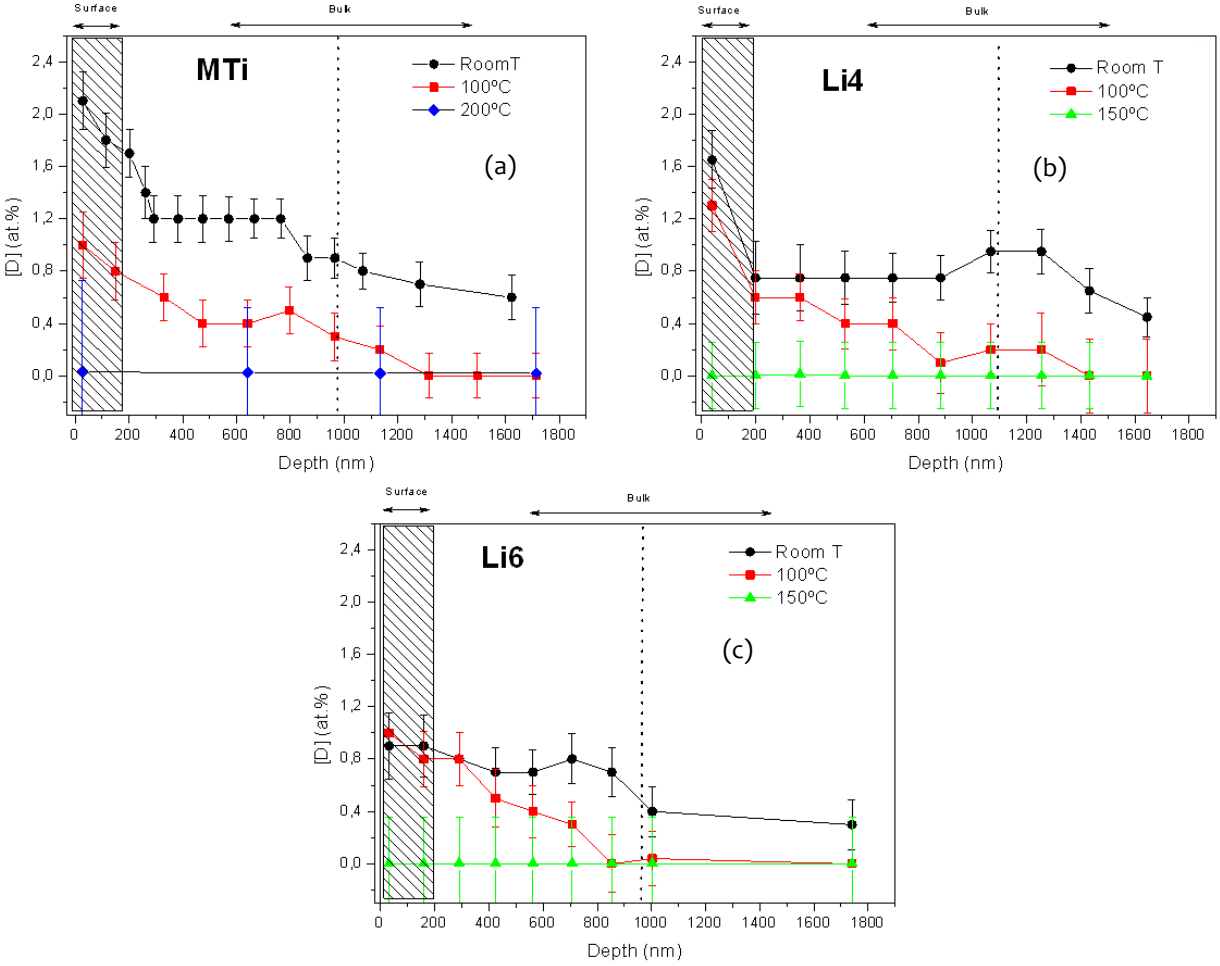

Figure 7.10: Atomic deuterium concentration depth-profiles of MTi (a), Li4 (b) and Li6 (c) samples at different temperatures. The dot line represents the expected SRIM maxima at room temperature for the materials at the implantation ion energy.

In order to have a clearer picture, the D concentration as a function of depth is evaluated into the whole samples as two separate regions: the surface and the bulk. The different D distributions, calculated as the mean value of the atomic deuterium concentration for depths below 200 nm (surface region) and from 200 nm to 1700 nm (bulk region), are shown in Figure 7.11.

A different D behavior is here clearly observed when annealing the titanate and the silicates ceramics. Annealing reduces the initial D-concentration at all depths for the titanate sample. However for the silicates, heating process decreases the D concentration in the bulk whereas it remains almost unchanged at the surface.

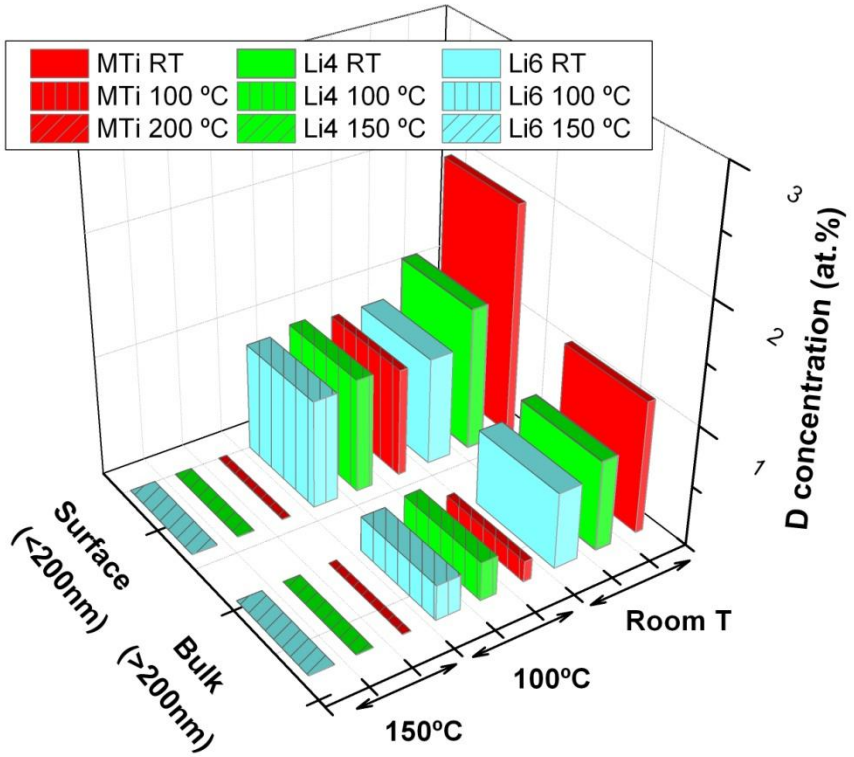

Figure 7.11: Distribution of D concentration along sample depth calculated from the NRA analysis at several temperatures in the three breeder blanket candidate materials studied. Data are calculated from the mean values found in the two regions: surface (<200 nm) and bulk (>200nm).

At room temperature, the largest D concentration is measured (see Fig. 7.11) at surface for the MTi ceramic (2.1 ± 0.2 at %) whereas significantly lower D concentrations are measured for the lithium-rich compounds (1.6 ± 0.2 at % for the Li4 and 1.0 ± 0.2 at % for the Li6). Such difference in the D concentration at surface between titanate and silicate samples is almost negligible after annealing. These results suggest that ceramics microstructure and/or chemical composition are playing an important role in the temperature-driven D transport, in close agreement with the literature [71,76,215,243] that reports a strong dependence of hydrogen isotopes behaviour from materials composition or microstructure.

From the above results it must be stressed that materials having very different microstructural characteristics but similar chemical composition show comparable elemental distributions in depth and at increasing temperatures. In particular the Li6 sample, having so low remaining porosity (just 5.5% of porosity compared to that of the other two less densified materials, see Table 7.2), still allows the implanted D to be easily released. Since this sample shows smaller grains in the sub-μm range

and therefore a larger density of grain boundaries than those with higher porosity (Li4, MTi), it suggests that grain boundaries might play a similar role than porous for D diffusion. These results agree with those previously reported by Federici et al. [71] and by Bertone et al. [244] who model the T transport in lithium ceramics by assuming a rather favourable and rate controlling grain boundary diffusion.

After this first approach to the deuterium behavior under thermal treatments, a second set of experiments was carried out. The objective was to assess the temperature and time dependence of the ion diffusion in a solid breeder blanket in order to obtain reliable activation energy of the diffusion process. Considering the time consuming measurements, only one material was selected. Due to the highest D-concentration observed at room temperature, the high crystallinity of its unique phase and the less complex microstructure, MTi ceramic was chosen. To check the temperature role, this set of measurements was effectuated at room temperature after each heating process, which generally presented a raising time of 3-4 minutes, an annealing time of approximately 20 minutes and a cooling time of 2 hours.

The samples were implanted at 10^{17} D^+/cm^2 with a 70 keV beam (the projected range of the implanted D ions was calculated by the SRIM code to be around 750 nm) at room temperature. To study the temperature and the time dependence of D behavior, samples were annealed in vacuum up to 200°C inside the NRA chamber with annealing times varying from 15 to 60 minutes. In all the cases, NRA spectra were registered after the indicated annealing treatment, at Room Temperature.

The study of the Deuterium release under time variation of annealing treatments at 100 °C is presented in Figure 7.12. In the three first cases (thermal treatments at room temperature, after a 100 °C during 15 min and after a 100 °C during 30 minutes), the depth profile curves show quite the same trend. After the annealing at 100°C during 60 minutes, the NR analysis evidences the lower D concentration (in at.%) to a 500 nm depth, with a quite constant gas diffusion of the gas at higher depths. Considering the time consuming experiments and the similarity in results found for the first two annealing times, the following measurements were performed after thermal treatments at 15 or 30 minutes of annealing times (Figure 7.13 and Figure 7.14 respectively).

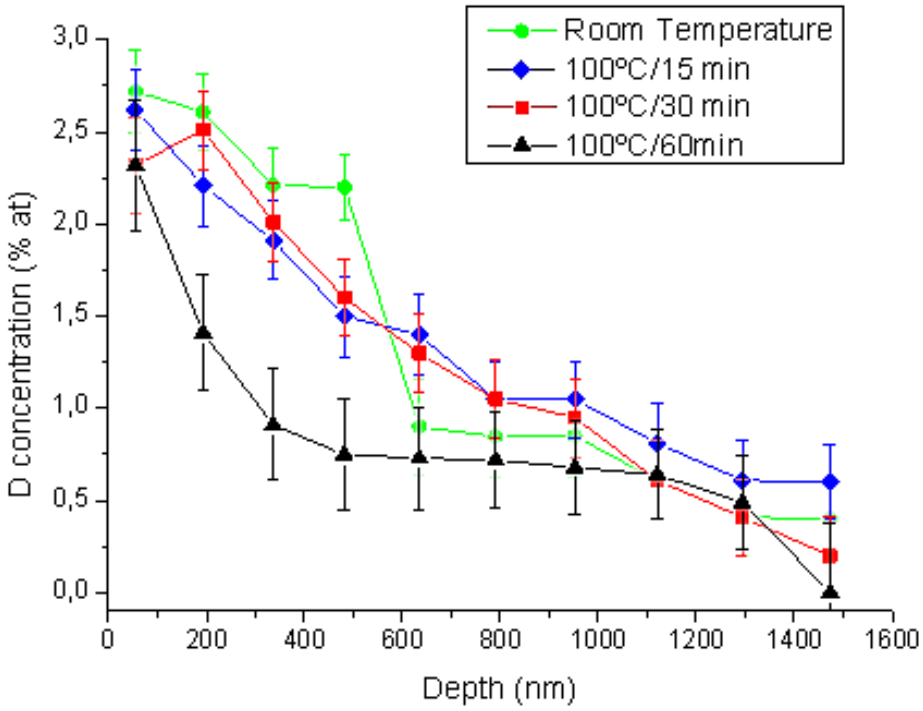

Figure 7.12: Deuterium concentration (in at. %) after thermal treatments at 100 °C during different annealing times.

In Figure 7.13 the deuterium concentration after annealing treatments of 15 minutes at different temperatures are presented. The effect of the surface as a barrier for D outgas in the first 200 nm, as observed in the previous experiments and in the literature [76,177] is observed after all the heating temperatures of the next set of measurements. At 125 °C it is possible to find the activation of different processes in the release of deuterium from the surface to 600 nm and from 700 to 1500 nm. The slope of D concentration (at. %) change after 100 °C, when the release process became faster. The confirmation of an almost complete release at 200 °C is found [177]. In Figure 7.14 the calculation of the activation energy calculated from the Arrhenius plot of the ion concentration in function of the temperature. A small difference between the activation processes for deuterium release is found between the surface and the implanted zone (about 750 nm).

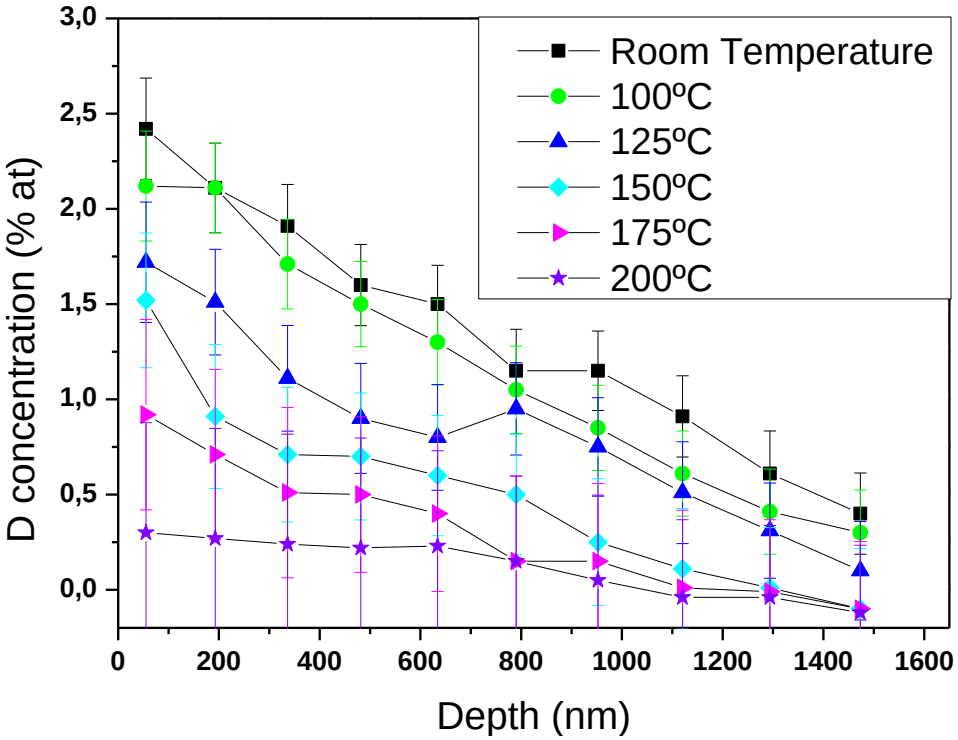

Figure 7.13: Deuterium concentration (in at. %) after annealing treatments of 15 minutes at different temperatures.

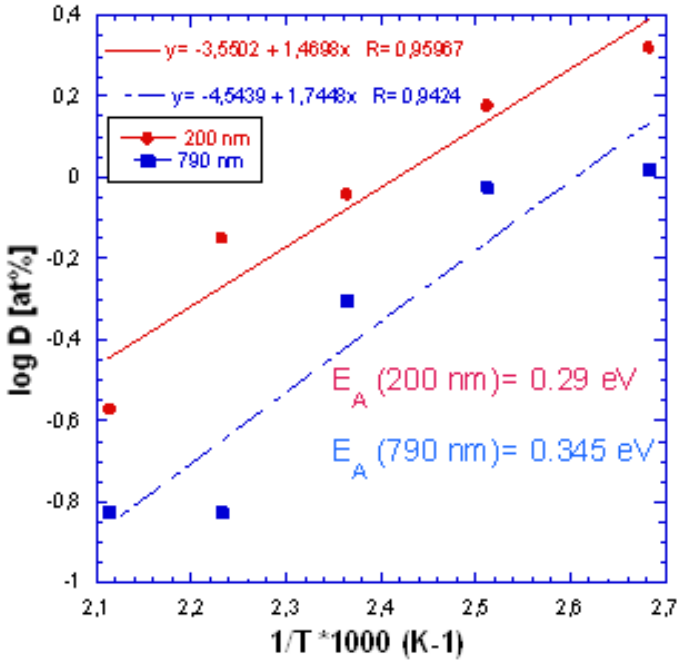

Figure 7.14: The Arrhenius plot of the deuterium atomic concentration as a function of the inverse of temperature for the calculation of the activation energy for deuterium diffusion. The superficial (red points) and bulk values (blue square) are calculated.

3.2.1.1. D-behaviour in damaged ceramics

With the aim of a better understanding of the release behavior in light ions under operational conditions, the diffusion profiles in damaged ceramics are studied. The same MTi sample batch used for temperature-induced diffusion experiments is previously irradiated by γ-ray to a total dose of 7.5 MGy and afterwards implanted by heavy-ion (Ti^{4+}). The idea is to induce bulk ionizing damage and atomic displacement to a depth of about 500 nm, just before the D-implanted zone (at 750 nm).

The D-depth profiles of the sample with both damages and only with the atomic one are shown in Figure 7.15 where the curves of the as-prepared ceramic after a thermal annealing at 100 °C / 30 min is shown for comparison.

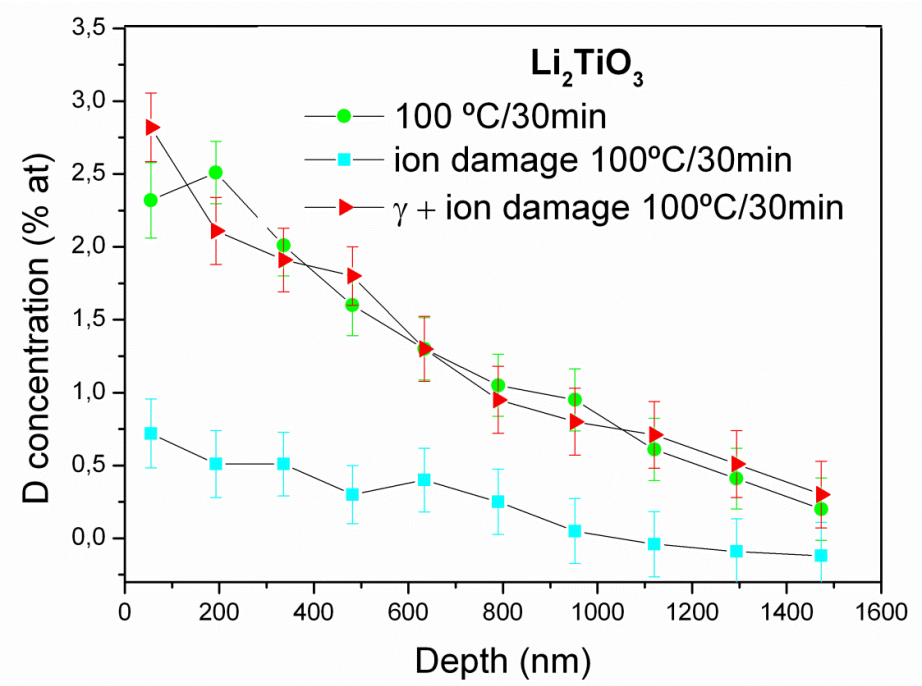

Figure7.15: NRA depth profiles evolution at 100 °C/30 min in Li_2TiO_3 ceramics under different conditions: as prepared (dot), ion-damaged (square) and ion-damaged after γ-irradiation (triangle).

The release behavior after a 100 °C/ 30 min heating is quite similar to the one find in the previous experiment, where NR analysis has been measured during the thermal treatment of 15 minutes. Thus a good reproducibility can be confirmed.

In the case of the sample previously damaged by heavy-ion implantation, a drastic decrease in deuterium concentration after thermal annealing at 100 °C is

found. It means a high release rate and a quite complete outgas of the implanted light ion. The thermal activation energy for diffusion as a function of temperature drops with heavy-ion degradation. From SRIM calculation (see Figure 7.16) it is possible to predict that Ti-implantation mainly generate O vacancies. These vacancies permit a rapid D release.

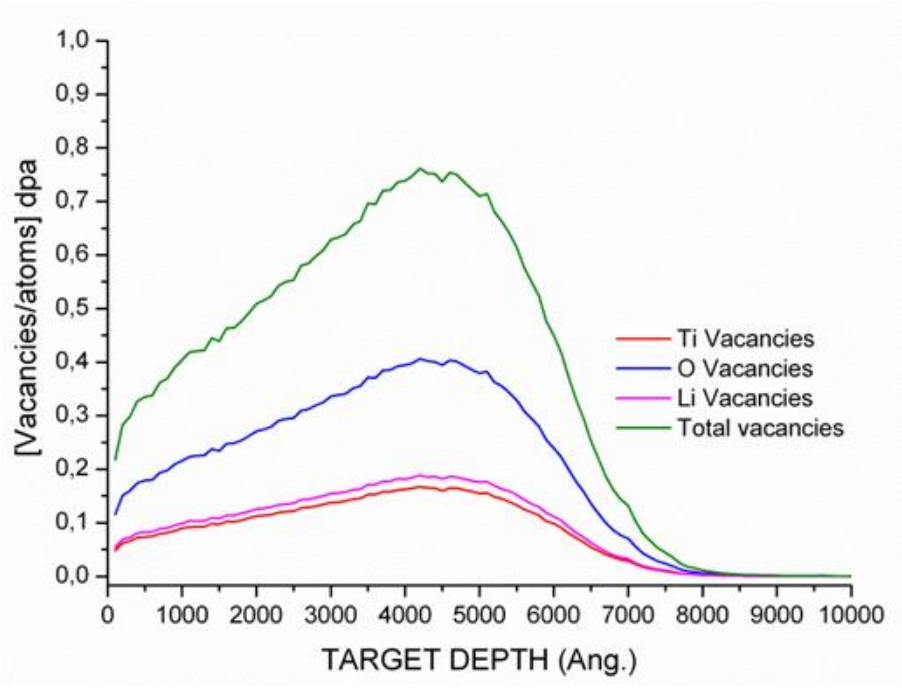

Figure 7.16: SRIM calculation of the vacancies created by Ti implantation in MTi ceramic.

The formation of Oxygen vacancies (of F^+ or F^0 type) after ion implantation is reported in literature [48]. The production mechanism of radiation defects by ion beam implantation can be described by the following reaction scheme:

(1) $Li_2TiO_3 \rightarrow Li_2TiO_3^*$ describes the production of excited MTi by ion beam irradiation.

(2) The equation $Li_2TiO_3^* \rightarrow (F^+ \cdot O^-) + h\nu$, shows the creation of a F^+ center, associated to an O^- interstitial under Coulomb interaction.

(3) The equations $2Li_2TiO_3^* \rightarrow 2F^+ + O_2 + 2h\nu'$ and $(F^+ \cdot O^-) + Li_2TiO_3^* \rightarrow 2F^0 + O_2 + 2h\nu'$ describe the formation of F^0 centers, generally observed at high temperature, after thermal activation.

The sample which has been gamma damaged prior to Ti^{4+} and D implantation, presents a deuterium concentration and behavior inside the ceramic bulk really similar to the one of the no-damaged material. As reported in literature [186], light ion release can be associated to the annihilation of defects. An electrical

modification like the one created by γ-irradiation could facilitate the trapping of electrons and the annihilation of the defects created by ion implantation. The result is that when only heavy-ion damage is present, the Deuterium release is easier and faster than when also γ effect is present.

Some complementary techniques are also used to understand the changes caused by the two kind of damage created in these last measurements. Thus a more complete discussion on radiation effects in light ion behavior will be provided in section 5 of this Chapter.

3.2.2.2. Structural characterization after experiments

The defects generated by irradiation and D-implantation are studied by **photoluminescence** technique. The measurements are carried out through a LabRAMAramis (Jobin-Yvon) confocal microscopy luminescence set-up equipped with an internal laser He-Ne, 633 nm at 2.0 eV and two external lasers (He-Cd and Argon lasers). The measurements are performed exciting at 633 nm with a grating of 150 lines/mm and an objective (x10) working with a diameter of 40 µm.

The photoluminescence emission spectra of the as prepared, gamma irradiated, and D-implanted samples normalized at 700 nm are shown in Figure 7.17. A change in the electronic state of the luminescent centres is indicated by a relative enhancement in the intensity of the 730-770 nm bands upon irradiation with deuterium (probably related to the loss of oxygen from the implanted/irradiated zone). Similarly when the breeder ceramic is irradiated by γ-rays its electrical configuration change, resulting in a relative decrease of photoluminescence peaks in the same wavelength range.

Regarding the combined effect of gamma ray plus ion implantation, it is possible to suppose that ionizing radiation modifies the charge of intrinsic defects, thus inverting the active centers, restoring the starting structure.

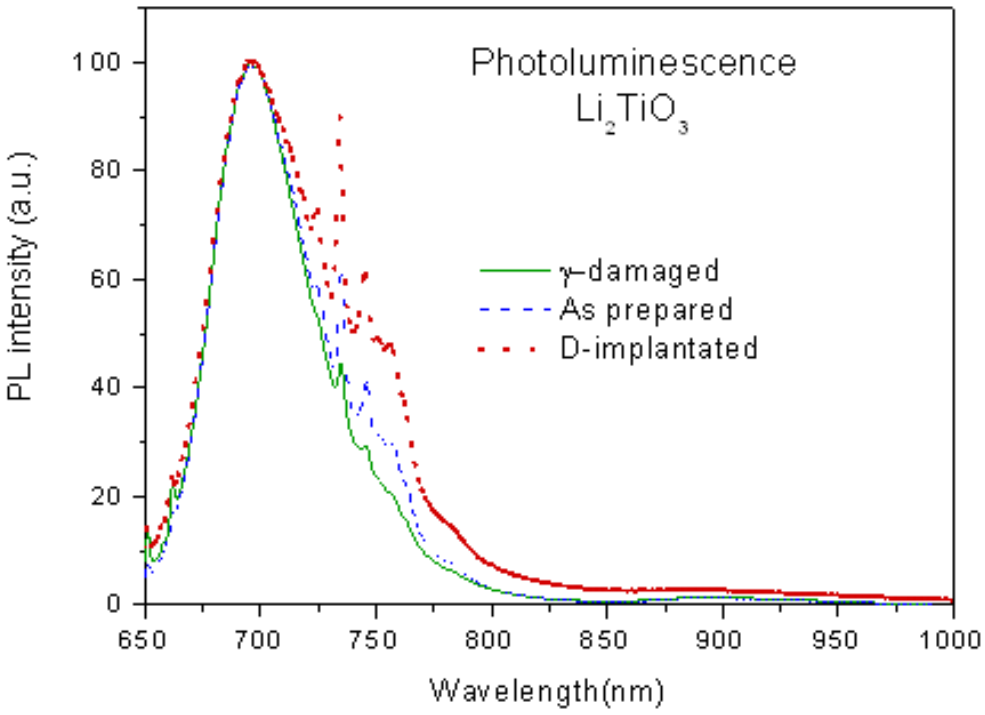

Figure 7.17: Normalized emission PL spectra for excitation at 633 nm of the Li_2TiO_3 as prepared and D-implanted and γ-damaged ceramic.

As expected, ionizing radiation does not really affect the surface layer of the ceramic material. The damage luminescence is varied principally by D – implantation.

The luminescent measurements are useful to study the kinetic aspects of defects production, but it does not provide any quantity information. The relevant aspect in our study is the effect of surface degradation on light ion release rather than the identification of the defects nature, a quite difficult task in these polycrystalline and poorly studied ceramics.

4. Helium-3 thermal behaviour experiments in Li_2TiO_3 ceramics

The study of ^3He behavior in solid breeder is interesting because tritium and ^3He presents some important characteristics in common: the spin value (+1/2) and the atomic mass (3.016 a.m.u.). Considering that this ceramic when exposed to high-energy neutrons will produce high concentration of gaseous transmutation products (^3H and ^4He), there are also considerable interests in studying ^3He thermal evolution for the fundamental understanding of its long-term behavior in breeder

blankets. Due to the limited solubility of helium in most glasses and ceramics (from 0.5 to 1 wt. %), local accumulation may occur in the form of bubbles which may cause swelling and affect many physical properties of the crystalline structure. Finally, it is relevant the consideration that radioactive tritium spontaneously decays to ^{3}He plus other particles (with a half-life of 12.3 years), thus the knowledge of its behavior in wasted ceramics covers a special interest in the handling and treatment of these materials.

Considering the time consuming experiments selected (each NRA measurement take approximately 1 day), only one material is chosen. Starting from previous results with D, where MTi shows higher ion retention and due to its good crystallinity, it has been selected as the best material to perform next experiments. The present study is focused only on the Li_2TiO_3 (MTi) ceramic. The principal idea of this set of experiments is the performing of a complete study on the temperature effect on He release.

The aim of this part of the work is the determination of He transport in an implanted breeder ceramic through the application of the ^{3}He (d, α)^{1}H NRA technique where ^{3}He and ^{2}H represents the implanted and incident nuclei respectively and ^{1}H particle and ^{4}He or α represent the nuclear reaction products. The total cross section for this reaction presents a broad resonance around 400 keV. Varying the beam energy it is possible to observe the distribution-in-depth profile of the implanted ion. Being interested in ^{3}He release dynamics under different thermal treatments and with the purpose of estimating the release coefficient, a detailed study on its isothermal behavior is also performed.

Thus, it becomes very important to understand the transport mechanisms of helium in nuclear materials in order to be able to make reliable extrapolations of their long term behavior. The microstructure after implantation and depth analysis is characterized by Transmission Electron Microscopies (TEM).

4.1. Experimental part: the DIADDHEM device

The evolution of ^{3}He depth profiles were performed in the framework of EMIR (Études des Matériaux sous IRradiation) network, in collaboration with CEMTHI (Conditions Extrêmes et Matériaux: Haute Température et Irradiation) laboratory. The experiments were performed using the device DIADDHEM (DIspositif d'Analyse de la Diffusion du Deutérium et de l'HElium dans le Materiaux), located at the end of a beam line in a Van der Graaff accelerator. This accelerator (see Figure 7.18) is a

High Voltage Engineering type (HVE) which can work with light ions (H^+, HH^+, D^+, DD^+, $^3He^+$, $^4He^+$) in the energy range 0.3 - 3 MeV, with a resolution of 2-3 keV.

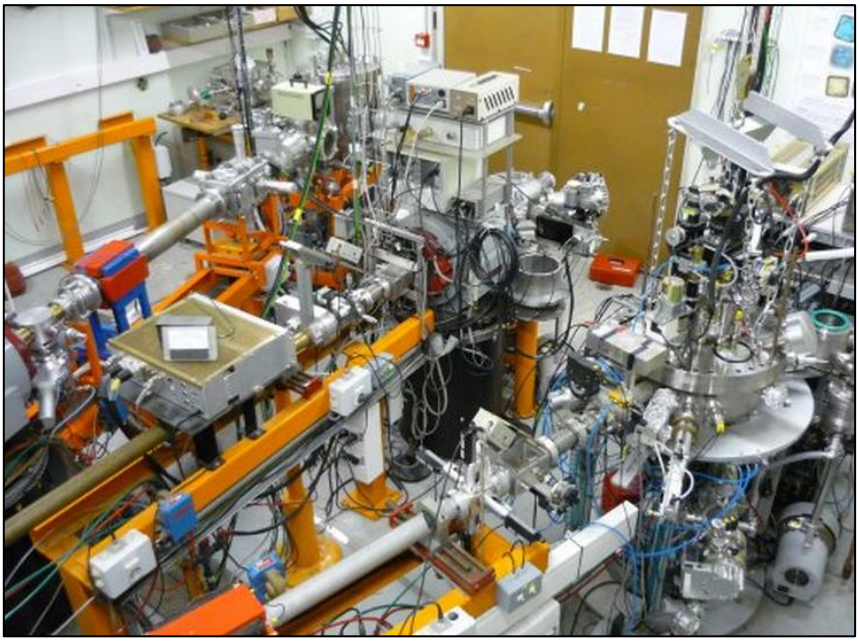

Figure 7.18: Van de Graaff accelerator in CEMHTI laboratory.

It is equipped with a radiofrequency source which generates plasma, permitting to obtain ions starting from a gas contained in a quartz bulb to a pressure of 10^{-3} to 10^{-2} mbar. The positive ions are extracted after pre-acceleration of the order of 1 kV through an extraction channel at a current of the order of several tens of µA. An analyzing magnet deflection angle of 90 ° allows obtaining beams with an energy resolution of a few keV with a transmission rate of the order of 30-50%.

For the implantation process, the sample is placed on a copper holder of 2.5 cm in diameter. This sample holder has a 200 µm thick and a 6 mm diameter window to permit the transmission and detection of protons at 0°. The sample holder is cooled to –120 °C for avoiding helium diffusion during implantation. The beam size used for implantation is approximately 2x2 mm^2 which is first adjusted at the center of the sample holder using an alumina target. The implantation is performed by scanning the beam pixel-by-pixel across the surface in Lissajous mode (10 Hz, 32000 points) of 126 lines. The distance between two pixels, which is given by the ratio of the scanned diameter and the number of lines, is equal to 0.2 mm. As a result the size of the beam is greater than the beam scanning step, and the implantation is considered homogeneous.

For the Nuclear Reaction Analysis the coincidence detection technique developed by CEMHTI (see Figure 7.19) was used. In this configuration parasite signals and backscattered particles rate are reduced by a factor of $4*10^4$ with a total suppression of the proton peak due to the simultaneous detection of emitted protons and α particles (they are detected at kinematically corresponding scattering angles). The system consists of three particle detectors: a 1200 mm^2 Passivated Implanted Planar Silicon (PIPS) detector at 0° for the detection of high energy protons; a 100 mm^2 annular PIPS detector at 178° for the detection of emitted α particles; a 1200 mm^2 detector at 150° to detect protons and to perform ^3He cartography. This geometrical arrangement allows the detection in coincidence of alpha particles and protons emitted from the ^3He (d, α)^1H nuclear reaction and detected at 178° and 0°. The helium depth profile is measured from the alpha particles energy spectrum by the coincidence detection mode just mentioned. The great advantage of this coincidence technique resides in large reduction of the intensity of the backscattered ^2H and others signals. The α particles spectra are also exempt of parasitic signals**.**

The set-up consists of a motorized goniometer (2 translations and 1 rotation), an electronic bombardment furnace, and a cooling system, composed of copper cooling exchanger where cold nitrogen gas circulates (see Figure 7.20). The temperature of the sample holder is measured indirectly by thermocouples placed on both jaws that hold the sample. During the thermal annealing the MTi sample is placed on an undrilled molybdenum sample holder (see inset of Figure 7.20) with an optimized thermal contact to ensure excellent temperature homogeneity. The temperature is measured by a pyrometer on the sample holder.

Some are the main potentialities of the DIADDHEM set-up: the possibility to perform the helium implantation in a large temperature range (-160 °C < T < 1400 °C) with the in situ thermal annealing of the sample by an electronic bombardment furnace (T_{max} = 1400 °C); the on-line measurement of ^3He desorption curve as a function of temperature allows the selection of precise points for an accurate measurement of the ^3He depth profiles.

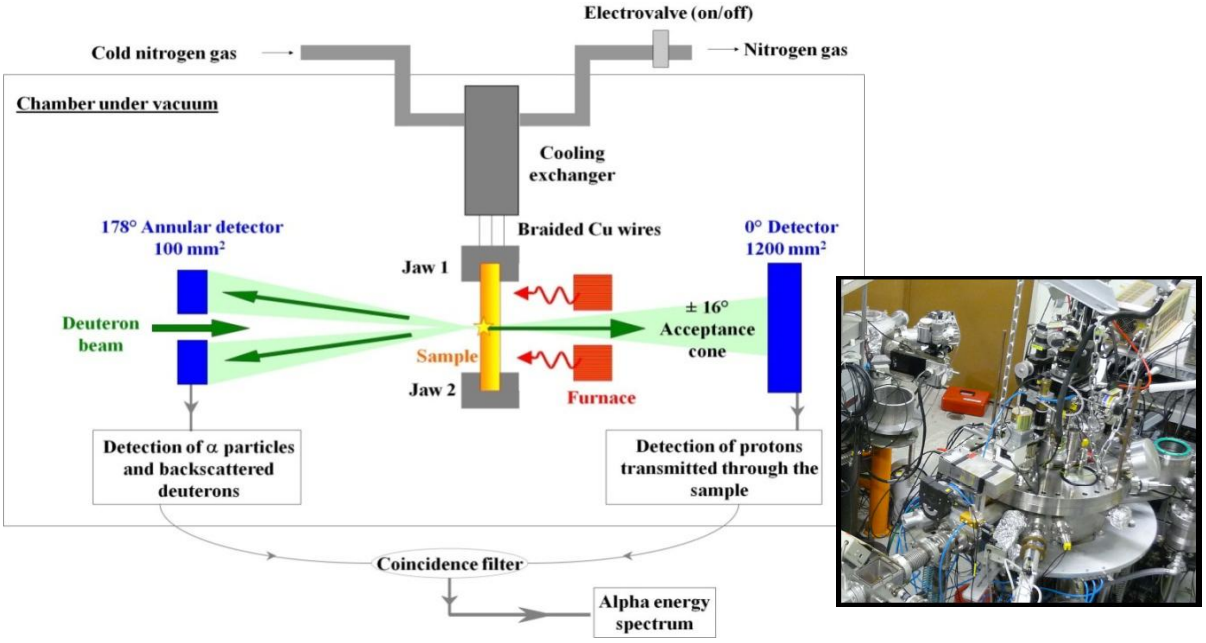

Figure 7.19: Experimental configuration of DIADDHEM set-up [46].Chamber image mounted at the end of NRA line.

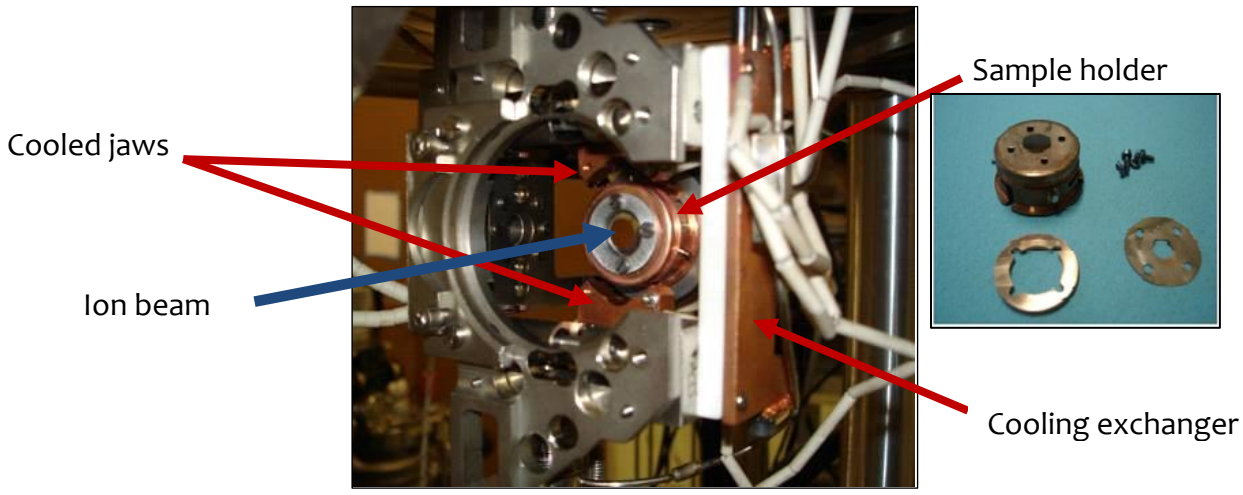

Figure 7.20: Core of DIADDHEM device. The arrows indicate the main elements of the experimental set-up in proximity to the sample. In the inset the disassembled sample holder.

The high performance provided by the DIADDHEM setup resides on the efficiency of the sample cooling system, the accuracy and regulation of the temperature measurements by pyrometer or thermocouples and the special

furnace geometry, offering coincidence yield of 100% and excellent temperature homogeneity of the sample.

In desorption measurements, a different sample holder with a SiC disc is used, to avoid the passage of the beam throughout the sample and obtain a uniform heating. On the other hand all the NRA measurements are effectuated in the same chamber, using the sample holder shown in the inset of Figure 7.20, with a 6 mm window to permit the coincidence detection mode.

The ^{3}He ions were implanted in sintered MTi ceramics at -120 °C and 600 keV to a fluence of $2*10^{16}$ at/cm^2 to characterize the ^{3}He thermal outgassing. Temperature is increased up to 900 °C (at 10 °C/min) and the curve of remaining ^{3}He registered during heating. The set-up has been developed to determine the He desorption rate as a function of temperature and time by on-line detection of protons emitted from the ^{3}He (D, p) ^{4}He nuclear reaction.

The experiment is complemented by the determination of ^{3}He distribution in the matrix as a function of depth at -120 °C after implantation, at -120 °C after 1h of annealing at 150 °C, and finally at RT after 5 min at the maximum temperature (900 °C).

Table 7.3: Implantation and depth profile parameters of the samples NRA measured.

Implantation parameters	600 keV $^{3}He^{+}$ beam $2x10^{16}$ at/cm^2 at -120 °C	600 keV $^{3}He^{+}$ beam $1x10^{17}$ at/cm^2 at RT
Thermal treatments	-120 °C 150 °C / 5 min 900 °C /5 min	400 °C / 70 min 500 °C / 90 min 600 °C / 60 min

After that, new ceramics are implanted using a ^{3}He ion beam at 600 keV to a fluence of $1x10^{17}$ at/cm^2 in normal incidence for a new set of experiments. Several thermal cycles are carried out on five different samples of the same batch in the temperature range between 400 °C and 600 °C and the ^{3}He behavior followed using a 2x2 mm^2 deuteron beam at 900 keV by two different approaches:

1) Helium depth profiling before and after each annealing;
2) Helium release during 60 to 120 min of isothermal annealing treatments.

At the beginning of each set of experiments, a standard SiC sample is analyzed to be sure that the energy calibration of the detector has been correctly determined. The ^{3}He depth profiles are obtained from emitted alpha particles energy spectra

using the RESNRA (RESolution in NRA) freeware, coupled to the SIMNRA software [245].

Further details concerning set-up description could be found elsewhere [246], while more details about the NRA coincidence technique are described by Sauvage et al. [247].

4.2.Results and discussion

4.1.1. Sample previous characterization

The MTi samples used during the implantation and NR analysis are 22% porous (3.43 g/cc of theoretical density). The structural characterization has been performed on the material prior to implantation and analysis. As determined by XRD analysis the MTi sample presents a unique phase of high crystallinity (see Chapter 5, section 6). The study of SEM fresh fracture microstructure (Figure 7.21) reveals that after sintering the open porosity network expected for breeder applications is met. Micro and nanopores (6 and 0.08 µm are the mean pore diameters measured using the Hg intrusion porosimetry) are observed to be interconnected in the MTi matrix. The grain size is bimodal with a size of about 8 and 20 µm.

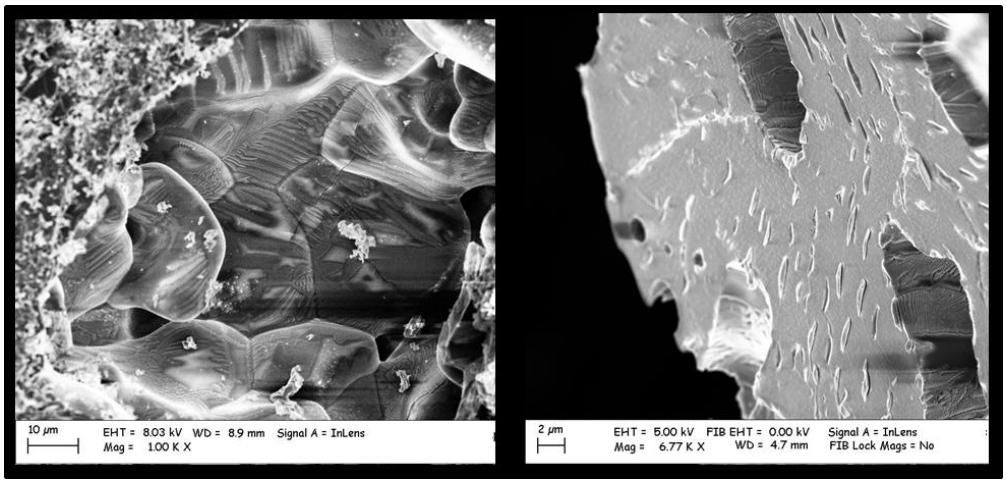

Figure 7.21: SEM transgranular fresh fracture image of the Li_2TiO_3 after sintering at 1150 °C. Open and close porosity of micro-pores can be observed, together with a bimodal grain size of about 8 and 20 µm.

To verify the thermal resistance during experimental temperatures, an as-sintered MTi sample with thickness of 275 µm is heated up to 700 °C in vacuum.

Table 7.4: Heating temperature and emissivity measured for a MTi sample.

Heating temp.(°C)	**400**	**500**	**600**	**700**	**400**	**600**	**700**	**Mean**	
Emissivity (ε)	0.25	0.14	0.18	0.2	0.15	0.18	0.19	0.17	±10 °C

The sample is fixed on the silicon carbide sample holder. The increase in temperature is of 50°C/min. The results of the emissivity measured by a pyrometer with wavelength of 0.6µm between 400°C and 700°C, are indicated in the Table 7.4. A mean value of 0.17 was considered for the following experiments.

After heating, the sample is not broken, but as observed in the Figure 7.22, became black in the two faces.

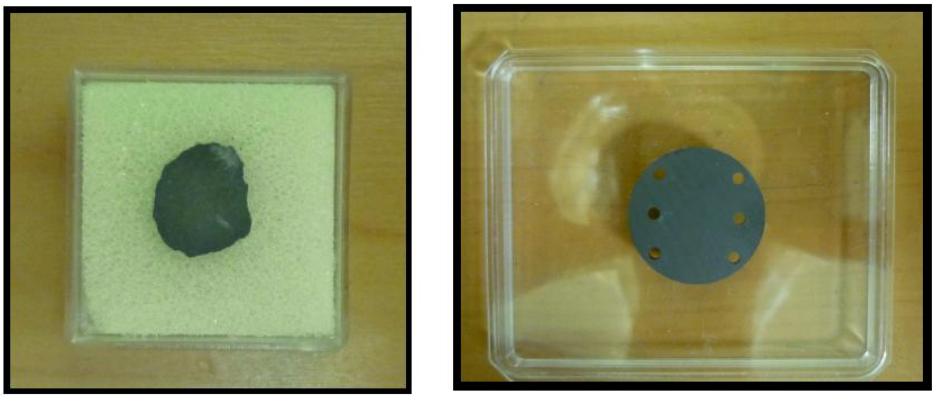

Figure 7.22: (left) Picture of the sample after annealing; (right) picture of the silicon carbide sample holder.

External X-ray photoelectron spectroscopy (XPS) measurements on these samples do not really explain what kind of chemical reactions turn the samples so dark. The best hypothesis is the presence of Oxygen defects, even not being clearly demonstrated.

To identify if silicon or carbon could be diffused in the matrix as impurities and detect the oxygen signals evolution on these heated samples, room temperature NR analysis with 900 keV deuterons are in-situ performed on the as-received and on the temperature-treated black sample. The analysis is performed only at this energy with the aim of observe the main elements present in the sample. Comparative spectra are shown in Figure 7.23 where neither a hypothetical reduction in O in the vacuum facing surface, nor the presence of a C signal, in that in contact with the SiC sample holder, could be evidenced after the heating process.

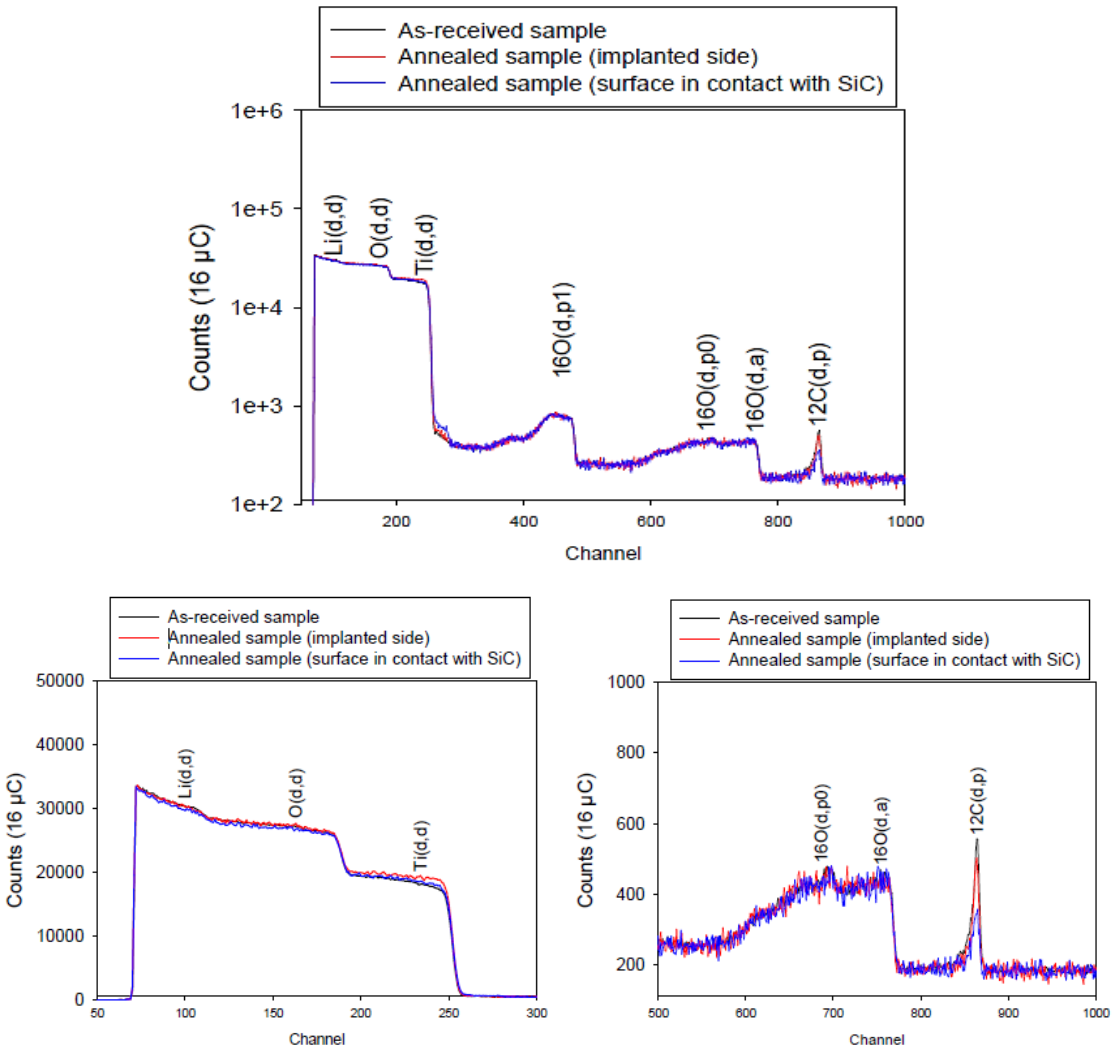

Figure 7.23: NRA spectra obtained on the as-received and the annealed (up to 700 °C) samples. In the upper part the general spectrum, in the lower part the focus on the signals for interest in the sample: Li, O, Ti and C.

The signals from oxygen and titanium are similar for the received and annealed samples. The oxygen loss or the O-to-Ti ratio stoichiometry evolution as a function of temperature, points out an insignificant stoichiometry change after the 700 °C thermal treatment in vacuum.

The depth profile resolution is close to 30 nm at the near-surface of the specimen and can be considered optimal because any foil to stop backscattering signal is placed in front of the annular detector. Based on SRIM calculations [238], the selected implanted energy is chosen to obtain a projected range at about 1.8 ±0.1 µm in depth with a maximum atomic concentration of 0.17 % for fluence of $4x10^{15}$ at/cm^2.

The experimental depth profile is compared to the simulated one in Figure 7.24 as histograms in which each bar width corresponds to the depth resolution of the NRA technique. The sample is stored during 4 days at room temperature between implantation and analysis.

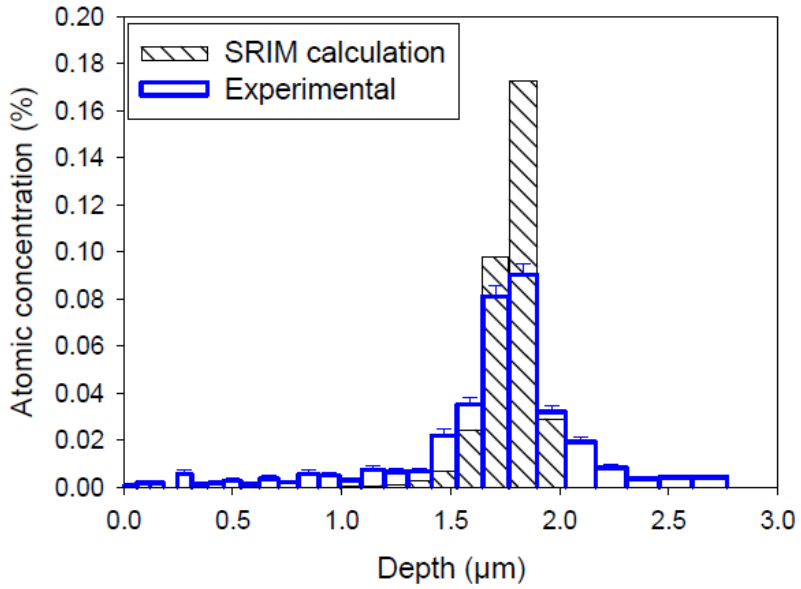

Figure 7.24: Helium depth profiling calculated by SRIM compared to the experimental one for a fluence of $4.2x10^{15}$ at/cm^2.

The maximum helium concentrations of experimental and simulated depth helium profiles are located at the same depth. However, the experimental depth profile by SRIM is broader than the simulated one with a maximum helium concentration almost two times lower than the SRIM profile. The hypothesis for this difference can reside in the Helium migration in relation with the material open porosity. The realization of complementary analysis on sample implanted at -120 ° C to determine the helium depth profile will allow us to confirm the hypothesis.

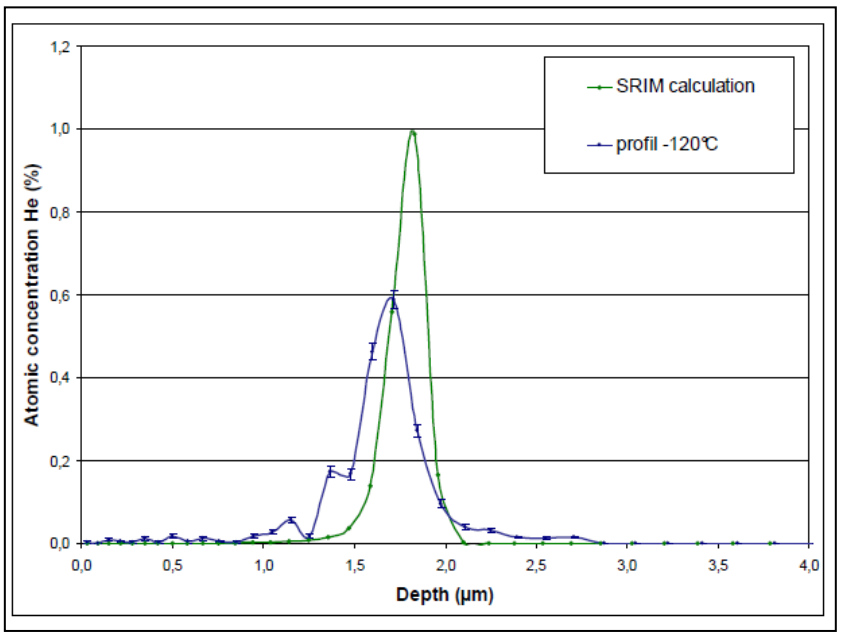

Figure7.25: Experimental depth profile of the MTi sample implanted at -120°C compared to the SRIM simulation.

Figure 7.25 shows the ^{3}He as-implanted distribution curve as a function of depth obtained using NRA at the initial temperature (-120 °C) in comparison with the SRIM calculation. The theoretical depth profile (which can be obtained applying SRIM calculations) shows an implantation maximum located at 1.7 µm. Comparing with the experimental curve, both maxima are almost coincident, the slight registered deviation being explained by the porosity of the real ceramic sample, which is not considered in the simulation program.

4.1.2. ^{3}He analytical determination

To select the best temperature for the following isothermal annealing, a ^{3}He isochronal desorption measurement is performed at the beginning of the experimental program. Each measurement is performed on a different sample of the same batch, to assure the same microstructural features. Sample is heated from room temperature to 900 °C at 10°C / min (Figure 7.26) allowing the measure of ^{3}He desorption as a function of temperature using a thermocouple on the 150° detector for monitoring the temperature variation affecting the signal acquisition.

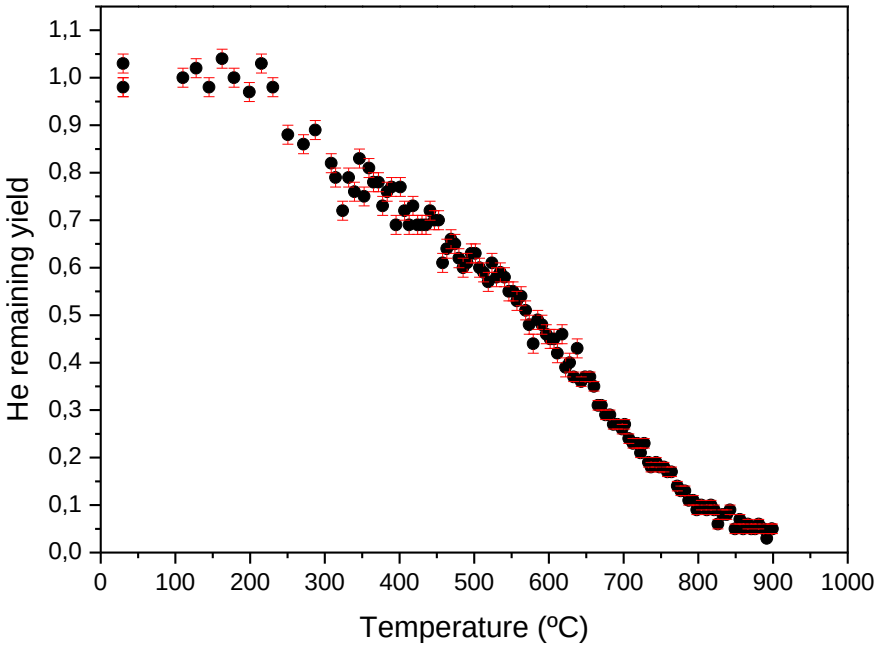

Figure 7.26: Isochronal desorption of the 1x10^{17} ^{3}He/cm^{2} implanted sample measured during heating from room temperature to 900 ºC at 10 ºC/min.

The helium remaining yield shows a first stage (T < 300°C) in which the ^{3}He mobility is not really effective and an almost constant plateau is registered. An increasing of the ^{3}He release rate at 550°C makes it the thermal threshold point for the mobility of the trapped helium fraction. The slope change at 550°C of the helium isochronal desorption curve is the relevant point to support this assumption. The helium release is about 90% of its initial concentration at 750 °C. Therefore the range between 300 °C and 750 °C is confirmed [222] as the interesting interval for the study of ^{3}He mobility. The outgas rate slowly decreases up to 900 °C where a 7-8% of the initial implanted amount is estimated to be the remaining helium after 5 minutes of annealing at the maximum temperature.

The gas release behaviour and its depth distribution could also be followed by the aid of NRA profiles at relevant annealing temperatures. A comparison of the depth profiles at three different annealing conditions is shown in Figure 7.27. Profiles are measured after ^{3}He implantation at -120°C, for sample annealing at 150 °C during 1 hour, and in sample annealed at 900 °C during 5 minutes. As expected from the above mentioned release results, the depth profiles before and after annealing at 150 °C / 1h are quite similar, the ion loss being negligible even after 1h at 150 °C. Therefore it is confirmed that ^{3}He diffusion is not effective at temperatures just above room temperature. After sample heating to 900 °C and a dwell time of 5

minutes, the remaining He curve shows a weakly intense maximum whose area under the curve confirmed the amount of gas concentration obtained from the release curve, approximately the 7-9 % of the initial concentration.

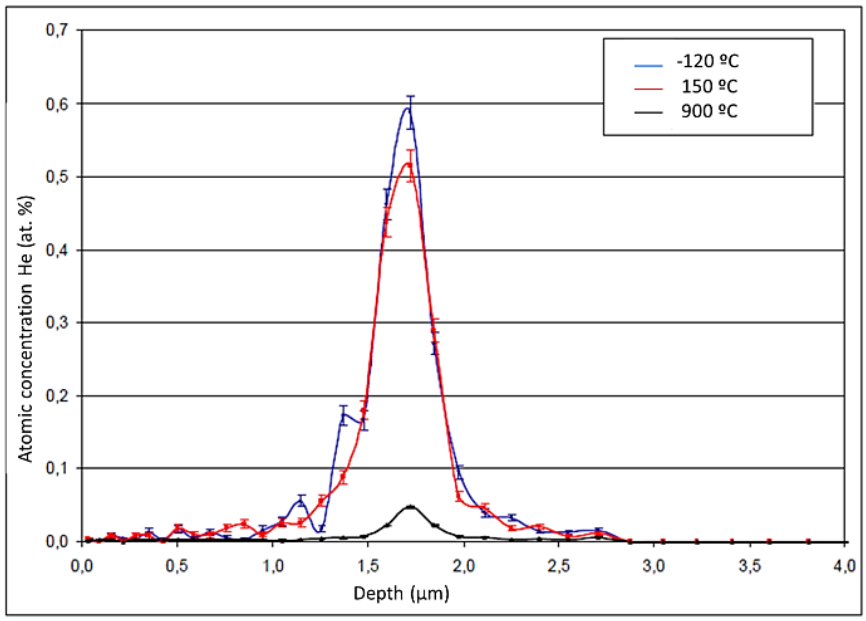

Figure 7.27: Experimental depth profile of the MTi sample sintered at 1150 °C before and after different heating treatments.

For the three measured temperatures, it must be pointed out that the experimental peaks denoting the ion implantation maxima position are located exactly at the same depth (centered at 1.7 µm in Figure 7.27). This independent evolution with temperature may indicate the stable arrangement of ^{3}He in the ceramic matrix even after high temperature processes. Figure 7.27 stress a fairly symmetrical implantation profile from the maximum to both sample surface, pointing out that heating seems not to diffuse the noble gas torward the surface of the material.

Table 7.5: Implantation and depth profile parameters.

Implantation paramenters	2x10^{16} at/cm^2 at -120 °C	2x10^{16} at/cm^2 at -120 °C	2x10^{16} at/cm^2 at -120 °C
Real ion fluence (10^{16}at/cm^2)	2.35±0.18	2.16±0.17	2.35±0.18
Thermal treatments	-120 °C	150 °C /1 hr	900 °C/5 min
[^{3}He] Max (at. %)	0.59±0.03	0.51±0.02	0.48±0.002

Once confirmed the stability of the system, a series of measurements with three temperatures, selected as the interesting range for fusion applications, is proposed. In Figure 7.28 the curves of isothermal annealing (ramp of 40°C / min) at three different dwell temperatures and times are shown. This set of measurements is done on the SiC sample holder and the response registered only from one detector. For each temperature a different sample of the same preparation batch is used, and the ^{3}He remaining yield is normalized to one at the beginning of the thermal cycle.

Desorption curves show two stages: a first helium fast release and a second asymptotic release. This behavior can be explained as follow: helium atoms being light and not chemically reactive with the matrix are able to escape from the material during thermal activation process. A high mobile fraction is identified as the weakly trapped helium and registered during the first stage of heating. The remaining ^{3}He is recognizable as an equilibrium state of the gas (presence of He trapped fraction) and needs higher activation energies to find a grain boundary path or an open pore for its release. These first results highlight that helium release does not follow a simple diffusion phenomenon.

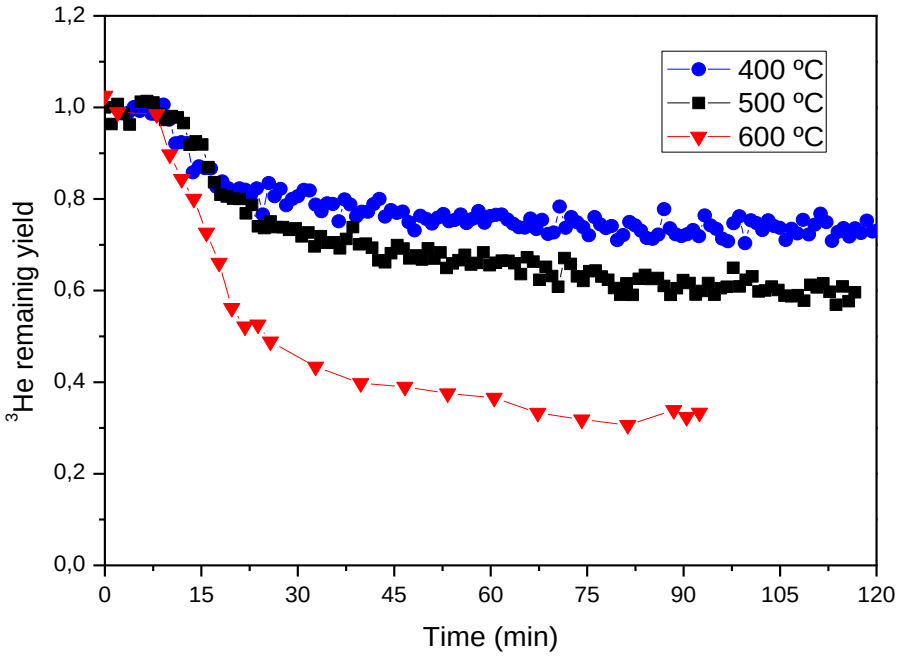

Figure 7.28: Helium desorption of Li_2TiO_3 implanted samples measured during three isothermal annealing treatments at 400 °C (blue circle), 500 °C (black squared) and 600 °C (red triangle).

To obtain the He distribution in depth and its evolution with annealing time for the three temperatures, the nuclear reaction profiles before and after each annealing treatment (Figure 7.29) are performed.

At 400°C the maximum helium concentration $[He]_{max}$ decreases as a function of time to reach a quasi-constant value after 120 minutes. It is worth mentioning that $[He]_{max}$ value is lower after 70 minutes than at longer annealing treatments. This discrepancy could be due to the analysis of a new region with a higher ^3He concentration (for example nanocracks or nanopores with trapped helium shown in section 4.3 of this chapter).

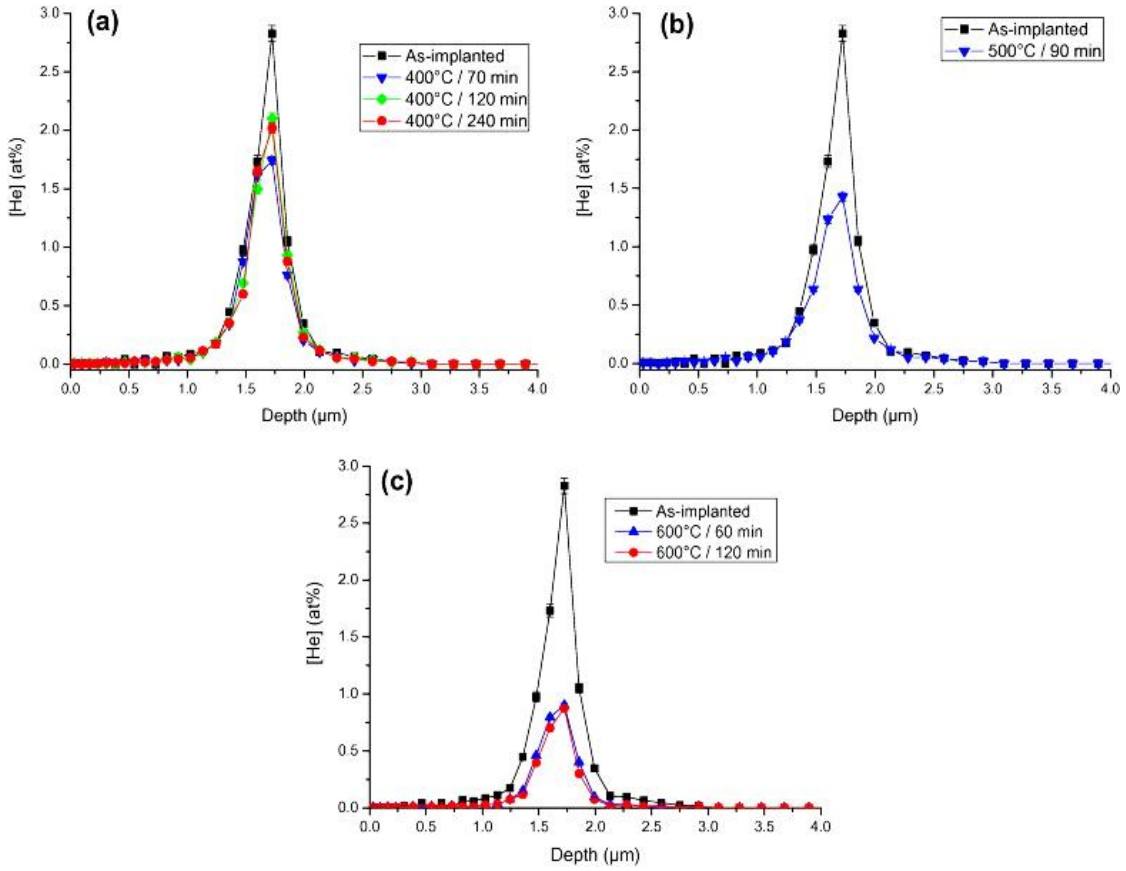

Figure 7.29: Experimental depth profiles before and after annealing treatments: (a) on as-implanted sample (black squared) and after a 400 °C annealing of 70 min (blue triangle), 120 min (green rhombus) and 240 min (red circle); (b) on as-implanted sample (black squared) and after a 500 °C annealing of 90 min (blue triangle); (c) on as-implanted sample (black squared) and after a 600 °C annealing of 60 min (blue triangle) and 120 min (red circle).

The annealing at 500 °C shows a lower $[He]_{max}$ value compared to the one obtained at 400 °C during 240 minutes. This confirms that helium mobility is based on thermal activation of trapped Helium. Finally, the depth profiling at 600 °C during 60 or 120 minutes does not present any broadening.

The depth profiles homothethy observed enables the comparison of helium release curves with the fluence evolution. The amount of loss helium estimated from the depth profiles and the release curves are in good agreement, confirming the good reproducibility of the experiments and the validity of NR measurements even though their time consuming characteristic.

Starting from all the previously observations a model for ^{3}He behavior is formulated (Equations 7.9). The ^{3}He loss factor K(T) is defined and deduced from the results using the following system of equations:

$$He_{total} = He_{trapped}\,t + He_{released}\,t$$

$$\frac{He_{trapped}(x,t)}{\partial t} = 0 \qquad (7.9)$$

$$\frac{\partial He_{released}(t)}{\partial t} = -K\,T\;He_{released}(t)$$

where $[He]_{total}$ is the total Helium concentration implanted in the material which can be distinguished in two contributions and the K(T) coefficient release represents the desorption rate in s^{-1}.

The model is based on the concept of the gas diffusion/migration along the interconnected open porosity through grain boundaries paths [71] and the Helium trapped in the cavities formed in the implanted region.

The K(T) helium loss term is determined from isothermal release experiments, when temperature is stable. In order to obtain quantitative data, the following equation is used:

$$N(t)/N(t_o) = [1 - N(t_\infty)/N(t_o)]\, e^{-K(T)*t} + N(t_\infty)/N(t_o)] \quad (7.10)$$

where N(t) is the number of protons detected from the ^{3}He(d,p)^{1}H nuclear reaction at the annealing time t; t_o the time at which the temperature T is reached; t the annealing time at the temperature T; t_∞ the time of acquisition and K(T) the helium loss term at the temperature of T. Table 7.6 represents the quantitative results deduced from the isothermal data fitting with an error of two standard deviations. The K(T) ^{3}He loss term is quite similar at 400 and 500 °C, while an increase of a factor of 1.4 is observed at 600 °C. None relevant changes with the annealing time in isothermal treatments are observed on the K loss factor between 400 and 500 °C.

At 600 °C there is a slight increase in helium loss factor because of the thermal activation observed in Figure 7.27.

Table 7.6: Helium loss factor K(T) measured for the three annealing temperatures studied in the present experiment.

Temperature (°C)	K factor (s^{-1}) ($x10^{-2}$)
400	0.068±0.010
500	0.065±0.008
600	0.09±0.020

The study on ^{3}He release shows a different temperature behavior. The isothermal measurements at 400 °C, 500 °C and 600 °C evidence a fraction of the ion strongly trapped in the material.

These results confirm the presence of a thermal threshold point around 550-600 °C which can activate the mobility of the trapped helium fraction (see Figure 7.25).

4.1.3. ^{3}He behavior in damaged ceramics

The effect of gamma irradiation on the behavior of ^{3}He transport is studied in this last part of the work. The samples are damaged prior to implantation by a ^{60}Co source in the Nayade pool-facility, at 6Gy/sec to a total dose of 7.3MGy, at room temperature.

The influence of the gamma irradiation on the light ion transport is quite unknown. Considering the relevance of the microstructure and the defect structure in the processes involving the transport of light ions, it is possible to suppose that also ionizing radiation can affect it.

In the following measurements, comparisons of the ^{3}He desorption during isothermal annealing in the case of as-prepared and irradiated samples are presented. In Figure 7.30 the effect of gamma irradiation on the isothermal release curves of ^{3}He are measured near the inflection point suggested from data in Figure 7.26. In both cases with gamma irradiation samples the ^{3}He remaining yield in the irradiated sample is lower than without irradiation. In the case of 500 °C isothermal annealing the effect is less evident, probably because, as clearly visible in the whole measurements, at 600 °C the activation of a new transport process occurs.

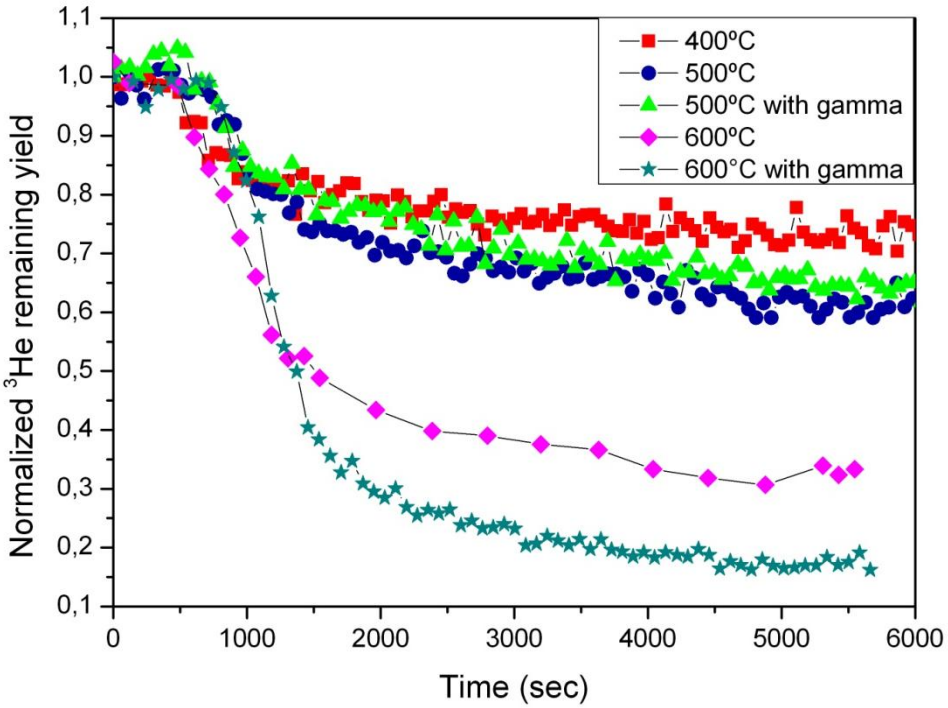

Figure 7.30: He desorption from Li_2TiO_3 implanted samples measured during isothermal annealing treatments at 400 °C, 500 °C, 600 °C and on 500 °C and 600 °C γ-damaged samples.

The high decrease in helium remaining yield between 400-500 and 600 °C obtained in these isothermal experiments, are in total agreement with the NRA profiles previously shown in Figure 7.29. Both confirm the thermal activation for helium release taking place in the vicinity of 550 °C. The gamma-irradiated samples follow a similar thermal behavior as the undamaged materials. The helium remaining concentration of the irradiated sample thermal treated at 600 °C present a notable decrease after 30 minutes compared to the unirradiated sample. The reason may be found in the nature of the defects created by ionizing radiation which accelerate the diffusion process. It is known from literature [248] that helium gas impurities in a solid matrix are confined in bubbles. These bubbles together with gamma irradiation seem to require lower temperatures to be activated. Thanks to gamma radiation the partial pressure required for migration of bubbles through the crystalline structure results to be lower at 600 °C.

The depth profiles before and after annealing at 600 °C are shown in Figure 7.31 and compared to the behavior of ^{3}He in a previously irradiated matrix. It must be pointed out again the absence of broadening in the distribution depth. The total

helium concentration decreasing is clearly visible after temperature annealing as well in the γ-irradiated MTi sample.

The results obtained suggest that when only ionizing radiation is present the diffusion and outgas of helium-3 is promoted. Even though the difference with the as prepared sample is not so big, it is possible to suppose that ionization induces valence changes in the activation energy for light ion diffusion. This hypothesis is known in literature as RED (Radiation Induced Diffusion) occurring in insulating materials by different mechanisms (ionization or displacement damage) [249].

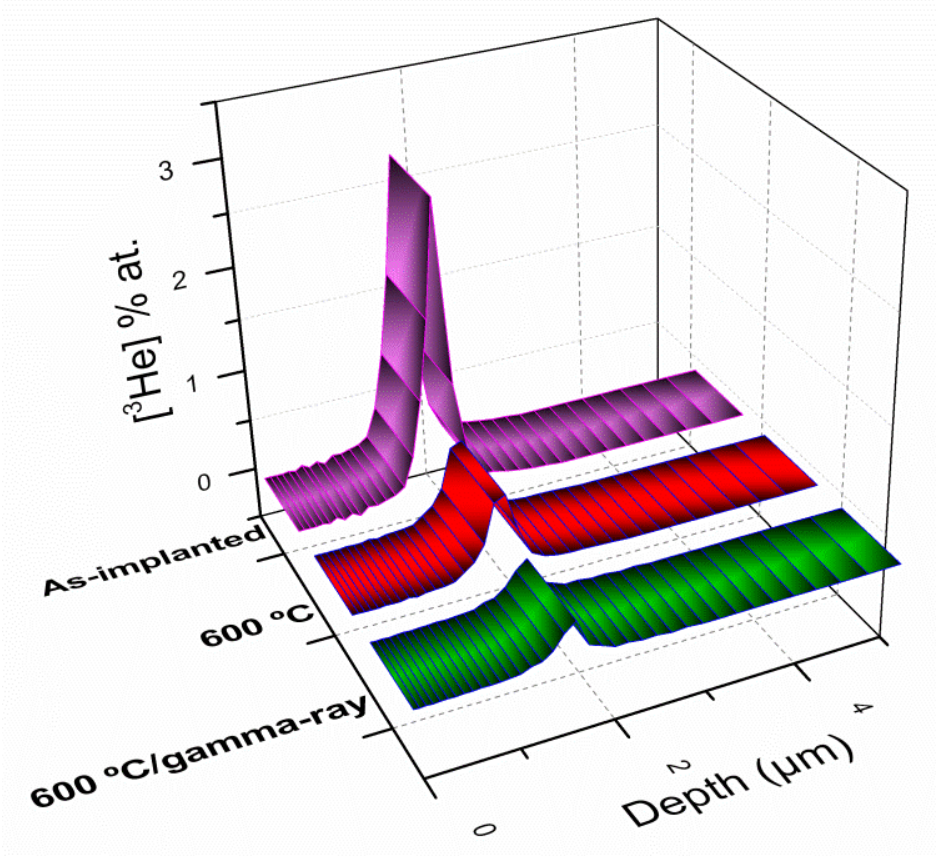

Figure 7.31: ^{3}He-depth profiles of the sample (purple) compared to the profiles after 600 °C annealing (red) and on pre-irradiated ceramic (green).

4.3. Microstructural and structural characterization after experiments

TEM characterization is an important support which can be used to understand the diffusion processes occurring after light ion implantation in the microstructure. The cross-section processing technique (described in Chapter 5 section 3.6) allows studying the microstructure of thin layers of material between surface and the maximum implanted gas concentration region.

The TEM observation (Figure 7.32) points out the existence of a highly stress region between 1.6 and 1.9 microns from the surface. In this region planes of interconnected cavities and nanocracks are visible in underfocused conditions which are arranged perpendicularly to the implantation beam direction (Figure 7.31 left). This TEM observation strongly suggests that helium concentrates and forms cavities within the nuclear cascades region during implantation. Cavity formation in He-implanted MTi exhibits wavy structure within an observable region of about 100 nm in depth (Figure 7.32 right).

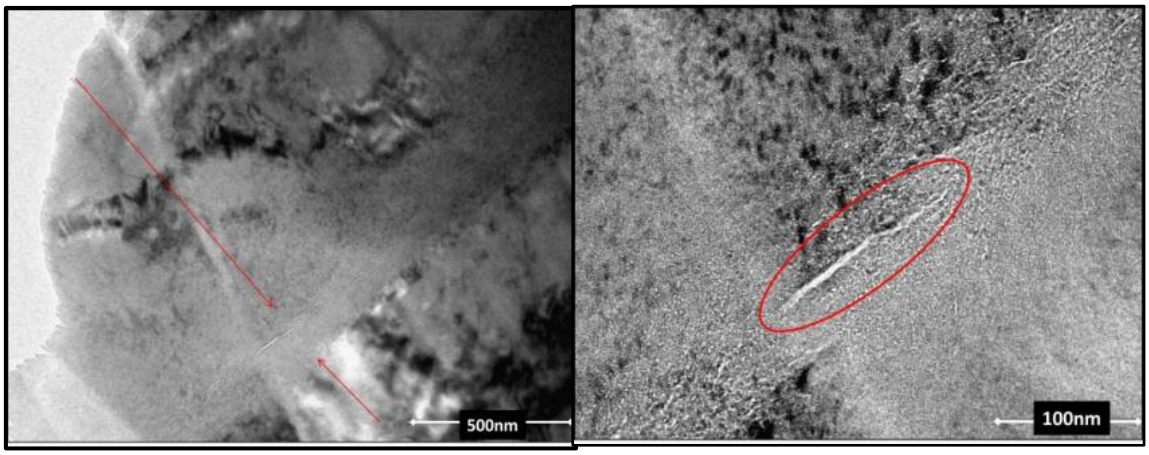

Figure 7.32: TEM images of the ^{3}He implanted zone. The formation of cavities and microcracks in the plane perpendicular to the irradiation direction, in the He-implanted peak region, is observed in underfocused conditions as low contrast (white) objects.

Assuming this assumption, the helium filling the nanocavities may release under thermal activation through grain boundaries paths towards the surface being mentioned above as the trapped He fraction in the implanted area when analyzing the NRA profiles. The presence of nanocracks can then explain the difference in the ^{3}He concentration peak values measured in different areas, when annealing time is

changed. In agreement with Zinkle [248] they could be assigned to He cavity formation associated to the dislocation loop region in irradiated oxide ceramics.

This phenomenon could be attributed to the diffusion or migration within the implantation plane that means within a highly damaged region [48]. The migration at the neighboring of grain boundaries is effective because the grain boundaries would act as sinks of defects and prevent the formation of helium bubbles.

At higher magnifications, "layers of nanocracks" have developed perpendicular to the irradiation direction in the He-implanted peak region.

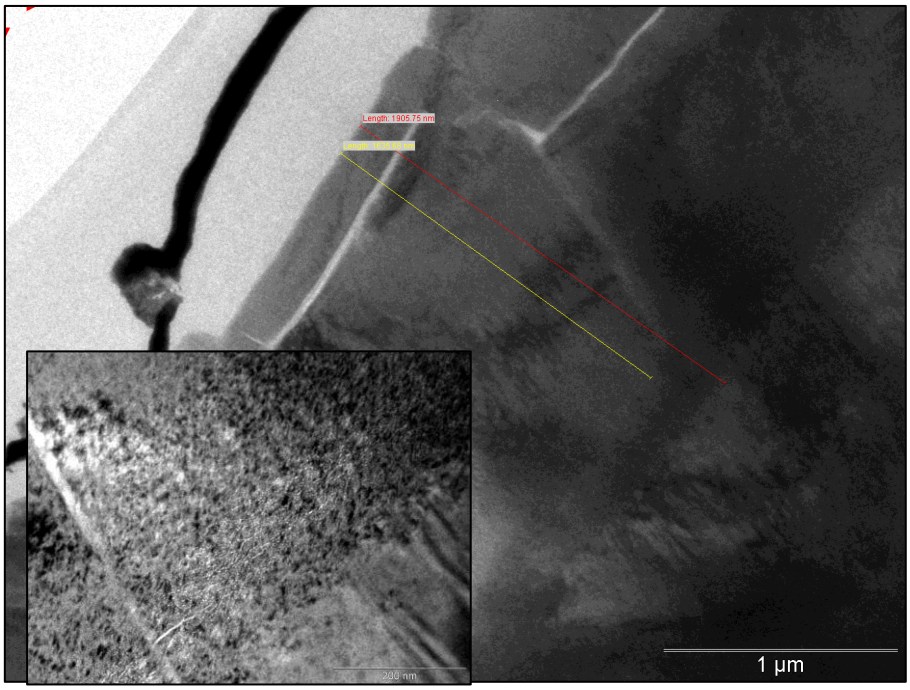

Figure 7.33: Implantation zone detected by TEM imaging. The distance from the surface corresponds to the one find in the depth profile analysis. In the inset the cavity microstructure (underfocused image).

As observed by Zinkle ion implantation generates localized stresses that may play a significant role in the cavity habit planes, slightly changing the microstructure. Differently from other crystalline materials, only one type of cavity is observed: along habit planes nearly parallel to the irradiated surface (rather than associated with matrix crystallographic orientations), which may indicate the stresses associated to ion implantation. The introduction of additional ionizing radiation before the ion implantation has no effect on cavity evolution.

Raman effect is the anelastic scattering of light (by molecule or point defects) due to emission or absorption of a vibrational mode. Thus is possible to observe the modification of the microstructure after implantation by Raman characterization.

From a generic study on MTi material with different exciting wavelengths, the intensity decrease and the loss of resolution in secondary vibrational modes can be appreciated (Figure 7.34). The vibrational spectra are interpreted using the results of group-theoretical analysis from the literature [250],[251,252]. The frequencies in the 700 – 550 cm^{-1} region are assigned to Ti-O stretches in TiO_6 octahedral (region I in Figure 7.34); if lithium is octahedrally coordinated by O, the 400-550 cm^{-1} region corresponds to Li-O stretches (region II); when the lithium coordination is tetrahedral, the 250-400 cm^{-1} region corresponds to Li-O stretching (region III). Raman peaks are perfectly coincident with the ones reported in literature [253].

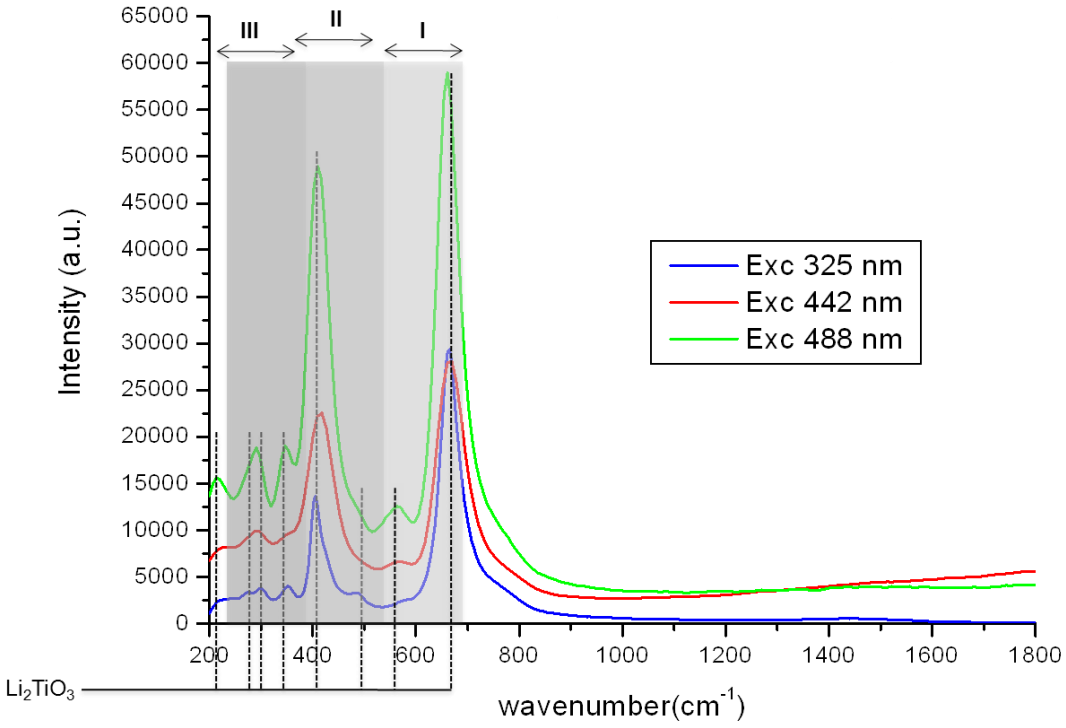

Figure 7.34: RAMAN spectra of the Li_2TiO_3 excited at 325 nm, 442 nm and 488 nm. Association of Raman frequencies for Li_2TiO_3 from literature: I - Ti-O stretching in octahedral TiO_6; II – Li-O stretching in LiO_4; III - Li-O stretching in LiO_6.

The modification of the microstructure after ^3He implantation is represented in Figure 7.35. The reduction of Raman lines as a consequence of ion-irradiation

indicates that the ordering of structural units in Li_2TiO_3, such as TiO_6, LiO_6 and LiO_4 units has been modified [254], generating structure distortions due to chemical reduction (like the loss of O-ions for preferential sputtering). Considering the results obtained in the case of irradiation and D-implantation, after the structural characterization by X-Ray diffraction at small angles (see section 3.2.2.2), it is possible to suppose that, presenting helium a small electronic stopping power, the disordering caused on the surface and detected by Raman, is not well appreciable.

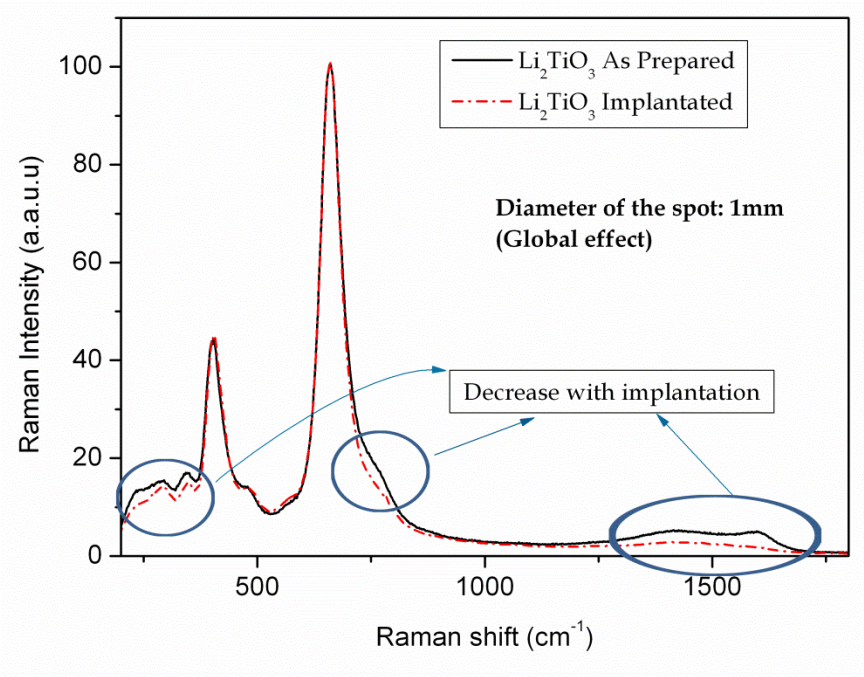

Figure 7.35: RAMAN spectra of the Li_2TiO_3 as prepared and ^{3}He-implanted ceramics.

5. Comparison and discussion of light ions behaviour

The study on the thermal-induced release of D and ^{3}He implanted in the matrix of a BB candidate ceramic would help to simulate light ions transport behavior in fusion reactor conditions and understand their transport mechanism.

From the TEM images of both implanted samples it is possible to define the implantation zone as a darker region (Figure 7.36). It is evident that while in the case of Deuterium this highly stressed area goes from surface to the implanted zone (Figure 7.36 left), in the ^{3}He case the dark zone corresponds to a band of about 300 nm around the implantation peak (Figure 7.36 right). In the case of deuterium

implantation the largest damaged area is reflexed in the depth profile shape found. For the noble gas, the diffusion inside the material needs to be activated from a thermal threshold, as shown by the experimental results. This "chemical" difference among the two elements is clearly visible in the implanted specimens. The results confirms the ones reported by Zinkle in other materials [248], where cavities and nanocracks production is of higher density and more spatially uniform in the case of He compared to H irradiation (where only a stressed region is identified).

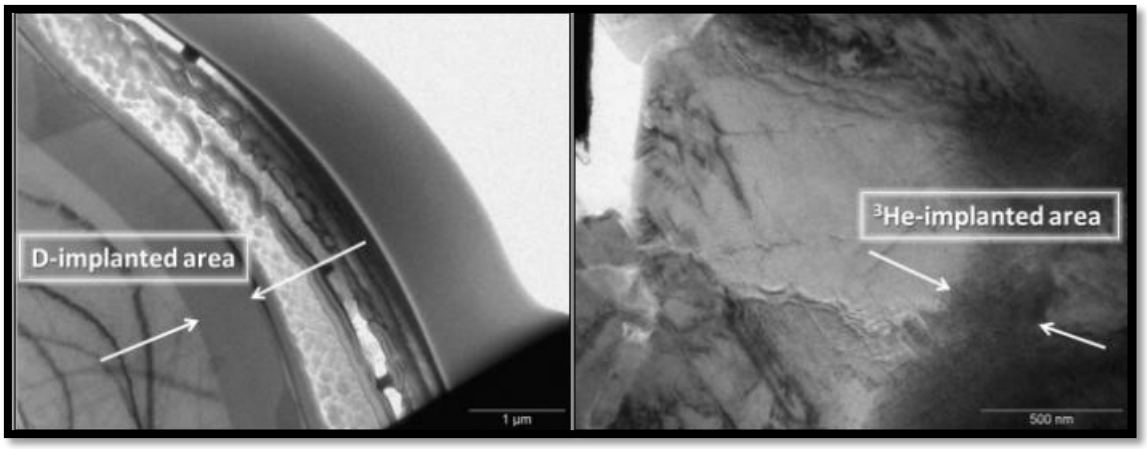

Figure 7.36: TEM images of the D (left) and ^{3}He (right) implanted zone, recognizable as a darker area.

When discussing deuterium-implantation data, is important to consider that the error in the determination of the D concentration at different depths depends on the shape of the profile, considering that there always will be a contribution of protons originating from the deuterium present close to the surface. It is important to observe that absorber foil technique (used for D-detection), results in a poorer depth resolution because of large energy straggling in the absorber foil, the sensitivity of the technique is partly improved because resonance exists in the case of D - ^{3}He cross section.

Deuterium depth distribution and thermal release are studied by R-NRA in three different candidates as solid breeder blanket: MTi, Li4 and a third one with a higher Li:Si proportion (Li6). Relevant correlations with the ceramic microstructural and morphological features (porosity, pore size distribution and grain size) are found. Thermal annealing at temperatures as low as 100°C promotes D diffusion while at temperatures equals or major than 150°C the whole D is driven to a complete release from all the studied ceramics. Deuterium atomic concentration is

significantly higher at the surface than in the bulk, i.e. 1.95% vs 1.11% for MTi, and 1.20% vs 0.75% for Li4 in the as-implanted conditions, indicating that ceramic surface play an important role in the D release. By comparing D release data for samples with high porosity and low grain boundary density to those for samples with low porosity and high grain boundary density, it can concluded that grain boundary might be an alternative path to porous for D diffusion.

In the case of helium gas the results show that outgas is not effective at room temperature and an inflexion point at 550 °C is found. Moreover after 5 minutes of thermal annealing at 900 °C, the remaining concentration is just a 7-8% of the initially implanted amount.

It is possible to distinguish different singularities on ^{3}He thermal behaviour:

1. Helium concentration distribution in depth is homothetic: it does not broad with increasing temperature.
2. For isothermal annealing, the release rate is governed by double stage decay as a function of time.
3. At high temperature (from 550 °C), the third stage of helium migration is attributed to the thermal activation of the helium trapped in growth and interconnection of nanosized cavities.
4. The depth profiling experiments confirm that helium release would occur through opened porosities and at the neighbouring of grain boundaries.

Preceding statements lead to conclude that fraction of helium atoms are able to easily escape from the material (weakly trapped fraction) while the remaining ^{3}He needs higher thermal activation energies to find a grain boundary path or an open pore to release throughout the surface.

X-Ray diffraction at small angles, Raman and PL characterizations can help to understand the structural variations under damage conditions. The hypothesis of the surface degradation caused by anionic sputtering observed by optical measurements is in good agreement with the results obtained for insulators materials [50]. The release in damaged MTi ceramic shows the important role played by a preferential sputtering on the surface through the formation of defects (F^{+} or F^{0}) improving D outgases. It is evident that both damages (ionizing radiation and atomic displacement) modify the diffusion and the release kinetics. If ion-implantation cause the formation of vacancies or chemical reduction (like O), the γ-irradiation is responsible of the electrical structure modification. Their combination seems to favor the annihilation of trapped defects, thus slowing the kinetics of

diffusion/trapping/detrapping for the release of the light ion. Therefore irradiation defects and temperature, participate in the whole mechanism altering the material stability, accelerating the diffusion process (as observed in the experiments). This theory finds different confirmations in the literature with works based on different measurements (luminescence [255,256], positron annihilation spectroscopy and Raman [254],[253], electrical spin resonance [257]).

The results obtained in this work about the effect of Ti-implantation on D-release are in good agreement with the phenomenology observed for Tritium release in neutron-damaged ceramics [186].

For the design of blanket systems, long-term effect of radiation on tritium release behavior and related microstructural and structural changes are critically important. Starting from light ions data and regarding the possible similar behavior of tritium, some hypothesis can be made. Tritium is produced inside the grains of BB ceramics during a damage process, caused by the neutron interaction with the crystal structure. It results in the chemical states of T^+ and T^- and can interact with the defects produced (like F^+ and F^0 centers), through which diffuse to the grain surface. Here it moves into the grain boundary, identified as the paths for light ion diffusion, till the surface of the pebble. Once there, from the reaction with the H present in the sweep gas and the oxygen from the material structure, it is released as T_2, T_2O or HT. Temperature–programmed desorption (TPD) experiments on irradiated samples, indicate that tritium is easily removed from lithium titanate at temperature as low as 300 °C [258].

The comparison of defects annihilation and tritium release shows that the slow process and the tritium release from bulk appear simultaneously. Hence the annihilation of oxygen vacancy in each sample, could play an important role in tritium release process [90,186]. Moritani et al. [187] studied tritium release kinetics of lithium ortho and meta-silicates throughout two types of temperature controlled annealing experiments. It is been confirmed that F^+ centre (an oxygen vacancy trapping an electron) and the F^0 centre (an oxygen vacancy trapping two electrons), commonly observed in ionic crystals, are formed by irradiation, playing an important role in tritium behaviour. Yamaki [89] observed the microstructural changes in lithium titanate by multi-ion irradiation through Raman spectroscopy suggesting the formation of TiO_2 by irradiation. The amount of TiO_2 formed, proportional to the average dpa, increases the amount of hydroxyl absorbed on or near the surface, which will act as traps for the tritium generated.

In general it is possible to state that when only one kind of defect is present, the creation of defects (of ionization type along the bulk or preferential sputtering on the surface layer), facilitate the release of light ions under thermal activation. The temperatures for thermal activate the trapped gas, change with ion nature. When both defects are present, the annihilation of defects occur affecting light ions release. Thus for correctly establish the dynamics of tritium and design its recovering system, is really important the contemporary study on the effect of the defects created by different kind of radiation.

Starting from these results, Ion Beam Analysis could be appreciated as a real-time diffusion controlling technique able to dynamically measure light ions behavior of fusion materials during operational conditions. At the same time PL and Raman analysis diagnose the changing structure adding interesting information to the characterization of the damage accumulated in irradiated polycrystalline materials.

6. Conclusions

NRA technique is used to figure out the dynamics of light ions transport in solid breeder ceramics.

In the case of deuterium the annealing at temperatures as low as 100 °C promotes its release while temperatures equal and higher than 150 °C drives the whole D to be completely outgassed. The surface plays an important role in the D release and grain boundary might be an alternative path to porous for D diffusion.

^{3}He outgas shows an infection point at 550 °C, the total release occurring in the estimated BB temperature range (300 °C ÷ 900 °C). In the case of helium an important cavity formation is observed in the implanted zone, with a consequent nanocrak creation.

Since in actual breeder-blanket designs (i.e the European HCPB concept) the operational temperature will be limited to 900°C, the presented results indicate that Li-based ceramics are very promising candidates for breeder applications.

Complementary studies have been carried out to understand the release dynamics in damaged breeder ceramics. The result is that when only heavy-ion damage is present, the deuterium release is easier and faster than when also γ

effect is present. The combined effect of the ionization and the structural defects created by heavy ions probably cause a recombination or the suppression of defects helping the release (as in the case of F^+ or E' defects favoring the isotopes exchange on the surface).

In the case of both ions it possible to state that the release rate of the damaged material is quite well comparable with the as prepared one, thus confirming the important role of annihilation process of oxygen vacancies for tritium release rate.

CHAPTER 8

CONCLUSIONS

The first task of this work was addressed to learn about these materials was manufacturing and processing. The initial challenge was not only to obtain stable ceramic compounds with the highest lithium content possible, but also their manufacture as ceramic spheres, as established by the international community to meet the strict requirements of breeder blanket components. The synthetic route of spray-dryier allows the achievement of small spheres, but with a very low rate of production (0.15 gr/h). The attempt to obtain a material with high lithium content (Li8, with a Li:Si=4:1 proportion) has been achieved using the solid state reaction as synthesis route. In parallel the instability at high temperature of Li_8SiO_6 phase, has been confirmed.

Furthermore a systematic study of the effect of gamma radiation in different silicate based ceramic matrices by varying the lithium content, was undertaken. The most important thing to note is that these ceramic compounds have generally a very good stability at different irradiation doses. The discussion of the results has been performed on the basis of similarity to the effect of lithium burning. Considering the shielding role of this component in a fusion reactor, the radiation stability is a very interesting result in terms of Li burn-up. The electrical stability is extremely interesting when considering breeder blanket durability and if their performances with the other models are compared.

At the same time a study on the electrical behavior of the two materials candidates for EU and Japan (Li_4SiO_4 and Li_2TiO_3 respectively renamed as Li4 and MTi in this work) was carried on. Although not showing great differences in the activation of the electrical conductivity processes, a variation is observed in their response with increasing dose of irradiation. The PAS measurements help to explain this behavior, identifying a greater number of defects in the undamaged Li4. This result is probably due to the different manufacture methods followed for the two

ceramics. Furthermore, it has been confirmed the good physicochemical stability of MTi. This is the reason why a new material with different proportions of metatitanate / orthosilicate, is being investigated by the KIT, head of European solid breeder blanket manufacture for ITER project. Currently pebbles of this mixed composition are being characterized in collaboration with our laboratory.

Another important part of the scientific work of this thesis was the study of the behavior of implanted light ions. For its proximity behavior with Tritium, the ions chosen for this study were the isotopes of hydrogen, deuterium, and helium-3.

The results show that, in the case of deuterium, degassing takes place with very low activation energy, totally expelled at 200 ° C. In addition, the amorphization and the diffusion of the deuterium along the structure are almost uniform throughout the area ranging from the surface to the implanted region. Undoubtedly important the role played by the preferential sputtering on the dynamics of ion diffusion by the surface. The formation of vacancies favors deuterium outgases from previously damaged ceramics, by heavy ions. On the other hand it has been observed the combined effect of ionizing radiation and structural damage. The presence of dual radiation means a recombination of defects which makes the gas release dynamics really similar to the one found in the undamaged material.

Regarding the microstructure, important in the diffusion process, a particularly interesting result is obtained in the case of a material (L6) with a clear bimodality grain size, suggesting that grain boundaries represent an alternative path for diffusion.

In the case of Helium-3 implanted only in MTi samples, the total outgas temperature is much higher than that of deuterium, but still within the range of breeder blanket module operation. The existence of a turning point in the dynamics of migration He situated at about 550 °C is found. The existence of nanoscopic bubbles observed by TEM, located in planes perpendicular to the implantation direction, suggests their activation at energies higher than 550 °C, with a rapid He release.

Finally, regarding tritium behavior it is possible to affirm that further investigation on the joint behavior of different types of radiation in these materials, is necessary.

CONCLUSIONES

El departamento de materiales del laboratorio nacional de fusion, especializado en materiales funcionales, aislantes y funcionales, se ha iniciado en la problemática de los *breeder blanket sólidos* en condiciones de operación mediante este trabajo. Esta tesis se centra en el estudio de los procesos físicos que ocurren en las estructuras expuestas a diferentes tipos de radiación, su efecto en las propiedades eléctricas y en los mecanismos de transporte de iones ligeros.

La primera tarea que se abordó para conocer de cerca estos materiales fue su fabricación y procesamiento. El reto inicial ha sido, no solo obtener compuestos cerámicos estables con el más alto contenido en litio posible, sino además conseguir su fabricación en forma de esferas cerámicas, establecido así por la comunidad internacional para poder cumplir los estrictos requerimientos de la envoltura regeneradora. Esta búsqueda ha abarcado desde la puesta en marcha de un nuevo sistema de fabricación, basado en el método del *spray drying*, hasta el seguimiento continuo de las variaciones en las propiedades físicas de las cerámicas al variar su contenido en litio, las condiciones de fabricación y sinterizacion. De esta forma se ha conseguido optimizar los compuestos para los estudios posteriores. La ruta de síntesis de *spray-dryier* permite obtener esferas perfectas y muy pequeñas, aunque con una tasa de producción de material cerámico muy baja (0.15 gr/h). El intento de conseguir un material con más alto contenido en litio (Li8, con la proporción Li:Si=4:1), se ha logrado utilizando la reacción en estado sólido como vía de síntesis; de forma paralela se ha confirmado la inestabilidad a alta temperatura de la fase Li_8SiO_6.

Por otro lado se ha llevado a cabo un estudio sistemático sobre el efecto de la radiación gamma en las diferentes matrices cerámicas con base silicato al variar el contenido en litio. Hay que mencionar que las medidas eléctricas se han efectuado en el material posteriormente a su irradiación. Lo más importante a destacar entre la gran cantidad de medidas tomadas y analizadas, es que estos compuestos cerámicos presentan, en general, una muy buena estabilidad frente a diferentes dosis de irradiación. Tal efecto se ha observado en todo el rango de

concentraciones de litio estudiado. Siendo las fases presentes en casi todos ellos siempre las mismas, la discusión de los resultados se ha realizado en base a la similitud con el efecto del quemado de litio (*Li burn-up*). Considerando el rol de este componente en un reactor de fusión, esta estabilidad frente a la radiación representa un resultado muy interesante en términos del quemado de litio, ya que además de la producción de tritio, es responsable del blindaje de los imanes. La estabilidad eléctrica resulta por lo tanto extremadamente interesante a la hora de considerar su durabilidad y comparar sus prestaciones en comparación con los otros modelos.

Paralelamente se ha estudiado el comportamiento eléctrico de los dos materiales candidatos por EU y Japón (Li_4SiO_4 y Li_2TiO_3 respectivamente, renombrados como Li4 y MTi en este trabajo) para este modelo de envoltura regeneradora. Aunque no presenten gran diferencia en la activación del proceso de conductividad eléctrica, sí se observa una variación en la respuesta al incrementar la dosis de irradiación. Las medidas de espectroscopia de positrones ayudan a explicar tal comportamiento, identificando un mayor número de defectos en el Li4 no dañado. Tal resultado es probablemente debido al diferente método de fabricación seguido en la cerámica comercial y la fabricada enteramente en nuestros laboratorios.

Por otro lado, se ha confirmado la buena estabilidad físico-química del MTi. Esta es la razón por la que la fabricación y propiedades de un nuevo material, con diferentes proporciones de metatitanato/ortosilicato, esté siendo investigado por el KIT, responsable europeo de la fabricación de los cerámicos que se probarán en ITER. Actualmente pebbles de esta composición mixta están siendo caracterizadas en colaboración con nuestro laboratorio.

Otra parte importante del trabajo científico de esta tesis ha recaído en el estudio del comportamiento de los iones ligeros implantados en varias cerámicas. El interés de comprender los mecanismos de migración del tritio (resultado de la reacción nuclear del litio) en el seno de la estructura policristalina del breeder blanket sólido ha llevado al planteamiento de experiemntos de degasificación inducida por temperatura de los materiales implantados. Por su proximidad en comportamiento con el Tritio, los iones elegidos para este estudio han sido otro de los isótopos del Hidrógeno, el Deuterio y el Helio-3. El trabajo ha abarcado la caracterización microestructural, el efecto de la temperatura en el proceso de salida del gas y medidas sobre el efecto de la radiación ionizante y del daño estructural causado por la implantación de iones pesados, en las propiedades de transporte en el sólido.

Conclusiones

Los resultados muestran que, en el caso del deuterio, la desgasificación transcurre con una energía de activación muy baja, ya que a 200 °C la concentración implantada inicialmente se ha expulsado completamente de la cerámica. Además, se observa la amorfización de la estructura y una difusión del deuterio casi uniforme en toda la zona que comprende desde la superficie a la región de frenado del ion (región implantada), confiriendo a la superficie un importante papel en la salida. Se ha podido observar el efecto de la radiación en el proceso de difusión y salida del ion a través de la superficie. Indudablemente a destacar el papel jugado por el *sputtering* preferencial en la dinámica de difusión del ion, por la superficie. La formación de vacantes favorece la salida del deuterio en cerámicas previamente dañadas con iones pesados. Por otro lado se ha podido observar el efecto conjunto de la radiación ionizante y del daño estructural. Se ha encontrado que la presencia de la doble radiación implica una recombinación de los defectos que hace que la dinámica de salida del gas sea similar a la encontrada en el material no dañado.

Respecto a la microestructura, parámetro importante en el proceso de difusión, se ha encontrado un resultado especialmente interesante en el caso de un material (L6), que posee una clara bimodalidad de tamaños de granos. La difusión de Deuterio, más fácil en este caso específico, hace suponer que la más alta cantidad de bordes de granos sea responsable de una diferente cinética.

En el caso del Helio introducido por implantación en muestras de MTi, la temperatura de salida del ion gaseoso es bastante más alta que la del deuterio, pero aun así dentro del rango de funcionamiento del módulo regenerador en el reactor. Se ha observado la existencia de un punto de inflexión en la dinámica de migración del Helio situado en aprox 550°C, que ha permitido sugerir la existencia de Helio atrapado fuertemente en el sólido. Este se correspondería con el confinado en burbujas de dimensiones nanoscópicas observadas por TEM que se situarían en planos perpendiculares al plano de implantación a profundidades entre 1.6 y 1.9 micras. A temperaturas superiores a 550°C, las nanoburbujas difunden con facilidad en estos planos hasta fronteras de grano próximas donde escapan hacia la superficie del pebble.

Finalmente para intentar concluir respecto al comportamiento del tritio, podemos afirmar que es fundamental investigar mejor el comportamiento conjunto de los diferentes tipos de radiaciones en el material. Se ha podido observar con mayor claridad el efecto de la radiación ionizante y del daño estructural con iones pesados y averiguar el rol de la superficie en la salida de iones.

Conclusiones

Se han encontrado resultados interesantes, además de los que quedan por discutir para comprender plenamente el efecto de la radiación en el comportamiento de los iones ligeros en las cerámicas de litio. No obstante, podemos afirmar que los datos generados por esta tesis han permitido confirmar datos antiguos y formular nuevas hipótesis sobre ellos. La trascendencia de los resultados y la discusión con varios expertos de la comunidad científica internacional, a las que los resultados han dado lugar, muestran que hay todavía bastante trabajo por hacer.

References

[1] V. Krey, L. Clarke, Role of renewable energy in climate mitigation: a synthesis of recent scenarios, Clim. Policy. 11 (2011) 1131–1158. doi:10.1080/14693062.2011.579308.
[2] IEA - International Energy Agency, World Energy Outlook Special Report 2013: Redrawing the Energy Climate Map, 2013.
[3] G. Clarke, Lithium availability wall map, June 2011, (2011).
[4] J.P. Riley, M. Tongudai, The lithium content of sea water, Deep Sea Res. Oceanogr. Abstr. 11 (1964) 563–568. doi:10.1016/0011-7471(64)90002-6.
[5] D. Clery, A piece of the sun: the quest for fusion energy, 2013.
[6] C. Smith, The need for fusion, Fusion Eng. Des. 74 (2005) 3–8. doi:10.1016/j.fusengdes.2005.08.015.
[7] A.M. Bradshaw, T. Hamacher, U. Fischer, Is nuclear fusion a sustainable energy form?, Fusion Eng. Des. 86 (2011) 2770–2773. doi:10.1016/j.fusengdes.2010.11.040.
[8] R.L. Klueh, Reduced Activation Materials for Fusion Reactors, ASTM International, 1990.
[9] G. McCracken, P. Stott, Fusion: The Energy of the Universe, Academic Press, 2012.
[10] L.J. Perkins, R. Betti, K.N. LaFortune, W.H. Williams, Shock Ignition: A New Approach to High Gain Inertial Confinement Fusion on the National Ignition Facility, Phys. Rev. Lett. 103 (2009) 045004. doi:10.1103/PhysRevLett.103.045004.
[11] International Fusion Materials Irradiation Facility, IFMIF, n.d. http://www.ifmif.org/c/index.htm.
[12] ITER, the way to new energy, n.d. http://www.iter.org/.
[13] K. Lackner, R. Andreani, D. Campbell, M. Gasparotto, D. Maisonnier, M.. Pick, Long-term fusion strategy in Europe, J. Nucl. Mater. 307–311, Part 1 (2002) 10–20. doi:10.1016/S0022-3115(02)00970-4.
[14] E.R. Hodgson, Challenges for insulating materials in fusion applications, Nucl. Instrum. Methods Phys. Res. Sect. B Beam Interact. Mater. At. 191 (2002) 744–751. doi:10.1016/s0168-583x(02)00645-6.
[15] T. Shikama, R. Knitter, J. Konys, T. Muroga, K. Tsuchiya, A. Moesslang, et al., Status of development of functional materials with perspective on beyond-ITER, Fusion Eng. Des. 83 (2008) 976–982. doi:10.1016/j.fusengdes.2008.07.034.
[16] A. Zurita, Overview of European Fusion Materials RTD, EUROPEAN COMMISSION RESEARCH DIRECTORATE-GENERAL, Commission Européenne, B-1049 Bruxelles / Europese Commissie, B-1049 Brussel - Belgium, 2007.

http://www.instytucja.pan.pl/images/stories/pliki/programy_ue/2007/06/2906/annex1_explanatory_note_materials_en.pdf.

[17] B. Gómez-Ferrer, R. Vila, D. Jiménez-Rey, C.J. Ortiz, F. Mota, J.M. García, et al., In situ resistivity measurements of RAFM base alloys at cryogenic temperatures: The effect of proton irradiation, J. Nucl. Mater. 447 (2014) 225–232. doi:10.1016/j.jnucmat.2014.01.016.

[18] M. Roldán, P. Fernández, J. Rams, D. Jiménez-Rey, C.J. Ortiz, R. Vila, Effect of helium implantation on mechanical properties of EUROFER97 evaluated by nanoindentation, J. Nucl. Mater. 448 (2014) 301–309. doi:10.1016/j.jnucmat.2014.02.020.

[19] E. Oyarzabal, A.B. Martin-Rojo, F.L. Tabarés, Electron-induced secondary electron emission coefficient of lithium, tungsten and stainless steel surfaces exposed to low-pressure plasmas, J. Nucl. Mater. 452 (2014) 37–40. doi:10.1016/j.jnucmat.2014.04.046.

[20] P. Martin, D. Jimenez-Rey, R. Vila, F. Sánchez, R. Saavedra, Optical absorption defects created in SiO2 by Si, O and He ion irradiation, Fusion Eng. Des. (n.d.). doi:10.1016/j.fusengdes.2014.02.041.

[21] A.R. Raffray, M. Akiba, V. Chuyanov, L. Giancarli, S. Malang, Breeding blanket concepts for fusion and materials requirements, J. Nucl. Mater. 307-311 (2002) 21–30. doi:10.1016/s0022-3115(02)01174-1.

[22] L.V. Boccaccini, A. Aiello, O. Bede, F. Cismondi, L. Kosek, T. Ilkei, et al., Present status of the conceptual design of the EU test blanket systems, Fusion Eng. Des. 86 (2011) 478–483. doi:10.1016/j.fusengdes.2011.02.036.

[23] M. (comp) Dalle Donne, C. Adelhelm, H. Zimmermann, E. Wiegner, H. Werle, P. Weimar, et al., Status report. KfK contribution to the development of DEMO-relevant test blankets for NET/ITER. Pt. 2: BOT helium cooled solid breeder blanket. Vol. 1 Summary, (1991).

[24] F. Franza, Tritium Transport Analysis in HCPB DEMO Blanket with the FUS-TPC Code, KIT Scientific Publishing, 2013.

[25] I. Ricapito, A. Ciampichetti, P. Agostini, G. Benamati, Tritium processing systems for the helium cooled pebble bed test blanket module, Fusion Eng. Des. 83 (2008) 1461–1465. doi:10.1016/j.fusengdes.2008.05.041.

[26] F. Cismondi, S. Kecskés, M. Ilic, G. Légrádi, B. Kiss, O. Bitz, et al., Design update, thermal and fluid dynamic analyses of the EU-HCPB TBM in vertical arrangement, Fusion Eng. Des. 84 (2009) 607–612. doi:10.1016/j.fusengdes.2008.12.042.

[27] M.A. Abdou, D. Graumann, Choice of coolant in commercial tokamak power plants, Argonne National Lab., IL (USA), General Atomic Co., San Diego, CA (USA), 1980. http://inis.iaea.org/Search/search.aspx?orig_q=RN:12630658 (accessed May 20, 2014).

[28] M. Enoeda, M. Akiba, S. Tanaka, A. Shimizu, A. Hasegawa, S. Konishi, et al., Overview of design and R&D of test blankets in Japan, Fusion Eng. Des. 81 (2006) 415–424. doi:10.1016/j.fusengdes.2005.08.097.

[29] A. Ying, M. Akiba, L. Boccaccini, S. Casadio, G. Dellorco, M. Enoeda, et al., Status and perspective of the R&D on ceramic breeder materials for testing in ITER, J. Nucl. Mater. 367-370 (2007) 1281–1286. doi:10.1016/j.jnucmat.2007.03.240.

[30] N. Roux, Properties and performance of tritium breeding ceramics, J. Nucl. Mater. 191-194 (1992) 15–22. doi:10.1016/S0022-3115(09)80005-6.

[31] L.V. Boccaccini, J.-F. Salavy, O. Bede, H. Neuberger, I. Ricapito, P. Sardain, et al., The EU TBM systems: Design and development programme, Fusion Eng. Des. 84 (2009) 333–337. doi:10.1016/j.fusengdes.2009.01.081.

[32] T. Nishitani, M. Enoeda, M. Akiba, T. Yamanishi, K. Hayashi, H. Tanigawa, Recent progress in solid breeder blanket development at JAEA, Fusion Sci. Technol. 52 (2007) 971–978.

[33] R. Knitter, M. Kolb, U. Kaufmann, A. Goraieb, Fabrication of modified lithium orthosilicate pebbles by addition of titania, J. Nucl. Mater. 442 (2013) S433–S436. doi:10.1016/j.jnucmat.2012.10.034.

[34] R. Knitter, B. Alm, G. Roth, Crystallisation and microstructure of lithium orthosilicate pebbles, J. Nucl. Mater. 367-370 (2007) 1387–1392. doi:10.1016/j.jnucmat.2007.04.002.

[35] J. Reimann, G. Wörner, Thermal creep of Li4SiO4 pebble beds, Fusion Eng. Des. 58-59 (2001) 647–651. doi:10.1016/s0920-3796(01)00513-0.

[36] D. Aquaro, N. Zaccari, Experimental and numerical analyses on LiSO4 and Li2TiO3 pebble beds used in a ITER test blanket module, J. Nucl. Mater. 367-370 (2007) 1293–1297. doi:10.1016/j.jnucmat.2007.03.242.

[37] N. Zaccari, D. Aquaro, Mechanical characterization of Li2TiO3 and Li4SiO4 pebble beds: Experimental determination of the material properties and of the pebble bed effective values, Fusion Eng. Des. 82 (2007) 2375–2382. doi:10.1016/j.fusengdes.2007.05.008.

[38] D. Papp, D. Truong, A. Ying, N. Zaccari, Characterization of high temperature mechanical properties for lithium metatitanate pebble beds, 56 (2009) 1058–1063.

[39] A. Abou-Sena, A. Ying, M. Abdou, Effective thermal conductivity of lithium ceramic pebble beds for fusion blankets: a review, Fusion Sci. Technol. 47 (2005). http://cat.inist.fr/?aModele=afficheN&cpsidt=16846167.

[40] B. Löbbecke, R. Knitter, M. Rohde, J. Reimann, Thermal conductivity of sintered lithium orthosilicate compacts, J. Nucl. Mater. 386-388 (2009) 1068–1070. doi:10.1016/j.jnucmat.2008.12.281.

[41] G. Piazza, Behaviour of ceramic breeder materials in long time annealing experiments, Fusion Eng. Des. 58-59 (2001) 653–659. doi:10.1016/s0920-3796(01)00517-8.

[42] G. Piazza, J. Reimann, E. Günther, R. Knitter, N. Roux, J.D. Lulewicz, Characterisation of ceramic breeder materials for the helium cooled pebble bed blanket, J. Nucl. Mater. 307-311 (2002) 811–816. doi:10.1016/s0022-3115(02)00983-2.

[43] P. Calderoni, A. Ying, T. Sketchley, M. Abdou, Experimental study of the interaction of ceramic breeder pebble beds with structural materials under thermo-mechanical loads, Fusion Eng. Des. 81 (2006) 607–612. doi:10.1016/j.fusengdes.2005.07.009.

[44] A. Ying, J. Reimann, L. Boccaccini, M. Enoeda, M. Kamlah, R. Knitter, et al., Status of ceramic breeder pebble bed thermo-mechanics R&D and impact on breeder material mechanical strength, Fusion Eng. Des. 87 (2012) 1130–1137. doi:10.1016/j.fusengdes.2012.02.090.

[45] J. Tiliks, Physicochemical processes in blanket ceramic materials, Fusion Eng. Des. 69 (2003) 519–522. doi:10.1016/s0920-3796(03)00120-0.

[46] E.Carella; M.González; M.T. Hernández, Impedance analysis on Li-based ceramics exposed to gamma irradiation, Proceeding 2nd Workshop Fusion Technol. TECHNOFUSIÓN. (2012). doi:ISBN: 978-84-695-6616-9.

[47] G. Piazza, F. Scaffidi-Argentina, H. Werle, Post-irradiation examinations of Li4SiO4 pebbles irradiated in the EXOTIC-7 experiment, J. Nucl. Mater. 283-287 (2000) 1396–1400. doi:10.1016/S0022-3115(00)00300-7.

[48] A. Ying, M. Akiba, L. Boccaccini, S. Casadio, G. Dellorco, M. Enoeda, et al., Status and perspective of the R&D on ceramic breeder materials for testing in ITER, J. Nucl. Mater. 367-370 (2007) 1281–1286. doi:10.1016/j.jnucmat.2007.03.240.

[49] H. Kleykamp, Phase equilibria in the Li–Ti–O system and physical properties of Li2TiO3, Fusion Eng. Des. 61–62 (2002) 361–366. doi:10.1016/S0920-3796(02)00120-5.

[50] G. Izquierdo, A.R. West, Phase equilibria in the system Li2O-TiO2, Mater. Res. Bull. 15 (1980) 1655–1660. doi:10.1016/0025-5408(80)90248-2.

[51] H. Kleykamp, Enthalpy, heat capacity and enthalpy of transformation of Li2TiO3, J. Nucl. Mater. 295 (2001) 244–248. doi:10.1016/S0022-3115(01)00550-5.

[52] J.C. Mikkelsen, Pseudobinary Phase Relations of Li2Ti3O7, J. Am. Ceram. Soc. 63 (1980) 331–335. doi:10.1111/j.1151-2916.1980.tb10732.x.

[53] J.F. Dorrian, R.E. Newnham, Refinement of the structure of Li2TiO3, Mater. Res. Bull. 4 (1969) 179–183. doi:10.1016/0025-5408(69)90054-3.

[54] S. Claus, Phase equilibria in the Li4SiO4_Li2SiO3 region of the pseudobinary Li2O_SiO2 system, J. Nucl. Mater. 230 (1996) 8–11. doi:10.1016/0022-3115(96)00022-0.

[55] F. Kracek, The Binary System Li2O–SiO2, J Phys Chem. 34 (1929) 2641–2650. doi:10.1021/j150318a001.

[56] W.Y. Ching, Y.P. Li, B.W. Veal, D.J. Lam, Electronic structures of lithium metasilicate and lithium disilicate, Phys. Rev. B. 32 (1985) 1203–1207.

[57] K.F. Hesse, Refinement of the crystal structure of lithium polysilicate, Acta Crystallogr. B. 33 (1977) 901–902. doi:10.1107/S0567740877004932.

[58] W.H. Baur, T. Ohta, The crystal structure of Li3.75Si0.75P0.25O4 and ionic conductivity in tetrahedral structures, J. Solid State Chem. 44 (1982) 50–59. doi:10.1016/0022-4596(82)90400-5.

[59] D. Tranqui, R.D. Shannon, H.Y. Chen, S. Iijima, W.H. Baur, Crystal structure of ordered Li4SiO4, Acta Crystallogr. B. 35 (1979) 2479–2487. doi:10.1107/S0567740879009730.

[60] Y. Duan, K. Parlinski, Density functional theory study of the structural, electronic, lattice dynamical, and thermodynamic properties of Li$_4$SiO$_4$ and its capability for CO$_2$ capture, Phys. Rev. B. 84 (2011) 104113+. doi:10.1103/physrevb.84.104113.

[61] R. Hofmann, R. Hoppe, Ein neues Oxogermanat: Li8GeO6 = Li8O2[GeO4]. (Mit einer Bemerkung über Li8SiO6 und Li4GeO4), Z. Für Anorg. Allg. Chem. 555 (1987) 118–128. doi:10.1002/zaac.19875551213.

[62] B.L. Dubey, A.R. West, Crystal chemistry of Li4XO4 phases: X = Si, Ge, Ti, J. Inorg. Nucl. Chem. 35 (1973) 3713–3717. doi:10.1016/0022-1902(73)80060-0.

[63] H. Völlenkle, A. Wittmann, H. Nowotny, Die Kristallstruktur von Li4SiO4, Monatshefte Für Chem. Chem. Mon. 99 (1968) 1360–1371. doi:10.1007/BF00902680.

[64] M.E. Sawan, M.A. Abdou, Physics and technology conditions for attaining tritium self-sufficiency for the DT fuel cycle, Fusion Eng. Des. 81 (2006) 1131–1144. doi:10.1016/j.fusengdes.2005.07.035.

[65] T. Hino, H. Shibata, Y. Yamauchi, Y. Nobuta, S. Suzuki, M. Akiba, Deuterium ion irradiation for tritium breeding material and evaluation for tritium inventories in test blanket module and blanket of a demonstration reactor, J. Nucl. Mater. 417 (2011) 713–717. doi:10.1016/j.jnucmat.2010.12.124.

[66] H. Kudo, K. Okuno, Kinetics and mechanism of tritium release from neutron-irradiated Li2O, J. Nucl. Mater. 133–134 (1985) 192–195. doi:10.1016/0022-3115(85)90132-1.

[67] K. Munakata, T. Shinozaki, K. Inoue, S. Kajii, Y. Shinozaki, R. Knitter, et al., Tritium release from lithium silicate pebbles produced from lithium hydroxide, Fusion Eng. Des. 83 (2008) 1317–1320. doi:10.1016/j.fusengdes.2008.05.039.

[68] M. Nishikawa, T. Kinjyo, Y. Nishida, Chemical form of tritium released from solid breeder materials, J. Nucl. Mater. 325 (2004) 87–93. doi:10.1016/j.jnucmat.2003.11.001.

[69] J.C. Leawoods, D.A. Yablonskiy, B. Saam, D.S. Gierada, M.S. Conradi, Hyperpolarized 3He gas production and MR imaging of the lung, Concepts Magn. Reson. 13 (2001) 277–293. doi:10.1002/cmr.1014.

[70] F. Mannone, Safety in Tritium Handling Technology, Springer Science & Business Media, 1993.

[71] G. Federici, A.R. Raffray, M.A. Abdou, Mistral: A comprehensive model for tritium transport in lithium-base ceramics, J. Nucl. Mater. 173 (1990) 185–213. doi:10.1016/0022-3115(90)90257-N.

[72] M.A. Abdou, M.S. Tillack, A.R. Raffray, Thermal, fluid flow, and tritium release problems in fusion blankets, Fusion Technol. 18 (1990) 165–200.

[73] T. Kinjyo, M. Nishikawa, M. Enoeda, S. Fukada, Tritium diffusivity in crystal grain of Li2TiO3 and tritium release behavior under several purge gas

conditions, Fusion Eng. Des. 83 (2008) 580–587. doi:10.1016/j.fusengdes.2007.11.011.

[74] O.D. Slagle, G.W. Hollenberg, D.L. Baldwin, The FUBR-1B irradiation experiment — Tritium release and physical stability of solid breeder materials, J. Nucl. Mater. 179-181 (1991) 843–846. doi:10.1016/0022-3115(91)90220-2.

[75] G. Federici, C. Wu, A. Raffray, M. Billone, Modeling of tritium release from ceramic breeders: Status and some implications for next-step devices, J. Nucl. Mater. 187 (1992) 1–31. doi:10.1016/0022-3115(92)90314-b.

[76] R.E. Avila, L.A. Peña, J.C. Jiménez, Surface desorption and bulk diffusion models of tritium release from Li2TiO3 and Li2ZrO3 pebbles, J. Nucl. Mater. 405 (2010) 244–251. doi:10.1016/j.jnucmat.2010.08.009.

[77] K. Kizu, A. Pisarev, T. Tanabe, Co-permeation of deuterium and hydrogen through Pd, J. Nucl. Mater. 289 (2001) 291–302. doi:10.1016/S0022-3115(01)00428-7.

[78] R.G. Macaulay-Newcombe, D.A. Thompson, W.W. Smeltzer, Deuterium diffusion, trapping and release in ion-implanted beryllium, Fusion Eng. Des. 18 (1991) 419–424. doi:10.1016/0920-3796(91)90158-M.

[79] T. Hino, K. Koyama, Y. Yamauchi, Y. Hirohata, Hydrogen retention properties of polycrystalline tungsten and helium irradiated tungsten, Fusion Eng. Des. 39–40 (1998) 227–233. doi:10.1016/S0920-3796(98)00157-4.

[80] A. Ciampichetti, F.S. Nitti, A. Aiello, I. Ricapito, K. Liger, D. Demange, et al., Conceptual design of Tritium Extraction System for the European HCPB Test Blanket Module, Fusion Eng. Des. 87 (2012) 620–624. doi:10.1016/j.fusengdes.2012.01.047.

[81] P.M. Alcalde, C. Moreno, Á. Ibarra, Parametric analysis of LIBRETTO-4 and 5 in-pile tritium transport model on EcosimPro, Fusion Eng. Des. 89 (2014) 1510–1515. doi:10.1016/j.fusengdes.2014.04.060.

[82] G.W. Hollenberg, H. Watanabe, I.J. Hastings, S.E. Berk, BEATRIX-II: A multi-national solid breeder experiment, Pacific Northwest Lab., Richland, WA (United States). Funding organisation: USDOE, Washington, DC (United States), 1991. http://inis.iaea.org/Search/search.aspx?orig_q=RN:23038125 (accessed September 2, 2014).

[83] M.M.W. Peeters, A.J. Magielsen, M.P. Stijkel, J.G. van der Laan, In-pile tritium release behaviour of lithiummetatitanate produced by extrusion–spheroidisation–sintering process in EXOTIC-9/1 in the high flux reactor, Petten, Fusion Eng. Des. 82 (2007) 2318–2325. doi:10.1016/j.fusengdes.2007.05.036.

[84] S. van Til, A.J. Magielsen, M.P. Stijkel, H.L. Cobussen, Out of pile tritium release behaviour and microscopic investigation of lithium metatitanate irradiated in the High Flux Reactor in Petten, Fusion Eng. Des. 85 (2010) 1143–1146. doi:10.1016/j.fusengdes.2010.02.022.

[85] K. Munakata, Tritium release from catalytic breeder materials, Fusion Eng. Des. 58-59 (2001) 683–687. doi:10.1016/S0920-3796(01)00530-0.

[86] K. Munakata, T. Shinozaki, K. Inoue, S. Kajii, Y. Shinozaki, T. Takeishi, et al., Tritium release from lithium orthosilicate pebbles deposited with palladium, J. Nucl. Mater. 386-388 (2009) 1091–1094. doi:10.1016/j.jnucmat.2008.12.298.

[87] M. Kiritani, Microstructure evolution during irradiation, J. Nucl. Mater. 216 (1994) 220–264. doi:10.1016/0022-3115(94)90014-0.

[88] M. González, V. Correcher, On the cathodoluminescence and thermoluminescence emission of lithium titanate ceramics, J. Nucl. Mater. 445 (2014) 149–153. doi:10.1016/j.jnucmat.2013.10.062.

[89] D. Yamaki, Observation of the microstructural changes in lithium titanate by multi-ion irradiation, J. Nucl. Mater. 329-333 (2004) 1279–1282. doi:10.1016/j.jnucmat.2004.04.231.

[90] M. Oyaidzu, Y. Morimoto, H. Kodama, M. Sasaki, H. Kimura, K. Munakata, et al., Correlation between annihilation of radiation defects and tritium release in Li2TiO3, J. Nucl. Mater. 329-333 (2004) 1313–1317. doi:10.1016/j.jnucmat.2004.04.223.

[91] E.R. Hodgson, General radiation problems for insulating materials in future fusion devices, J. Nucl. Mater. 258–263, Part 1 (1998) 226–233. doi:10.1016/S0022-3115(98)00347-X.

[92] W.D. Kingery, Introduction to ceramics, (1960). http://www.bcin.ca/Interface/openbcin.cgi?submit=submit&Chinkey=81664 (accessed January 16, 2014).

[93] C. Kittel, P. McEuen, Introduction to solid state physics, Wiley New York, 1986. http://tocs.ulb.tu-darmstadt.de/125610068.pdf (accessed March 26, 2014).

[94] A. Chroneos, M.J.D. Rushton, R.W. Grimes, 1.02 - Fundamental Point Defect Properties in Ceramics, in: R.J.M. Konings (Ed.), Compr. Nucl. Mater., Elsevier, Oxford, 2012: pp. 47–64. http://www.sciencedirect.com/science/article/pii/B9780080560335000021 (accessed January 16, 2014).

[95] D.S. Billington, J.H. Crawford, Radiation damage in solids, Princeton University Press, 1961.

[96] N.J. Carron, An Introduction to the Passage of Energetic Particles through Matter, CRC Press, 2006.

[97] G.H. Kinchin, R.S. Pease, The displacement of atoms in solids by radiation, Rep. Prog. Phys. 18 (1955) 1–51.

[98] M.J. Norgett, M.T. Robinson, I.M. Torrens, A proposed method of calculating displacement dose rates, Nucl. Eng. Des. 33 (1975) 50–54. doi:10.1016/0029-5493(75)90035-7.

[99] S.J. Zinkle, C. Kinoshita, Defect production in ceramics, J. Nucl. Mater. 251 (1997) 200–217. doi:10.1016/S0022-3115(97)00224-9.

[100] D. Leichtle, Displacement damage parameters for fusion breeder blanket materials based on BCA computer simulations, J. Nucl. Mater. 307–311, Part 1 (2002) 793–797. doi:10.1016/S0022-3115(02)00999-6.

[101] C.J. Ortiz, A. Souidi, C.S. Becquart, C. Domain, M. Hou, Recent radiation damage studies and developments of the Marlowe code, Radiat. Eff. Defects Solids. 169 (2014) 592–602. doi:10.1080/10420150.2014.920018.

[102] S.J. Zinkle, E.R. Hodgson, Radiation-induced changes in the physical properties of ceramic materials, J. Nucl. Mater. 191–194, Part A (1992) 58–66. doi:10.1016/S0022-3115(09)80011-1.

[103] Y.-M. Chiang, D.P. Birnie, W.D. Kingery, Physical Ceramics: Principles for Ceramic Science and Engineering, Wiley, 1996.

[104] L. Hobbs, F. Clinardjr, S. Zinkle, R. Ewing, Radiation effects in ceramics, J. Nucl. Mater. 216 (1994) 291–321. doi:10.1016/0022-3115(94)90017-5.

[105] A. Abramenkovs, J. Tiliks, G. Kizane, V. Grishmanovs, A. Supe, Basic study of influence of radiation defects on tritium release processes from lithium silicates, J. Nucl. Mater. 248 (1997) 116–120. doi:10.1016/s0022-3115(97)00206-7.

[106] H. Mehrer, Diffusion in Solids: Fundamentals, Methods, Materials, Diffusion-Controlled Processes, Springer, 2007.

[107] S.J. Zinkle, Ceramics radiation effects issues for ITER, Plasma Devices Oper. 3 (1994) 139–149. doi:10.1080/10519999408201810.

[108] A. Tsuchiya, Y. Yamauchi, Y. Nobuta, T. Hino, M. Akiba, M. Enoeda, Influence of surface condition on deuterium release from Li2TiO3 pebble, Fusion Eng. Des. (n.d.). doi:10.1016/j.fusengdes.2014.03.054.

[109] J.H. Crawford, L.M. Slifkin, Point Defects in Solids: General and ionic crystals, Plenum Press, 1972.

[110] S.T. Murphy, B.P. Uberuaga, J.B. Ball, A.R. Cleave, K.E. Sickafus, R. Smith, et al., Cation diffusion in magnesium aluminate spinel, Solid State Ion. 180 (2009) 1–8. doi:10.1016/j.ssi.2008.10.013.

[111] A. Chroneos, D. Parfitt, J.A. Kilner, R.W. Grimes, Anisotropic oxygen diffusion in tetragonal La2NiO4+δ: molecular dynamics calculations, J. Mater. Chem. 20 (2009) 266–270. doi:10.1039/B917118E.

[112] D. Leichtle, U. Fischer, Qualification of irradiation effects on ceramic breeder materials in fusion and fission systems, Fusion Eng. Des. 51-52 (2000) 1–10. doi:10.1016/s0920-3796(00)00307-0.

[113] K. Okuno, H. Kudo, Tritium diffusivity in lithium-based ceramic breeders irradiated with neutrons, Fusion Eng. Des. 8 (1989) 355–358. doi:10.1016/S0920-3796(89)80131-0.

[114] A. Morales, Phase transformations on lithium silicates under irradiation, Mater. Lett. 50 (2001) 36–40. doi:10.1016/s0167-577x(00)00409-2.

[115] E. Feldbach, A. Kotlov, I. Kudryavtseva, P. Liblik, A. Lushchik, A. Maaroos, et al., Low-temperature irradiation effects in lithium orthosilicates, Nucl. Instrum. Methods Phys. Res. Sect. B Beam Interact. Mater. At. 250 (2006) 159–163. doi:10.1016/j.nimb.2006.04.100.

[116] J. Osuo, M. Kobayashi, R. Kurata, A. Hamada, W. Wang, T. Fujii, et al., Dependence of gamma-ray dose on annihilation processes of irradiation defects in Li2TiO3, Fusion Eng. Des. 86 (2011) 2362–2364. doi:10.1016/j.fusengdes.2011.04.080.

[117] G.P. Pells, Radiation effects and damage mechanisms in ceramic insulators and window materials, J. Nucl. Mater. 155–157, Part 1 (1988) 67–76. doi:10.1016/0022-3115(88)90228-0.

[118] F. Agulló-López, C.R.A. Catlow, P.D. Townsend, Point defects in materials, Academic Press, 1988.

[119] L. Wegmann, THE HISTORICAL DEVELOPMENT OF ION IMPLANTATION, in: J.F. Ziegler (Ed.), Ion Implant. Sci. Technol., Academic Press, 1984: pp. 3–49. http://www.sciencedirect.com/science/article/pii/B9780127806204500069 (accessed March 28, 2014).

[120] P.D. Townsend, Optical effects of ion implantation, Rep. Prog. Phys. 50 (1987) 501. doi:10.1088/0034-4885/50/5/001.

[121] C. Abromeit, Aspects of simulation of neutron damage by ion irradiation, J. Nucl. Mater. 216 (1994) 78–96. doi:10.1016/0022-3115(94)90008-6.

[122] G.S. Was, R.S. Averback, 1.07 - Radiation Damage Using Ion Beams, in: R.J.M. Konings (Ed.), Compr. Nucl. Mater., Elsevier, Oxford, 2012: pp. 195–221. http://www.sciencedirect.com/science/article/pii/B9780080560335000070 (accessed January 16, 2014).

[123] D.J. Mazey, Fundamental aspects of high-energy ion-beam simulation techniques and their relevance to fusion materials studies, J. Nucl. Mater. 174 (1990) 196–209. doi:10.1016/0022-3115(90)90234-E.

[124] G.L. Kulcinski, J.L. Brimhall, H.E. Kissinger, Production of voids in pure metals by high energy heavy ion bombardment, Battelle-Northwest, Richland, Wash. (USA). Pacific Northwest Lab, 1971. http://inis.iaea.org/Search/search.aspx?orig_q=RN:3017537 (accessed July 1, 2014).

[125] J.G. van der Laan, H. Kawamura, N. Roux, D. Yamaki, Ceramic breeder research and development: progress and focus, J. Nucl. Mater. 283-287 (2000) 99–109. doi:10.1016/s0022-3115(00)00352-4.

[126] A. Ying, J. Reimann, L. Boccaccini, M. Enoeda, M. Kamlah, R. Knitter, et al., Status of ceramic breeder pebble bed thermo-mechanics R&D and impact on breeder material mechanical strength, Fusion Eng. Des. 87 (2012) 1130–1137. doi:10.1016/j.fusengdes.2012.02.090.

[127] V.A. Chuyanov, D.J. Campbell, L.M. Giancarli, TBM Program implementation in ITER, Fusion Eng. Des. 85 (2010) 2005–2011. doi:10.1016/j.fusengdes.2010.07.005.

[128] J.M. Miller, H.B. Hamilton, J.D. Sullivan, Testing of lithium titanate as an alternate blanket material, J. Nucl. Mater. 212-215 (1994) 877–880. doi:10.1016/0022-3115(94)90961-X.

[129] H. Pfeiffer, Reaction mechanisms and kinetics of the synthesis and decomposition of lithium metazirconate through solid-state reaction, J. Eur. Ceram. Soc. 24 (2004) 2433–2443. doi:10.1016/S0955-2219(03)00630-7.

[130] T. Tang, Z. Zhang, J.-B. Meng, D.-L. Luo, Synthesis and characterization of lithium silicate powders, Fusion Eng. Des. 84 (2009) 2124–2130. doi:10.1016/j.fusengdes.2009.02.017.

[131] D. Mandal, M.R.K. Shenoi, S.K. Ghosh, Synthesis & fabrication of lithium-titanate pebbles for ITER breeding blanket by solid state reaction & spherodization, Fusion Eng. Des. 85 (2010) 819–823. doi:10.1016/j.fusengdes.2010.06.018.

[132] X. Wu, Z. Wen, X. Xu, X. Wang, J. Lin, Synthesis and characterization of Li4SiO4 nano-powders by a water-based sol–gel process, J. Nucl. Mater. 392 (2009) 471–475. doi:10.1016/j.jnucmat.2009.04.010.

[133] A. Deptula, M. Brykala, W. Lada, T. Olczak, B. Sartowska, A.G. Chmielewski, et al., Preparation of spherical particles of Li2TiO3(with diameters below 100μm) by sol–gel process, Fusion Eng. Des. 84 (2009) 681–684.

[134] D. Vollath, Improved methods for fabrication of lithium silicates, J. Nucl. Mater. 133-134 (1985) 221–225. doi:10.1016/0022-3115(85)90138-2.

[135] D. Cruz, H. Pfeiffer, S. Bulbulian, Synthesis of Li2MO3 (M=Ti or Zr) by the combustion method, Solid State Sci. 8 (2006) 470–475. doi:10.1016/j.solidstatesciences.2006.01.003.

[136] C.-H. Jung, Sintering characterization of Li< sub> 2</sub> TiO< sub> 3</sub> ceramic breeder powders prepared by the solution combustion synthesis process, J. Nucl. Mater. 341 (2005) 148–152.

[137] K. Tsuchiya, Fabrication development of Li2O pebbles by wet process, J. Nucl. Mater. 253 (1998) 196–202. doi:10.1016/s0022-3115(97)00312-7.

[138] J. Lulewicz, Fabrication of Li2TiO3 pebbles by the extrusion/spheronisation sintering process, J. Nucl. Mater. 307-311 (2002) 803–806. doi:10.1016/s0022-3115(02)00981-9.

[139] J.T. Van Lew, A. Ying, M. Abdou, A discrete element method study on the evolution of thermomechanics of a pebble bed experiencing pebble failure, Fusion Eng. Des. (n.d.). doi:10.1016/j.fusengdes.2014.04.066.

[140] S. Lagos, R. Becerra, Methodology for the recovery of lithium from lithium titanate, J. Nucl. Mater. 347 (2005) 134–139. doi:10.1016/j.jnucmat.2005.08.013.

[141] C. Alvani, Li2TiO3 pebbles reprocessing, recovery of 6Li as Li2CO3, J. Nucl. Mater. 307-311 (2002) 837–841. doi:10.1016/s0022-3115(02)01119-4.

[142] R. Knitter, B. Lobbecke, Reprocessing of lithium orthosilicate breeder material by remelting, J. Nucl. Mater. 361 (2007) 104–111. doi:10.1016/j.jnucmat.2006.11.005.

[143] R. Knitter, P. Chaudhuri, Y. Feng, T. Hoshino, I. Yu, Recent developments of solid breeder fabrication, J. Nucl. Mater. (2013). doi:10.1016/j.jnucmat.2013.02.060.

[144] Y.J. Feng, K.M. Feng, Q.X. Cao, J. Hu, H. Tang, Fabrication and characterization of Li4SiO4 pebbles by melt spraying method, Fusion Eng. Des. 87 (2012) 753–756. doi:10.1016/j.fusengdes.2012.02.016.

[145] X. Wu, Z. Wen, X. Xu, Y. Liu, Fabrication of Li4SiO4 pebbles by a sol–gel technique, Fusion Eng. Des. 85 (2010) 222–226. doi:10.1016/j.fusengdes.2010.01.018.

[146] S. Zimin, Simplified methods for estimations of 3T production in boronized shielding materials and Li burn up in breeder blankets, Fusion Eng. Des. 23 (1993) 1–16. doi:10.1016/0920-3796(93)90106-R.

[147] D. Vollath, H. Wedemeyer, On the preparation of the lithium siclicates series from LiSiO to LiSiO in alcoholic media, J. Nucl. Mater. 141-143 (1986) 334–338. doi:10.1016/s0022-3115(86)80060-5.

[148] H. Kawamura, Evaluation of effective thermal diffusivity of Li2TiO3 pebble bed under neutron irradiation, Fusion Eng. Des. 69 (2003) 263–267. doi:10.1016/s0920-3796(03)00351-x.

[149] T. Fehr, E. Schmidbauer, Electrical conductivity of Li2TiO3 ceramics, Solid State Ion. 178 (2007) 35–41. doi:10.1016/j.ssi.2006.11.002.

[150] R. Bud, D.J. Warner, Instruments of Science: An Historical Encyclopedia, Taylor & Francis, 1998.

[151] R. Jenkins, R. Snyder, Introduction to X-Ray Powder Diffractometry, John Wiley & Sons, 2012.

[152] B.E. Warren, X-ray Diffraction, Courier Dover Publications, 1969.

[153] F.A. Settle, Handbook of Instrumental Techniques for Analytical Chemistry, Edición: Har/Cdr, Prentice-Hall, Upper Saddle River, NJ, 1997.

[154] A. Benninghoven, F.G. Rüdenauer, H.W. Werner, Secondary Ion Mass Spectrometry: Basic Concepts, Instrumental Aspects, Applications, and Trends, J. Wiley, 1987.

[155] S. Lowell, Characterization of Porous Solids and Powders: Surface Area, Pore Size and Density, Springer, 2004.

[156] T. Allen, Particle Size Measurement: Volume 2: Surface Area and Pore Size Determination., Springer, 1997.

[157] D. McMullan, Scanning electron microscopy 1928–1965, Scanning. 17 (1995) 175–185. doi:10.1002/sca.4950170309.

[158] D.B. Williams, C.B. Carter, The Transmission Electron Microscope, in: Transm. Electron Microsc., Springer US, 1996: pp. 3–17. http://link.springer.com/chapter/10.1007/978-1-4757-2519-3_1 (accessed May 12, 2014).

[159] N.F. Cheville, J. Stasko, Techniques in Electron Microscopy of Animal Tissue, Vet. Pathol. Online. 51 (2014) 28–41. doi:10.1177/0300985813505114.

[160] M. Baram, W.. Kaplan, Quantitative HRTEM analysis of FIB prepared specimens, J. Microsc. 232 (2008) 395–405. doi:10.1111/j.1365-2818.2008.02134.x.

[161] M. González, R. Román, C. Maffiotte, J. González-Casablanca, R. Perez, D. Hole, A broad chemical and structural characterization of the damaged region of carbon implanted alumina, Nucl. Instrum. Methods Phys. Res. Sect. B Beam Interact. Mater. At. 267 (2009) 1468–1471. doi:10.1016/j.nimb.2009.01.086.

[162] Z. Lu, A.Y. Ying, M.A. Abdou, Numerical and experimental prediction of the thermomechanical performance of pebble beds for solid breeder blanket, Fusion Eng. Des. 49–50 (2000) 605–611. doi:10.1016/S0920-3796(00)00348-3.

[163] K. Tsuchiya, H. Kawamura, S. Tanaka, Evaluation of contact strength of Li2TiO3 pebbles with different diameters, Fusion Eng. Des. 81 (2006) 1065–1069. doi:10.1016/j.fusengdes.2005.07.031.

[164] H. Migge, Estimation of free energies for Li8SiO6 and Li4SiO4 and calculation of the phase diagram of the Li-Si-O system, J. Nucl. Mater. 151 (1988) 101–107. doi:10.1016/0022-3115(88)90061-x.

[165] D.F. Fletcher, B. Guo, D.J.E. Harvie, T.A.G. Langrish, J.J. Nijdam, J. Williams, What is important in the simulation of spray dryer performance and how do current CFD models perform?, Appl. Math. Model. 30 (2006) 1281–1292. doi:10.1016/j.apm.2006.03.006.

[166] W.R. Niessen, Combustion and Incineration Processes: Applications in Environmental Engineering, Third Edition, CRC Press, 2002.

[167] E. Carella, M.T. Hernandez, High lithium content silicates: A comparative study between four routes of synthesis, Ceram. Int. (n.d.). doi:10.1016/j.ceramint.2014.02.023.

[168] K. Buijs, C.J.. Schutte, The infra-red spectra and structures of Li2CO3 and anhydrous Na3CO3, Spectrochim. Acta. 17 (1961) 927–932. doi:10.1016/0371-1951(61)80028-3.

[169] W. De Almeida, P. O'Malley, Ab initio infrared and Raman spectra of the H3SiO4− monomeric anionic species, Vib. Spectrosc. 5 (1993) 325–335. doi:10.1016/0924-2031(93)87008-h.

[170] P.J. Swedlund, R.D. Hamid, G.M. Miskelly, Insights into H4SiO4 surface chemistry on ferrihydrite suspensions from ATR-IR, Diffuse Layer Modeling and the adsorption enhancing effects of carbonate, J. Colloid Interface Sci. 352 (2010) 149–157. doi:10.1016/j.jcis.2010.08.011.

[171] P. Tarte, Identification of Li-O bands in the infra-red spectra of simple lithium compounds containing LiO4 tetrahedra, Spectrochim. Acta. 20 (1964) 238–240. doi:10.1016/0371-1951(64)80014-x.

[172] T. Tang, P. Chen, W. Luo, D. Luo, Y. Wang, Crystalline and electronic structures of lithium silicates: A density functional theory study, J. Nucl. Mater. 420 (2012) 31–38. doi:10.1016/j.jnucmat.2011.08.040.

[173] M. Nocuń, M. Handke, Identification of Li–O absorption bands based on lithium isotope substitutions, J. Mol. Struct. 596 (2001) 145–149. doi:10.1016/s0022-2860(01)00702-5.

[174] H. Aguiar, J. Serra, P. González, B. León, Structural study of sol–gel silicate glasses by IR and Raman spectroscopies, J. Non-Cryst. Solids. 355 (2009) 475–480. doi:10.1016/j.jnoncrysol.2009.01.010.

[175] G. Ilyushin, Cluster self-organization of germanate systems: Suprapolyhedral nanocluster precursors and self-assembly of the Li8GeO6, Li4GeO4, and Li6Ge2O7 crystal structures, Crystallogr. Rep. 57 (2012) 478–489. doi:10.1134/s1063774512040074.

[176] T. Nakazawa, D. Yamaki, K. Noda, A study on irradiation-induced structural change of lithium orthosilicate by infrared spectroscopy analysis with MNDO

calculation, J. Nucl. Mater. 248 (1997) 121–127. doi:10.1016/s0022-3115(97)00168-2.

[177] E. Carella, M. Gonzalez, R. Gonzalez-Arrabal, D-depth profiling in as-implanted and annealed Li-based Breeder Blanket ceramics, J. Nucl. Mater. (2013). doi:10.1016/j.jnucmat.2013.02.073.

[178] T. Shikama, K. Yasuda, S. Yamamoto, C. Kinoshita, S.J. Zinkle, E.R. Hodgson, Irradiation effects in ceramics for fusion reactor applications, J. Nucl. Mater. 271–272 (1999) 560–568. doi:10.1016/S0022-3115(98)00872-1.

[179] S. Konishi, H. Ohno, Electrical Conductivity of Polycrystalline Li2SiO3 and γ-LiAlO2, J. Am. Ceram. Soc. 67 (1984) 418–419. doi:10.1111/j.1151-2916.1984.tb19727.x.

[180] E.R. Hodgson, General radiation problems for insulating materials in future fusion devices, J. Nucl. Mater. 258–263, Part 1 (1998) 226–233. doi:10.1016/S0022-3115(98)00347-X.

[181] T. Shikama, R. Knitter, J. Konys, T. Muroga, K. Tsuchiya, A. Moesslang, et al., Status of development of functional materials with perspective on beyond-ITER, Fusion Eng. Des. 83 (2008) 976–982. doi:10.1016/j.fusengdes.2008.07.034.

[182] M. Decreton, T. Shikama, E. Hodgson, Performance of functional materials and components in a fusion reactor: the issue of radiation effects in ceramics and glass materials for diagnostics, J. Nucl. Mater. 329-333 (2004) 125–132. doi:10.1016/j.jnucmat.2004.04.012.

[183] S. González de Vicente, A. Moroño, E. Hodgson, A model for electrical degradation of insulators due to ionic bombardment, J. Nucl. Mater. 417 (2011) 790–793. doi:10.1016/j.jnucmat.2010.12.161.

[184] R.Z. Mekhtieva, Effect of Gamma Irradiation on the Piezoelectric Properties of K2Sr4Nb10O30–K6Li4Nb10O30 Solid Solutions, Inorg. Mater. 38 (2002) 831–833. doi:10.1023/A:1019787013348.

[185] F. Alessandrini, In-situ tritium release (CORELLI-2 experiment) and ex-reactor ionic conductivity of substoichiometric LiAlO2 breeder ceramics, J. Nucl. Mater. 224 (1995) 236–244. doi:10.1016/0022-3115(95)00075-5.

[186] Y. Nishikawa, M. Oyaidzu, A. Yoshikawa, K. Munakata, M. Okada, M. Nishikawa, et al., Correlation between tritium release and thermal annealing of irradiation damage in neutron-irradiated Li2SiO3, J. Nucl. Mater. 367-370 (2007) 1371–1376. doi:10.1016/j.jnucmat.2007.03.251.

[187] K. Moritani, Tritium release kinetics of lithium silicates with irradiation defects, Fusion Eng. Des. 39-40 (1998) 675–683. doi:10.1016/S0920-3796(98)00102-1.

[188] K. Noda, M. Arita, Y. Ishii, H. Saka, T. Imura, K. Kuroda, et al., Mechanical properties of lithium oxide at high temperatures, J. Nucl. Mater. 141–143, Part 1 (1986) 353–356. doi:10.1016/S0022-3115(86)80064-2.

[189] K. Okuno, H. Kudo, Chemical states of tritium and interaction with radiation damages in Li2O crystals, J. Nucl. Mater. 138 (1986) 31–35. doi:10.1016/0022-3115(86)90251-5.

[190] T. Tang, D.-L. Luo, Density functional theory study of electronic structures in lithium silicates: Li2SiO3 and Li4SiO4, J. At. Mol. Sci. (2010). doi:10.4208/jams.110609.113009a.

[191] Z. Wan, Y. Yu, H.F. Zhang, T. Gao, X.J. Chen, C.J. Xiao, First-principles study of electronic, dynamical and thermodynamic properties of Li2TiO3, Eur. Phys. J. B. 85 (2012) 1–7. doi:10.1140/epjb/e2012-20666-5.

[192] L. Padilla-Campos, A theoretical investigation of occupation sites for tritium atoms in lithium titanate, J. Mol. Struct. THEOCHEM. 621 (2003) 107–112. doi:10.1016/s0166-1280(02)00538-9.

[193] M. Vijayakumar, S. Kerisit, Z. Yang, G.L. Graff, J. Liu, J.A. Sears, et al., Combined 6,7Li NMR and Molecular Dynamics Study of Li Diffusion in Li2TiO3, J. Phys. Chem. C. 113 (2009) 20108–20116. doi:10.1021/jp9072125.

[194] P. Agarwal, M.E. Orazem, L.H. Garcia-Rubio, Measurement Models for Electrochemical Impedance Spectroscopy I . Demonstration of Applicability, J. Electrochem. Soc. 139 (1992) 1917–1927. doi:10.1149/1.2069522.

[195] J. Bauerle, Study of solid electrolyte polarization by a complex admittance method, J. Phys. Chem. Solids. 30 (1969) 2657–2670. doi:10.1016/0022-3697(69)90039-0.

[196] J. Fleig, The influence of non-ideal microstructures on the analysis of grain boundary impedances, Solid State Ion. 131 (2000) 117–127. doi:10.1016/S0167-2738(00)00627-5.

[197] S.B. Adnan, N.S. Mohamed, K.A. Norwati, Li4SiO4 Prepared by Sol-gel Method as Potential Host for LISICON Structured Solid Electrolytes, World Acad. Sci. Eng. Technol. 74 (2011) 670–673.

[198] M. Wilkening, P. Heitjans, Extremely slow cation exchange processes in Li4SiO4 probed directly by two-time 7Li stimulated-echo nuclear magnetic resonance spectroscopy, J. Phys. Condens. Matter. 18 (2006) 9849–9862. doi:10.1088/0953-8984/18/43/007.

[199] A.A. Morales, H. Pfeiffer, A. Delfin, S. Bulbulian, Phase transformations on lithium silicates under irradiation, Mater. Lett. 50 (2001) 36–40. doi:10.1016/S0167-577X(00)00409-2.

[200] Bernard A. Boukamp, EQUIVCRT Software, University of Twente, Enschede, Netherlands, 1993.

[201] Scribner Associates, Inc, ZView, Southern Pines, North Carolina, n.d. http://www.scribner.com/zplot-and-zview-for-windows-software-downloads.html.

[202] J.W. Fergus, Ceramic and polymeric solid electrolytes for lithium-ion batteries, J. Power Sources. 195 (2010) 4554–4569. doi:10.1016/j.jpowsour.2010.01.076.

[203] K. Munakata, Y. Yokoyama, Ab Initio Study of Electron State in Li4SiO4 Crystal, J. Nucl. Sci. Technol. 38 (2001) 915–918. doi:10.1080/18811248.2001.9715117.

[204] N. Mott, Conduction in glasses containing transition metal ions, J. Non-Cryst. Solids. 1 (1968) 1–17. doi:10.1016/0022-3093(68)90002-1.

[205] S. Pizzini, Ionic conductivity in lithium compounds, J. Appl. Electrochem. 1 (1971) 153–161. doi:10.1007/bf00616937.

[206] T. van Dijk, A.J. Burggraaf, Grain boundary effects on ionic conductivity in ceramic GdxZr1–xO2–(x/2) solid solutions, Phys. Status Solidi A. 63 (1981) 229–240. doi:10.1002/pssa.2210630131.

[207] J. Fleig, J. Maier, A Finite Element Study on the Grain Boundary Impedance of Different Microstructures, J. Electrochem. Soc. 145 (1998) 2081–2089. doi:10.1149/1.1838600.

[208] F.H. El Batal, A.H. Ashour, Effect of gamma irradiation on the electrical conductivity of ternary borate glasses, Mater. Chem. Phys. 77 (2003) 677–686. doi:10.1016/S0254-0584(02)00127-X.

[209] S.T. Murphy, P. Zeller, A. Chartier, L. Van Brutzel, Atomistic Simulation of the Structural, Thermodynamic, and Elastic Properties of Li2TiO3, J. Phys. Chem. C. 115 (2011) 21874–21881. doi:10.1021/jp204678c.

[210] J. Du, L.R. Corrales, Characterization of the Structural and Electronic Properties of Crystalline Lithium Silicates, J. Phys. Chem. B. 110 (2006) 22346–22352. doi:10.1021/jp056879s.

[211] W. Schmidt, Positron Annihilation Spectroscopy, in: F. Schüth, K.S.W. Sing, J. Weitkamp (Eds.), Handb. Porous Solids, Wiley-VCH Verlag GmbH, 2002: pp. 506–532. http://onlinelibrary.wiley.com/doi/10.1002/9783527618286.ch15/summary (accessed June 16, 2014).

[212] M. Nagai, M. Hibino, T. Nishino, K. Noda, Effect of γ-ray irradiation on Li2O ceramics, J. Mater. Sci. Lett. 12 (1993) 107–109. doi:10.1007/bf00241862.

[213] E. Carella, M. Leon, T. Sauvage, M. Gonzalez, On ion implantation and damage effect in Li2TiO3 as a fusion breeder blanket: A technological approach for degradation testing, Fusion Eng. Des. (n.d.). doi:10.1016/j.fusengdes.2014.02.072.

[214] S. Sato, T. Nishitani, C. Konno, Effects of lithium burn-up on TBR in DEMO reactor SlimCS, Fusion Eng. Des. 87 (2012) 680–683. doi:10.1016/j.fusengdes.2012.02.006.

[215] C.E. Johnson, Tritium behavior in lithium ceramics, J. Nucl. Mater. 270 (1999) 212–220. doi:10.1016/S0022-3115(98)00905-2.

[216] H. Zhang, A. Ying, M. Abdou, Integrated simulation of tritium permeation in solid breeder blankets, Fusion Eng. Des. 85 (2010) 1711–1715. doi:10.1016/j.fusengdes.2010.05.018.

[217] J.A. Sawicki, L.M. Howe, K. Noda, Chemisorption and implantation of hydrogen isotopes in lithium-based fusion blanket ceramics and their thermal release, Atomic Energy of Canada Ltd., Chalk River, ON (Canada). Chalk River Nuclear Labs, 1988. http://inis.iaea.org/Search/search.aspx?orig_q=RN:21048126 (accessed July 7, 2014).

[218] C. Kang, X. Wang, C. Xiao, X. Gao, M. Gu, J. Liu, et al., Out-of-pile tritium release study on Li4SiO4 pebbles from TRINPC-I experiments, J. Nucl. Mater. 412 (2011) 62–65. doi:10.1016/j.jnucmat.2011.02.018.

[219] K. Morita, H. Suzuki, E. Iizuka, T. Hayashi, K. Soda, H. Iwahara, A New Model for Exchange of Deuterium in Oxide Ceramics for Protium in Light Water Molecule at Room Temperature, J. Nucl. Sci. Technol. 38 (2001) 930–935. doi:10.1080/18811248.2001.9715119.

[220] H. Khodja, C. Brosset, N. Bernier, Deuterium inventory in plasma facing materials by means of NRA: A microbeam probe approach, Nucl. Instrum. Methods Phys. Res. Sect. B Beam Interact. Mater. At. 266 (2008) 1425–1429. doi:10.1016/j.nimb.2007.11.027.

[221] E. Carella, M. Gonzalez, R. Gonzalez-Arrabal, D-depth profiling in as-implanted and annealed Li-based breeder blanket ceramics, J. Nucl. Mater. 438 (2013) 193–198. doi:10.1016/j.jnucmat.2013.02.073.

[222] E. Carella, M. González, 3He Behaviour in Li2TiO3 Ceramics for Fusion Breeding Blanket Applications, Energy Procedia. 41 (2013) 26–33. doi:10.1016/j.egypro.2013.09.003.

[223] C.E. Johnson, J.P. Kopasz, S.-W. Tam, Advanced understanding of the tritium recovery process from the ceramic breeder blanket, J. Nucl. Mater. 248 (1997) 91–100. doi:10.1016/s0022-3115(97)00203-1.

[224] A. Tsuchiya, T. Hino, Y. Yamauchi, Y. Nobuta, M. Akiba, M. Enoeda, Removal of Deuterium in Lithium Titanate by Sweep Gas Exposure, (n.d.).

[225] E.C. M. Gonzalez, 2011 technical advances in the framework of the Materials Characterization Techniques Lab of TechnoFusión, Proceeding 2nd Workshop Fusion Technol. Contrib. TECHNOFUSIÓN. (2012). doi:ISBN: 978-84-695-6616-9.

[226] W.R. Wampler, Ion beam analysis for fusion energy research, Nucl. Instrum. Methods Phys. Res. Sect. B Beam Interact. Mater. At. 219–220 (2004) 836–845. doi:10.1016/j.nimb.2004.01.173.

[227] M. Rubel, Analysis of plasma facing materials: material migration and fuel retention, Phys. Scr. 2006 (2006) 54. doi:10.1088/0031-8949/2006/T123/007.

[228] R.C. Bird, J.S. Williams, Ion Beams for Materials Analysis, Elsevier, 1990.

[229] Handbook Modern Ion Beam Materials Analysis Volume 1 2nd Edition | Materials science | Cambridge University Press, (n.d.). http://www.cambridge.org/us/academic/subjects/engineering/materials-science/handbook-modern-ion-beam-materials-analysis-volume-1-2nd-edition (accessed April 14, 2014).

[230] J.F. Ziegler, Stopping of energetic light ions in elemental matter, J. Appl. Phys. 85 (1999) 1249–1272. doi:10.1063/1.369844.

[231] J. Bottiger, A review on depth profiling of hydrogen and helium isotopes within the near-surface region of solids by use of ion beams, J. Nucl. Mater. 78 (1978) 161–181. doi:10.1016/0022-3115(78)90515-9.

[232] F. Pászti, Microanalysis of He using charged particle accelerators, Nucl. Instrum. Methods Phys. Res. Sect. B Beam Interact. Mater. At. 66 (1992) 83–106. doi:10.1016/0168-583X(92)96143-M.

[233] Y. Isobe, Analysis of deuterium and lithium on titanium surface by NRA method, Nucl. Instrum. Methods Phys. Res. Sect. B Beam Interact. Mater. At. 170 (2000) 171–179. doi:10.1016/s0168-583x(00)00090-2.

[234] V. Alimov, M. Mayer, J. Roth, Differential cross-section of the D(3He,p)4He nuclear reaction and depth profiling of deuterium up to large depths, Nucl. Instrum. Methods Phys. Res. Sect. B Beam Interact. Mater. At. 234 (2005) 169–175. doi:10.1016/j.nimb.2005.01.009.

[235] W. Möller, F. Besenbacher, A note on the 3He + D nuclear-reaction cross section, Nucl. Instrum. Methods. 168 (1980) 111–114. doi:10.1016/0029-554X(80)91239-2.

[236] I.G. Hughes, R. Behrisch, A.P. Martinelli, Depth profiling of deuterium using nuclear reaction analysis, Nucl. Instrum. Methods Phys. Res. Sect. B Beam Interact. Mater. At. 79 (1993) 487–489. doi:10.1016/0168-583X(93)95395-L.

[237] W. MÖLLER, B.M.U. SCHERZER, R. BEHRISCH, THE APPLICATION OF ION BEAM METHODS TO DIFFUSION AND PERMEATION MEASUREMENTS, in: H.H. ANDERSEN, J. BØTTIGER, H. KNUDSEN (Eds.), Ion Beam Anal., Elsevier, 1980: pp. 289–294. http://www.sciencedirect.com/science/article/pii/B9781483228891500487 (accessed June 25, 2014).

[238] J.F. Ziegler, M.D. Ziegler, J.P. Biersack, SRIM – The stopping and range of ions in matter (2010), Nucl. Instrum. Methods Phys. Res. Sect. B Beam Interact. Mater. At. 268 (2010) 1818–1823. doi:10.1016/j.nimb.2010.02.091.

[239] M. Mayer, SIMNRA User's Guide, 2002. http://www2.if.usp.br/~lamfi/guia-simnra.pdf (accessed November 13, 2013).

[240] J.A. Fernando, D.D.L. Chung, Pore Structure and Permeability of an Alumina Fiber Filter Membrane for Hot Gas Filtration, J. Porous Mater. 9 (2002) 211–219.

[241] S.-J. Lee, I.-K. Yu, S. Cho, SYNTHESIS AND SINTERING BEHAVIOUR OF Li 4 SiO 4 FABRICATED BY A PVA POLYMER SOLUTION ROUTE, J. Ceram. Process. Res. 12 (2011) 183–186.

[242] X. Gao, X. Chen, M. Gu, C. Xiao, S. Peng, Fabrication and characterization of Li4SiO4 ceramic pebbles by wet method, J. Nucl. Mater. 424 (2012) 210–215. doi:10.1016/j.jnucmat.2012.02.018.

[243] M.H.H. Kolb, M. Bruns, R. Knitter, S. van Til, Lithium orthosilicate surfaces: Characterization and effect on tritium release, J. Nucl. Mater. 427 (2012) 126–132. doi:10.1016/j.jnucmat.2012.04.024.

[244] P.C. Bertone, The kinetics that govern the release of tritium from neutron-irradiated lithium oxide, J. Nucl. Mater. 151 (1988) 293–300. doi:10.1016/0022-3115(88)90022-0.

[245] G. Martin, T. Sauvage, P. Desgardin, P. Garcia, G. Carlot, M. Barthe, Accurate automated non-resonant NRA depth profiling: Application to the low 3He concentration detection in UO2 and SiC, Nucl. Instrum. Methods Phys. Res. Sect. B Beam Interact. Mater. At. 258 (2007) 471–478. doi:10.1016/j.nimb.2007.01.288.

[246] F. Chamssedine, T. Sauvage, S. Peuget, DIADDHEM set-up: New IBA facility for studying the helium behavior in nuclear glasses, Nucl. Instrum. Methods Phys. Res. Sect. B Beam Interact. Mater. At. 268 (2010) 1862–1866. doi:10.1016/j.nimb.2010.02.031.

[247] T. Sauvage, H. Erramli, S. Guilbert, L. Vincent, M.-F. Barthe, P. Desgardin, et al., Profile measurements of helium implanted in UO2 sintered pellets by using the 3He(d, α)1H nuclear reaction analysis technique, J. Nucl. Mater. 327 (2004) 159–164. doi:10.1016/j.jnucmat.2004.02.002.

[248] S.J. Zinkle, Effect of H and He irradiation on cavity formation and blistering in ceramics, Nucl. Instrum. Methods Phys. Res. Sect. B Beam Interact. Mater. At. 286 (2012) 4–19. doi:10.1016/j.nimb.2012.03.030.

[249] A. Ibarra, E.R. Hodgson, The ITER project: the role of insulators, Nucl. Instrum. Methods Phys. Res. Sect. B Beam Interact. Mater. At. 218 (2004) 29–35. doi:10.1016/j.nimb.2003.12.048.

[250] I.A. Leonidov, O.N. Leonidova, L.A. Perelyaeva, R.F. Samigullina, S.A. Kovyazina, M.V. Patrakeev, Structure, ionic conduction, and phase transformations in lithium titanate Li4Ti5O12, Phys. Solid State. 45 (2003) 2183–2188. doi:10.1134/1.1626760.

[251] V.V. Fomichev, E.V. Proskuryakova, Vibrational Spectra and Energy Characteristics of the Superionics Li4SiO4and Li4GeO4, J. Solid State Chem. 134 (1997) 232–237.

[252] E.V. Proskuryakova, O.I. Kondratov, N.V. Porotnikov, K.I. Petrov, Interpretation of $LaCrO_3$ and $YCrO_3$ vibrational spectra, (1986). http://inis.iaea.org/Search/search.aspx?orig_q=RN:18030760 (accessed August 25, 2014).

[253] T. Nakazawa, V. Grismanovs, D. Yamaki, Y. Katano, T. Aruga, Disordering in Li2TiO3 irradiated with high energy ions, Nucl. Instrum. Methods Phys. Res. Sect. B Beam Interact. Mater. At. 206 (2003) 166–170. doi:10.1016/S0168-583X(03)00712-2.

[254] T. Nakazawa, A. Naito, T. Aruga, V. Grismanovs, Y. Chimi, A. Iwase, et al., High energy heavy ion induced structural disorder in Li2TiO3, J. Nucl. Mater. 367-370 (2007) 1398–1403. doi:10.1016/j.jnucmat.2007.04.003.

[255] K. Moritani, H. Moriyama, In situ luminescence measurement of irradiation defects in ternary lithium ceramics under ion beam irradiation, J. Nucl. Mater. 248 (1997) 132–139. doi:10.1016/s0022-3115(97)00194-3.

[256] H. Katsui, S. Nagata, B. Tsuchiya, T. Shikama, Hydrogen trapping and luminescence characteristic in ion-implanted Li2TiO3 and Li2ZrO3, Nucl. Instrum. Methods Phys. Res. Sect. B Beam Interact. Mater. At. 272 (2012) 275–279. doi:10.1016/j.nimb.2011.01.082.

[257] M. Kobayashi, K. Toda, Y. Oya, K. Okuno, Dependency of irradiation damage density on tritium migration behaviors in Li2TiO3, J. Nucl. Mater. 447 (2014) 1–8. doi:10.1016/j.jnucmat.2013.12.001.

[258] J.P. Kopasz, J.M. Miller, C.E. Johnson, Tritium release from lithium titanate, a low-activation tritium breeding material, J. Nucl. Mater. 212-215 (1994) 927–931. doi:10.1016/0022-3115(94)90971-7.

Publications and conference contributions

PUBLICATIONS

E. Carella, B. Gomez-Ferrer, M. Gonzalez, R. Gonzalez-Arrabal, C.Salgado, R.Vila
"*Annual progress in the technical development of the TechnoFusión Materials Characterization Area*"
1st Workshop on Fusion Technologies and the Contribution of TECHNOFUSIÓN, Proceedings, Sección de Publicaciones de la UPM (2011).

E. Carella, T. Hernández
"*Ceramics for fusion Reactors. The role of the Lithium orthosilicate as breeder*"
Physica B: Condensed Matter, Vol. 407, Issue 22, (2012) 4431-4435.

E.Carella, M.Gonzalez, T. Hernandez
"*Impedance analysis on Li-based ceramics exposed to gamma irradiation*"
2nd Workshop on Fusion Technologies and the Contribution of TECHNOFUSIÓN, Proceedings, Sección de Publicaciones de la UC3M (2012).

E. Carella, M. Gonzalez, R. Gonzalez-Arrabal
"*D-depth profiling in as-implanted and annealed Li-based Breeder Blanket ceramics*"
Journal of Nuclear Materials, 438, Issues 1–3 (2013) 193-198 .

E.Carella, M.González
"*^{3}He Behaviour in Li_2TiO_3 Ceramics for Fusion Breeding Blanket Applications*"
Energy Procedia, 41 (2013) 26-33.

E.Carella, R. Gonzalez-Arrabal, Q.Zhao, A.Ibarra, M.Gonzalez
"*Influence of the microstructure on the light species behaviour in ceramic breeder blanket materials*"
Proceedings of the 17th IEA International Workshop on Ceramic Breeder Blanket Interactions (CBBI-17), ISBN978-3-7315-0101-5 (2013) 85-98.

E.Carella, T.Hernandez, A.Ibarra, E.Chinarro, B.Moreno

"*Correlation between electrical behavior and tritium release in γ-irradiated Li_4SiO_4 breeder pellets and pebbles*"
Proceedings of the 17th IEA International Workshop on Ceramic Breeder Blanket Interactions (CBBI-17), ISBN978-3-7315-0101-5 (2013) 219-232.

M.Gonzalez, E.Carella, A.Ibarra, B. Courtois, R.Bes, T.Sauvage
"*He thermal induced diffusion in lithium titanate*"
Proceedings of the 17th IEA International Workshop on Ceramic Breeder Blanket Interactions (CBBI-17), ISBN978-3-7315-0101-5 (2013) 233-247.

E. Carella, T. Hernández
"*High lithium content silicates: A comparative study between four routes of synthesis*"
Ceramics International, *40*, Issue 7, Part A, (August 2014) 9499–9508.

E.Carella, T.Sauvage, R.Bès, B.Courtois, M.González.
"*Nuclear Reaction Analysis as a tool for the ^3He thermal evolution in Li_2TiO_3 ceramics*"
Nuclear Instruments and Methods B, 332, 1 (August 2014) 85–89.

E.Carella, M.Leon, T. Sauvage, M.Gonzalez
"*On ion implantation and damage effect in Li_2TiO_3 as a fusion breeder blanket: a technological approach for degradation testing*"
Fusion Engineering and Design, 89, Issue 7-8 (March 2014) 1529 – 1533.

E.Carella, M.T. Hernández
"
Fusion Engineering and Design, *Accepted, under revision.*

CONFERENCES CONTRIBUTIONS

X Reunión Nacional de Electrocerámica-Madrid 13-15/07/2011
Contribución oral:
ESPECTROSCOPIA DE IMPEDANCIA COMO MEDIDA DE LA MOVILIDAD DEL LITIO EN CERÁMICAS PARA FUSIÓN
E.Carella, M.Gonzalez, M.T.Hernandez

12th Conference of European Ceramic Society-Stockholm 19-23/06/2011
Poster:
CERAMICS FOR FUSION REACTORS. THE ROLE OF THE LITHIUM ORTHOSILICATE AS BREEDER
E.Carella, M.T. Hernández

Ion-irradiation Workshop-Oxford 26-28/09/2011
Poster:
THERMAL DIFFUSION PROFILE BY NRA OF DEUTERIUM IMPLANTED IN SOLID BREEDER BLANKET MATERIALS
E.Carella, Q.Zhao, M.González, R.Gonzalez-Arrabal

15th International Conference on Fusion Reactor Materials, Charleston, South Carolina, USA, 16-22 October 2011.
Poster:
ANALYSIS OF H AND HE IMPLANTATION BEHAVIOUR IN FUSION SOLID BREEDERS USING ION BEAM TECHNIQUES
E. Carella, M. González, MT. Hernández, D. Jiménez-Rey and R. González-Arrabal.

2° Workshop Programa TECHNOFUSIÓN-CM, Madrid, Spain 18-19/06/2012
Contribución oral:
ANÁLISIS DE IMPEDANCIA EN CERÁMICAS DE LITIO EXPUESTAS A RADIACIÓN GAMMA
E. Carella, M. González, M.T. Hernández

Electroceramics XIII – Univ. of Twente, Enschede, Netherlands 24-27/06/2012
Poster:
IMPEDANCE SPECTROSCOPY ON LITHIUM-BASED CERAMICS
E.Carella, M.González, M.T. Hernández

International Workshop on the "Modification an Analysis of Materials for Future Energy Source", Energy 2012, Madrid-CMAM/UAM, 17-20/09/2012

Contribución oral:
^{3}He BEHAVIOR IN Li_2TiO_3 CERAMICS FOR FUSION BREEDING BLANKET APPLICATIONS
E.Carella, M.González, T.Sauvage, R.Bès, B.Courtois, R.Gonzalez-Arrabal, D. Jiménez-Rey

21st International Conference on Ion Beam (IBA–2013), Seattle, Washington, USA, 23-28/06/2013
Poster:
NUCLEAR REACTION ANALYSIS AS A TOOL FOR THE ^{3}HE THERMAL EVOLUTION IN Li_2TiO_3 CERAMICS
E.Carella, T.Sauvage, R.Bès, B.Courtois, M.González

17th IEA International Workshop: Ceramic Breeder Blanket Interactions (CBBI-17), Barcelona, Spain 12-14/09/2013
Contribuciones orales:

1. INFLUENCE OF THE MICROSTRUCTURE ON THE LIGHT SPECIES BEHAVIOUR IN CERAMIC BREEDER BLANKET MATERIALS
   E.Carella, R. Gonzalez-Arrabal, Q.Zhao, A.Ibarra, M.Gonzalez

2. CORRELATION BETWEEN ELECTRICAL BEHAVIOUR AND TRITIUM RELEASE IN γ-IRRADIATED Li_4SiO_4 BREEDER PELLETS AND PEBBLES
   E.Carella, T.Hernandez, A.Ibarra, E.Chinarro, B.Moreno

11th International Symposium on Fusion Nuclear Technology, Barcelona, Spain 16-20/09/2013
Poster:
ON ION IMPLANTATION AND DAMAGE EFFECT IN Li_2TiO_3 AS A FUSION BREEDER BLANKET: A TECHNOLOGICAL APPROACH FOR IN-SITU DEGRADATION TESTING
E.Carella, M.Leon, T. Sauvage, M.Gonzalez